KINETICS AND THERMODYNAMICS OF DYE (GROUP VIII METAL)-SENSITIZED NANOCRYSTALLINE TITANIUM DIOXIDE PHOTOELECTRODES

Thesis by

Elizabeth Idonia Mayo

In Partial Fulfillment of the Requirements for the

degree of

DOCTOR OF PHILOSOPHY

CALIFORNIA INSTITUTE OF TECHNOLOGY

Pasadena, California

2004

(Defended June 3rd, 2004)

This thesis is dedicated to my grandmother,
Sarah Ethel Schultheis,
despite the fact that she never wanted me to be a scientist.

ACKNOWLEDGEMENTS

As I began to compose this ever important acknowledgements section, it became clear that I owe a great deal to many people: my advisors, my colleagues, fellow students, my family and my friends. After a grueling two months of non-stop writing and editing, it is a wonder that I have any family or friends left at all, let alone ones as wonderful and reliable as they. The thesis writing process is a miserable rite of passage which, in my case, involved fits of anger that would have rivaled Attila the Hun and bouts of depression that made the wall street stock-market crash of 1929 look like a bull market. Yet somehow, they all managed to stand by me and support me through all of it.

I will begin with directly thanking my collaborator and friend, Dr. Kristine Kilså Jensen. Without her, this would have never happened. She motivated me from the very beginning to push ahead, to plan projects with an end goal in mind, not just the endless rambling through experiments that I had previously called my technique. She counseled me more than I can begin to cover here. The majority of the work presented here was done in collaboration with Kristine, and full chapters represent weeks of our standing side-by-side in the laser lab and of our tag-teaming various experiments. Kristine forgave my many flaws, or has hopefully done so by now. The most difficult for her to accept was undoubtedly my ability to be so easily distracted. What began as a working relationship, rapidly turned into a friendship that involved evenings of Kubb playing; strange Swedish food that looked funny – but tasted awesome; a late night trip to Mexico; and some very unhealthy alcohol that tasted a lot like isopropanol. Kristine is now a professor in Copenhagen and I have the utmost confidence that she will be a great advisor, as she was in many ways my advisor here at Caltech.

As for my official advisors, I was lucky enough to have two of the greatest bosses, Harry B. Gray and Nathan S. Lewis, that Caltech has to offer. I am often asked if I got to do it over again, would I still choose a joint project. The answer requires no thought on my part, because although frustrating at times (two group meetings, two sets of paper revisions, etc.), I have learned so much from both of my advisors, that I can't imagine having it any other way. I am truly lucky in that no matter what endeavor I choose to undertake, between Harry and Nate I will have more support in my corner than anyone could ever ask. I will cover my thanks to them in alphabetical order so neither will feel slighted.

Harry is one of the many reasons I came to Caltech. The first time I met him, he drank me under the table and told me to come to Caltech and do some science. From the first day I walked onto campus, Harry has always greeted me with a hug and smile. He supported me to no end. I was always amazed by his ability never to lose sight of the big picture in the midst of many failures. Harry's advisory abilities went far beyond mere science and he has counseled me in life and love, often over many glasses of wine. Harry embraced my mischievous nature and always encouraged my numerous prankish activities. I will miss Harry both professionally and personally, and I am a better person for having known him.

Nate was my main advisor for my first two years and taught me the bulk of the science I needed to undertake this project. Nate always had a suggestion about what to do next, and while none of them only took five minutes, they were always just what I needed to kick start the project again. He is one of the smartest people I have ever met, and when I can keep up with him, we have very enjoyable scientific discussions. Outside

of science, Nate enjoys spending time with his group. Over the years, there have been horseback riding, mountain biking, keg stands, bonfires and some pretty impressive bouncy castle action. Nate also taught me that even when you're right, you can't always win. I'm not sure what will happen when I don't have Nate to keep me in check, but I guess the rest of the world is about to find out.

Continuing on a professional note, I would like to acknowledge my committee for their support over the last five years. One of the nicest things about Caltech is the wonderful, supportive attitude of all of the faculty. Jackie Barton, my committee chair, has always had an open door for my impromptu visits. She supported my efforts to prevent the installation of Vectors and more importantly, counseled me on knowing when to walk away. She has always been honest with me (often brutally so) and her advice has been sound. Brian Stoltz renewed my faith in academics. His ability to be an outstanding new faculty, while maintaining outside interests and raising a family is nothing short of amazing. Even as a young faculty, he appears to have the student's interest at the forefront of his thoughts and his lectures are nothing short of legendary. And while his cart driving skills are slightly less than par, he can certainly rock! I got to know Bill Goddard my first year here at Caltech when I took his class. Over the last five years, it has been my pleasure to get to know him as more than a professor. I have worked with his family, judging local science fairs, crashed more than one of his parties, and no one appreciates being part of a prank more than Bill. He personally funded the DVD project by buying so many calendars. Overall, I am lucky to be able to look at my committee as more than just a group of faculty who will sign off on my degree, but as my friends and colleagues.

This degree will be especially nice because now I will no longer have to endure the endless barrage of questions from my family about when I am going to graduate. Despite much teasing about being a permanent student, I would like to thank my parents for all the support, both emotional and financial, over the years. My cousin, Gwynn, has been a key motivator always telling me to keep writing. In particular, she was a wonderful resource while job hunting. Sharon, my best friend since high school, has been my most ardent supporter. She has listened to me vent and whine and brag and complain about everything Caltech related. She has always been on my side, even when I was wrong. Despite the fact the we have a bicoastal friendship, the joy of the cell phone makes it feel like she's right here.

From my very first summer, I have had the opportunity to work with a number of very talented undergraduate researchers. Having undergrads constantly asking you questions will very quickly teach you what you don't know, but probably should. I have been very lucky in the undergrads I have worked with (Mark Baker, Cody Geary, Dan O'Hanlon, Carey Tanner, Bryan Tiedemann, Tim Tirrell, Kevin Trotter, Don Walker and Sina Yeganeh) and would like to take this opportunity to thank them.

Jay Winkler, the director of the Beckman Institute Laser Resource Center, has been a well of good advice and discussions; and I think I might have actually see him smile twice. My lab and office space are a part of the Molecular Materials Resource Center. Michael Freund was the director of this center when I first arrived at Caltech. He was an amazing resource, with an abundance of suggestions and advice regarding my project. The mixed halide project arose from a discussion with him regarding some papers he had read. I was lucky enough to become friends with him and his family

during his time here. Michael was not a person to wait around to be pranked on and I would like to commend him for his creativity in executing an excellent preemptory prank. I would never have imagined that anyone could truly fill the expansive shoes left by Michael, until I met Bruce Brunschwig. Bruce has always had an open door for me (when it wasn't locked) to discuss science, and pretty much any topic you can imagine. He has listened to enumerable tantrums and rants without ever holding them against me. Bruce was a never ending font of knowledge and support, without which, I don't know that I could have survived the last year.

Anyone who says there aren't enough strong women in science, hasn't met "The Committee." Cora MacBeth, Wendy Belliston Bittner, Yen Nguyen and I have spent many an evening talking science, our futures, putting together FRESH, and discussing politics and songs. Wendy has been a close friend, and many a bottle of wine has been consumed while commiserating together. It is hard to imagine a day without a coffee break, lunch break, dinner break or evening drink with Wendy. Cora has always looked out for my best interests and has a love of science that is unparalleled. Yen has not only been a part of the committee, but has been my roommate and pool protégé. Lauren Webb has been both a great lab mate and a true friend. The last four years with Lauren have been filled with chick flick nights, chats about world politics and religion, general gossip, and most importantly, Six Flags. I would like to especially thank Lauren and Wendy for all the time they devoted to helping me edit this thesis. Only a true friend will tell you when you are writing gibberish and be willing to read it again afterwards. Dave Michalak has been my friend from my first visit to Caltech. He has always been ready to undertake some outside enterprise, some of which he ran and some which I did. Dave

and I make a good team no matter what the project and hopefully we will still have endeavors together for years to come. Julie Fry was always willing to kidnap me and whisk me away for a day at the track or a night of karaoke. My officemates, Colin Cameron, Brian Sisk, Jeremiah Miller and James Harris (both old and new), have been ever patient with my rather odd taste in music and have been a handy distraction for many a conversation. One of them even enjoyed working with me so much that they went and got the same job I did, just so they could share an office with me again. I would also like to thank Colin Cameron, Brian Leigh, Dave Michalak and Brian Sisk for all the good times working on the various prank-related projects.

I can't leave Caltech without acknowledging all of the many people who have helped me take care of the "details" for the last five years. Catherine May and Rick Jackson, have booked every BI function and/or party. No matter what my need, they knew who to talk to or were willing to find out for me. Nannette Pettis and Sherry Feick have to be acknowledged, not just for everything they did for me, but for their seemingly never-ending patience in general. I would like to thank Dian Buchness, Chris Smith and all of the people in Noyes: Steve Gould, Tom Dunn, Ann Penney, Margaret Collins and Suzette Furbeyre, for five years of great conversations and problem solving (anyone who knows me, knows I can create problems). They have always had an open door and a smile, thus making Caltech a more pleasant place to be.

I would be remiss to not thank the people who I have dealt with at Caltech outside of the realm of science. Bob O'Rourke always had a New England hello for me and encouraged my extra curricular activities. Denise Nelson Nash counseled me throughout

the many discussions regarding Vectors and was still willing to be my colleague afterwards.

I could never have survived my time at Caltech if it had not been for my very tight circle of outside friends: Cindy Hahm was my travel buddy over the years and many a late night phone call brought the necessary pep talk. Dawn Davis was always happy to listen and forgave a very unpleasant gummy bear incident. Dave (Bubba) Brinza is one of the more brilliant people I know. As a former techer, he always knew what to say to make the process endurable. In the last few years of my degree, Ellen and Sergio have always been there to supply me with guacamole and margaritas and to understand when I'm too busy to talk. My Paracel friends have been key to my sanity, providing a place to vent and get away. In particular, my lunches with Jane Culbertson and the many evenings of distraction with Dave (Monica) Morrell and Tristan Gill must be acknowledged.

This dissertation is dedicated to my grandmother, Sarah Ethel Schultheis, because I inherited every stubborn bone in my body from her, and a Ph.D. is 90% about persistence. Even though she never wanted me to be a scientist (and she more than made sure I was aware of it), she was always proud of me and encouraged me. And in closing, I would like to thank one of my former high school teachers and now friend, Linda Ellis, for always counseling me to be "a sweet and wonderful child, not an evil, rotten one." I'm not sure if I've succeeded, but I've tried.

ABSTRACT

This thesis reports a comprehensive series of experiments involving complementary kinetics and thermodynamic measurements directed at isolating the important individual reactions in dye-sensitized nanocrystalline titanium dioxide solar cells (DSSCs). These experiments were done in conjunction with steady-state photoelectrochemical measurements; a combination which allowed a greater understanding of the overall mechanisms and driving forces of these systems.

Alternative two-electron redox couples were studied and efficiency increases of >40% were achieved when compared to similar systems using iodide/triiodide. Surface treatment with carboxylic acids minimized direct reduction of the redox couple by electrons in the titanium dioxide, and interestingly, the photocurrent also increased resulting in overall efficiency increases as high as 20%. Bridging ligands were used in an attempt to minimize recombination of the injected electrons with the resulting oxidized dyes, but DSSCs with these sensitizers showed poor conversion efficiencies and no distance dependence for injection or recombination was observed. The lack of distance dependence was attributed to the flexible single carboxyl anchoring group. To further investigate the effect of binding mode, a series of carboxyl-modified ruthenium bipyridyl sensitizers were studied. A single carboxyl anchoring group resulted in unstable DSSCs due to enhanced desorption as well as poor photon-to-current conversion efficiencies. These dyes injected efficiently into TiO_2 on the nanosecond timescale, and regeneration of the oxidized sensitizers competed effectively with recombination. Consequently, individual kinetics measurements could not explain the decreased steady-state

performance. The regeneration rates of these dyes in solution were found to rapid, approaching the diffusion controlled limit. The regeneration rate was dependent on the number and electron-withdrawing nature of the pendant groups, with the rate decreasing with increasing number of electron withdrawing substituents. Iridium dyes with cyclometalating ligands were shown to be efficient sensitizers in DSSCs, with quantum yields on the order of a ruthenium analogue having similar spectral overlap. Overall, the repeated inconsistencies between the steady-state behavior and the measured individual kinetics processes indicate that the current kinetic model is insufficient to accurately predict photoelectrochemical behavior.

TABLE OF CONTENTS

LIST OF FIGURES

Page

Chapter I. Semiconductor/Liquid Junctions

Chapter II. Instrumentation and Experimental Techniques

Chapter III. Increased Efficiencies with Alternative Redox Couples

LIST OF TABLES

CHAPTER 1:

SEMICONDUCTOR/LIQUID JUNCTIONS

Chapter 1

SEMICONDUCTOR/LIQUID JUNCTIONS

Environmental and economic questions regarding the control of air pollution and carbon dioxide emissions have motivated the development of alternatives to carbon-based energy sources. In light of these concerns, solar energy can easily be considered the most attractive renewable energy source as it is abundant, clean, safe and allows for energy generation in remote areas.[1]

The average intensity of sunlight just outside the atmosphere is 1366 W m^{-2} (the solar constant). Solar radiation is unevenly distributed around the globe, however, and varies in intensity from one geographic location to another depending upon the latitude, season, and time of day. Some of this massive amount of radiation is reflected back into space as it passes through the atmosphere. More still is absorbed by clouds and the air mass, driving the dynamics of the atmosphere. Even when these radiation losses are accounted for, the amount of solar radiation that actually reaches the surface of the earth amounts to no less than 12,000 TW. In 1998, the world energy consumption was reported as 12.8 TW (with the US accounting for 3.3 TW).[2] These numbers make it clear that solar power is an abundant resource that has the potential for playing a major role in the world's energy picture.

Solar energy conversion and storage can be achieved by a variety of photoelectrochemical processes (Figure **1**), with photosynthesis being the most obvious

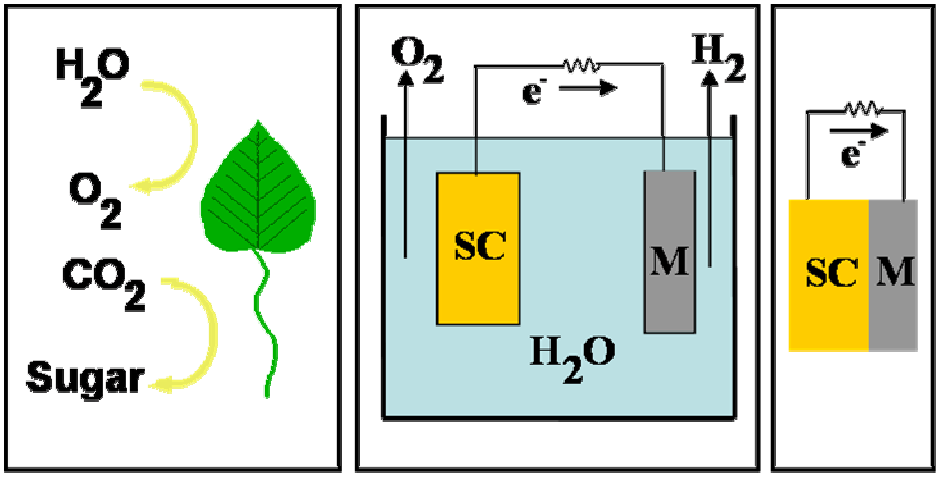

Figure 1. Solar energy conversion strategies. Schematic of common means by which sunlight can be converted to chemical fuels and/or electricity, where SC is a semiconductor and M is a metal: (a) photosynthesis (b) photoelectrochemical cells and (c) solid-state photovoltaic devices.

and successful example of production of chemical fuel (Figure **1**a). Over geological spans of time, photosynthesis has driven the production and storage of fossil fuels that are currently the primary power source worldwide. With average efficiencies for the conversion of sunlight into fuel of 3% to 5%, with an upper limit of 13%, photosynthesis does not offer much hope for supplying the planet with the large quantities of energy required to meet rising demands.[3] Furthermore, photosynthesis only produces chemical fuel, rather than electricity. The most efficient solar energy conversion approach employs solid-state photovoltaics consisting of a semiconductor/semiconductor junction. In particular, efficiencies as high as 28% have been reported for silicon photovoltaic devices (Figure **1**c).[3-6] However, the overwhelming cost of these devices, nearly an order of magnitude greater than conventional energy sources, is a major limitation to their widespread utilization.[2] Furthermore, these devices can only produce electricity, limiting their overall usefulness, because electricity comprises only ~15% of global energy use.[2] An alternative strategy is to use semiconductor/liquid junction solar cells that can produce both chemical fuels and electricity, depending on how the devices are constructed and the materials used (Figure **1**b).

The energetics of semiconductor/liquid junctions have been studied in detail, and a number of review articles have been written on this topic. Therefore only a brief description of the theory will be included here. Figure **2** illustrates the method by which an electric field is created at an n-type semiconductor/liquid interface. The equilibration processes at semiconductor/liquid junctions involving either n-type or p-type electrodes are so closely related that this discussion will be restricted to the case of an n-type

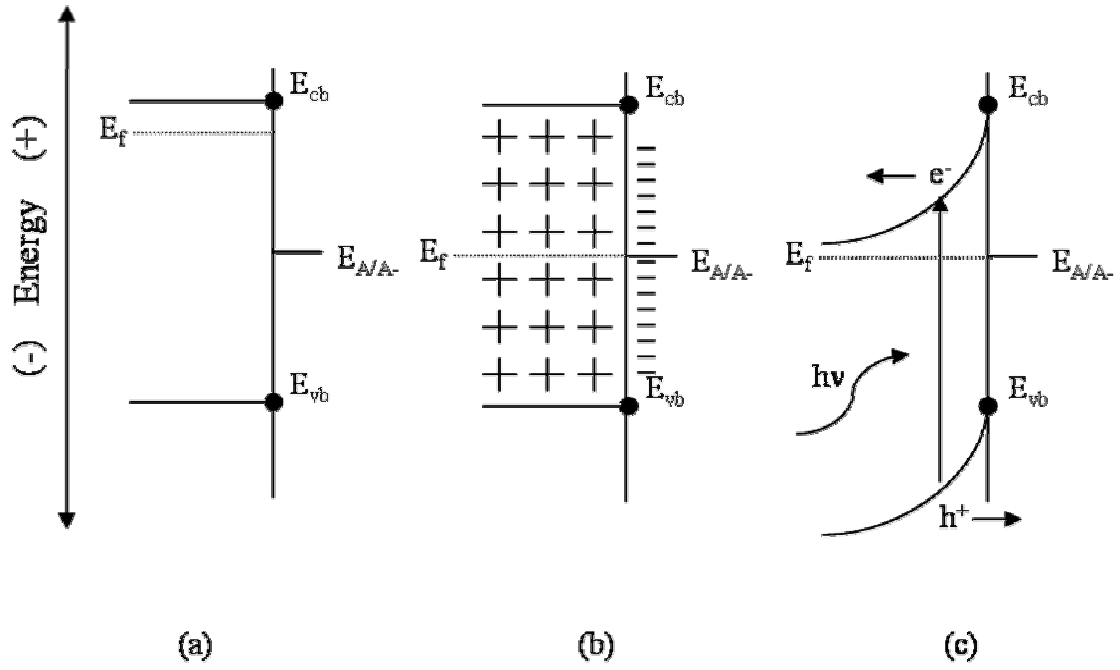

Figure 2. Band bending of an n-type semiconductor. The energy band diagrams of an n-type semiconductor in contact with a redox couple in solution (a) before and (b) after equilibration of the Fermi levels. (c) Integration of the charge distribution caused by ionization of dopant atoms with respect to position gives the electric field strength and a second integration yields the electric potential difference (band bending). Photo-initiated charge separation is driven by the electric gradient.

semiconductor, although an analogous model can be derived for p-type semiconductors. The electrochemical potential of the semiconductor is defined by its Fermi level (E_f), which is dependent on the dopant density (N_d). The solution electrochemical potential is determined by the Nerstian potential ($E_{A/A}$-) of the redox-active species in the particular solvent. Before charge equilibration, the energy bands are uniform and the entire semiconductor is neutral (Figure **2**a). Upon immersion of the semiconductor in the solution containing the redox active species, the electrochemical potentials of the two phases, (E_f) and ($E_{A/A}$-), respectively, must equilibrate (Figure **2**b). The potential drop required for equilibration primarily occurs through ionization of the dopant atoms in the semiconductor, creating an electric potential gradient which is often referred to as band bending.

Upon illumination, the semiconductor absorbs photons of sufficient energy to overcome the forbidden energy gap between the valence and the conduction bands (Figure **2**c). This results in the generation of an electron-hole pair when an electron is promoted from the valence band (VB) to the conduction band (CB), leaving behind a positively charged VB vacancy, or hole. The photoexcited electron moves away from the interface and is driven by the electric field toward an external circuit, while the hole migrates toward the semiconductor/solution interface. At the interface, the hole oxidizes an electron donor in solution. The electron enters an external circuit, and is then returned to the cell through a counter electrode, where the electron reduces the hole carrier in the electrolyte solution. While this electric field separates the electron and the hole, a finite concentration of electrons remains at the semiconductor surface. These electrons can

recombine with the redox species in solution and limit the overall efficiency of the photoelectrochemical energy conversion device.

The energy conversion capabilities of a photoelectrochemical cell rely on the ability of the semiconductor material to absorb a significant fraction of the solar spectrum and therefore on its band gap energy (E_{bg}). Unfortunately, many materials with appropriate band gaps for efficient absorption of solar radiation are susceptible to photocorrosion. Metal oxide semiconductors such as TiO_2 and SnO_2 are stable to corrosion, but have band gaps too large for significant collection of visible light.[7,8] The poor spectral sensitivity of these semiconductors can be overcome by adsorption of dyes with favorable spectral overlap (Figure **3**).

Absorption of incident radiation by a molecular sensitizer adsorbed onto the surface of a single crystal semiconductor will be limited by the low number of photons a monolayer of dye is capable of capturing. A successful alternative approach involves the use of high internal surface area films consisting of nanocrystalline oxide particles with diameters of 10 to 20 nm. Depending on the thickness of the film, surface areas on the order of 130 m^2/g can be achieved, more then 1,000 times greater than for a single crystal sample.[9,10] When light penetrates the dye-covered nanocrystalline network, it travels through hundreds of adsorbed dye monolayers and can be efficiently captured. A great deal of research has been done to maximize the properties of the nanocrystalline metal oxide phase and light harvesting efficiencies (LHE) as high as 97% can be readily achieved.[11]

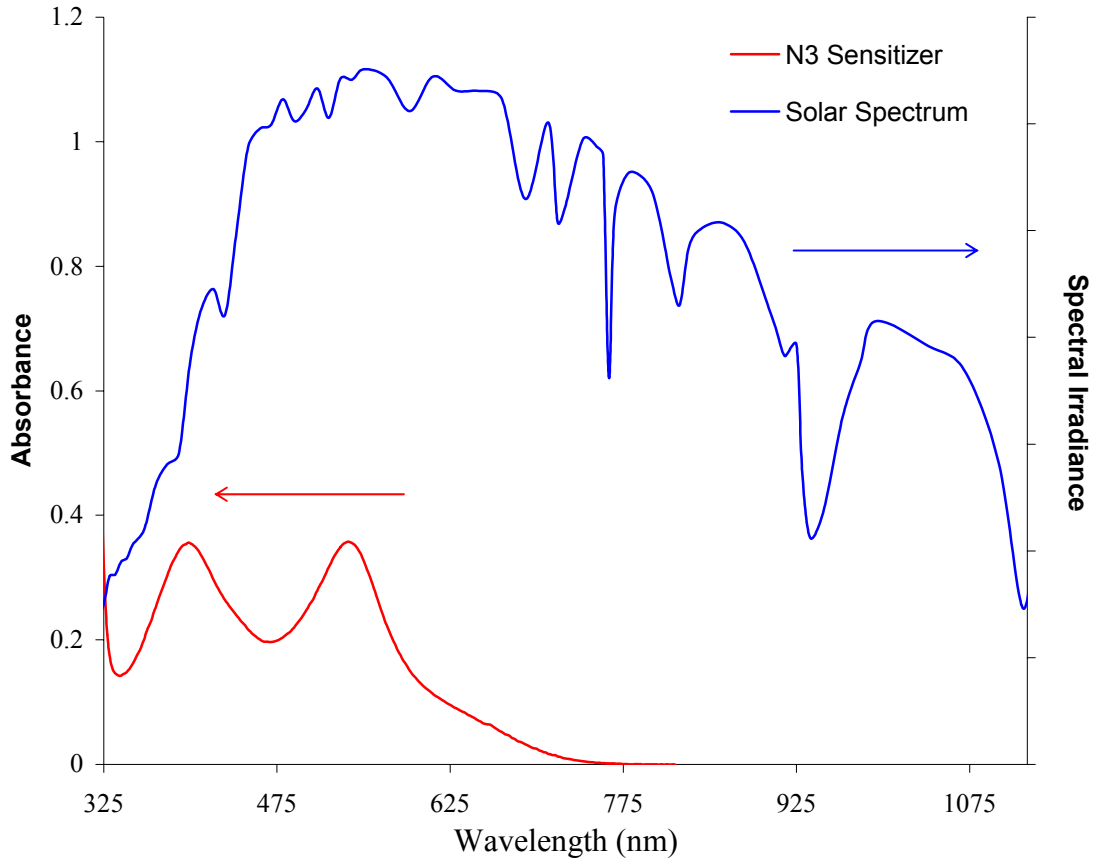

Figure 3. Spectral overlap of N3 at AM 1.0. Spectral overlap of Ru(4,4′-dicarboxylic acid-2,2′-bipyridine)$_2$(NCS)$_2$ (abbreviated as the N3 sensitizer).

These types of dye-sensitized nanocrystalline metal oxide semiconductors have shown promise for use in low-cost, efficient photovoltaic devices.[11,12] These systems incorporate a semiconductor/liquid junction with a sensitized, wide band gap semiconductor to achieve efficient charge separation under solar illumination. Such dye-sensitized solar cells (DSSCs) have been demonstrated to yield energy conversion efficiencies of >10% under AM (Air Mass) 1.0 conditions, which is defined as the relative path length of the direct solar beam radiance through the atmosphere when the sun is directly above a sea-level location.[13,14] The chemical stability of these systems has been reported to be adequate to provide a lifetime of >10 years in sunlight.[15] The low cost of the semiconductor materials used in DSSCs, combined with the ease of the junction formation, offers the potential for a significant improvement of the cost-to-efficiency ratio when compared with solid-state photovoltaic devices that use expensive single-crystal or large grain size semiconductors such as Si, GaAs and InP. In principle, efficiencies of >20% are attainable with DSSCs. If such an efficiency could be combined with stable long-term operation, estimates indicate that such a DSSC could substantially lower the cost of photovoltaic energy conversion relative to the cost per peak watt of conventional Si- or GaAs-based devices.[16]

Figure **4** shows a schematic of a typical DSSC. An inexpensive, nanocrystalline semiconductor material, titanium dioxide (TiO_2), is sintered onto a conductive, fluorine doped tin oxide (SnO_2:F) coated glass substrate. Sensitization of the wide band gap semiconductor by a variety of inorganic and organic dyes can provide very efficient charge injection into the semiconductor. The high surface area of these mesoporous,

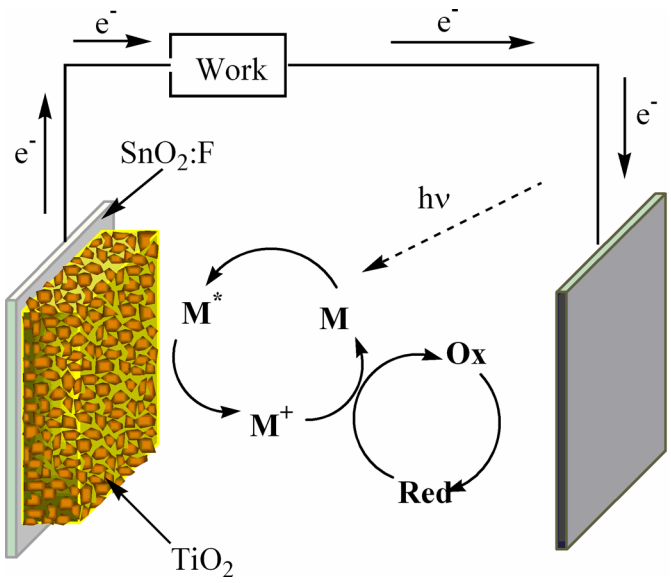

Figure 4. Schematic of a DSSC. Light absorption by the ground state of the adsorbed dye (M) results in the formation of an excited state (M^*) that injects an electron into the TiO_2. The resulting oxidized dye molecule (M^+) is reduced by the reduced species in the electrolyte (Red). The injected electron percolates to the SnO_2:F back contact producing a current before reducing the oxidized species in solution (Ox).

nanocrystalline TiO_2 films allows for nearly 100% absorption of incident light above the absorption threshold energy of the dye. The excited state of the dye then injects an electron into the conduction band of the TiO_2. Donation of an electron from a mobile redox species in the electrolyte solution subsequently regenerates the transiently oxidized dye. The injected electron percolates to the back contact, where it produces a current through an external load. The semiconductor nanoparticles (~10–20 nm) are not large enough to support an electric field (Figure **2**c), so transport of the injected electrons through the film is most likely driven by a concentration gradient. The oxidized redox molecule diffuses through solution to the counter electrode, where it can be reduced, completing the circuit. Therefore, no net chemical reaction occurs because every oxidation reaction at the photoelectrode has a corresponding reduction reaction at the counter electrode.

Figure **5** summarizes the essential electron-transfer processes in a typical DSSC. Initially, the inorganic sensitizer absorbs sunlight, resulting in the formation of an excited state with rate constant k_1. Excitation is followed by relaxation to the ground state, with rate constant k_{-1}, or by charge injection into TiO_2, with rate constant k_2. It has been shown that injection rates for most dyes proceeds on the femtosecond timescale,[17-19] whereas the lifetime of the dye excited state is on the order of nanoseconds, indicating that k_2 far exceeds k_1.[20] Once injected, the electron can percolate to the back contact of the SnO_2:F conductive layer to be collected (10^{-6}–10^{-3} s),[21] or the electron can be lost to recombination with either the oxidized dye (10^{-8}–10^{-3} s, rate constant k_3)[22] or by reaction with the hole carrier in the electrolyte solution (rate constant k_4). After passing through an

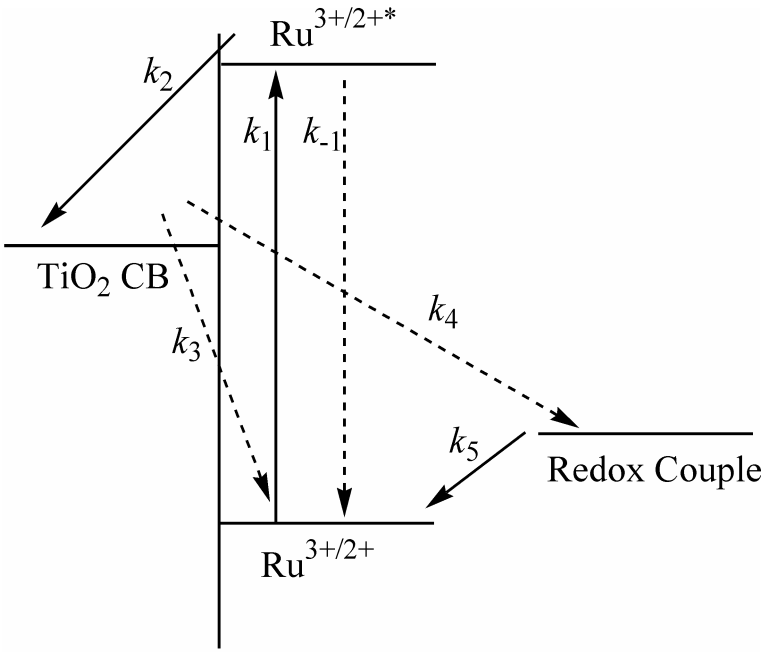

Figure 5. Rate processes in a ruthenium based DSSC. Current producing electron transfer processes (solid arrows) are absorption (k_1), injection (k_2) and regeneration (k_5). Deleterious back reactions (dashed arrows) are relaxation (k_{-1}), recombination with oxidized dye (k_3) and recombination with the electrolyte (k_4).

external circuit, the electron reduces the hole carrier at the counter electrode, which subsequently reduces the oxidized dye (10^{-8}–10^{-3} s, rate constant k_5).[23]

The power, P, produced by the solar cell is determined by product of the maximum photocurrent density (short-circuit current density, J_{sc}), the maximum photovoltage (open-circuit voltage, V_{oc}), and the fill factor (ff) (Eq. 1, Figure **6**).

$$P_{max} = J_{sc} \times V_{oc} \times ff \quad (1)$$

The value of J_{sc} depends on the sensitizer light absorption efficiency and on the electron injection efficiency. The value of V_{oc} is determined by the energetics of the system; the theoretical maximum attainable V_{oc} is determined by the energy difference between the conduction band and the electrochemical potential of the redox couple. The overall photon-to-current conversion efficiency (η) is defined by Eq. 2, where I_s is the incident light intensity.

$$\eta = (J_{sc} \times V_{oc} \times ff)/I_s \quad (2)$$

Recombination reactions will in effect reduce both V_{oc} and J_{sc}. Therefore, the performance of DSSCs depends on both the thermodynamic properties of the materials as well as the kinetics of the reactions occurring in the DSSC.

The nanoporous nature of the TiO_2 allows for migration of the redox couple throughout the metal oxide network which is crucial for efficient dye regeneration. However, injected electrons near the surface can be captured by the oxidized species in solution (I_3^-) resulting in reverse charge flow. This process can in principle take place not only at the TiO_2 interface, but also at the SnO_2:F back contact. This deleterious reaction

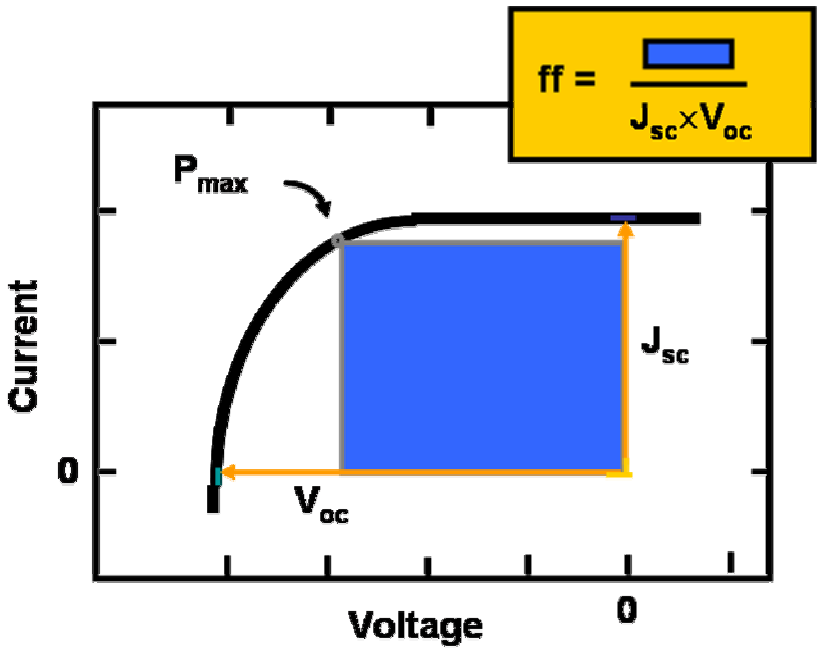

Figure 6. Parameters of a current-potential measurement of a DSSC. Illumination intensity (I_s); Short circuit current density (J_{sc}); open circuit potential (V_{oc}); maximum electric power produced (P_{max}); fill factor (ff).

is often referred to as the dark current and can be estimated by the electrochemical properties of the DSSC in the absence of illumination.

Currently, a key barrier to achieving higher efficiency DSSCs is a lack of understanding of how to alter or replace the molecular components of the cell with alternative materials that will increase the photovoltage while maintaining high photocurrents. The most efficient DSSCs to date use a Ru^{2+}-bipyridyl based dye with two isothiocyanate ligands adsorbed on a nanocrystalline TiO_2 electrode through carboxyl groups on the bipyridine ligands (Figure **7**). This dye-coated electrode is immersed in a non-aqueous solution containing the I_3^-/I^- redox couple.[14,24] Upon absorption (Figure **5**, k_1), an electron is promoted through a metal to ligand charge transfer (MLCT) process from the t_{2g} orbital on the ruthenium metal center to a π^* orbital on a bound bipyridyl ligand. While providing high current densities under illumination, this combination of materials results in a thermodynamic limitation on the maximum attainable photovoltage, due to a less than optimal separation of the Fermi level of the redox couple and the conduction band edge of the semiconductor. While there have been many design iterations, few have resulted in substantial increases in overall conversion efficiency.[12,14] A more accurate and detailed description of the individual mechanisms of charge-transfer in DSSCs is necessary for a rational approach to improving such systems.

The current theoretical model is not able to describe the overall system with broad and accurate predictive power. Still largely unclear is the driving force for electron injection, transport and collection, the nature of the acceptor states on the TiO_2 surface, and a microscopic description of the dye regeneration mechanism by the redox

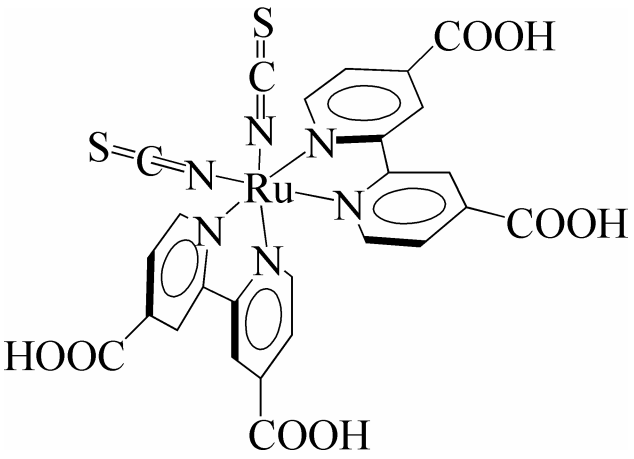

Figure 7. Structure of the N3 dye. Ru(4,4′-dicarboxylic acid-2,2′-bipyridine)$_2$(NCS)$_2$ (referred to herein as [Ru(H_2L')$_2$(NCS)$_2$]^0).

couple.[13,25,26] Perhaps most baffling is the difficulty in finding a redox couple other than I_3^-/I^- that allows realization of comparable solar energy conversion efficiencies.[27-29]

Several approaches are possible to achieve an increase in the conversion efficiencies of DSSCs. These can be generally divided into kinetics and thermodynamic approaches. This thesis is a comprehensive series of experiments involving complementary kinetics and thermodynamic measurements directed at isolating the important individual reactions of the system. These measurements were done in conjunction with steady-state current density vs. potential measurements such that the discrete pieces of information, when put together, will allow for a greater understanding of the overall mechanisms and driving forces of these systems. The chemical aspects of the light absorption and charge separation, the interfacial dynamics that affect injection and recombination, and the interaction between the molecular and semiconductor components of the system have been studied.

CHAPTER 2:

INSTRUMENTATION AND EXPERIMENTAL TECHNIQUES

C h a p t e r 2

INSTRUMENTATION AND EXPERIMENTAL TECHNIQUES

Materials

Chemicals

Lithium iodide (Alfa, 99%, anhydrous) was used as received and was stored under N_2(g) in a dry box until use. Iodine (Aldrich, 99.99%+) was sublimed under vacuum before use. Pyridinium triflate (Aldrich) was purified by dissolving the material into a minimum amount of warm acetonitrile and precipitating the salt by addition of diethyl ether. The precipitate was filtered through a medium-porosity glass frit and was washed with ether and then dried overnight under vacuum. Pyridine (J.T. Baker) was distilled before use. Anhydrous lithium perchlorate (Aldrich) was dried at 180°C for 48 h under active vacuum. All solvents used were reagent grade (EM Science), except for absolute ethanol, which was purchased from Quantum Chemicals. Acetonitrile was distilled over CaH_2 under N_2(g). Films of nanocrystalline TiO_2 (crystallite size ~15 nm) that were 10 μm thick were prepared by screen printing on conductive glass (SnO_2:F) substrates (Institut für Angewandte Photovoltaik, Germany).

1,1′-dimethyl-4-4′-bipyridinium (referred to throughout as methyl viologen or MV^{2+}) dihexafluorophosphate was prepared via salt exchange from the dichloride salt (Aldrich, 98%) as follows: a saturated aqueous solution of ammonium hexaflurophosphate (Aldrich) was added dropwise to a saturated aqueous solution of

methyl viologen dichloride. Upon cooling in an ice bath, the PF_6^- salt precipitated as a white solid. The solution was filtered and washed with H_2O and dried under vacuum. The freshly prepared methyl viologen PF_6^- salt was stored in a vacuum dessicator to prevent decomposition.

Dye Compounds

The standard dye for use in DSSCs is Ru(4,4′-dicarboxylic acid-2,2′-bipyridine)$_2$(NCS)$_2$ (referred to herein as $[Ru(H_2L')_2(NCS)_2]^0$ or abbreviated as the N3 dye) (Figure **7**). An analogue of this dye uses cyano ligands in place of the thiocyanates, Ru(4,4′-dicarboxylic acid-2,2′-bipyridine)$_2$(CN)$_2$ (referred to herein as $[Ru(H_2L')_2(CN)_2]^0$). Both of these dyes were purchased from Solaronix and were used as received. A series of ruthenium trisbipyridine derivatives were also used, $[Ru(H_2L')_3]^{2+}$, $[Ru(H_2L')L_2]^{2+}$, and $[Ru(HL'')L_2]^{2+}$ where L is 2,2′-bipyridine, H_2L' is 4,4′-dicarboxylic acid-2,2′-bipyridine, HL" is 4-carboxylic acid-4′-methyl-2,2′-bipyridine. L′ and L″ are the corresponding deprotonated carboxylate bipyridine ligands. With the exception of $[Ru(HL'')L_2]^{2+}$, the synthesis of these dyes and their osmium counterparts have been previously described, and these dyes were available in our labs.[30]

The monocarboxylated ligand, L'', was obtained by oxidation of 4,4'-dimethyl 2,2'-bipyridine as follows:[31] a solution of 4,4-dimethyl 2,2'-bipyridine (0.2 M) was refluxed with selenium dioxide (SeO_2, 0.2 M) in 1, 4 – Dioxane (50 mL) under N_2 for 24 h. The solution was filtered while hot to remove precipitated Se and was allowed to equilibrate. The filtrate was evaporated to dryness and was recrystallized in ethyl acetate. The $[Ru(HL'')L_2](PF_6)_2$ complex was synthesized in the same manner as

$[Ru(H_2L')L_2](PF_6)_2$ except that L′′ was substituted for L′ in the synthesis.[30,32] The counter ion for all $[Ru(bpy)_3]^{2+}$-type dyes was PF_6^-.

Preparation of Dye-coated Electrodes

TiO_2 strips were cut to 0.5 inch wide x 15 mm long electrodes, with care taken to avoid contact with the TiO_2 surface. The exposed bare electrode surfaces were cleaned with acetone and the TiO_2-coated surfaces were covered with 3-4 drops of 0.2 M $TiCl_4$(aq) and allowed to sit overnight. The 0.2 M $TiCl_4$ solution was unstable and was freshly made before each use from a stable 2 M stock solution prepared as previously reported.[30] The $TiCl_4$-coated electrodes were rinsed with nanopure water and ethanol, dried with nitrogen, yielding a freshly prepared hydroxylated titania surface. The slides were sintered in a tube furnace under flowing air at 450ºC for 30 minutes and then at 120ºC for 2 h. The electrodes were removed from the furnace and immediately submerged in ethanol solutions of 20 mM dye. Unless otherwise stated, the electrodes were left in the dye solutions for at least 24 h to achieve maximum dye adsorption. For experiments where similar dye coverages were required, dye adsorption was monitored by UV-vis spectroscopy of the MLCT absorbance max with correction for differences in extinction coefficients. Non-bound dyes were removed by rinsing and drying the slides before measurement. When the desired coverage was achieved, the slides were placed in a N_2(g) purged dessicator until use, typically within 24 h.

Electrolyte

The electrolyte was 0.5M LiI and 0.04M I_2 with 20 mM pyridine and 20 mM pyridinium triflate unless otherwise mentioned. The pyridine and pyridinium triflate were included to act as a pH buffer to prevent dye desorption and to stabilize the conduction-band edge of the TiO_2. In experiments where the concentration of the lithium iodide was decreased, lithium perchlorate was added to maintain a 0.5 M cation concentration unless otherwise noted. Solutions were sensitive to oxygen and were prepared and stored under N_2. All electrolytes were prepared the day prior to beginning experimentation and were allowed to sit overnight. Solutions were used within three days of preparation.

Electrochemistry

Cell Photoelectrochemistry

Current-potential (*I-V*) measurements were recorded using a custom three electrode configuration with a platinum wire pseudo-reference electrode in contact with the solution and with a platinum gauze counter electrode (Figure **8**). The dye-coated TiO_2 slide acted as the working electrode. The distance between the working and counter electrode was 2 mm and measurements were made in the absence of stirring. Electrolyte was injected into the cell from the lower port and the data were obtained with the cell upright to prevent air bubbles. Illumination was achieved using a 150 W Oriel solar simulator with a 385 nm long pass filter to prevent direct excitation of the TiO_2. Illumination was through the back of the working electrode (dye-coated TiO_2 sample) which had an illumination area of 0.25 cm^2. The "back" of the electrode is defined as the

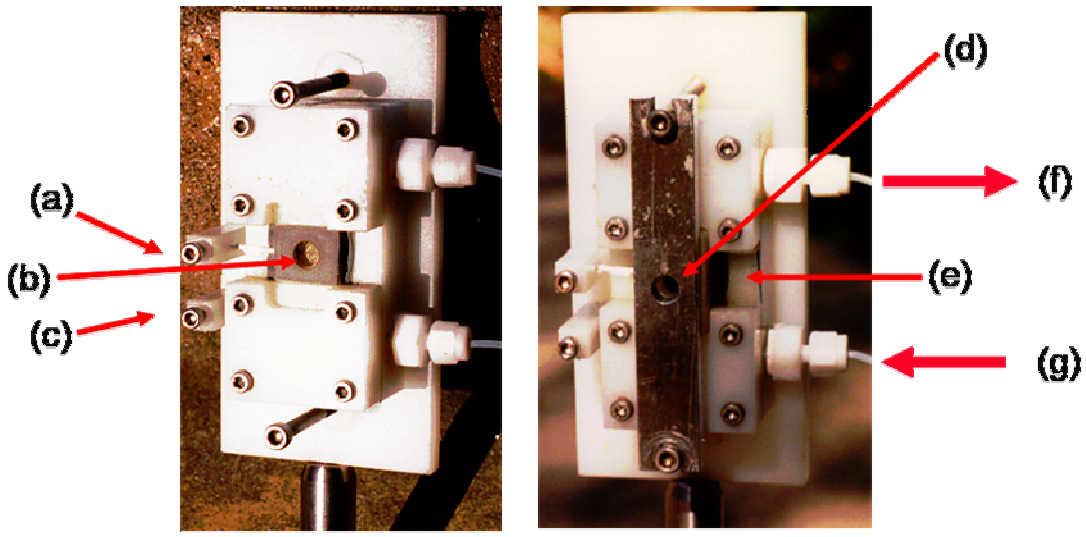

Figure 8. Custom three electrode cell holder. (a) Electrode connected to a platinum wire pseudo-reference electrode (not shown) in contact with the solution; (b) platinum gauze counter electrode in contact with the solution and opposite the TiO_2 working electrode (distance 2 mm); (c) electrode connected to the platinum gauze counter electrode; (d) cover plate that controls the illumination area to 0.25 cm^2; (e) TiO_2 slide working electrode in contact with the solution. Electrolyte was injected into the cell from the lower port (g) and flowed through the cell and exited through the upper port (f), preventing air bubbles.

non-coated side of the glass. As such, illumination occurred through the glass slide and the SnO_2:F coating before reaching the TiO_2 layer. A Solarex, Inc. diode was used to calibrate the incident light intensity. All curves were measured using a BAS 100B potentiostat. Typical parameters for an *I-V* measurement were from 200 mV to -600 mV and back to 200 mV with a scan rate of 20 mV s^{-1}. All curves were corrected for uncompensated cell resistance which was measured in the same cell except that a platinum working electrode was used instead of the TiO_2 electrode. Two cell holders were used for the experiments described herein with the predominant difference being the existence of a back window in one cell holder for use in transient kinetics experiments. The cell resistance differed slightly between the two cells (64 Ω for the holder with the back window and 52 Ω for the other). Corrections to the current-potential curves were made using the appropriate cell resistance value.

Solution Electrochemistry

Solution electrochemistry was performed using a simple three electrode configuration in which the working electrode was either a piece of platinum foil or a TiO_2 slide that had been modified to remove any non TiO_2-coated SnO_2:F surface. In all cases a platinum wire was used as the counter electrode. As these water-sensitive measurements were typically performed in acetonitrile or ethanol, a custom methanolic saturated calomel electrode (SCE) was used as the reference electrode (Figure **9**). The methanol SCE was prepared as follows: a modified H shaped glass tube was custom made with an outer diameter ~4–5 mm. A platinum wire was folded in half and twisted around itself to make the wire more durable. The wire was cleaned with an acidic

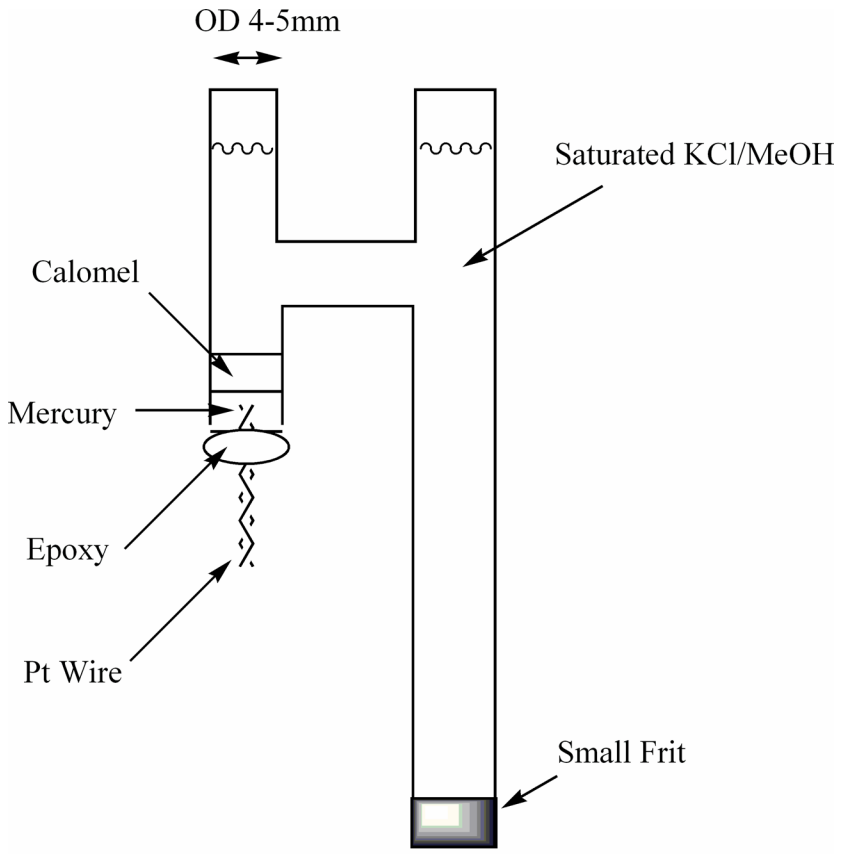

Figure 9. Methanolic saturated calomel reference electrode (MeOH SCE). Non-aqueous reference electrode filled with a saturated solution of potassium chloride (KCl) in dry methanol (MeOH).

solution (1:3 nitric acid:hydrochloric acid), rinsed and dried. The platinum wire was epoxied into the bottom part of the shorter tube opening with care taken to prevent the wire from touching the inner glass walls. The epoxy was allowed to set overnight and then heated at 125ºC for 1 h. A frit (small) was attached to the bottom of the longer tube using heat shrink tubing. A minimal amount of mercury was added to the shorter tube to ensure full coverage of the platinum wire. An equal amount of mercurous chloride (calomel) was layered on top of the mercury. The completed electrode was filled with a saturated solution of potassium chloride in methanol with care taken to prevent air bubbles. The methanol SCE was stored capped at the two top openings and the frit was submerged in a saturated KCl/methanol solution until to use. The MeOH SCE was calibrated versus an aqueous SCE (23 mV MeOH SCE vs. aq. SCE).

Transient Spectroscopy

Luminescent decay and transient absorption spectra were recorded with a nanosecond time-resolved flash photolysis instrument (NS1). A simplified schematic of this custom-made setup is shown in Figure **10**. The essentials of this instrument have been described previously,[33,34] so only a few points will be covered here. The pump source for NS1 was a Spectra-Physics Nd:YAG laser coupled with a master optical parametric oscillator (MOPO). The Nd:YAG unit produced pulses at 1064 nm with a 10 ns duration. The near-IR pulse energy is tripled, resulting in pulses at 355 nm of approximately 300 mJ/pulse. The 355 nm coherent beam was used to drive the MOPO and produced light that was tuned over the region of interest (400 – 800 nm) at approximately 40 mJ/pulse. For sample measurements, the excitation power was

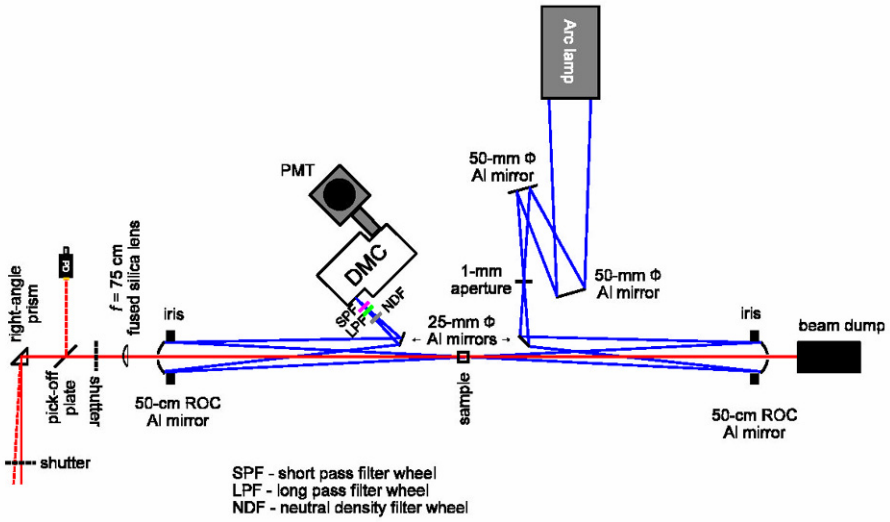

Figure 10. Diagram of the nanosecond 1 (NS1) system. The Nd:YAG laser excitation source (red line) is not shown.

modulated with neutral density filters to yield pulses with energies between 1 and 3 mJ/pulse. The probe light was provided by a 75 W Xe arc lamp that was operated in either continuous wave or pulsed mode. This lamp was pulsed for a 500 μs duration, allowing for a greater signal-to-noise ratio for timescales less than 500 μs. For measurements on timescales greater than or equal to 500 μs, the lamp was not pulsed. A 385 nm long pass filter was placed in the probe beam to prevent direct band gap excitation of the titanium dioxide.

The laser and probe beams were collinear, and the sample was blocked from excess excitation and probe light by computer-controlled shutters. Scattered excitation light was rejected from the detection system by use of suitable long pass or short pass filters. After striking the sample, the probe beam passed through an Instruments SA DH-10 monochromator with 1 mm slits (spectral resolution ~5 nm). The transmitted light was detected with a photomultiplier equipped with a R928 photocathode. Data sampling was at 200 MHz, and the time resolution of the entire spectrometer system was ~10–20 ns. The same apparatus was used to measure nanosecond luminescence transients.

The emission decay and transient absorption spectra were fitted to a series of exponential decay functions: monoexponential (Eq. 3), biexponential (Eq. 4), triexponential (Eq. 5). The fits were optimized with a linear least squares regression method.

$$y(t) = c_0 + c_1 e^{-k_1 t} \tag{3}$$

$$y(t) = c_0 + c_1 e^{-k_1 t} + c_2 e^{-k_2 t} \tag{4}$$

$$y(t) = c_0 + c_1 e^{-k_1 t} + c_2 e^{-k_2 t} + c_3 e^{-k_3 t} \tag{5}$$

These functions are valid when the data represents one or more first-order reactions, and are not valid for more than three exponentials, as this can result in inaccurate fits.[35]

Kinetics Measurements

For dyes that are adsorbed onto the TiO_2 slides, the TiO_2 acts as the electron acceptor (Figure **11**a). Upon excitation of the ground state of the dye, an excited state is formed that undergoes ultrafast electron injection into the TiO_2, resulting in the photo-oxidized dye molecule and photo-reduced TiO_2. Quenching of the natural luminescence of the dyes upon adsorption to TiO_2 was used to determine the relative injection rates. The oxidized dye can either be reduced through recombination of the injected electron or through reduction by an electron donor in the system. The rate of recombination of the injected electrons with the oxidized dye was found by monitoring the bleach and recovery of the ground state after excitation.

Regeneration rates were similarly determined, except measurements were done in the presence of an electron donor. To study the regeneration rates of the dyes in solution, the dyes were oxidized using a flash/quench technique (Figure **11**b). In this method, excitation of the dye results in a reactive excited state. The excited state can then interact with an exogenous electron acceptor, commonly referred to as a quencher, because quenching causes an observable decrease in the lifetime of the excited state of the putative donor or acceptor. For all experiments described in this dissertation, methyl viologen was used as a quencher, with typical concentrations of 10 mM. The photo-oxidized dye molecule is conventionally referred to as an acceptor in that it will ultimately receive an electron for some kind of donor molecule. After the flash/quench,

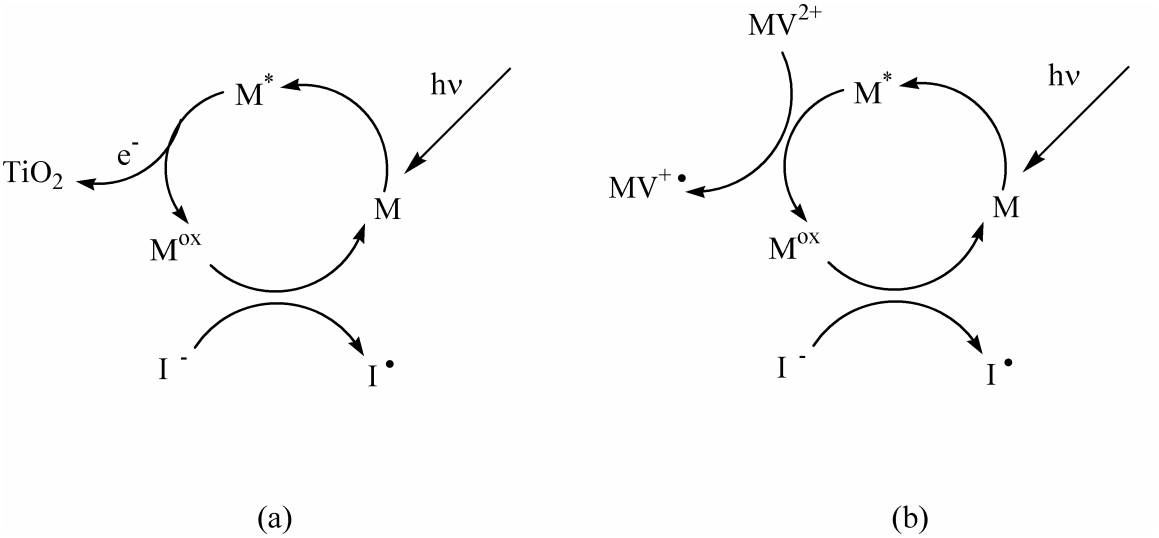

Figure 11. Kinetics measurement schemes. Illustration of measurement of the regeneration rates in (a) DSSCs and (b) solution. (a) Excitation of the inorganic sensitizer (M) results in the excited state (M^*) that is quenched by electron injection into the TiO_2. (b) Excitation of the inorganic sensitizer (M) results in an excited state (M^*) that is quenched by methyl viologen (MV^{2+}) in solution. The resulting oxidized dye (M^{ox}) in both schemes is reduced by the electron donor in solution (I^-).

the acceptor can then either react with the reduced quencher, MV^{+}, or with another electron donor in the system. For the studies herein, the electron donor was typically lithium iodide and electrolyte concentrations were 0.5 M LiI with 20 mM pyridine and 20 mM pyridinium triflate. When lithium iodide was absent or present in decreased concentration, lithium perchlorate was added to maintain a constant Li^{+} cation concentration.

CHAPTER 3:

INCREASED EFFICIENCIES WITH ALTERNATIVE REDOX COUPLES

Chapter 3

INCREASED EFFICIENCIES WITH ALTERNATIVE REDOX COUPLES

Introduction

Over the last 13 years, significant advances have been made in the fundamental understanding of the operation of DSSCs. However, despite this massive effort, there has been little improvement in the overall energy efficiency, with the highest reported efficiency (10.4%) [14,24] being only marginally better the original version (7.9%) reported by Grätzel in 1991.[12]

The most efficient DSSCs contain a liquid electrolyte comprised of a redox active couple, triiodide/iodide (I_3^-/I^-), in acetonitrile. The function of this redox couple is twofold: reduction of the dye cation which results from electron injection into the TiO_2, and transport of the resulting hole to the counter electrode. As the TiO_2 films are porous, the electrolyte is attracted by capillary forces to the nanoporous network. The conductivity of the triiodide/iodide redox couple in acetonitrile (~0.1 Ω^{-1} m^{-1})[36] and the diffusion coefficient of the redox couple in TiO_2 ($3x10^{-6}$ cm^2 s^{-1}) [37] allow for the redox couple to move freely through the nanostructured films. This mobility results in efficient regeneration of all dye molecules, which is crucial to cell performance.

There are two major charge recombination pathways that limit conversion efficiencies of DSSCs: recombination of injected electrons with oxidized dye molecules (Figure **5**, k_3) and recombination with the oxidized form of the redox species in the

electrolyte solution (Figure **5**, k_4). Assuming a rapid rate of reduction of the oxidized dye molecules, recombination with the oxidized dye will be minimal in these systems. Rather, the dominant loss channel is recapture of the injected electrons by the redox couple in the electrolyte solution (Eq. 6).

$$2e^{-}(TiO_2) + I_3^{-} \rightarrow 3I^{-} \qquad (6)$$

Even when maximum coverage of the sensitizer is achieved, some regions of the TiO_2 remain exposed to the redox couple, allowing for reverse charge flow, i.e., recapture of the injected electron in the TiO_2 by the redox couple in the electrolyte solution. This process can, in principle, take place not only at the TiO_2 interface, but also at the SnO_2 back contact. It is reported, however, that back electron transfer occurs almost entirely at the TiO_2 particle/solution interface as a result of the high surface area of the nanocrystalline film.[38]

In the present generation of dye-sensitized cells, the photon-to-current conversion yields approach unity throughout the region where the dye absorbs light, typically starting at ~2.0 eV in photon energy.[24] Furthermore, a wide array of dyes has been designed, some of which feature an expansive overlap with the solar spectrum, capturing most of the photons available between 400 and 775 nm.[14] Thus, the short-circuit current densities are near their limiting values for these well studied systems. The difference between the conduction-band edge of the TiO_2 and the I_3^-/I^- potential defines the theoretical maximum possible open circuit potential (V_{oc}) and is ~1.1 V. However, the resulting photovoltage is only ~0.72 V (in highly efficient cells).[13,24] As such, these systems still yield photovoltages that are significantly lower (~35%) than theoretically

possible. Significant improvements in the photovoltage should be obtainable, and this is clearly the key area in which significant improvement can directly translate into significant gains in photovoltaic energy conversion efficiency. Additionally, improved photovoltages would allow the use of another class of dyes — ones which have extended red wavelength absorption – to trade photocurrent for photovoltage. At present, this tradeoff is not of value as the use of dyes whose absorption spectrum has optimized overlap with AM 1.0 sunlight (thresholds of 1.1–1.7 eV) is unfavorable on an energy conversion basis.[32]

There are two approaches to obtaining significant improvements in efficiency from such systems. The first approach involves moving both the conduction band of the semiconductor and the excited state of the dye more negative in potential, while optimizing the energetics of the M^{3+}/M^{2+} potential relative to the I_3^-/I^- system. However, this will most likely result in losses in short circuit current density due to the decreased spectral overlap as a result of shifting the excited state of the dye to more negative potentials. The second approach involves keeping the conduction band and the dye excited-state energetics constant, but replacing the I_3^-/I^- redox couple with another redox couple that has a more positive Fermi level. In the $Ru(H_2L')_2(NCS)_2/TiO_2$ system, the reduction potential of the sensitizer is 0.56 V more positive than the I_3^-/I^- reduction potential meaning that more than 0.5 V is wasted in the oxidation of I_3^-/I^- by the Ru^{3+}. Therefore replacing the I_3^-/I^- redox couple with another system with a more positive redox potential would raise the cell photovoltage because less energy would be lost in the reduction of the oxidized dye. However, while there are innumerable redox couples that

have more positive redox potentials than I_3^-/I^-, attempts to use alternative redox couples have predominantly failed.[29,39,40] This is because none of them possesses the unique ability of the triiodide species to resist recombination with the injected electron (Figure **5**, k_4).[28,29]

This deleterious reaction is often referred to as the dark current, because in the absence of illumination, this electron transfer process dominates. As such, electrochemical measurements of the dye-coated photoelectrodes in the absence of illumination should be an indication of the rate of reaction of electrons in TiO_2 with the redox couple in solution. The relative rates of this reaction for different redox couples can be inferred from the magnitude of the dark current as a function of the electrode potential. Less negative potentials required to drive the same current density in the dark indicate more facile electron transfer processes between TiO_2 and oxidized species in the electrolyte.

As the regeneration of the oxidized dye is in essence a one-electron process, it would be simpler to use one-electron redox couples in place of the complex I_3^-/I^- two-electron redox couple. In fact, a wide variety of kinetically fast, one-electron redox couples have been shown to efficiently regenerate the oxidized dye, indicating that they have sufficiently fast regeneration kinetics for use in DSSCs. Unfortunately, these couples also have facile recombination with the injected electron in the TiO_2, rendering them useless in DSSCs. It is clear that there are unique properties within the two-electron nature of the I_3^-/I^- couple that result in slow electron transfer kinetics with TiO_2. It is likely that a complex set of one-electron transfer processes, and the resulting

intermediates, are key components in the success of I_3^-/I^- in achieving simultaneously rapid regeneration and slow electron transfer with TiO_2. It is also clear that a more detailed understanding of the one-electron processes that comprise the complicated two-electron redox couple will be necessary before the effectiveness of alternative one-electron couples can be predicted.

Surprisingly, there has been little progress over the last 10 years in elucidating the regeneration mechanism in DSSCs using the I_3^-/I^- couple. The overall reaction is shown in Eq. 7, where M is the inorganic sensitizer.

$$TiO_2/M^{ox} + \frac{3}{2} I^- \rightarrow TiO_2/M + \frac{1}{2} I_3^- \qquad (7)$$

The outer-sphere one-electron oxidation of iodide by transition metal coordination complexes has been well studied, and the simplest description is the bimolecular reaction in solution (Eq. 8).[41,42]

$$TiO_2/M^{ox} + I^- \rightarrow TiO_2/M + I^{\bullet} \qquad (8)$$

The idea of a non-bimolecular regeneration that is second order in iodide has been previously suggested to be more thermodynamically favorable (Eq. 9).[41-43]

$$TiO_2/M^{ox} + 2I^- \rightarrow TiO_2/M + I_2^{\bullet -} \qquad (9)$$

Higher order reactions are expected to dominate if (I^-, I^-) or (M^{ox}, I^-) ion pairs are present in significant amount.[42] This is a reasonable assumption based on the high I^- concentration (0.5 M) used in DSSCs.

It has been reported that by electrostatic control of surface charge the rate of regeneration is affected as a result of differences in the association of I^- with the oxide

surface and/or with the adsorbed dye.[44,45] Consequently, the role of surface adsorbed species cannot be neglected when attempting to decipher the complicated mechanism of regeneration of the oxidized dye by I_3^-/I^-. The protons released upon sensitizer binding to the TiO_2 surface result in protonation of the TiO_2 surface. Furthermore, adsorption of cations, such as Li^+, can also modulate the surface charge. Providing that the surface carries a sufficient positive charge, iodide could electrostatically adsorb onto the surface in the vicinity of the oxidized sensitizer. This will allow a surface-mediated regeneration mechanism involving the adsorbed iodide species (Eq. 10).

$$TiO_2/M^{ox} + I^-_{ads} \rightarrow TiO_2/M + I^{\bullet} \qquad (10)$$

A surface-mediated reaction similar to the non-bimolecular reaction shown in Eq. 9 can in theory occur through adsorption of one or both iodide species (Eq. 11).

$$TiO_2/M^{ox} + 2I^-_{ads} \rightarrow TiO_2/M + I_2^{\bullet -} \qquad (11)$$

Furthermore, there are any number of reactions that can be occurring to consume the transiently generated radical species. Two of the most likely candidates can be written as

$$2I^{\bullet} + I^- \rightarrow I_3^- \qquad (12)$$

$$2I_2^{\bullet -} \rightarrow I^- + I_3^- \qquad (13)$$

where the radical products are connected through the equilibrium represented in Eq. 14:

$$I^{\bullet} + I^- \leftrightarrow I_2^{\bullet -} \qquad (14)$$

Recovery of the ground-state absorption of the dye, after electron injection into TiO_2, does not follow a simple kinetic law. [46,47] The rate of the direct reduction of I_3^- by

injected electrons was measured from intensity modulated experiments and was found to be second order in the electron density.[48] Due to the complex kinetics that comprise these two key processes, it is unlikely that a one-electron redox couple will have the necessary complexity to both rapidly regenerate the oxidized dye and maintain slow electron transfer with the TiO_2.

It is possible, however, that other two-electron redox couples could have the necessary intermediates to modulate the appropriate electron transfer kinetics. If these couples have formal redox potentials more positive than that of I_3^-/I^-, they may result in increased photovoltages. The absorption properties of the I_3^-/I^- redox couple have severely limited the spectroscopic study of this couple in functional DSSCs. Alternative two-electron redox couples should not only offer the possibility of increased photovoltages, but should be useful in the development of a broader understanding of the regeneration mechanism if they have more suitable absorption spectra.

When considering alternative redox couples, it is clear that there are both thermodynamic and kinetics factors that must be considered. The potential should be more positive than the I_3^-/I^- redox couple for enhancements in V_{oc}. The kinetics of regeneration of the oxidized dye must be fast enough to compete with recombination of the injected electrons (Figure **5**, k_5). The redox couple should be inert to any quenching of the excited state, which may otherwise compete with the kinetics of injection. Perhaps the most important kinetics requirement is that the alternative redox couple must have slow electron transfer with the TiO_2 surface.

The thiocyanogen/thiocyanate couple is a well established two-electron redox couple that has a more positive electrochemical potential than the 0.023 V vs. SCE for the I_3^-/I^- couple (Eq. 15).

$$E^o = 0.55 \text{ V vs. SCE} \qquad (SCN)_2 + 2e^- \rightarrow 2SCN^- \tag{15}$$

Furthermore, the one-electron outer-sphere oxidation of SCN^- by M^{3+} complexes in aqueous solutions has been shown to occur via the same path as I^- (Eq. 16).[41,42]

$$M^{3+} + 2SCN^- \rightarrow M^{2+} + I_2^{\bullet -} \tag{16}$$

Selenocyanogen undergoes a similar two-electron reduction to selenocyanate and is also more positive than the I_3^-/I^- couple (Eq. 17).[29]

$$E^o = 0.24 \text{ V vs. SCE} \qquad (SeCN)_2 + 2e^- \rightarrow 2SeCN^- \tag{17}$$

It is well known that the two-electron tribromide/bromide (Br_3^-/Br^-) redox couple undergoes one-electron transfer processes similar to those for I_3^-/I^-. As such, it is possible that the regeneration of oxidized dye molecules by this couple should occur via a similar mechanism and that the more positive formal reduction potential (0.44 V vs. SCE) of this couple should result in enhanced photovoltages.

The addition of bromide or chloride to a solution of I_3^-/I^- has been shown to shift the redox potential to more positive values. This has been shown to be the result of the formation of not only the triiodide species, I_3^-, but also the mixed halide species, I_2Br^- and I_2Cl^-. This may allow for kinetics similar to those in the I_3^-/I^- redox couple, but with enhanced photovoltages due to thermodynamic improvements.

In the work described here, the two pseudohalogen redox couples, $(SCN)_2/SCN^-$ and $(SeCN)_2/SeCN^-$, and the Br_3^-/Br^- system, were investigated as alternative redox

couples in DSSCs. A second approach to enhancing the photovoltage was also investigated by shifting the I^-/I_3^- redox potential to more positive values using mixed halide redox couples.

Experimental

Materials

17.8 MΩ cm resistivity water was obtained from a Barnstead NANOpure filtration system. Ethanol (Aapor) and anhydrous pyridine (Aldrich) were used as received. Acetonitrile (MeCN) (Merck) was freshly distilled over CaH_2 prior to use. Lithium iodide (Aldrich) and anhydrous lithium perchlorate (J. T. Baker) were stored under nitrogen and used as received. Iodine (Alfa-Aesar) was sublimed under vacuum and stored under nitrogen. Pyridinium triflate (Aldrich) was recrystallized from diethyl ether and stored in a drybox. Tetrabutyl ammonium iodide (TBAI) (98%), tetrabutyl ammonium chloride hydrate (TBACl) (98%), tetrabutyl ammonium bromide (TBABr) (99%) and lithium chloride hydrate (LiCl) (99.99%) were purchased from Aldrich and used as received. Sodium thiocyanate (NaSCN) (Alfa-Aesar, 98%), potassium selenocyanate (KSeCN) (Alfa-Aesar, 98%) and lead thiocyanogen ($Pb(SCN)_2$) (Aldrich, 99%) were used as received. $[Ru(H_2L')_2(CN)_2]^0$ and $[Ru(H_2L')_2(NCS)_2]^0$ complexes were used as received from Solaronix. $[Ru(H_2L')L_2](PF_6)_2$ and $[Ru(H_2L')_3](PF_6)_2$ complexes, as well as their osmium analogues, were synthesized as described previously.[30,32]

Nanocrystalline titanium dioxide films (thickness 6 μm, crystallite size ~15 nm) deposited by screen printing on conductive glass (SnO_2:F) were obtained from the Institut für Angewandte Photovoltaik, Germany. Before adsorption of sensitizers, the films were cut into the desired size and pretreated as follows: the conductive glass was cleaned with acetone, and the TiO_2 electrodes were covered with several drops of freshly prepared 0.2 M $TiCl_4$(aq) and left overnight in a sealed chamber to prevent evaporation. After rinsing with water and ethanol, the slides were annealed at 450ºC in air for 30 min, then slowly cooled to 120ºC. The hot electrodes were then submerged into ethanolic solutions of the various dye complexes. Sensitized slides were rinsed with ethanol and dried with nitrogen prior to use.

Electrolyte

A solution of $Pb(SCN)_2$ (2.5 mmol) in acetonitrile (50 mL) was cooled to 0ºC in an ice bath. A solution of Br_2 (0.1 M) in acetonitrile (25 mL) was slowly added to the cooled $Pb(SCN)_2$ solution while stirring. Care was taken during addition to maintain a colorless solution by controlling the Br_2 addition rate. Once addition was complete, the solution was stirred at 0ºC for 20 minutes. Precipitated $PbBr_2$ was filtered out to yield a clear colorless solution of thiocyanogen, $(SCN)_2$ as evidenced by the absorption peak at 295 nm. The concentration of $PbBr_2$ corresponded to ~100% reaction efficiency. A solution of NaSCN (0.4 M) in acetonitrile (25 mL) was added dropwise to the $(SCN)_2$ solution. This yielded final concentrations of 0.1 M SCN^- and 0.025 M $(SCN)_2$. If the concentrations were increased significantly or if the NaSCN was added too quickly,

parathiocyanogen $(SCN)_x$ would begin to precipitate from the solution resulting in unknown $SCN^-/(SCN)_2$ concentrations.

The $SeCN^-/(SeCN)_2$ couple was prepared analogously. A solution of KSeCN (0.1 M) in acetonitrile (50 mL) was cooled to 0ºC in an ice bath. A solution of Br_2 (0.1 M) in acetonitrile (25 mL) was added to the KSeCN solution in the dark while stirring. Precipitated KBr was removed by filtration yielding a light yellow solution of selenocyanogen $(SeCN)_2$. KSeCN (0.4 M) in acetonitrile (25 mL) was added to the filtered solution. This yielded final concentrations of 0.1 M $SeCN^-$ and 0.025 M $(SeCN)_2$.

The halide electrolytes used were 0.5 M LiX and 0.04 M X_2 (where X = I^- or Br^-) with 20 mM pyridine and 20 mM pyridinium triflate except for comparison with the $SeCN^-/(SeCN)_2$ and $SCN^-/(SCN)_2$ where the concentrations were 0.1 M LiX and 0.025 M X_2. Pyridine and pyridinium triflate were included to control the proton activity of the electrolyte and to stabilize the conduction band edge of the TiO_2 in the photoelectrochemical measurements. Solutions were sensitive to oxygen and were prepared using airless techniques and then stored under N_2. All electrolytes were prepared the day prior to beginning experimentation and were allowed to sit overnight. Electrolyte solutions were used within three days of preparation.

Electrochemistry

Photoelectrochemical measurements were recorded using a custom three-electrode configuration with a platinum wire pseudo-reference electrode in contact with the solution and a platinum gauze counter electrode. The distance between the working

and counter electrode was 2 mm and measurements were made in the absence of stirring. Illumination was achieved using a 150 W Oriel solar simulator with a 385 nm long pass filter to prevent direct excitation of the TiO_2. Illumination was performed through the back of the working electrode (dye-coated TiO_2 sample), with the surface area of illumination being 0.25 cm^2. A Solarex Inc. diode was used to calibrate the light intensity. All J-V curves were measured using a BAS model 100B potentiostat. Typical parameters for a photoelectrochemical measurement were from 200 mV to -800 mV and back to 200 mV with a scan rate of 20 mV s^{-1}. All data were corrected for uncompensated cell resistance (measured in the same cell except with a platinum working electrode in the place of the TiO_2 electrode, 52 Ω), but no corrections were made for any concentration overpotentials.

The electrochemical potentials of the redox couples were determined using a BAS model 100B potentiostat equipped with a glassy carbon working electrode, a methanolic saturated calomel reference electrode (SCE), and a Pt flag counter electrode. The potential of the methanolic SCE was determined both by measurement against a standard saturated calomel electrode and by calibration relative to the formal potential of ferrocene in ethanol obtained from cyclic voltammetry scan. All potentials are reported relative to aq. SCE.

Current-potential (*I-V*) measurements with the $(SCN)_2$/ SCN^- and $(SeCN)_2$/$SeCN^-$ were performed in solution, rather than the custom three electrode cell holder, with a blank TiO_2 slide (cut to remove any exposed SnO_2:F coated glass) as the working electrode. Measurements for these systems (and the analogous I_3^-/I^- and Br_3^-/Br^- were

performed in acetonitrile with a platinum wire reference electrode in the solution and a platinum flag counter electrode.

Spectroscopy

Steady-state absorption spectra were measured using a diode array Agilent 8453 UV-vis spectrometer. The absorbance of the sensitizer coated onto TiO_2 was measured on dry films. In all cases the scattering signal from TiO_2 slides without sensitizer was subtracted from the total absorbance.

Nanosecond transient absorption spectra were measured using a setup described previously.[49] The regeneration kinetics of the dye-sensitized TiO_2 slides were measured in the custom-designed three-electrode cell filled with acetonitrile containing 0.50 M $LiClO_4$, 0.020 M pyridine and 0.020 M pyridinium triflate. For kinetics measurements the excitation energy (λ_{ex} = 480 nm) was 1 mJ for a ~1 cm^2 beam, unless otherwise stated. A broad beam was necessary to ensure uniform excitation of the samples. Time-resolved TiO_2 data are very sample specific; thus the reported data set was obtained on the same day with slides from the same preparation.

Results

Alternative Two-Electron Redox Couples

The preparation and electrochemistry of $(SCN)_2/SCN^-$ solutions were complicated by the repeated formation of parathiocyanogen. This placed an upper limit of 0.1 M SCN and 0.025 $(SCN)_2$ on the concentrations that could be obtained. The solution potentials in acetonitrile of these two electrolytes at these concentrations were measured to be 0.24 V

vs. SCE for the $(SeCN)_2/SeCN^-$ couple and 0.55 V vs. SCE for the $(SCN)_2/SCN^-$ couple and were in good agreement with previous reports.[29] The potential of the Br_3^-/Br^- redox couple at the same concentrations was measured to be 0.44 V vs. SCE. All three are significantly more positive than the I_3^-/I^- redox couple (0.023 V vs. SCE).

Trends in the rate of recombination of injected electrons with the various redox couples were evaluated from the potential necessary to produce a fixed amount of cathodic dark current density (0.1 mA cm^{-2}) at the TiO_2–solution interface, where a less negative potential is indicative of more facile electron transfer between TiO_2 and the redox couple in solution (Figure **12**). Due to the instability of the $(SCN)_2/SCN^-$ couple, these measurements were performed in solution with a TiO_2 working electrode, platinum wire counter electrode and versus a methanol SCE reference electrode, rather than in the atmosphere-controlled cell holder. Clearly, the thiocyanate and selenocyanate redox couples showed very facile electron transfer with the TiO_2, while the Br_3^-/Br^- couple required a more negative potential to drive the same amount of current as the I_3^-/I^- couple. The inability of the pseudohalide couples to resist this crucial electron transfer process indicated that these couples are not well suited for application in functional DSSCs. As such, a more detailed study was focused on the photoelectrochemical behavior of the Br_3^-/Br^- system.

Both iodide and bromide have large equilibrium constants for trihalide formation in acetonitrile (10^7) when mixed with iodine and bromine, respectively. UV-vis studies were done to determine the relative absorption peaks for I_3^-/I^- and the Br_3^-/Br^- systems

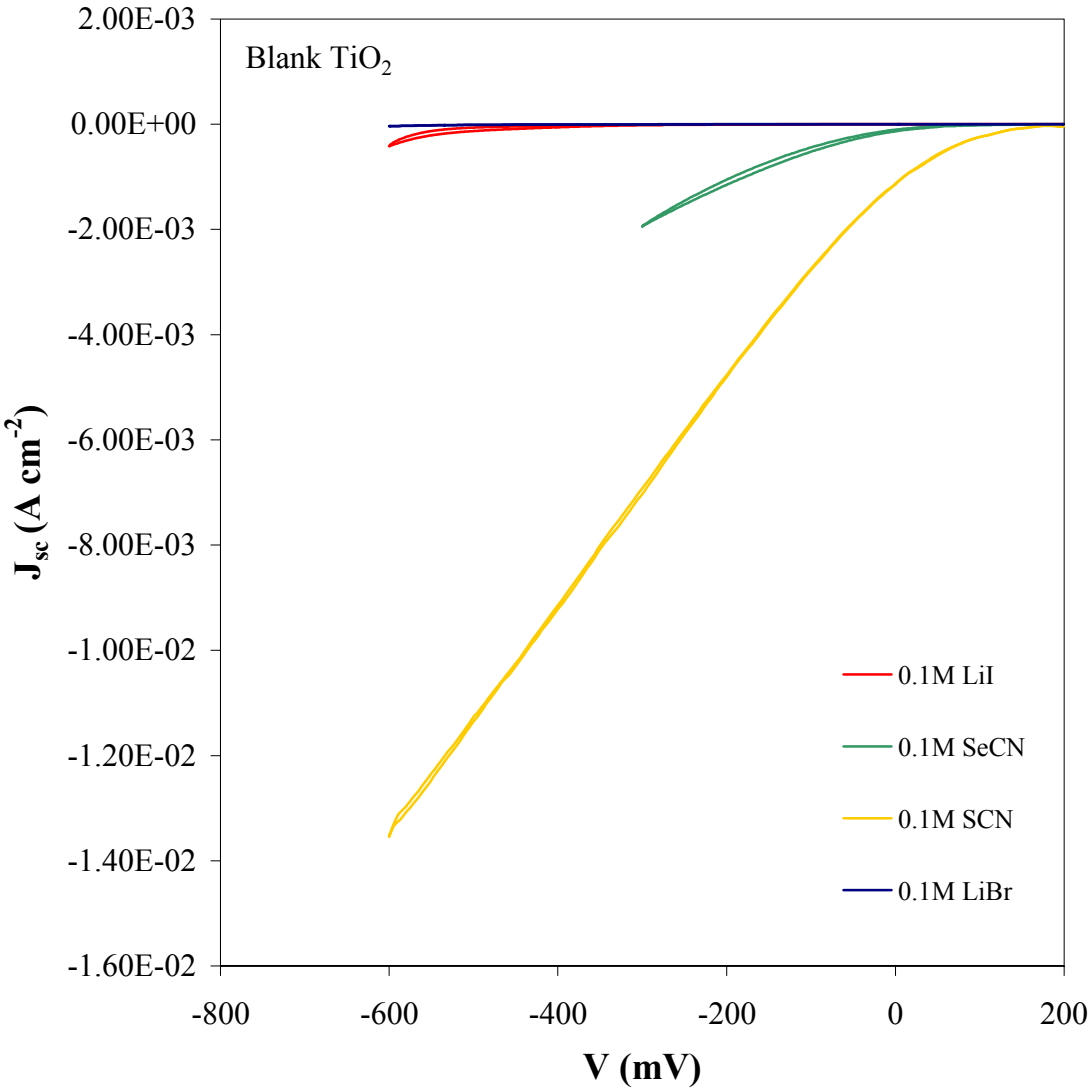

Figure 12. Dark current versus potential characteristics for a TiO_2 electrode with $(SCN)_2/SCN^-$; $(SeCN)_2/SeCN^-$; Br_3^-/Br^-; and I_3^-/I^-. Electrolyte concentrations were 0.1 M reduced species and 0.025 M oxidized species in all cases.

(Figure **13**). Addition of iodine results in essentially 100% formation of triiodide, as evidenced by the lack of an absorption at 460 nm corresponding to iodine. The electronic absorption spectrum of I_3^- is dominated by two broad bands centered at 285 and 360 nm. The assignment of these intervalence bands has been quite controversial and is still not settled.[50-55] The Br_3^-/Br^- redox couple absorbed at higher energy than the I_3^-/I^- couple with only one band (285 nm) measurable on this wavelength scale. The interactions of these complexes with ruthenium tris-bipyridyl, $[Ru(bpy)_3]^{2+}$, (10 mM) was also examined by UV-vis spectroscopy (Figure **14**). Neither couple showed evidence of complexation with the metal bipyridyl complex in solution. The Br_3^-/Br^- absorption was blue-shifted relative to the metal-to-ligand charge transfer band of the ruthenium tris-bipyridyl, while the I_3^-/I^- absorption edge overlapped the MLCT band (Figure **14**).

To probe the relative ability of the Br_3^-/Br^- couple to reduce oxidized $[Ru(bpy)_3]^{2+}$-type sensitizers, transient kinetics experiments were performed in solution. The oxidized form of the dyes (Ru^{3+}) was generated by the flash-quench method (Figure **11**a). In the presence of MV^{2+}, excitation of the $[Ru(bpy)_3]^{2+}$ MLCT resulted in the formation of an excited state that was subsequently oxidatively quenched by the MV^{2+}. $[Ru(bpy)_3]^{2+}$ (30 mM) was studied in the presence of methyl viologen (10 mM) with varying concentrations of bromide. The reduction of Ru^{3+} to Ru^{2+} was measured as a function of the halide concentration (Figure **15**a). The recovery of the MLCT absorption following pulsed-laser excitation accelerated significantly when bromide was added to the electrolyte (Figure **15**a). Fitting the data to single exponentials produced the $[Br^-]$-dependent rate constants (k'_5). Under pseudo first-order conditions, a second-order rate

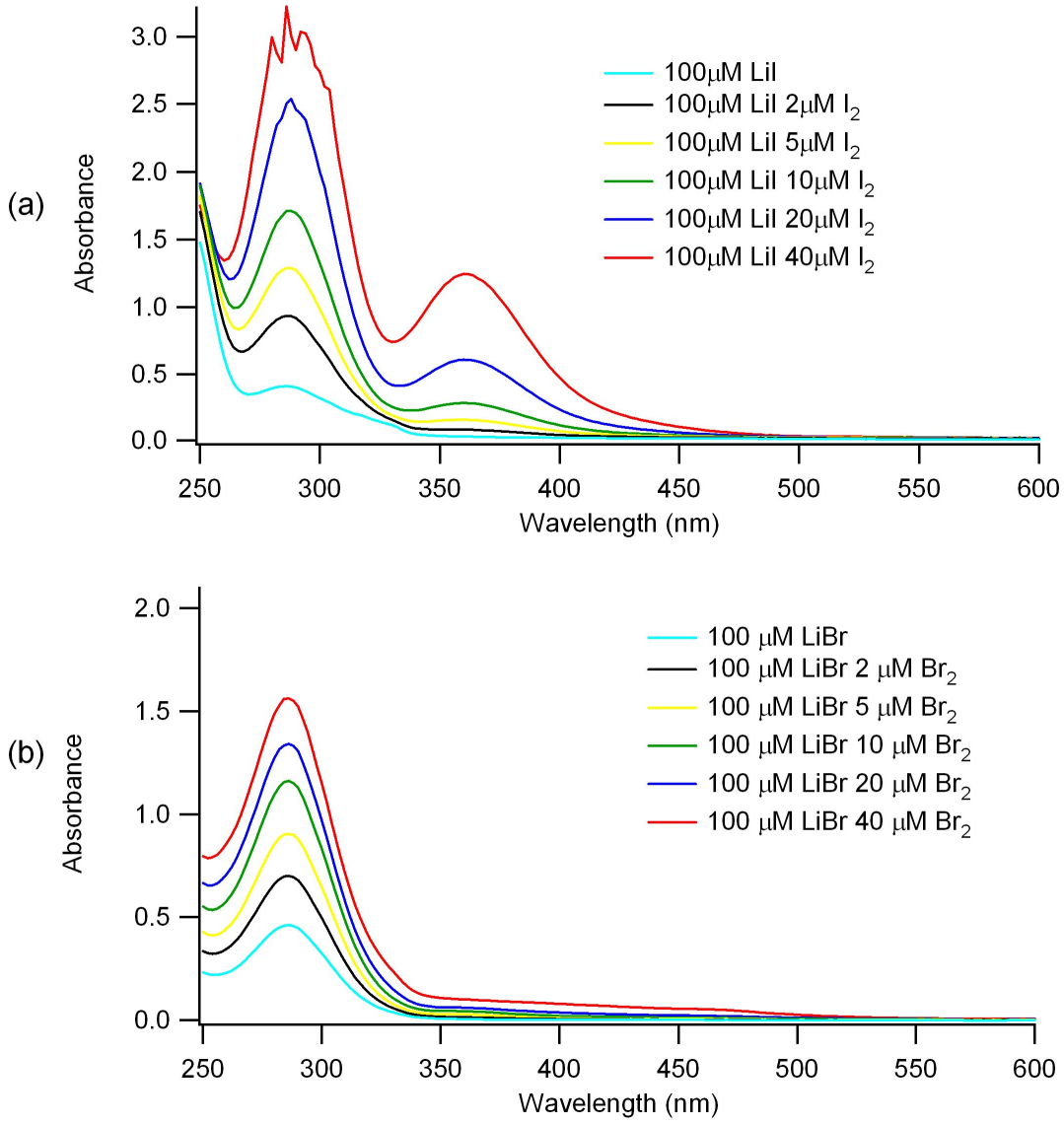

Figure 13. UV-vis spectra of I_3^-/I^- and Br_3^-/Br^- in acetonitrile. (a) 100 μM LiI solution with increasing concentration of I_2 and (b) 100 μM LiBr solution with increasing concentration of Br_2.

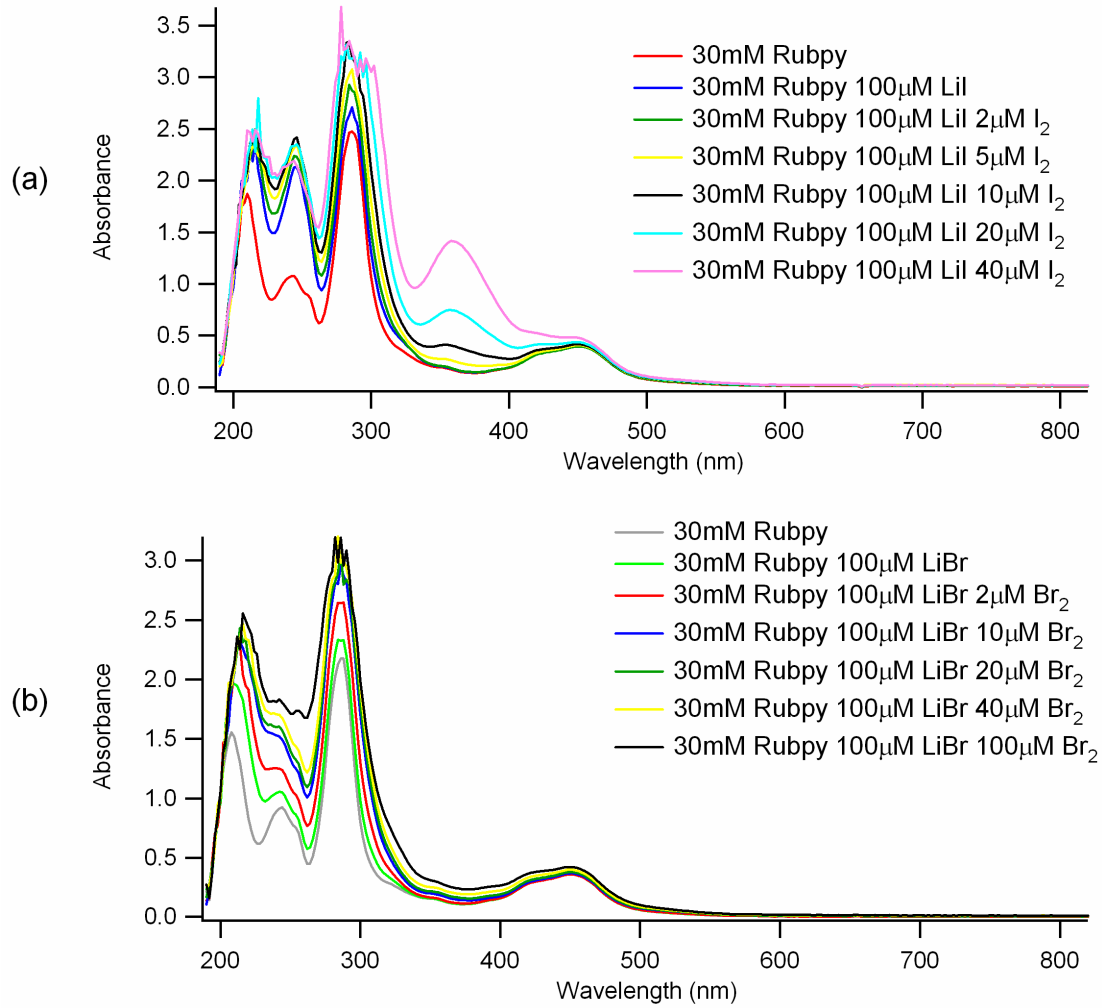

Figure 14. UV-vis spectra of $[Ru(bpy)_3]^{2+}$ with I_3^-/I^- and Br_3^-/Br^- in acetonitrile. (a) 30 mM $[Ru(bpy)_3]^{2+}$ with 100 μM LiI solution with increasing concentration of I_2 and (b) 30 mM $[Ru(bpy)_3]^{2+}$ with 100 μM LiBr solution with increasing concentration of Br_2.

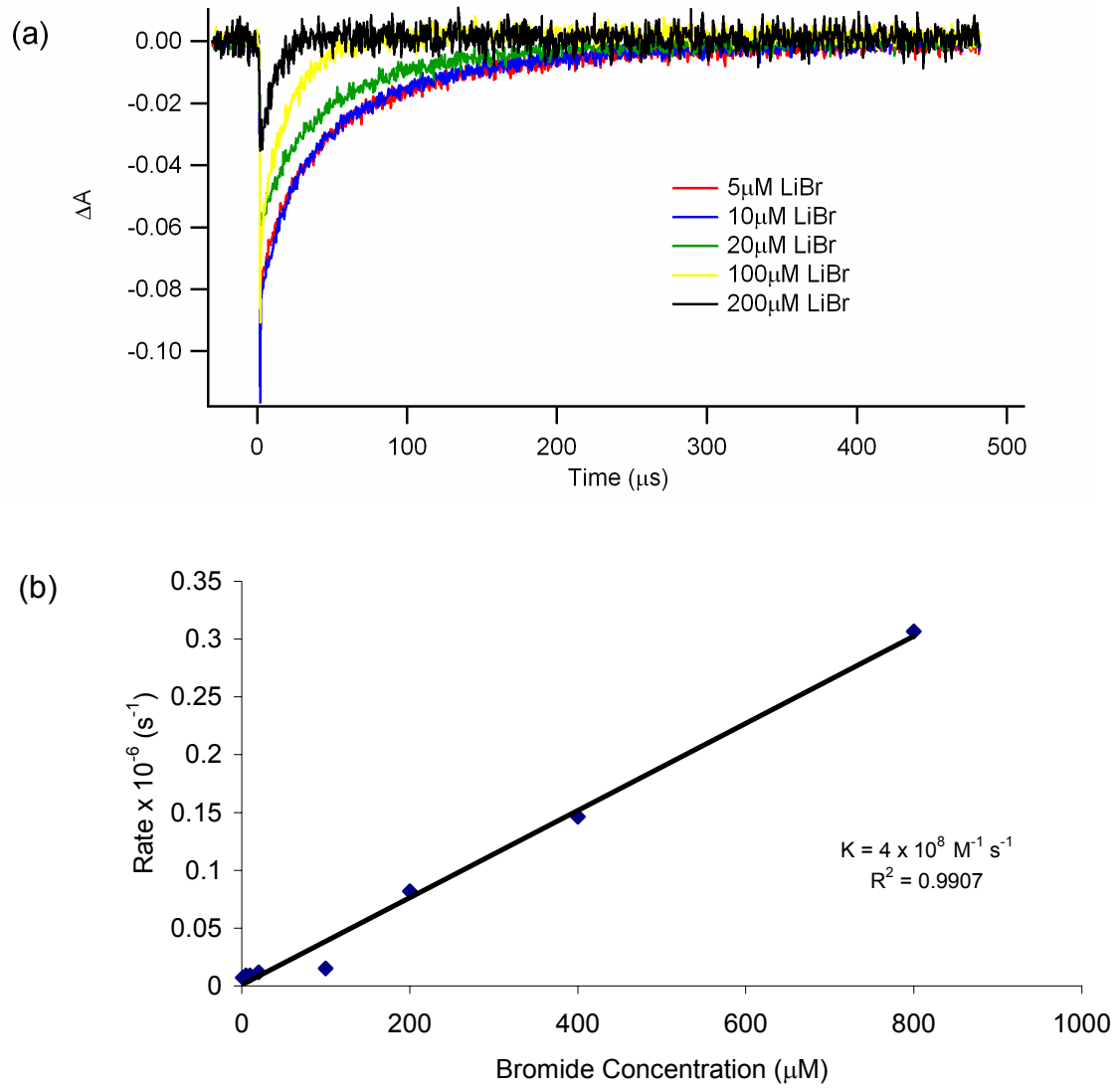

Figure 15. Pseudo-first-order reduction of $[Ru(bpy)_3]^{3+}$ by bromide. (a) $[Ru(bpy)_3]^{2+}$ solution regeneration kinetics as a function of halide concentration. 30 mM $[Ru(bpy)_3]^{2+}$ with 10 mM MV^{2+} and varying concentrations of LiBr. λ_{ex} = 470 nm; λ_{obs} = 500 nm. (b) Pseudo-first-order Stern-Volmer plot of 30 mM $[Ru(bpy)_3]^{2+}$ with 10 mM MV^{2+} and varying concentrations of LiBr.

constant was determined. Figure **15**b shows the pseudo-first-order rate constant plot for $[Ru(bpy)_3]^{2+}$ with bromide. Clearly, the addition of low concentrations of bromide rapidly reduced the oxidized ruthenium complex ($4x10^8\ M^{-1}\ s^{-1}$), although this quenching rate was slower than the quenching rate with iodide ($1x10^{10}\ M^{-1}\ s^{-1}$).

As shown in Figure **12**, the Br_3^-/Br^- couple had very slow electron transfer with the TiO_2 surface. This is more clearly seen in the dark current-potential measurements of a blank TiO_2 slide in a functional DSSC (Figure **16**). The decreased dark current for the Br_3^-/Br^- couple correlated with an increase in V_{oc}. Figures **17**–**21** show the dark (dashed) and light (solid) current curves for a series of dye-coated slides with iodide/triiodide and with bromide/tribromide electrolytes. In all cases, the dark current shifted to more negative potentials when working with the bromide system, and this correlated with a larger V_{oc} in the light. Surprisingly, the increase in V_{oc} in many of these systems was accompanied by a decrease in photocurrent. Table **1** reports the photovoltages and photocurrents for a series of dyes of varying formal oxidation potentials. As the ground-state reduction potential of the sensitizer became more positive, the loss in J_{sc} became less. For the two dyes with the most positive ground-state reduction potentials, $[Ru(H_2L')_3]^{2+}$ and $[Ru(H_2L')L_2]^{2+}$, only a minimal loss in photocurrent was observed, and both of these dyes showed significantly enhanced solar cell efficiencies (Table **1**). The I_3^-/I^- and Br_3^-/Br^- couples both yielded stable, working DSSCs over the course of 1 h, although the photocurrent with the Br_3^-/Br^- couple was noticeably more variable (Figure **22**).

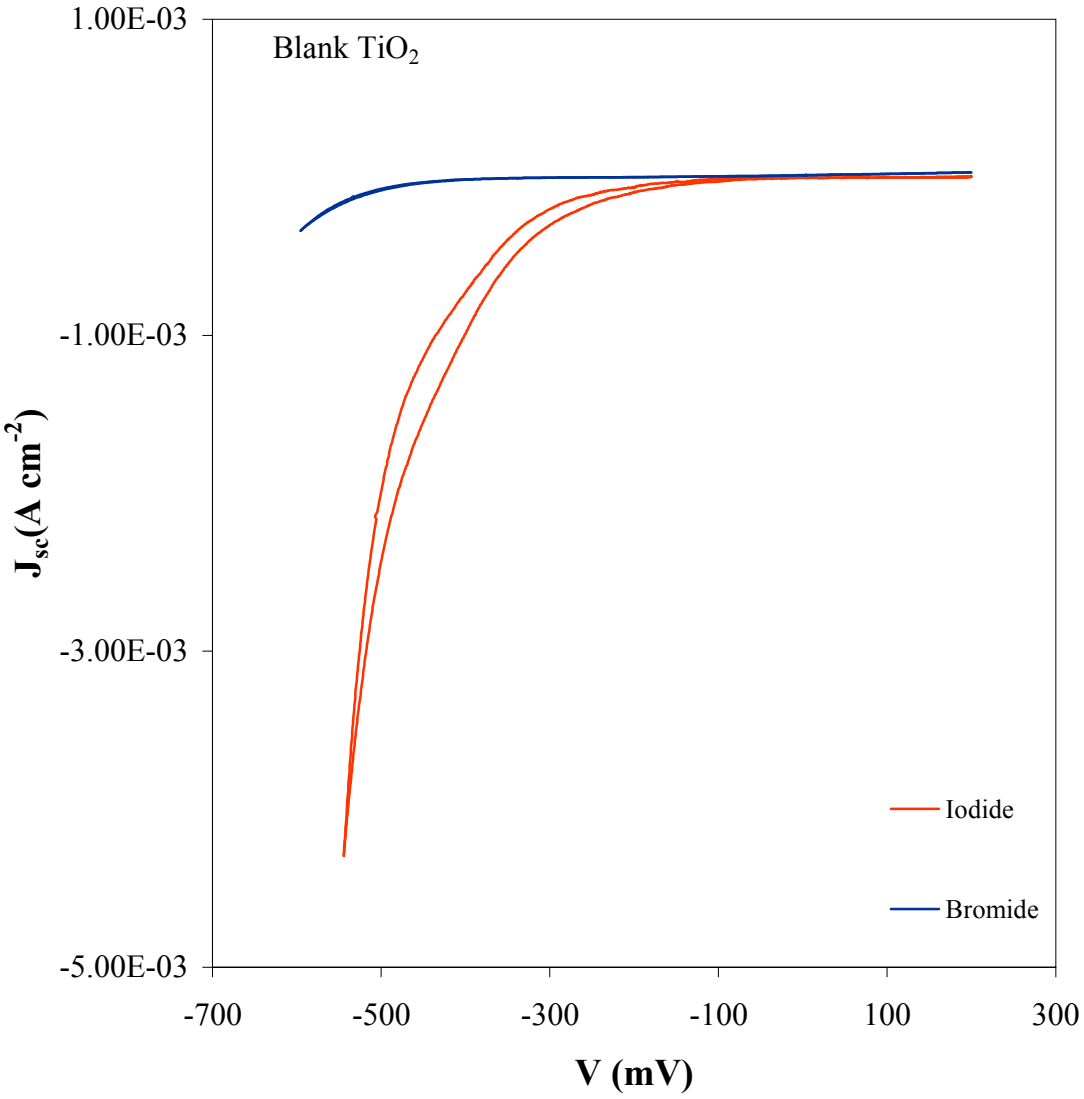

Figure 16. Dark current versus potential characteristics for a TiO_2 electrode with I_3^-/I^- and Br_3^-/Br^- electrolytes. Electrolyte concentrations: 0.50 M LiI, 0.040 M I_2, 0.020 M pyridine, and 0.020 M pyridinium triflate in acetonitrile (red) and 0.50 M LiBr, 0.040 M Br_2, 0.020 M pyridine, and 0.020 M pyridinium triflate in acetonitrile (blue).

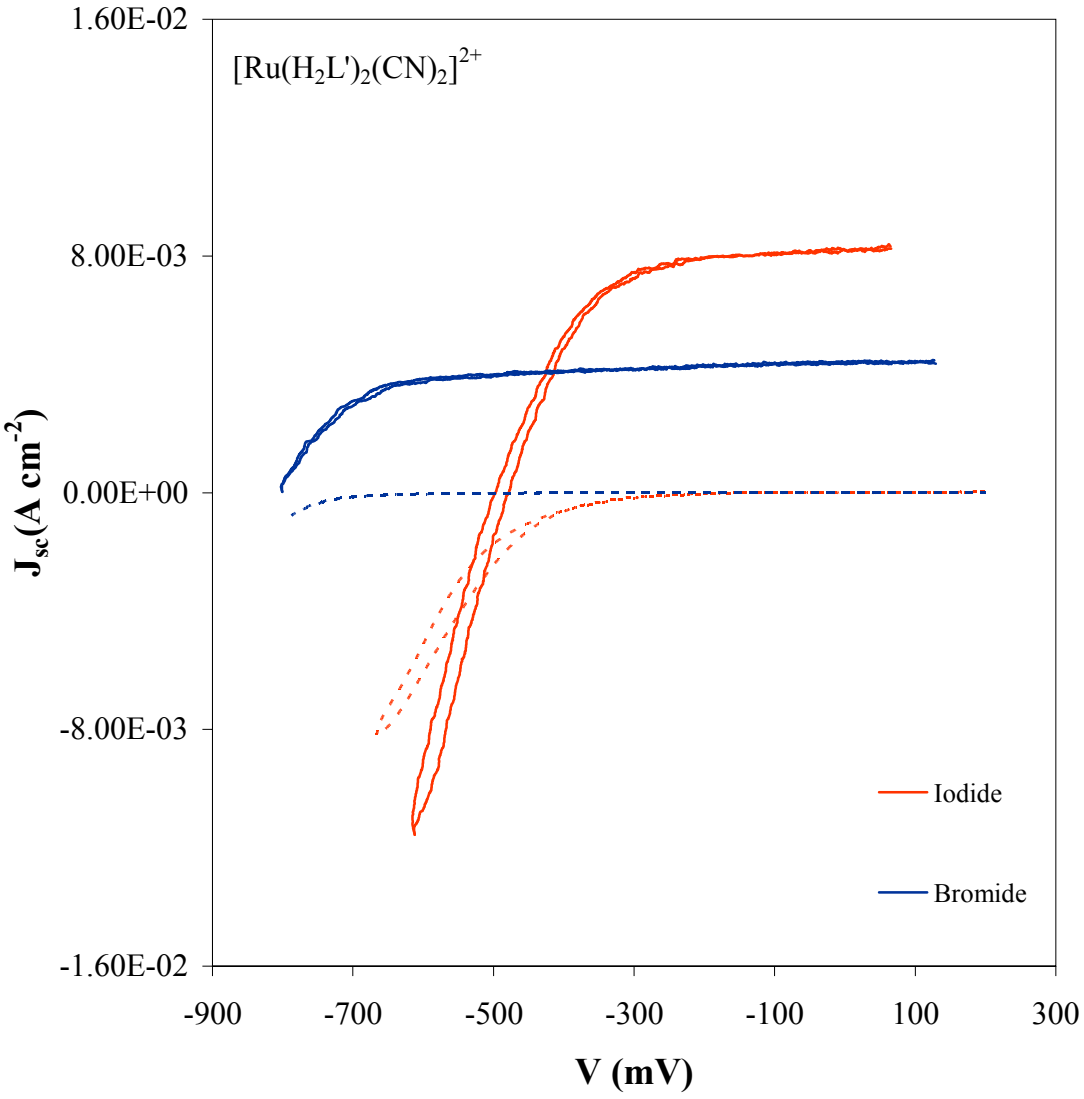

Figure 17. Current versus potential characteristics for a $[Ru(H_2L')_2(CN)_2]^{2+}$ sensitized TiO_2 electrode with I_3^-/I^- and Br_3^-/Br^- electrolytes. Electrolyte concentrations: 0.50 M LiI, 0.040 M I_2, 0.020 M pyridine and 0.020 M pyridinium triflate in acetonitrile (red) and 0.50 M LiBr, 0.040 M Br_2, 0.020 M pyridine, and 0.020 M pyridinium triflate in acetonitrile (blue). The behavior under simulated Air Mass 1.0 (100 mW cm^{-2}) conditions (solid lines) and in the dark (dashed) is shown.

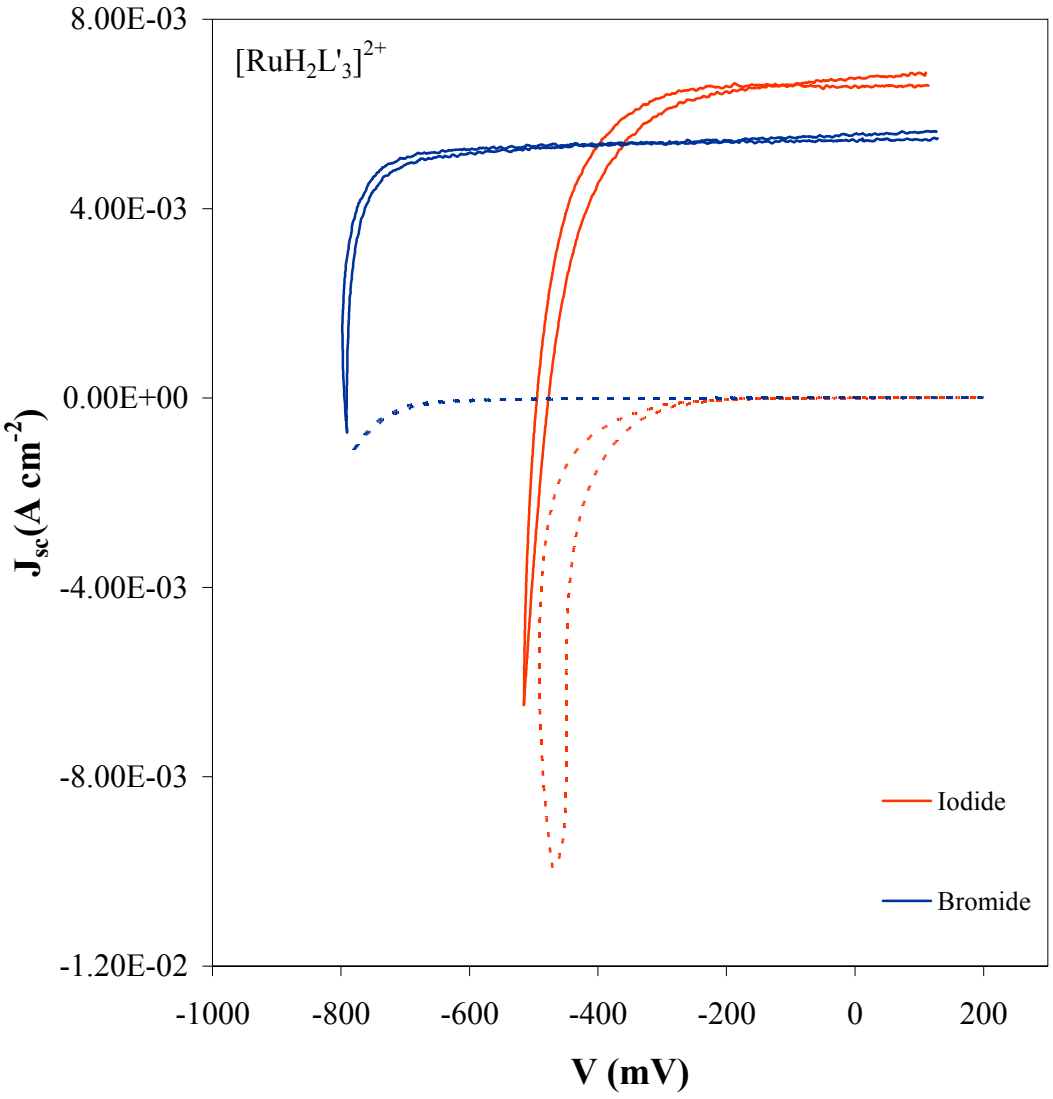

Figure 18. Current versus potential characteristics for a $[Ru(H_2L')_3]^{2+}$ sensitized TiO_2 electrode with I_3^-/I^- and Br_3^-/Br^- electrolytes. Electrolyte concentrations: 0.50 M LiI, 0.040 M I_2, 0.020 M pyridine and 0.020 M pyridinium triflate in acetonitrile (red) and 0.50 M LiBr, 0.040 M Br_2, 0.020 M pyridine, and 0.020 M pyridinium triflate in acetonitrile (blue). The behavior under simulated Air Mass 1.0 (100 mW cm^{-2}) conditions (solid lines) and in the dark (dashed) is shown.

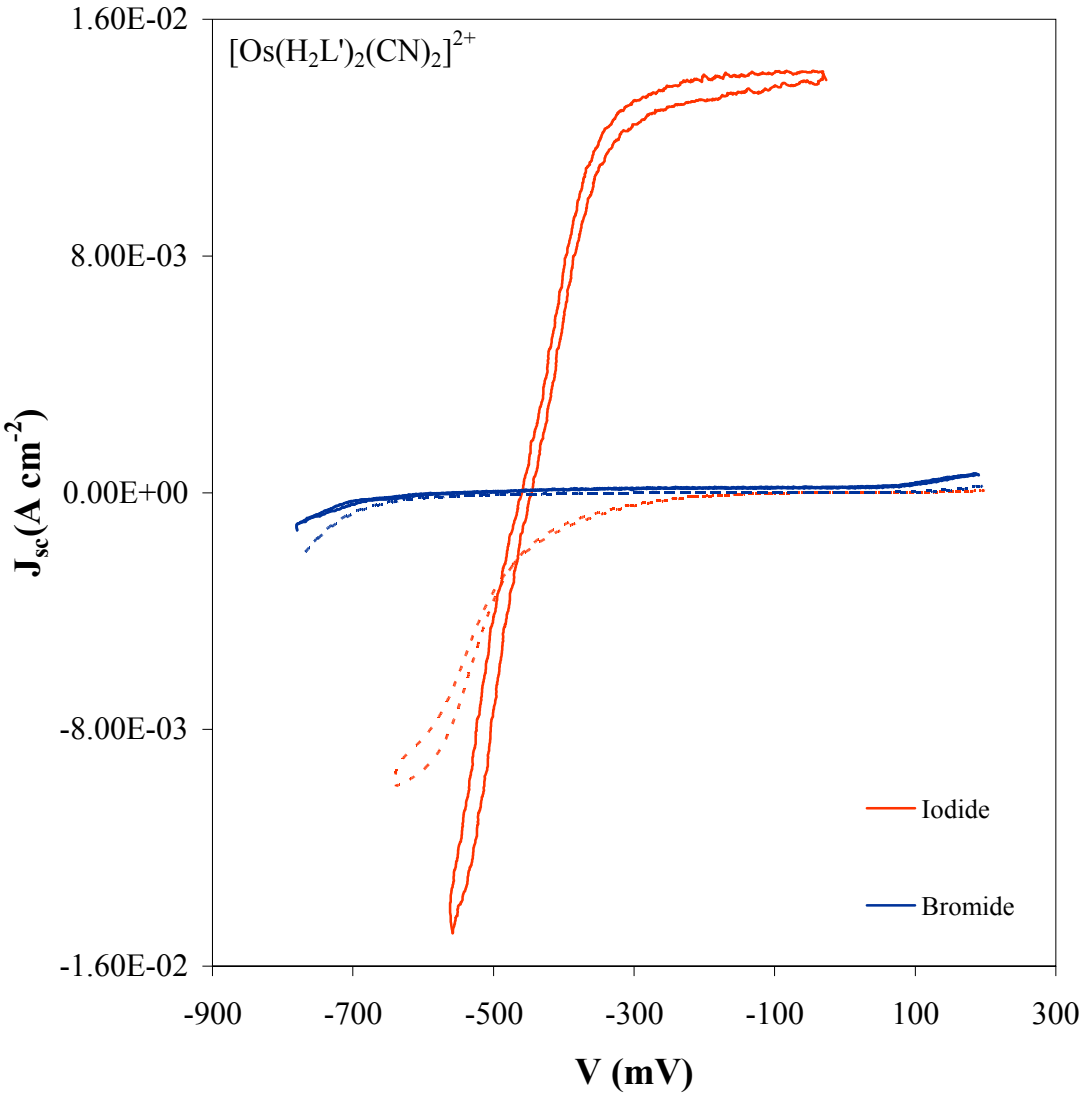

Figure 19. Current versus potential characteristics for a $[Os(H_2L')_2(CN)_2]^{2+}$ sensitized TiO_2 electrode with I_3^-/I^- and Br_3^-/Br^- electrolytes. Electrolyte concentrations: 0.50 M LiI, 0.040 M I_2, 0.020 M pyridine and 0.020 M pyridinium triflate in acetonitrile (red) and 0.50 M LiBr, 0.040 M Br_2, 0.020 M pyridine, and 0.020 M pyridinium triflate in acetonitrile (blue). The behavior under simulated Air Mass 1.0 (100 mW cm^{-2}) conditions (solid lines) and in the dark (dashed) is shown.

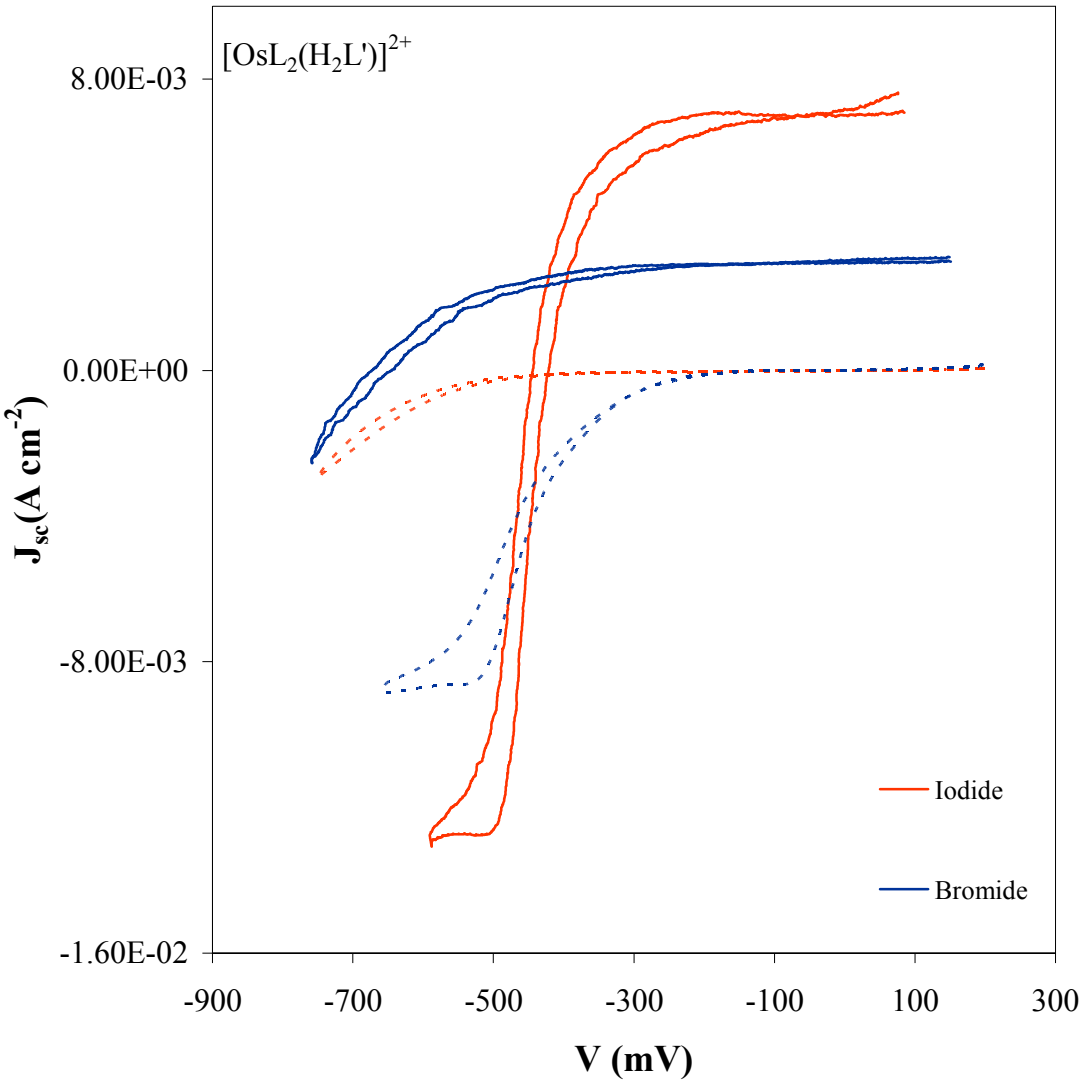

Figure 20. Current versus potential characteristics for a $[OsL_2(H_2L')]^{2+}$ sensitized TiO_2 electrode with I_3^-/I^- and Br_3^-/Br^- electrolytes. Electrolyte concentrations: 0.50 M LiI, 0.040 M I_2, 0.020 M pyridine and 0.020 M pyridinium triflate in acetonitrile (red) and 0.50 M LiBr, 0.040 M Br_2, 0.020 M pyridine, and 0.020 M pyridinium triflate in acetonitrile (blue). The behavior under simulated Air Mass 1.0 (100 mW cm^{-2}) conditions (solid lines) and in the dark (dashed) is shown.

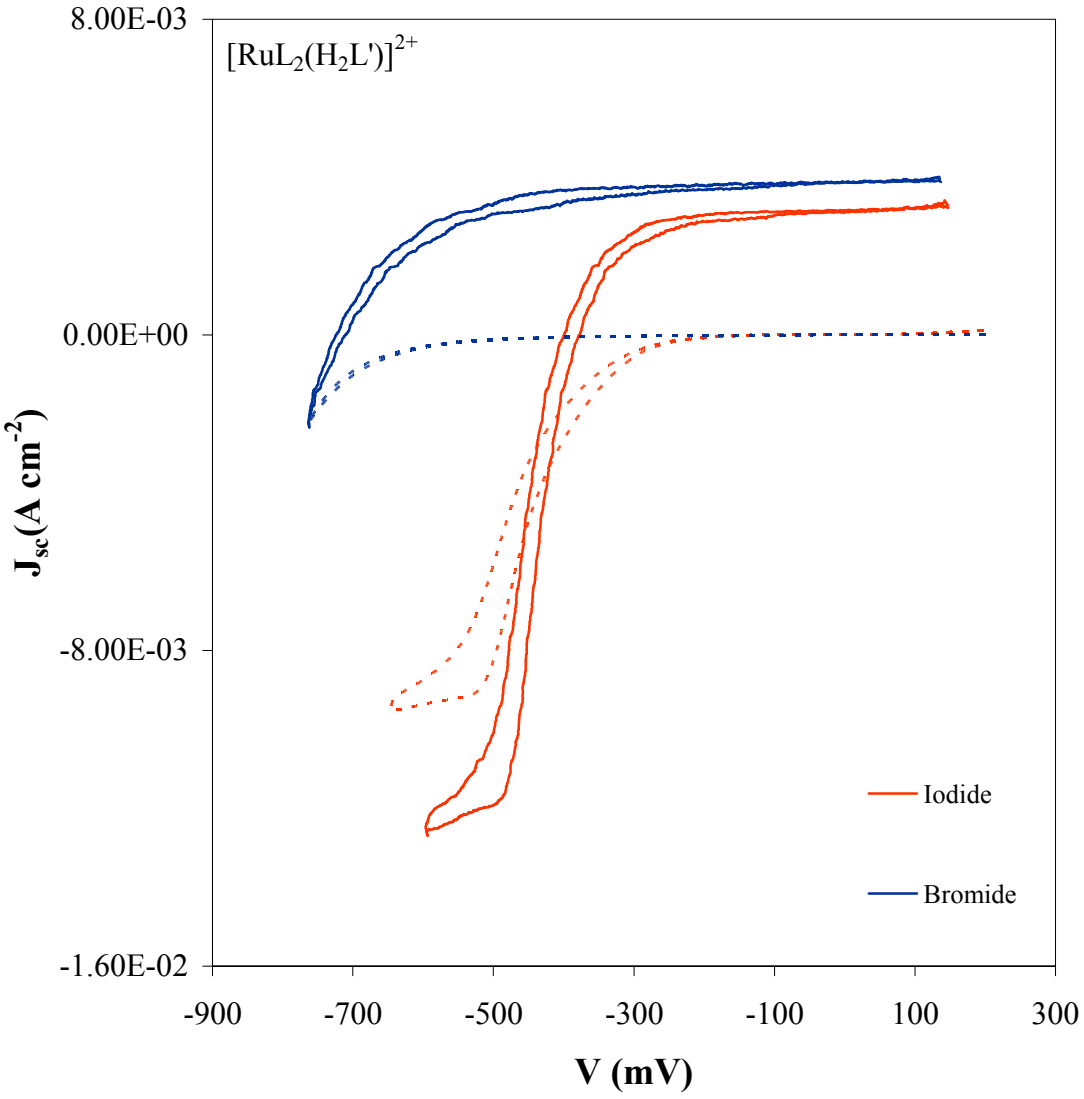

Figure 21. Current versus potential characteristics for a $[RuL_2(H_2L')]^{2+}$ sensitized TiO_2 electrode with I_3^-/I^- and Br_3^-/Br^- electrolytes. Electrolyte concentrations: 0.50 M LiI, 0.040 M I_2, 0.020 M pyridine and 0.020 M pyridinium triflate in acetonitrile (red) and 0.50 M LiBr, 0.040 M Br_2, 0.020 M pyridine, and 0.020 M pyridinium triflate in acetonitrile (blue). The behavior under simulated Air Mass 1.0 (100 mW cm^{-2}) conditions (solid lines) and in the dark (dashed) is shown.

Table 1. Photoelectrochemical data for DSSCs with I_3^-/I^- and Br_3^-/Br^-.[a]

	$[Os(H_2L')_2(CN)_2]^{2+}$		$[Os(H_2L')L_2]^{2+}$		$[Ru(H_2L')_2(CN)_2]^{2+}$		$[Ru(H_2L')L_2]^{2+}$		$[Ru(H_2L')_3]^{2+}$	
$E^{o'}$	0.72 V vs. SCE		0.81 V vs. SCE		1.08 V vs. SCE		1.23 V vs. SCE		1.4 V vs. SCE	
X	I	Br	I	Br	I	Br	I	Br	I	Br
V_{dark}[b]	-325	-680	-290	-570	-380	-770	-325	-650	-375	-740
V_{oc} (mV)[c]	-460	-540	-440	-670	-495	-815	-400	-670	-495	-795
J_{sc} (mA)[d]	14.1	0.2	7.1	3	8.2	4.4	3.3	3.4	6.7	5.9
ff[e]	0.64	0.58	0.64	0.56	0.58	0.67	0.64	0.61	0.64	0.81
Efficiency[f]	4.2	0.1	2.0	1.1	2.4	2.4	0.8	1.7	2.2	3.6

a: The electrolyte was acetonitrile containing 0.50 M LiX, 0.040 M X_2, 0.020 M pyridine and 0.020 M pyridinium triflate, where X=I or Br.

b: Potential required to drive a cathodic current density of 0.5 mA cm^{-2} in the dark. Standard deviations over many trials are ±0.05 V

c: Standard deviations over many trials are ±0.01 V.

d: Standard deviations over many trials are ±0.2 mA cm^{-2}.

e: The fill factor (ff) is calculated as $P_{max}/(J_{sc} \times V_{oc})$, where P_{max} is the most negative value of J × V.

f: Calculated as $(J_{sc} \times V_{oc} \times ff \times 100\%)/I_{light}$, where I_{light} = 100 mW cm^{-2}.

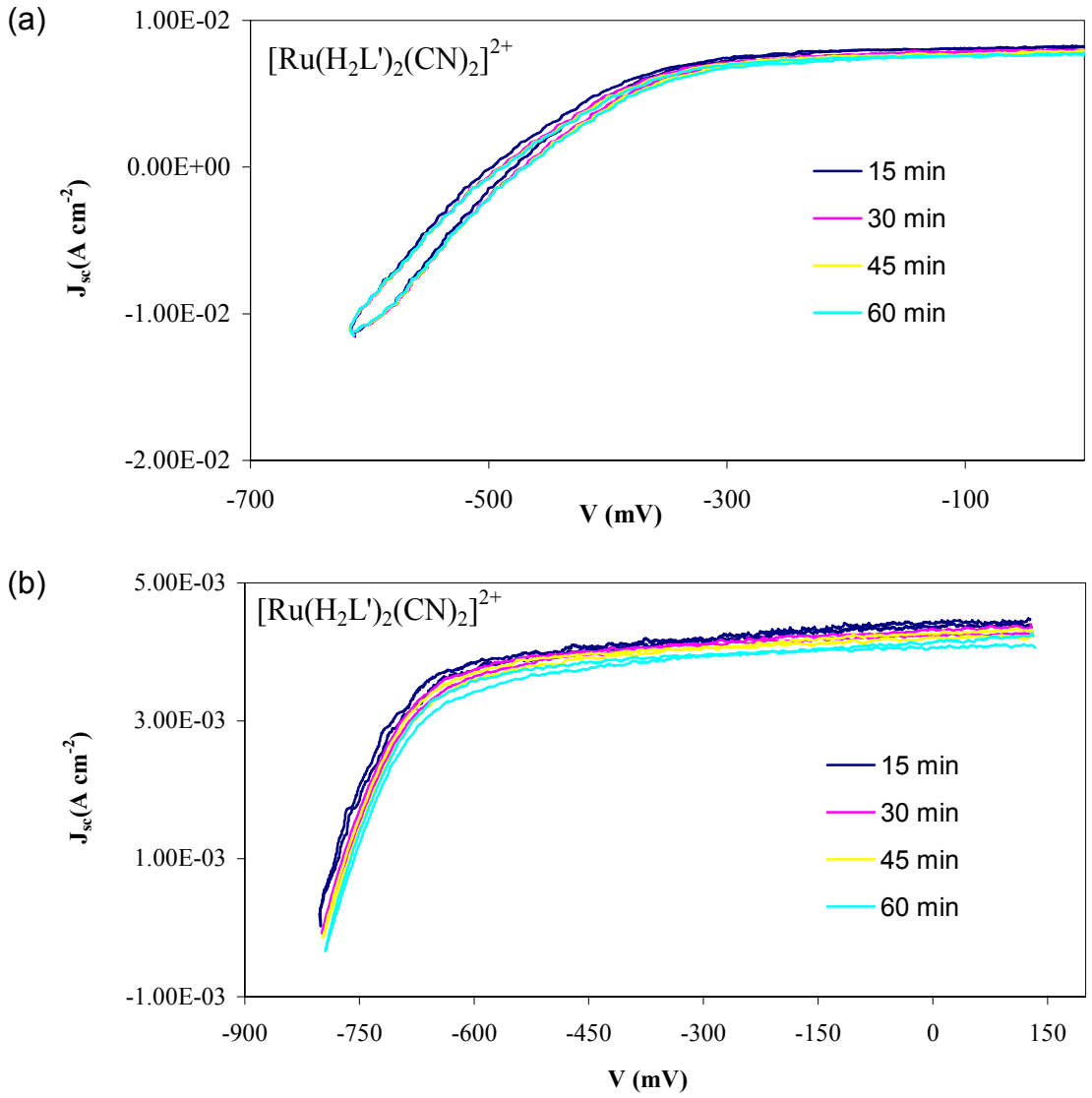

Figure 22. Stability of DSSCs with I_3^-/I^- and Br_3^-/Br^-. Current density versus potential characteristics as a function of time for nanocrystalline TiO_2 photoelectrodes sensitized with $[Ru(H_2L')_2(CN)_2]^{2+}$. Electrolyte concentrations: (a) 0.50 M LiI, 0.040 M I_2, 0.020 M pyridine and 0.020 M pyridinium triflate in acetonitrile and (b) 0.50 M LiBr, 0.040 M Br_2, 0.020 M pyridine and 0.020 M pyridinium triflate in acetonitrile.

If the loss in photocurrent is caused by slow kinetics of regeneration, then increasing the bromide concentration should produce a corresponding increase in photocurrent. To test this hypothesis, the current-potential behavior of a $[Ru(H_2L')_2(CN)_2]^0$ sensitized photoelectrode was measured as a function of the LiBr concentration (Figure **23**). Above a minimum concentration, there was no noticeable difference in J_{sc} or V_{oc}. To ensure that the mobility of Br_3^-/Br^- was sufficient to achieve facile regeneration, the effect of ionic strength on the photocurrent was measured. However, addition of 1.0 M $LiCO_4$ to the Br_3^-/Br^- electrolyte solution had no effect on the photocurrent.

Light-intensity effects were also investigated for a $[Ru(H_2L')_2(CN)_2]^0$ coated slide with Br_3^-/Br^- electrolyte. Figure **24** clearly shows that the photocurrent linearly depended on the light intensity and no saturation was observed in the power window studied. Furthermore, the open circuit voltage depended exponentially on the photocurrent, $I_{ph,}$ and consequently the light intensity, as expected based on Eq. 18, where I_0 is the dark current:

$$I_{ph} = I_o \, e^{(-qV_{oc}/KT)} \qquad (18)$$

The regeneration of oxidized dye with iodide and bromide was measured as function of the ground-state reduction potential of the sensitizer in functional DSSCs. This was achieved by monitoring the time-resolved disappearance of the MLCT transient absorption bleach in the presence of iodide or bromide. The recovery of the MLCT absorption for both $[Os(H_2L')L_2]^{2+}$ (Figure **25**) and $[Ru(H_2L')_3]^{2+}$ (Figure **26**) following pulsed-laser excitation accelerated significantly when iodide was added to the electrolyte.

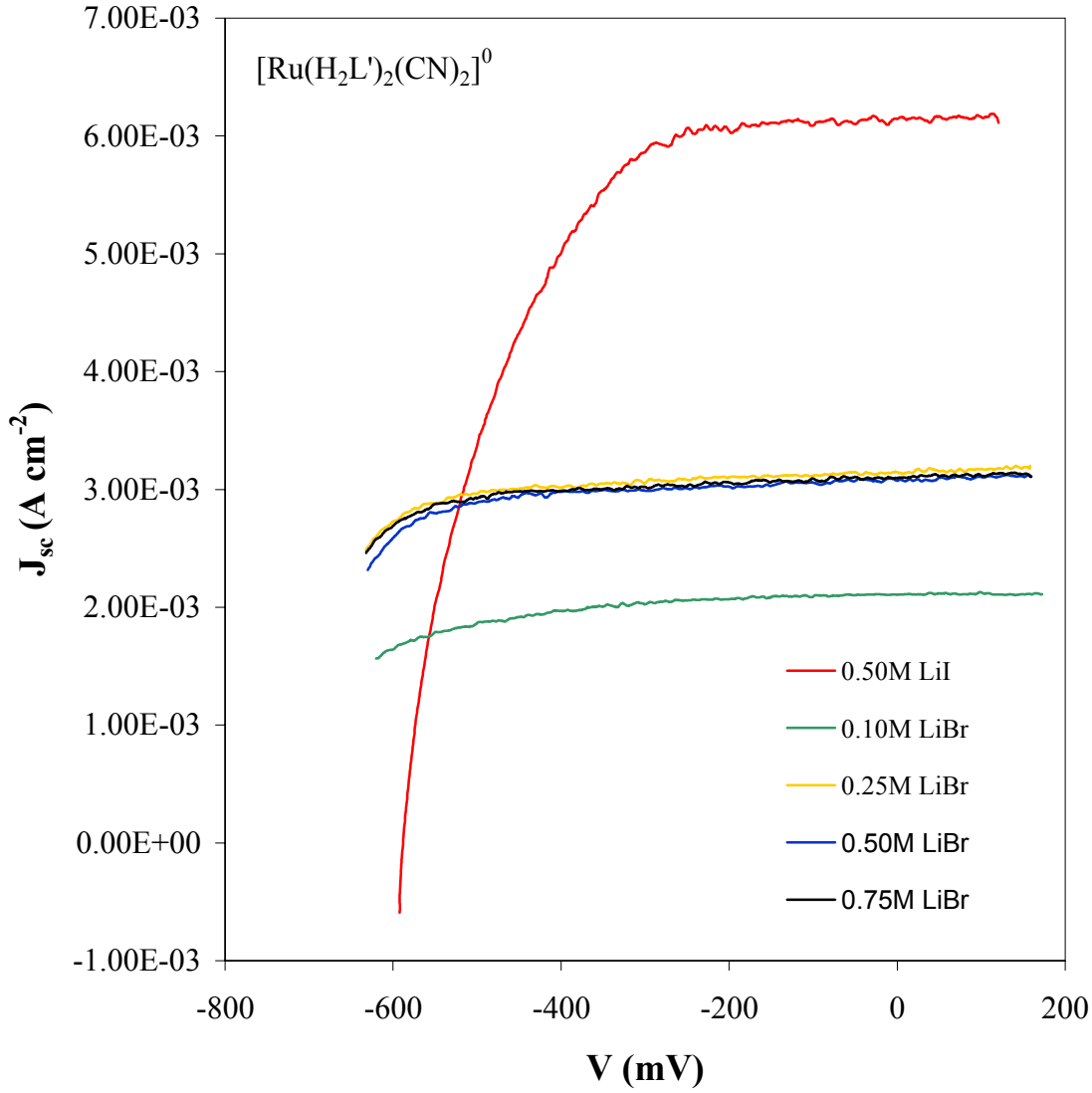

Figure 23. Bromide concentration dependence. Current density versus potential characteristics of a $[Ru(H_2L')_2(CN)_2]^{2+}$ sensitized TiO_2 electrode in contact with 0.040 M Br_2, 0.020 M pyridine and 0.020 M pyridinium triflate in acetonitrile with varying concentrations of LiBr. Also included for comparison is the performance of a $[Ru(H_2L')_2(CN)_2]^{2+}$ in contact with 0.05 M LiI, 0.040 M I_2, 0.020 M pyridine and 0.020 M pyridinium triflate in acetonitrile (red).

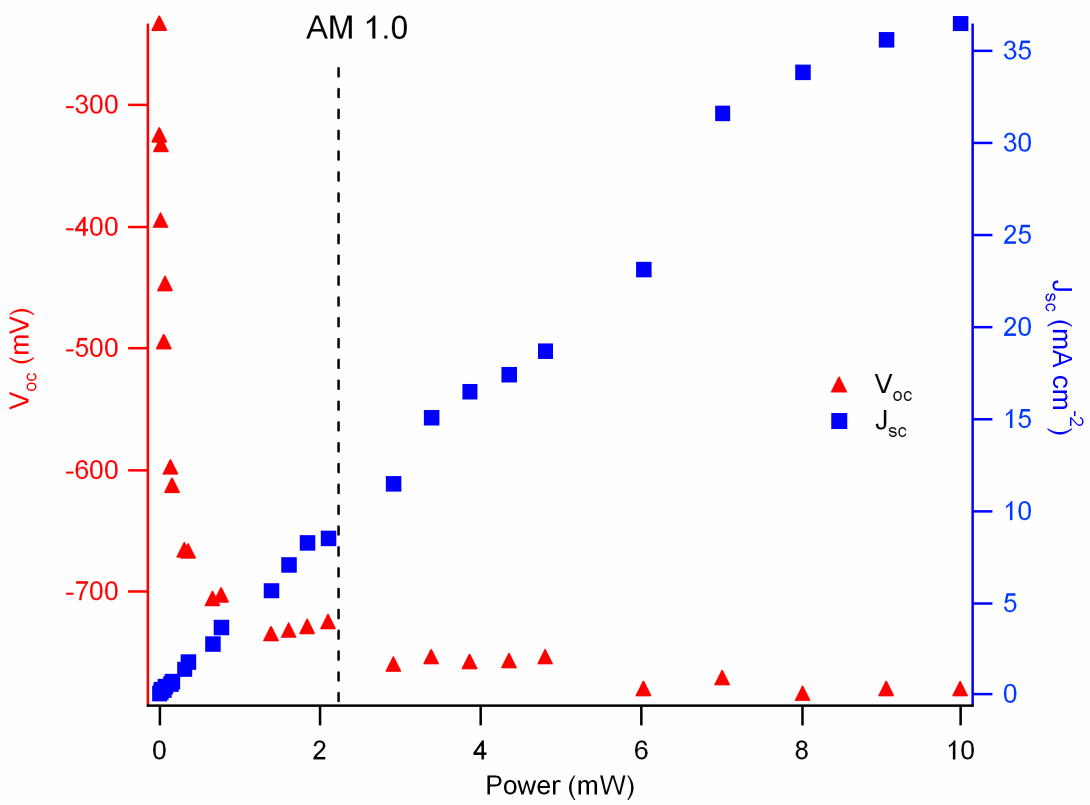

Figure 24. Solar cell performance as a function of light intensity. Short circuit current density (J_{sc}, blue squares) and open circuit potential (V_{oc}, red triangles) at varying incident light intensities for a nanocrystalline TiO_2 photoelectrodes sensitized with $[Ru(H_2L')_2(CN)_2]^{2+}$ in contact with 0.5 M LiBr, 0.040 M Br_2, 0.020 M pyridine and 0.020 M pyridinium triflate in acetonitrile.

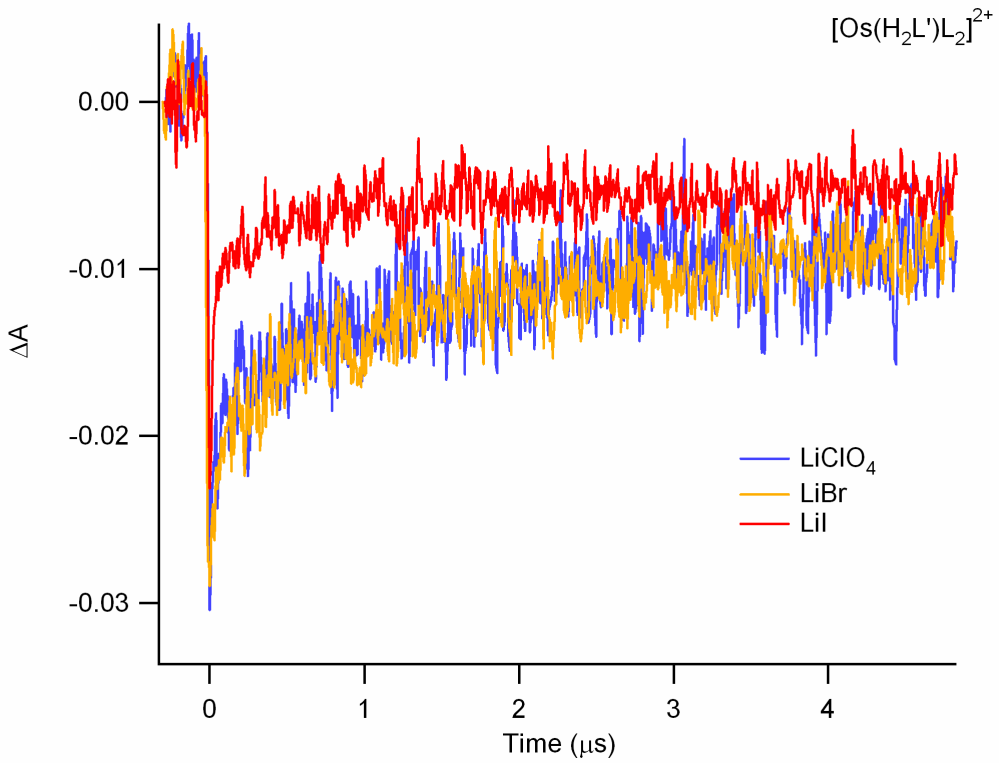

Figure 25. Transient kinetics data for $[Os(H_2L')L_2]^{2+}$ dye. λ_{ex} = 490 nm, λ_{ta} = 550 nm. Transient absorption (blue) of $[Os(H_2L')L_2]^{2+}$ dye on TiO_2 in the presence of 0.50 M $LiClO_4$, 0.020 M pyridine, and 0.020 M pyridinium triflate in acetonitrile. Transient absorption (red) of $[Os(H_2L')L_2]^{2+}$ dye on TiO_2 in presence of 0.5 M LiI, 0.020 M pyridine, and 0.020 M pyridinium triflate in acetonitrile. Transient absorption (yellow) of $[Os(H_2L')L_2]^{2+}$ dye on TiO_2 in presence of 0.5M LiBr, 0.020 M pyridine, and 0.020 M pyridinium triflate in acetonitrile.

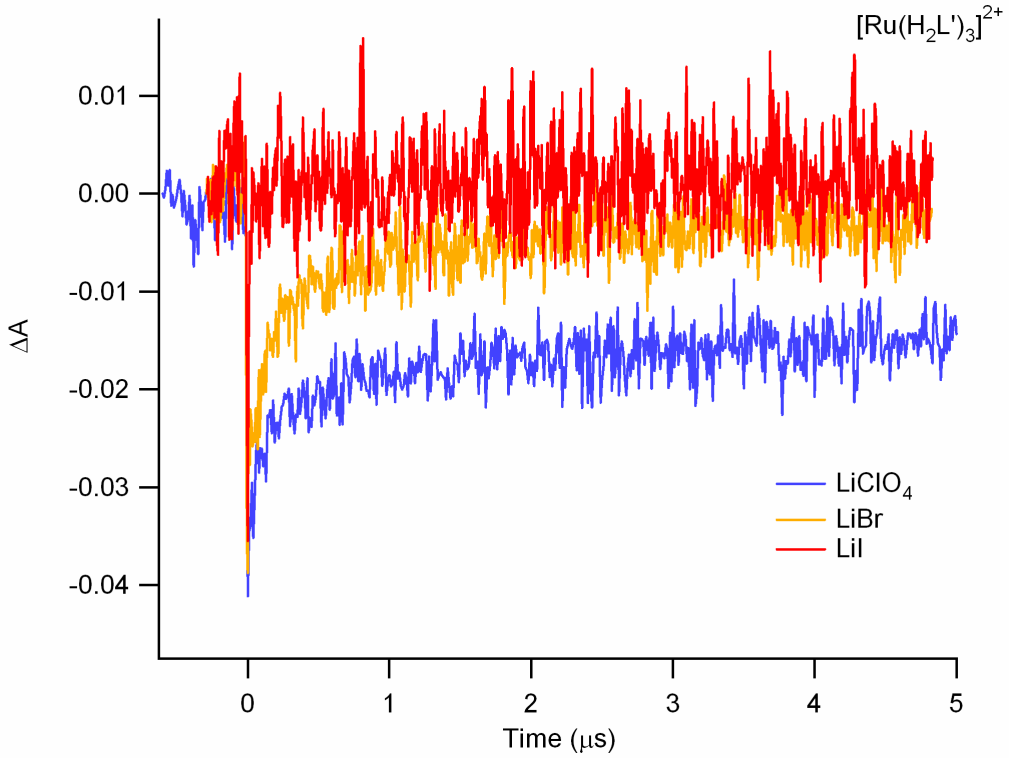

Figure 26. Transient kinetics data for $[Ru(H_2L')_3]^{2+}$ dye. λ_{ex} = 475 nm, λ_{ta} = 500 nm. Transient absorption (blue) of $[Ru(H_2L')_3]^{2+}$ dye on TiO_2 in the presence of 0.50 M $LiClO_4$, 0.020 M pyridine, and 0.020 M pyridinium triflate in acetonitrile. Transient absorption (red) of $[Ru(H_2L')_3]^{2+}$ dye on TiO_2 in presence of 0.5 M LiI, 0.020 M pyridine, and 0.020 M pyridinium triflate in acetonitrile. Transient absorption (yellow) of $[Ru(H_2L')_3]^{2+}$ dye on TiO_2 in presence of 0.5M LiBr, 0.020 M pyridine, and 0.020 M pyridinium triflate in acetonitrile.

For the least positive dye, $[Os(H_2L')L_2]^{2+}$, no influence on the recovery of the MLCT was observable upon addition of 0.5 M LiBr (Figure **25**). As the ground-state reduction potential of the dye became more positive, addition of bromide resulted in more rapid recovery of the ground state, but this regeneration rate was significantly slower than that observed with iodide (Figure **26**).

Mixed Halides

Absorption spectra of iodine solutions with varying concentrations of bromide (Figure **27**b) or chloride (Figure **27**c) clearly showed new absorption peaks assigned to I_2Br^- (277 nm, 360 nm) and I_2Cl^- (228 nm, 261 nm, 289 nm, 362 nm). These features were shifted to slightly higher energy than the I_3^- absorptions (293 nm, 363 nm) (Figure **27**a). Cyclic voltammetry was used to determine the relative shift in potential of the I_3^-/I^- couple upon halide addition. The electrochemistry was problematic for the Cl^- system, although repeated attempts indicated a shift to more positive potentials (Figure **28**a). However, a pronounced shift to more positive potentials was observed upon addition of Br^- (Figure **28**b). This shift in potential correlated with a decreased dark current for a blank TiO_2 slide in contact with an I_3^-/I^- electrolyte with varying concentrations of Br^- and Cl^- (Figure **29**a,b and Table **2**). When $[Ru(H_2L')L_2]^{2+}$ was adsorbed onto the slide, the shifts in the dark current were slightly decreased, but were still observable (Figure **29**c,d and Table **2**). These shifts were significantly smaller (~42 mV) than those observed with the Br_3^-/Br^- electrolyte (~350 mV). However, under AM 1.0 illumination V_{oc} increased with Br^- and Cl^- addition, and a corresponding increase in photocurrent was observed (Figure **30**a,b and Table **2**). However, the photocurrent increase was inversely

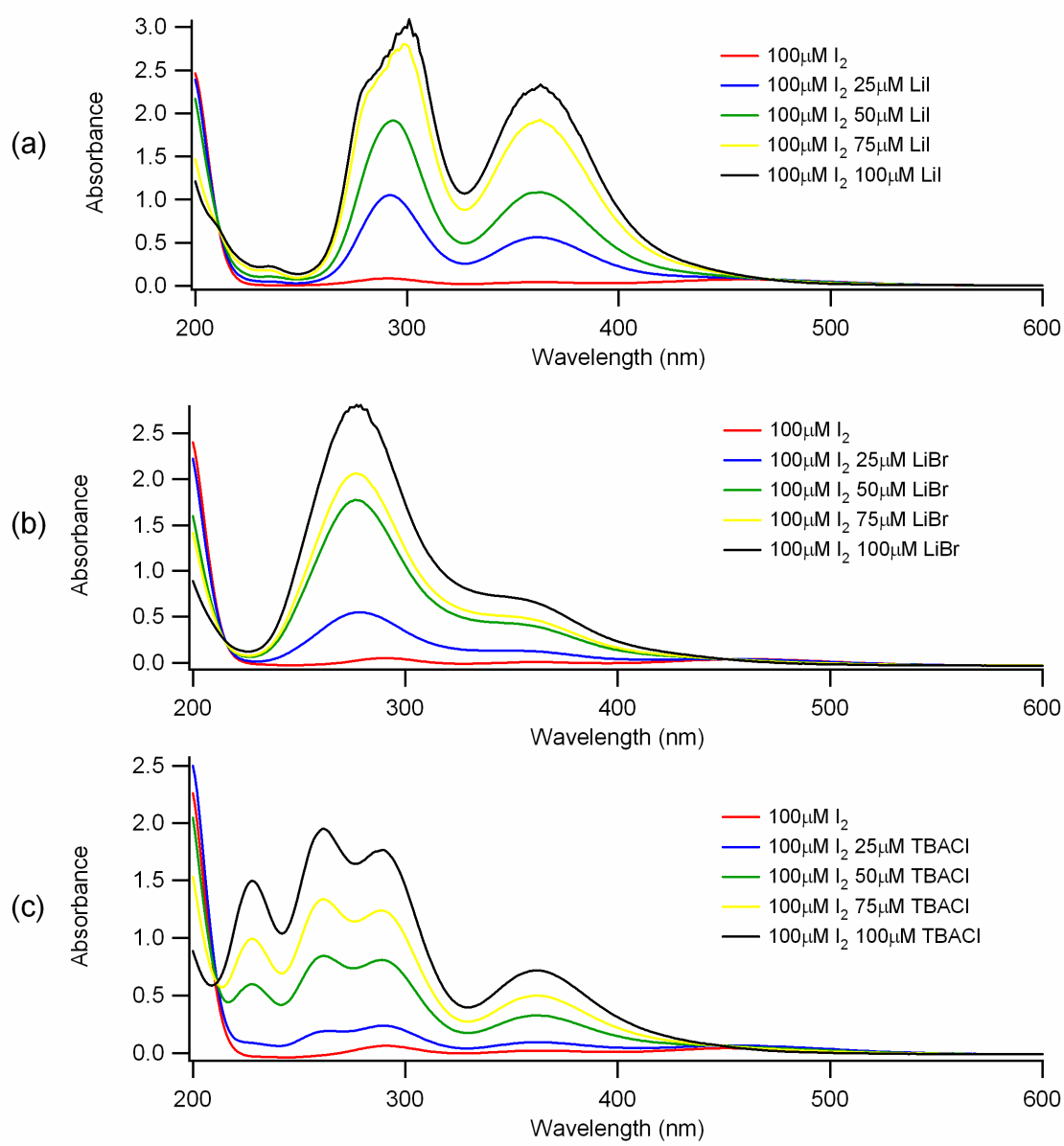

Figure 27. UV-vis spectra of I_2Cl^- and I_2Br^- in acetonitrile. A solution of 100 μM I_2 in acetonitrile with increasing concentration of (a) LiI, (b) LiBr or (c) TBACl.

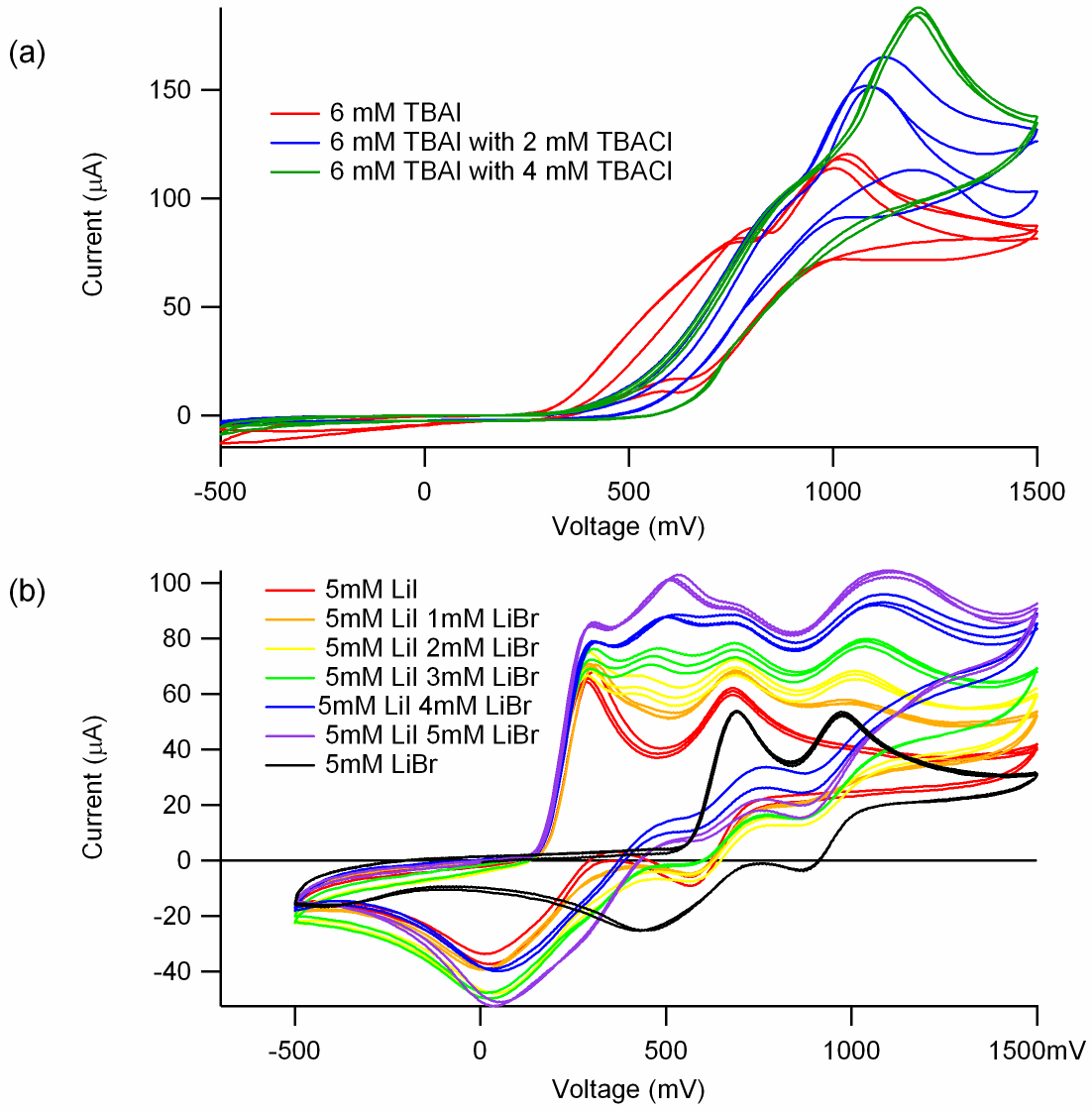

Figure 28. CVs of mixed halide electrolytes. (a) A solution of TBAI (6 mM) in acetonitrile with increasing concentrations of TBACl. (b) A solution of LiI (5 mM) in acetonitrile with increasing concentrations of LiBr. Spectra were obtained with a glassy carbon working electrode, platinum wire counter electrode and versus a methanol SCE reference.

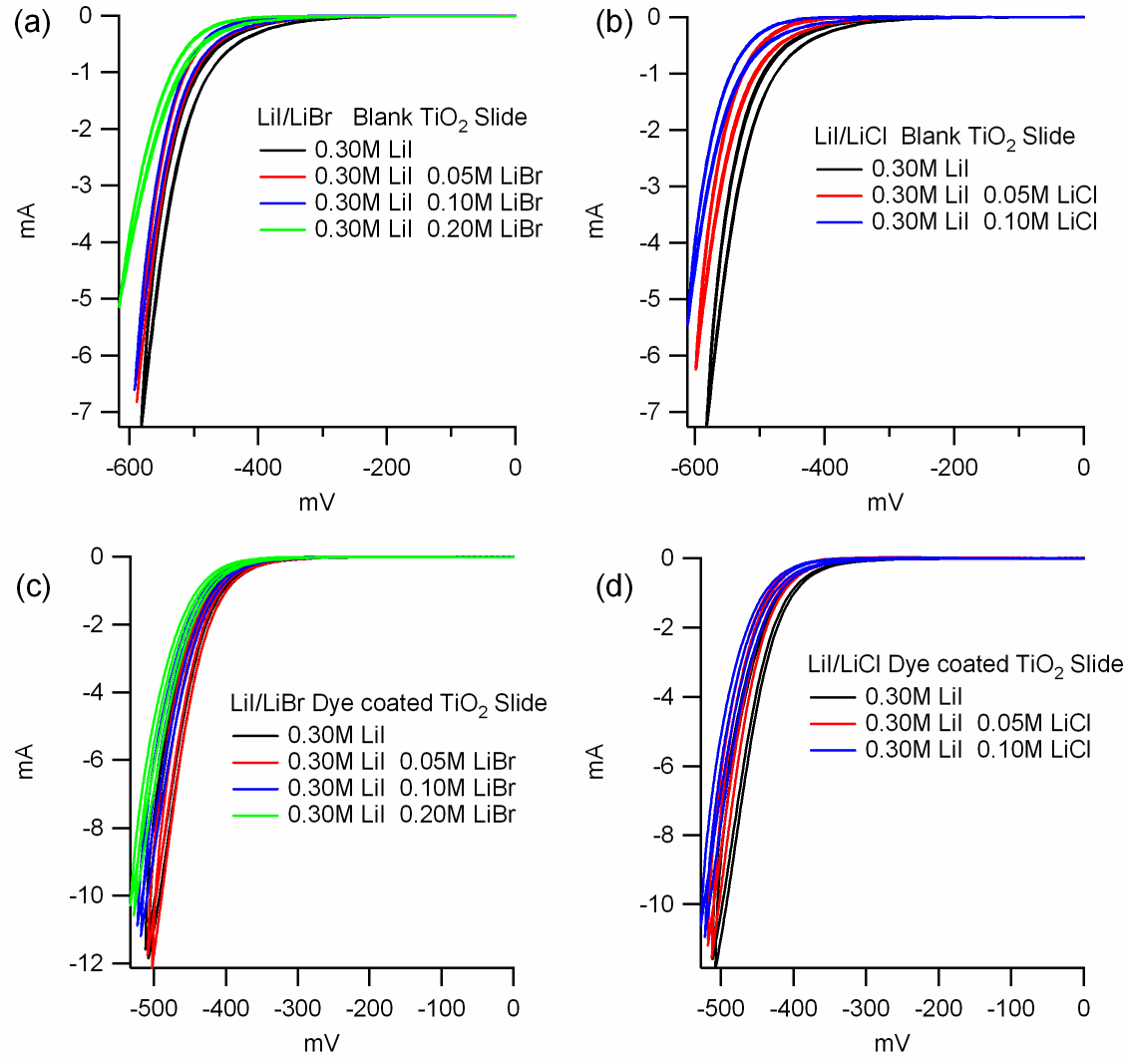

Figure 29. Dark current versus potential characteristics of TiO_2 electrodes with mixed halide electrolytes. Electrolyte concentrations: 0.30 M LiI, 0.040 M I_2, 0.020 M pyridine and 0.020 M pyridinium triflate in acetonitrile and varying concentrations of (a) LiBr and (b) LiCl. Dark current versus potential characteristics of $[RuL_2(H_2L')_2]^{2+}$ sensitized TiO_2 electrodes in contact with 0.30 M LiI, 0.040 M I_2, 0.020 M pyridine and 0.020 M pyridinium triflate in acetonitrile varying concentrations of (c) LiBr and (d) LiCl.

Table 2. Photoelectrochemical data for DSSCs with mixed halide electrolytes.[a]

	0.3 M LiI, 0.04 M I_2, 20 mM pyridine, 20 mM pyridinium triflate with:					
	0M LiBr	0.05M LiBr	0.1M LiBr	0.2M LiBr	0.05M LiCl	0.1M LiCl
V_{dark}[b] (mV)	-420	414	-424	-434	-430	-434
V_{oc} (mV)	-445	-458	-464	-470	-462	-504
J_{sc} (mA)	3.71	5.95	5.09	4.74	5.41	5.14
ff[c]	0.75	0.73	0.72	0.72	0.71	0.67
Efficiency[d]	1.25	1.98	1.71	1.61	1.79	1.73

a: The electrolyte was acetonitrile containing 0.30 M LiI, 0.040 M I_2, 0.020 M pyridine and 0.020 M pyridinium triflate, with either LiBr or LiCl added. $LiClO_4$ was added as needed to maintain a 0.5M Li^+ concentration.

b: Potential required to drive a cathodic current density of 0.1 mA cm^{-2} in the dark.

c: The fill factor (ff) is calculated as $P_{max}/(J_{sc} \times V_{oc})$, where P_{max} is the most negative value of $J \times V$.

d: Calculated as $(J_{sc} \times V_{oc} \times ff \times 100\%)/I_{light}$, where I_{light} = 100 mW cm^{-2}.

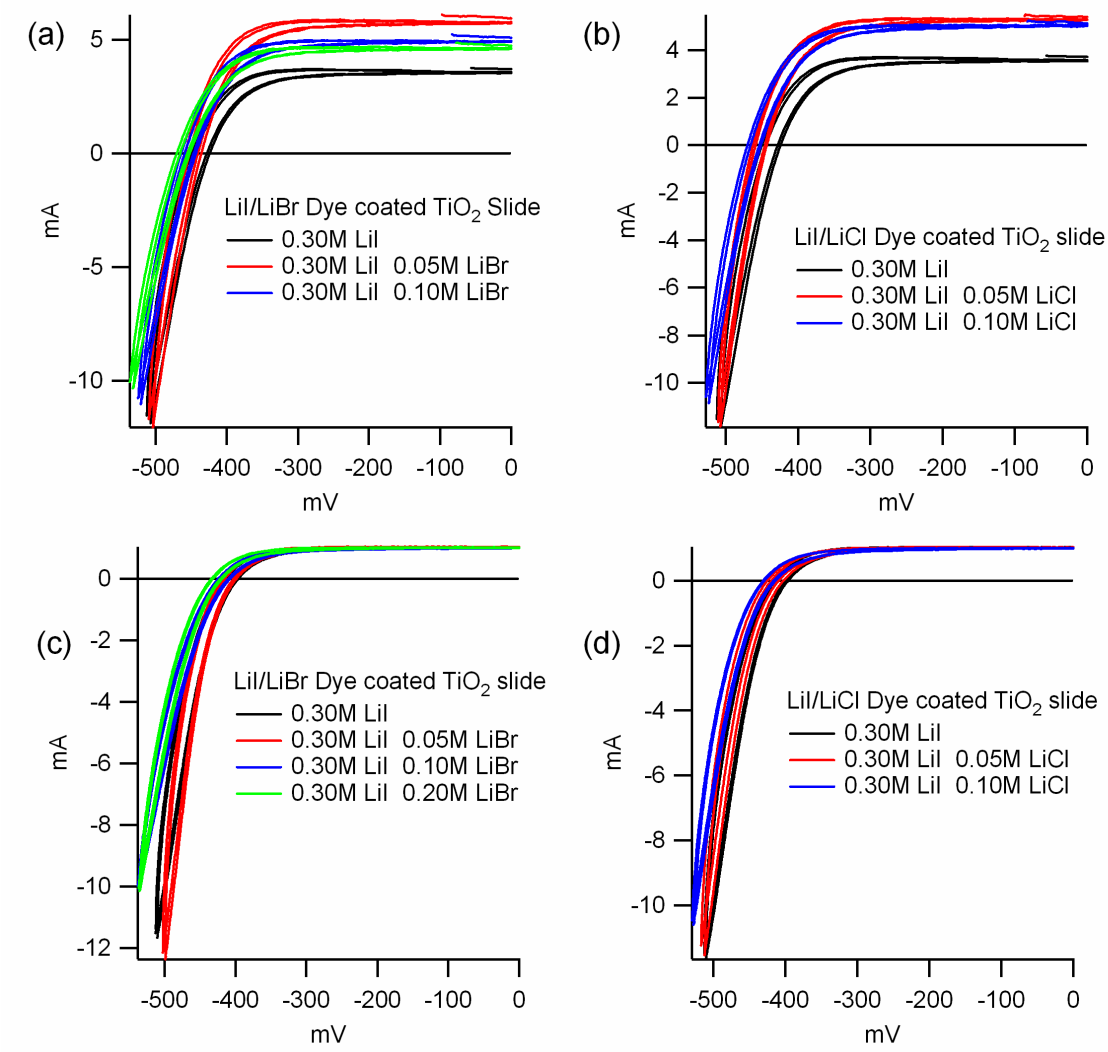

Figure 30. Current versus potential characteristics under AM 1.0 illumination of $[RuL_2(H_2L')_2]^{2+}$ sensitized TiO_2 electrodes with mixed halide electrolytes. Electrolyte concentrations: 0.30 M LiI, 0.040 M I_2, 0.020 M pyridine and 0.020 M pyridinium triflate in acetonitrile with varying concentrations of (a) LiBr or (b) LiCl. Behavior at a constant photocurrent (incident light intensity was set to maintain J_{sc} ~1 mA cm^{-2}) with varying concentrations of (c) LiBr or (d) LiCl.

related to the concentration of added halide. A direct comparison between the open circuit potentials was made by controlling the incident light intensity to maintain a constant photocurrent (Figure **30**c,d).

Discussion

Alternative Two-Electron Redox Couples

The complications and difficulties of working with the pseudohalides apparently limit their overall usefulness in functional DSSCs. Even more problematic are their facile electron transfer properties with TiO_2. However, the Br_3^-/Br^- couple showed a decreased dark current when compared with I_3^-/I^-. Furthermore, this couple showed very efficient regeneration of $[Ru(bpy)_3]^{2+}$. The regeneration rate constant for reduction of $[Ru(bpy)_3]^{3+}$ by bromide (10^8 M^{-1} s^{-1}) is less than the rate for reduction with iodide (10^{10} M^{-1} s^{-1}) but is still very fast for these systems. This indicates that bromide has sufficiently rapid kinetics for the regeneration of $[Ru(bpy)_3]^{2+}$-type dyes such as those used in DSSCs.

A significant shift in the dark current to more negative potentials was observed when working with the bromide system. This shift correlated with a larger V_{oc} in the light. However, the increase in V_{oc} was often accompanied by a decrease in photocurrent. Despite this loss in photocurrent, switching from I_3^-/I^- to Br_3^-/Br^- resulted in an increase in the overall cell efficiency for dyes with ground-state reduction potentials >1 V.

The loss in photocurrent decreased with increasing potential difference between the Br_3^-/Br^- redox potential and the ground-state redox potential of the dye. This

indicates that a minimum driving force is necessary for rapid regeneration of the oxidized dye. Thus, the dyes with more negative M^{3+}/M^{2+} ground-state redox potentials are expected to have the highest ratio of the rate of recombination with electrons in TiO_2 relative to the rate of reduction of the adsorbed M^{3+} complex with I_3^-/I^- in the electrolyte. This high rate ratio allows the back reaction of electrons with M^{3+} to compete with the regeneration of M^{2+} through reaction with I^-.

It has been previously reported that the ground-state potential of $[Os(H_2L')_2(NCS)_2]^{2+}$ (0.4 V vs. SCE) was a lower limit for the ground-state redox potential of the dye in the current configuration of the electrochemical cell and I_3^-/I^- redox couple (0.023 V vs. SCE). While the potential difference cannot be discussed in terms of a true driving force for regeneration, it is surprising that for the Br_3^-/Br^- redox couple (0.44 V vs. SCE), the ground-state potential of $[Ru(H_2L')_2(CN)_2]^{2+}$ (1.08 V vs. SCE) was a lower limit for the ground-state redox potential of the dye in order to have sufficient regeneration by Br_3^-/Br^-.

The decreased regeneration for dyes with more negative ground-state reduction potentials can be clearly seen in the transient kinetics for recovery of the ground state for dyes adsorbed onto TiO_2 (Figures **25** and **26**). The natural recovery from M^{3+} to M^{2+} is dominated by the recombination of electrons in TiO_2 with the oxidized dye, and can be determined by monitoring the time-resolved disappearance of the MLCT transient absorption bleach in the absence of a reductant. The kinetics of recombination and regeneration for both dyes were multiexponential. This is likely due to the heterogeneity of the TiO_2 surface and the wide distribution of energetic states from which

recombination of injected electrons in TiO_2 with the oxidized dye can occur. The kinetics are possibly further complicated by the ability of the reductants to adsorb onto the TiO_2 surface.

It is important to monitor the relative amplitudes of MLCT bleach due to formation of Ru^{2+*}. If the rate of regeneration is exceedingly fast, a great deal of the rate information will be lost due to kinetics too fast to be observed on the timescale of the experiment. Further complicating the kinetics, the recovery in the presence of iodide for these dyes is, in reality, made up of both recombination of electrons in TiO_2 with the oxidized dye as well as regeneration of the oxidized dye by iodide.

However, the general shapes of the decay kinetics can be compared with the literature values that have been determined from more rigorous measurements. Using a direct comparison with the literature values, the regeneration rate by iodide can be estimated as 10^8 s^{-1}.[19] For the least oxidizing dye, addition of bromide does not affect the natural recovery to ground state, while iodide rapidly accelerates the bleach recovery. The slower rates observed with bromide allowed for fitting of the MLCT recovery and an average regeneration rate for the bromide was directly determined (2.5×10^6 s^{-1}) for $[Os(H_2L')L_2]^{2+}$, only slightly faster than recombination (1.2×10^6 s^{-1}). This diminished regeneration rate is consistent with the concept of a decreased driving force for regeneration of this dye and explains the observed loss in photocurrent. This indicates that a thermodynamic threshold corresponding to a sufficient driving force for oxidation of bromide has been crossed.

Significant differences in the regeneration kinetics were observed for the more oxidizing dye $[Ru(H_2L')_3]^{2+}$, which showed a minimal decrease in photocurrent in DSSCs using the Br_3^-/Br^- redox couple (Table **1**). The rate of reduction of the oxidized dye ($8.9x10^6$ s^{-1}) was faster than in the previous case, but still slower than reduction by iodide. However, for this dye, both regeneration by iodide and bromide were so rapid that a decrease in the initial bleach was observed, indicating that both are significantly rapid reduction processes and that the rate of regeneration for this dye is faster than for the $[Os(H_2L')L_2]^{2+}$. This increase in rate is consistent with the increased driving force for oxidation of bromide by this dye due to its more positive ground-state reduction potential.

If the loss in photocurrent is caused by slow rates of regeneration, then by increasing the bromide concentration, the photocurrent should increase. However, there was essentially no dependence of the efficiency on the Br^- concentration (Figure **23**). Thus, while it is clear that the regeneration rates are a factor in the diminished photocurrents of dyes with more negative redox potentials, this simple kinetics loss does not explain the decreased photocurrent (50% less) for $[Ru(H_2L')(CN)_2]^{2+}$ dye, in which regeneration competed efficiently for recombination.

One of the many disadvantages of the triiodide/iodide couple is that when employed in high concentrations the triiodide ion absorbs over a significant part of the visible spectrum (Figure **13**). These absorption properties prevent the study of injection, recombination and regeneration kinetics in the presence of I_3^-/I^- concentrations as high as those used in a functional DSSC. It is quite possible that I_3^- or another species generated from the two-electron reduction is involved in the regeneration of the oxidized dye. The

inability to monitor regeneration processes with both iodide and triiodide present has significantly hindered the elucidation of this mechanism. The Br_3^-/Br^- couple absorbs at significantly higher energy and should provide fewer problems spectroscopically.

Mixed Halides

While resulting in enhanced open circuit voltages, the significantly more positive Br_3^-/Br^- couple (0.46V vs. SCE) will limit the dyes that can be used to those that are positive enough to maintain a sufficient driving force for regeneration, essentially limiting the degree of spectral overlap. Addition of bromide or chloride ions to an iodine solution resulted in the formation of the interhalide species, I_2Br^- and I_2Cl^-, respectively (Figure **27**). However, in the presence of iodide, the formation of I_3^- dominates the spectra (Figure **31**). The two-electron reduction potentials of these species are known to be more positive than that of I_3^- (Figure **28**).[56] This shift in potential resulted in a suppression of the dark current (Figures **29** and **30**, Table **2**) which corresponded to an increase, albeit minor, in the output photovoltages. It is intriguing that the photocurrent increased as well, with the largest increase seen with the lowest concentration of added Br^-. There are a number of factors that can affect the photocurrent. The first and most obvious is a decrease in dark current. However, the dark current decreased with increasing halide addition. In contrast, the photocurrent was highest at low concentrations of halide, but began to decrease again as the halide concentration was increased. This phenomenon cannot be explained by a conduction band edge shift as the concentration of Li^+ cations was constant in all cases and should fix the conduction band edge. Furthermore, a conduction band edge shift cannot explain the fact that the

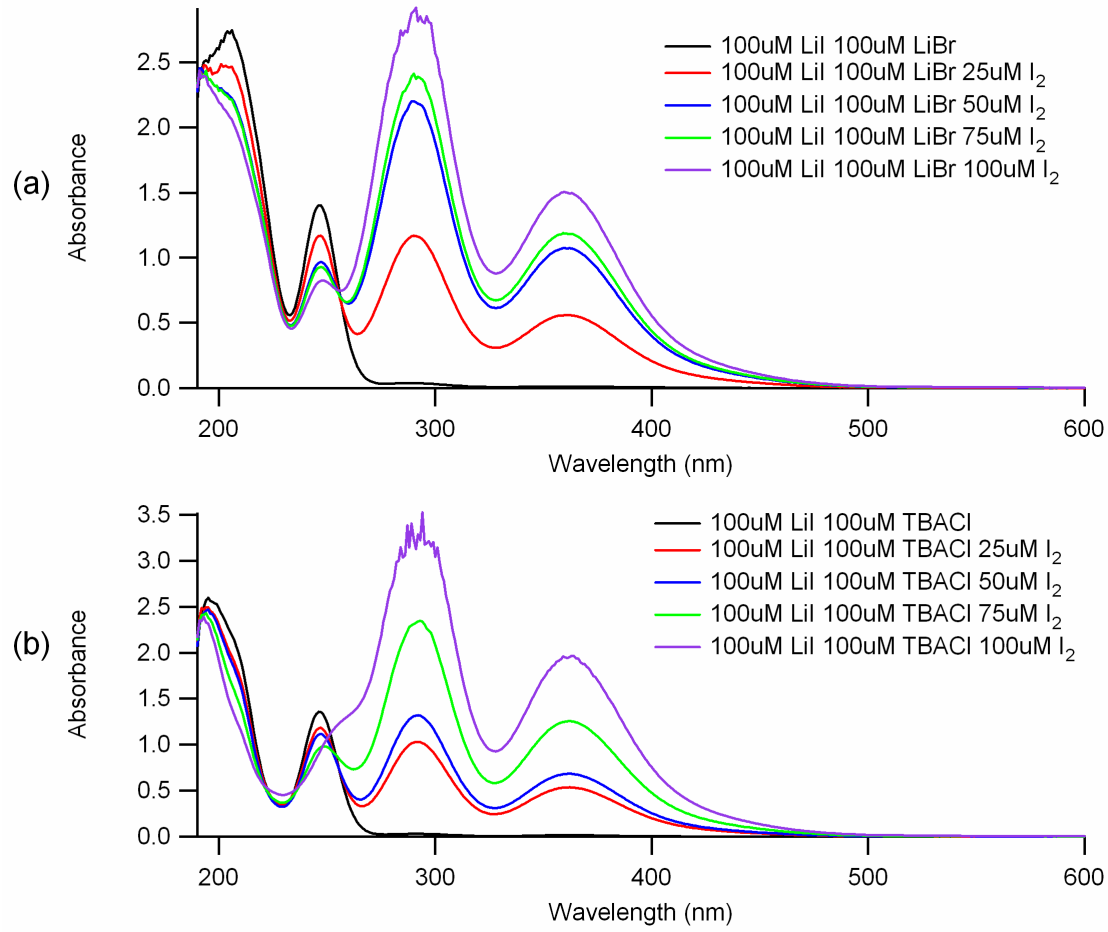

Figure 31. UV-vis spectra of I_2Cl^-/I^- and I_2Br^-/I^- in acetonitrile. A solution of 100 μM LiI in acetonitrile with (a) 100 μM LiBr and increasing concentrations of I_2 and (b) 100 μM TBACl and increasing concentrations of I_2

increased photocurrent occurred only at low halide concentrations. Iodide can reductively quench the excited state of the dyes, but the rate of this quenching is small relative to the ultrafast injection that occurs in most systems.[57] We have recently discovered that triiodide can quench the excited state as well.[58] It is therefore plausible that the anomalous behavior in the photocurrent is a result of modulation of this quenching rate. At low halide concentrations, bromide or chloride ions should dominate. As the concentration is increased, the concentration of the interhalide species I_2Br^- and I_2Cl^- should increase. It is still difficult to reconcile the concept that quenching is decreased (and thus the photocurrent increased) at low Br^- or Cl^- concentrations, but that the quenching becomes more predominant as the concentration is increased. This is an interesting problem that may lend insight into the unique behavior of the I_3^-/I^- system and warrants further investigation.

Conclusions

The Br_3^-/Br^- redox couple appears to behave in a similar fashion to the I_3^-/I^- couple as it maintains slow electron transfer rates with TiO_2. By using the more positive Br_3^-/Br^- couple, significant enhancements in the open circuit potential were achieved under AM 1.0 illumination. This increase in V_{oc} (>300 mV more negative) correlated with nearly a twofold increase in the solar cell efficiency over DSSCs using the I_3^-/I^- couple in conjunction with dyes with ground-state reduction potentials more positive than 1.08 V vs. SCE. This report indicates that the potential of the $[Ru(H_2L')_2(CN)_2]^{2+}$ dye is a lower limit for use in DSSCs with the Br_3^-/Br^- couple. This may ultimately limit the

usefulness of this couple in DSSCs as dyes with such positive potentials usually have limited spectral overlap.

The pseudohalogens, while having suitably more positive redox potentials, exhibited facile electron transfer with the TiO_2 surface, rendering them useless in functional DSSCs. The ability of the I_3^-/I^- and Br_3^-/Br^- couples to form polyhalide species is likely key to their slow electron transfer properties with TiO_2. Interhalide species formed upon addition of Cl^- and Br^- to the I_3^-/I^- couple exhibited similar dark currents and shifted the solution redox potentials to more positive values. This resulted in significant enhancements in the efficiency as a result of increases in both V_{oc} and J_{sc} (>40% efficiency increase). It is surprising that these mixed halide systems exhibited enhanced photocurrents, as they should not affect the photon absorption or injection properties. A more likely explanation is that the interhalide species show enhanced rates of regeneration or a decreased rate of quenching of the dye excited state.

CHAPTER 4:

TITANIUM DIOXIDE SURFACE PROTECTION

Chapter 4

TITANIUM DIOXIDE SURFACE PROTECTION

Introduction

As discussed in the previous chapter, the ability to use redox couples other than iodide/triiodide is crucial to the development of more efficient DSSCs. However, recombination of the injected conduction-band electrons with the redox species in the electrolyte is very facile for most redox couples other than I_3^-/I^- or Br_3^-/Br^-. In order to realize incorporation of alternative redox couples, it is important to learn how to suppress this deleterious back reaction.

The gain in open circuit voltage that can be achieved by minimization of the dark current can be calculated from the diode equation:

$$V_{oc} = \frac{nRT}{F} \ln \left(\frac{I_{ph}}{I_o}\right) \qquad (19)$$

where n is the ideality factor whose value is between 1 and 2 for the DSSC, I_{ph} is the photocurrent, and I_o is the reverse saturation current. Thus, for each order of magnitude decrease in the dark current, the V_{oc} would increase 59 mV at room temperature. Clearly, the ability to control the dark current would be indispensable to the goal of raising the overall efficiency of the these systems.

Whether charge transfer occurring through the solid/liquid interface proceeds directly from free electrons in the conduction band or is mediated by surface states is

vital in understanding the mechanism and kinetics of the back electron transfer reaction. A distribution of energetically different traps for electrons could be responsible for the observed multi-exponential kinetics for back electron transfer.[59-61] As such, the kinetics of recombination across the semiconductor/solution interface will be dependent upon the occupancy and energetics of the electronic states in the nanoparticle.

It has been shown in other systems that surface modification can reproducibly protect semiconductor surfaces and increase overall efficiencies. This was accomplished by preventing the formation of electronic surface states lying below the conduction band edge which mediate recombination of the injected conduction band electrons by chemical modification of the surfaces.[62-64] In particular, some suppression of back electron transfer in TiO_2 and other semiconductor systems has been achieved by passivating recombination centers with a variety of pyridine derivitives.[65-67]

It is difficult to directly measure the energetics of the surface state or to isolate the states that are directly participating in electron transfer with the redox couple in solution. The kinetics of electron transfer, however, can be indirectly measured by monitoring the dark current. An understanding of the effect of surface modification on the relative rates of this electron transfer process will open the door to a better understanding of the mechanism behind the recombination reaction and may ultimately result in increases in overall cell efficiency.

In an attempt to mimic the ester linkage of the ruthenium bipyridyl dyes, we investigated the effect of adsorbing carboxylic acids of various lengths to exposed surfaces of the TiO_2 to create a physical barrier between the TiO_2 and the redox couple in

solution. These compounds have the possibility of forming a tightly packed insulating monolayer, pushing the acceptor away from the surface and consequently blocking the dark current. The thickness of the blocking layer will increase with increasing blocker length, assuming the blocking layer is perpendicular to the surface. An alternative approach involves the polymerization of silanes onto the TiO_2 surface. If the blocking layer extends past the adsorbed dye, it is possible that it will prevent regeneration of the oxidized dye. Regardless of the method of surface protection, it will be important to find a balance between maximum surface coverage and efficient regeneration.

Experimental

Materials

Acetic acid, butyric acid, tert-butyl acetic acid, heptanoic acid, lauric acid, stearic acid and lithium perchlorate were purchased from Aldrich and were used without further purification. Lithium iodide (Aldrich, 99.9%) and lithium bromide (Aldrich, 99.99%) were used as received and stored under an inert atmosphere. Iodine (Aldrich, 99%) was sublimed before use. Pyridinium triflate (Aldrich, 97%) was purified by recrystallization ($MeCN/Et_2O$) and dried overnight under vacuum. Pyridine (J.T. Baker) was distilled before use. $TiCl_4$ (Aldrich, 99.99%), polyacrylic acid (Polysciences, Inc.) and absolute ethanol (Quantum Chemicals) were used as received. Acetonitrile (EM Science, reagent grade) was dried over CaH_2 and distilled over P_2O_5. All other solvents were reagent grade and were purchased from EM Science. Water (17.7 MΩ cm resistivity) was obtained from a Barnstead NANOpure Inc. filtration system. Ferrocene was sublimed using a 95^{o}C water bath and dry/ice acetone in a cold finger for 6 hours (Found: C

64.50%, H 5.48%; Calculated : C 64.5%, H 5.42%). Ferrocenium tetrafluoroborate was synthesized by dissolving freshly sublimed ferrocene (0.7967g, 2.44 mmoles) with p-benzoquinone (0.133g, 1.2 mmoles) in 35 mL of THF in a 125 mL Erlenmeyer flask. Using an addition funnel, 0.75 mL of HBF_4 (54% in ether) was added, resulting in a dark green precipitate. The solution was cooled in an ice bath for 10 minutes and then filtered through a medium-porosity glass frit funnel, washed with cold THF and cold ether and then dried under vacuum for four hours and stored in a glove box until use. Elemental Analysis was performed by Midwest Microlab, Inc. (Found: C 43.79%, H 3.62%; Calculated : C 44%, H 3.69%). The so-called N3 dye, Ru(4,4'-dicarboxy 2,2'-bipyridyl)$_2$(NCS)$_2$ (herein abbreviated as $[Ru(H_2L')_2(NCS)_2]^0$) was purchased from Solaronix SA and used as received. All other dyes were synthesized as described previously and were available in our labs.[30]

Electrolyte

The halide electrolytes used were 0.5M LiI and 0.04M I_2 with 20 mM pyridine and 20 mM pyridinium triflate unless otherwise noted. Ferrocene electrolytes were prepared at 0.1M ferrocene and 0.01M ferrocenium with 0.1M $LiClO_4$. The decreased concentration is due to lower solubility and the $LiClO_4$ acts as the supporting electrolyte.

Slide Preparation

All TiO_2 slides were treated with $TiCl_4$ as discussed previously (Chapter 2, General Introduction). Dye adsorption was achieved by submersion of hot, freshly prepared TiO_2 into ethanolic solutions of $[Ru(H_2L')_2(SCN)_2]^0$ and left overnight. The dye-coated slides were then submerged in ethanolic solutions of the various carboxylic

acids (0.1 M). For surface modification of blank TiO_2 slides with no dye, the hot, freshly prepared TiO_2 slides were submerged in ethanolic solutions of the various carboxylic acids (0.1 M), typically for 1 h. In all cases, the slides were rinsed thoroughly with ethanol after submersion in the acidic solutions to remove any non-bound acid.

Silane Polymerization

Polymerization of trichloromethyl silane onto the TiO_2 surface was achieved as follows: a smaller vial was placed inside of a larger vial and both vials were dried overnight at 150^{o}C. After cooling to just above room temperature, 2 mL of CH_3SiCl_3 were added to the inner vial and, the outer vial was capped and left to equilibrate for 1 h. TiO_2 slides, pretreated with $TiCl_4$, were reheated at 120^{o}C for 10 min and placed in the outer vial. Polymerization was allowed to occur for varying times. Slides were removed and rinsed with a 2% solution of pyridine in acetonitrile and dried in an oven (120^{o}C) for 30 min before current-voltage measurements were made.

Characterization

Electrolyte solution potentials were measured using a voltmeter, and current-potential measurements were made on a BAS100B electrochemical workstation with an aqueous SCE double junction reference electrode. Current-potential measurements were performed in the custom designed cell using standard procedures (Chapter 2, General Experimental). X-ray photoelectron spectroscopy (XPS) was run in an M-probe surface spectrometer (Fisons) pumped by a CTI-cryogenics 8 cryo pump. Monochromatic Al K_α X-rays ($h\nu$ = 1486.6 eV) incident at 35^{o} from the sample surface were used to excite electrons from the sample, while the emitted photo-electrons were collected by a

hemispherical detection analyzer at a takeoff angle of 35^{o} from the plane of the sample surface. Data collection and analysis were done with the M-probe package software version 3.4.

Results

Electrochemical measurements of TiO_2 photoelectrodes in the absence of illumination were performed to investigate the rate of electron transfer of electrons in TiO_2 to the redox couple in solution. The relative rates of this reaction for different carboxylic acid modified slides can be inferred from the dark current density as a function of electrode potential. Less negative potentials required to drive the same current density in the dark indicate more facile electron transfer processes between TiO_2 and oxidized species in the electrolyte. Figure **32**a shows current-voltage curves of uncoated TiO_2 after submersion in 0.1M ethanolic solutions for 1 h. The hysteresis in these samples is not unusual for such low current densities and scan rates (20 mV s^{-1}). However, if only the reverse scans are plotted (Figure **32**b), it is clear that there was a shift to more negative potentials with increasing carboxylic acid length. The voltage required to produce a current density of 0.5 mA cm^{-2} will be referred to as the dark voltage (V_{dark}), where a more positive V_{dark} correlates with more facile electron transfer. The V_{dark} for non-sensitized TiO_2 slides shifted to more negative potentials for the surfaces treated with the carboxylic acids, with more negative values being observed for the longer carboxylic acids. The largest shift (-59 mV) was found for the stearic acid modified surface. A similar shift is observed if $[Ru(H_2L')_2(NCS)_2]^0$ dye-coated slides are treated with the carboxylic acid solutions. (Figure **33**a). Once again, a plot of the reverse

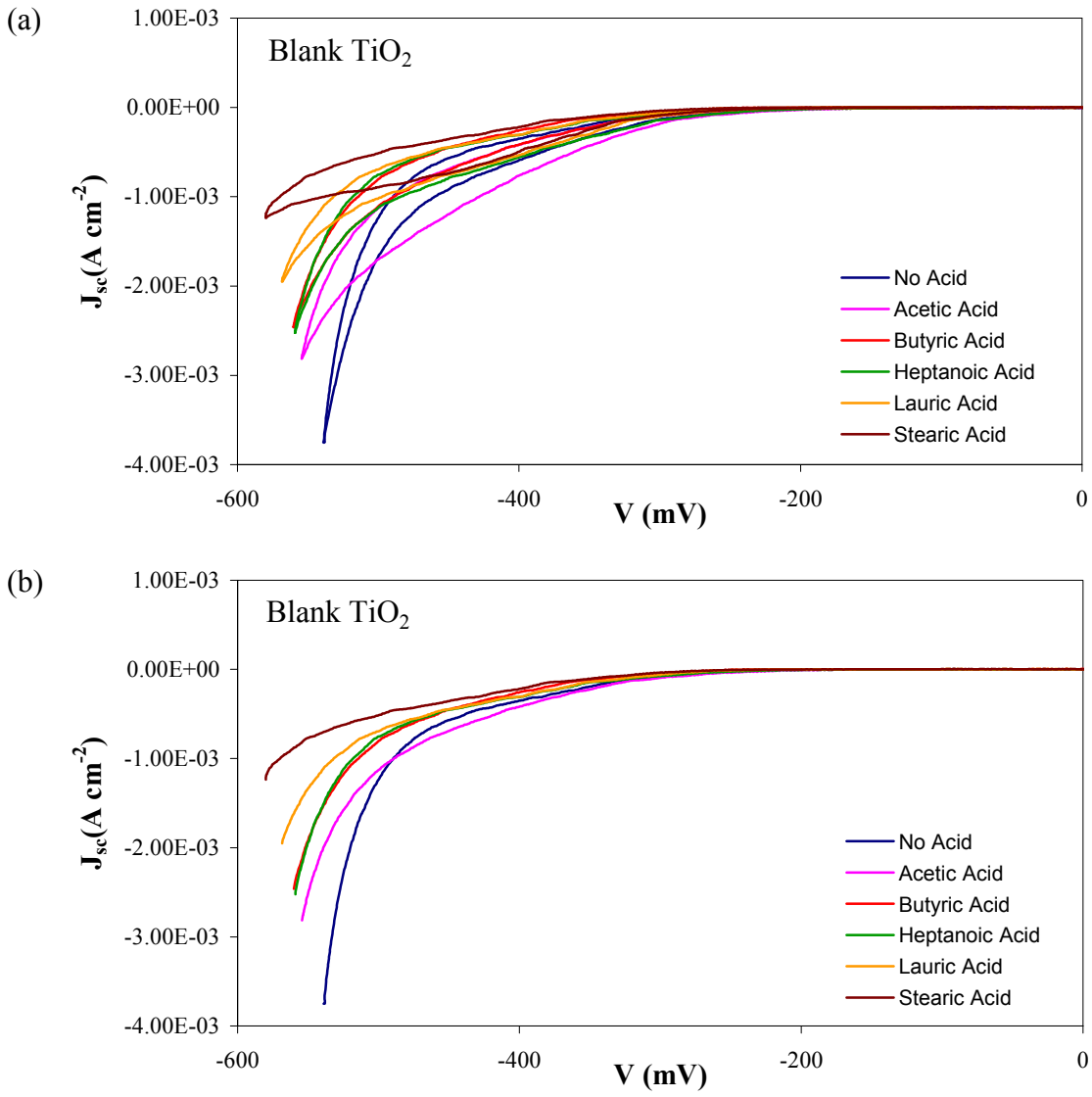

Figure 32. Dark current versus potential characteristics of TiO_2 electrodes treated with carboxylic acids. (a) After treatment for 1 h in an ethanolic solution of 0.1 M carboxylic acids. Electrolyte concentrations: 0.5 M LiI and 0.04 M I_2 with 20 mM pyridine and 20 mM pyridinium triflate. (b) Single sweep reverse scan only.

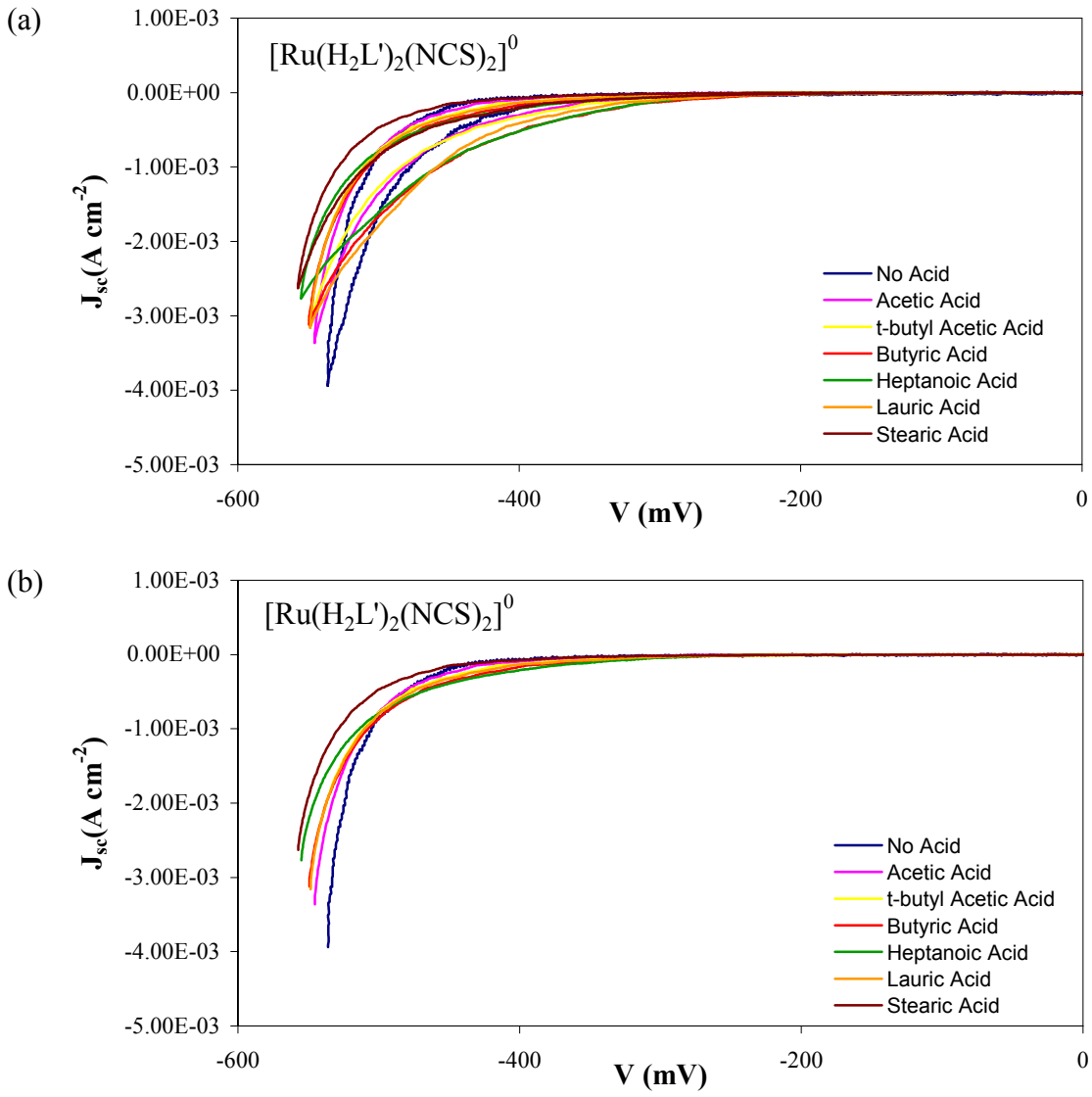

Figure 33. Dark current versus potential characteristics of $[Ru(H_2L')_2(NCS)_2]^0$ sensitized TiO_2 electrodes treated with carboxylic acids. (a) After treatment for 1 h in an ethanolic solution of 0.1 M carboxylic acids. Electrolyte concentration: 0.5 M LiI and 0.04 M I_2 with 20 mM pyridine and 20 mM pyridinium triflate. (b) Single sweep reverse scan only.

scans as a function of acid showed a shift to more negative potentials upon acid treatment, although the shift was significantly smaller (Figure **33**b). As before, the largest shift (-20 mV) is seen for the stearic acid treated surface (Table **3**).

When the same $[Ru(H_2L')_2(NCS)_2]^0$ dye-coated samples with adsorbed acid are irradiated with AM 1.0 light, there is a slight increase in both J_{sc} and V_{oc} when compared to the non-acid treated $[Ru(H_2L')_2(NCS)_2]^0$ coated TiO_2 slide (Figure **34**, Table **3**). The increases in photocurrent and open circuit potential are consistent with an increase in efficiency by a reduction in recombination. However, the average improvement was small with V_{oc} increasing by only 58 mV and J_{sc} increasing by 1.9 mA (Table **3**). These enhancements in current and potential resulted in relatively small efficiency enhancements (<10%) for most of the acid treated samples. Interestingly, however, the stearic acid modified surface showed significant improvement over the next longest acid (lauric acid) with an efficiency enhancement of ~20%.

Alternative adsorption methods were explored in an attempt to maximize surface coverage of the acid. Figure **35**a shows a plot of the current-voltage curves obtained when the surface was exposed to acid for 1 h and for 3 days. It is clear that increased adsorption time does not affect the current-potential behavior. By adsorbing the acid to the TiO_2 surface before adsorption of the dye, maximum coverage by the carboxylic acids can be achieved (Figure **35**a). However, this resulted in a diminished photocurrent that can likely be attributed to a decrease in the amount of dye adsorbed onto the surface. Likewise, when the surface was exposed to a mixture of dye and acid, there was a similar

Table 3. Photoelectrochemical data for $[Ru(H_2L')_2(NCS)_2]^0$ sensitized TiO_2 electrodes treated with carboxylic acids.[a]

	P_{max} (mV A)	Voc (mV)	Jsc (mA)	ff[b]	Eff[c] %	V_{dark}[d] (mV)
Untreated	-5.48	-517	13.3	0.80	5.48	-480
Acetic Acid	-5.83	-567	14.6	0.70	5.83	-483
Butyric Acid	-5.60	-558	13.9	0.72	5.60	-471
t-Butyl Acetic Acid	-5.79	-567	14.6	0.70	5.79	-479
Lauric Acid	-5.78	-563	14.5	0.71	5.78	-476
Stearic Acid	-6.64	-575	15.2	0.76	6.64	-502
Polyacrylic acid	-5.08	-540	13.5	0.70	5.08	-480

a: The electrolyte was acetonitrile containing 0.50 M LiI, 0.040 M I_2, 0.020 M pyridine and 0.020 M pyridinium triflate.

b: The fill factor (ff) is calculated as $P_{max}/(J_{sc} \times V_{oc})$, where P_{max} is the most negative value of $J \times V$.

c: Calculated as $(J_{sc} \times V_{oc} \times ff \times 100\%)/I_{light}$, where $I_{light} = 100$ mW cm^{-2}.

d: Potential required to drive a cathodic current density of 0.5 mA cm^{-2} in the dark.

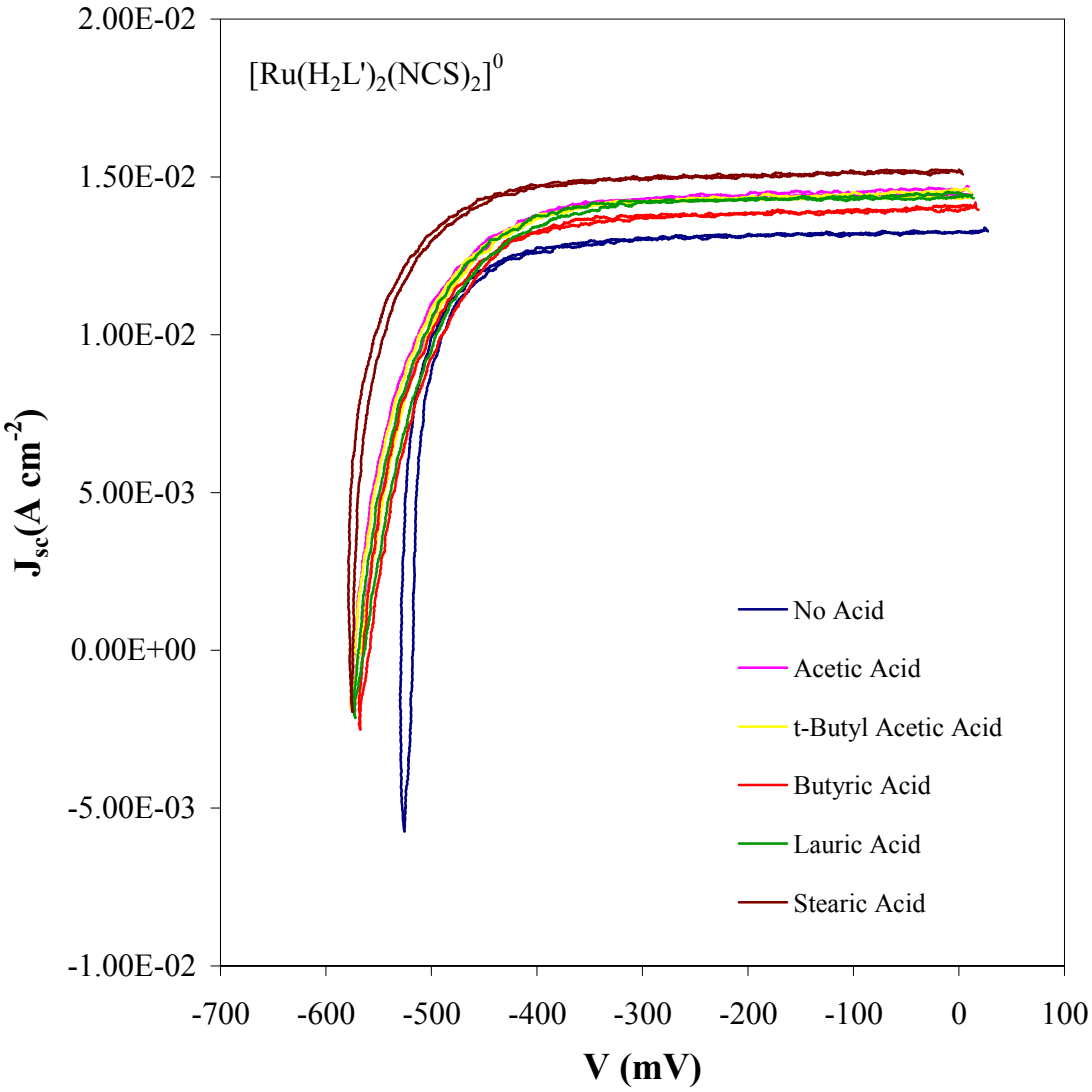

Figure 34. Current versus potential characteristics under AM 1.0 illumination of $[Ru(H_2L')_2(NCS)_2]^0$ sensitized TiO_2 electrodes treated with carboxylic acids. After treatment for 1 h in an ethanolic solution of 0.1 M carboxylic acids. Electrolyte concentrations: 0.5 M LiI and 0.04 M I_2 with 20 mM pyridine and 20 mM pyridinium triflate.

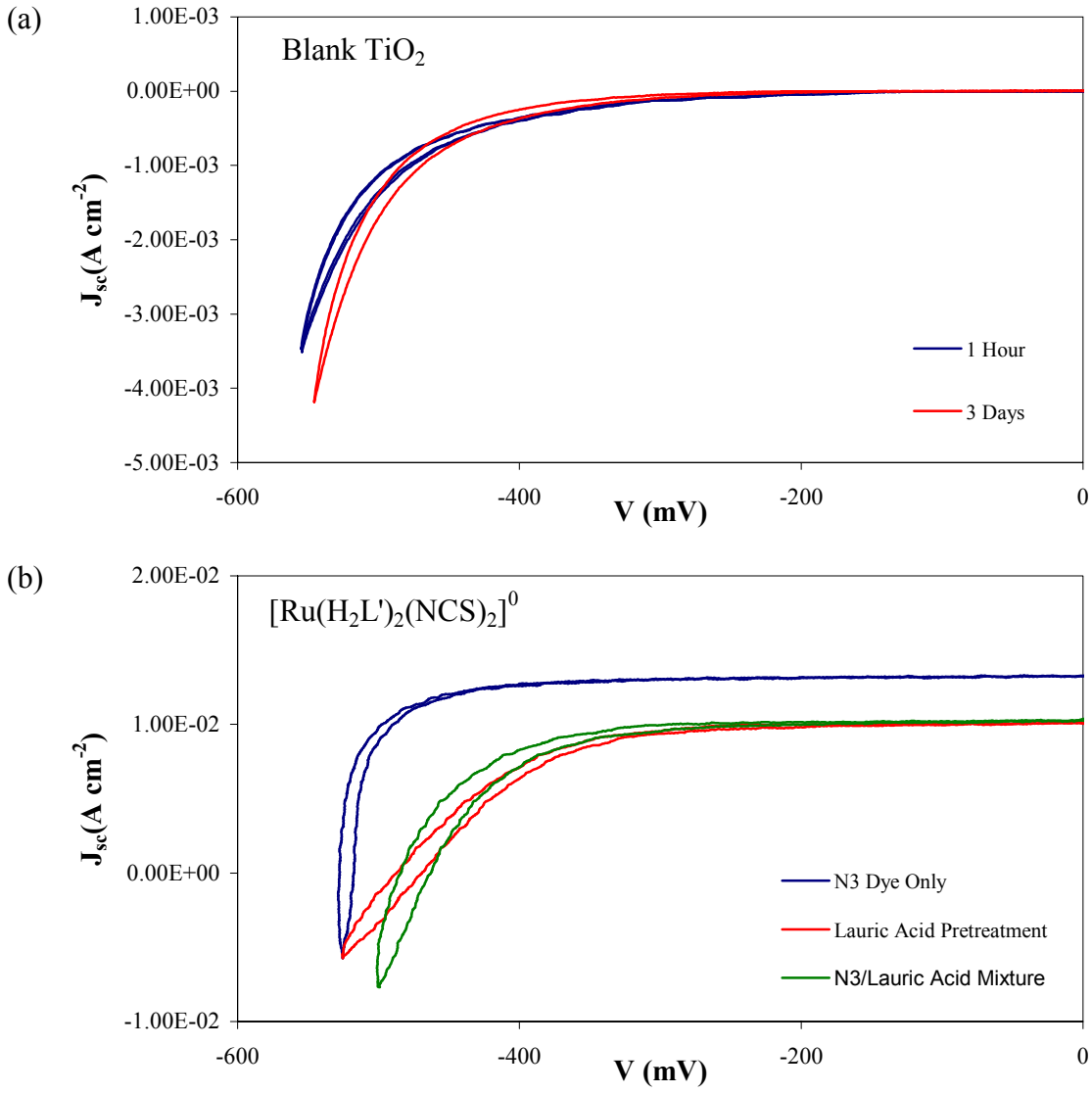

Figure 35. Effect of varying the conditions of carboxylic acid treatment. (a) Dark current-potential characteristics of a TiO_2 electrode after treatment for 1 h versus 3 days in an ethanolic solution of 0.1 M carboxylic acids. (b) behavior under AM 1.0 illumination of a $[Ru(H_2L')_2(NCS)_2]^0$ coated TiO_2 slide after treatment for 1 h in an ethanolic solution of 0.1 M lauric acid prior to dye adsorption (red), and after simultaneous exposure to an ethanolic solution with ~50 mM dye and 0.1 M lauric acid (green); no acid treatment (blue).

decrease in photocurrent, indicating a decrease in dye adsorption due to competitive binding (Figure **35**b).

To learn if these effects are specific to the acids used in these experiments or hold for other types of surface adsorbants, similar adsorption experiments were done with polyacrylic acid, which contains multiple carboxylic acid groups. $[Ru(H_2L')_2(NCS)_2]^0$ dye-coated TiO_2 slides were immersed in a 0.1 M ethanolic solution of polyacrylic acid and the dark and light current-voltage characteristics were measured (Figure **36**, Table **3**). Despite the marginal increases in V_{oc} and J_{sc}, the fill factor was diminished, resulting in decreased efficiencies for the polyacrylic acid treated $[Ru(H_2L')_2(NCS)_2]^0$ sensitized TiO_2 slide.

A second surface protection strategy was investigated in hopes of achieving more uniform surface coverage than was achieved with the acids. In this approach, methyltrichlorosilane (CH_3SiCl_3) was polymerized onto the TiO_2 surface. Gregg et al. recently reported that silane polymerization such as this produced rectification for the first time in TiO_2 cells with ferrocene/ferrocenium ($Fc^{+/0}$) as the redox couple. A comparison of the current-potential characteristics of $[Ru(H_2L')_2(NCS)_2]^0$ sensitized TiO_2 slides with ferrocene/ferrocenium and with the iodide/triiodide redox couple is shown in Figure **37**a. The iodide systems clearly show rectification with a large photovoltage and photocurrent. However, the ferrocene/ferrocenium system is diode-like with no significant current at negative potentials, while at more positive values, there is a sharp increase in current, most likely due to oxidation of ferrocene at the SnO_2 back contact (Figure **37**b).

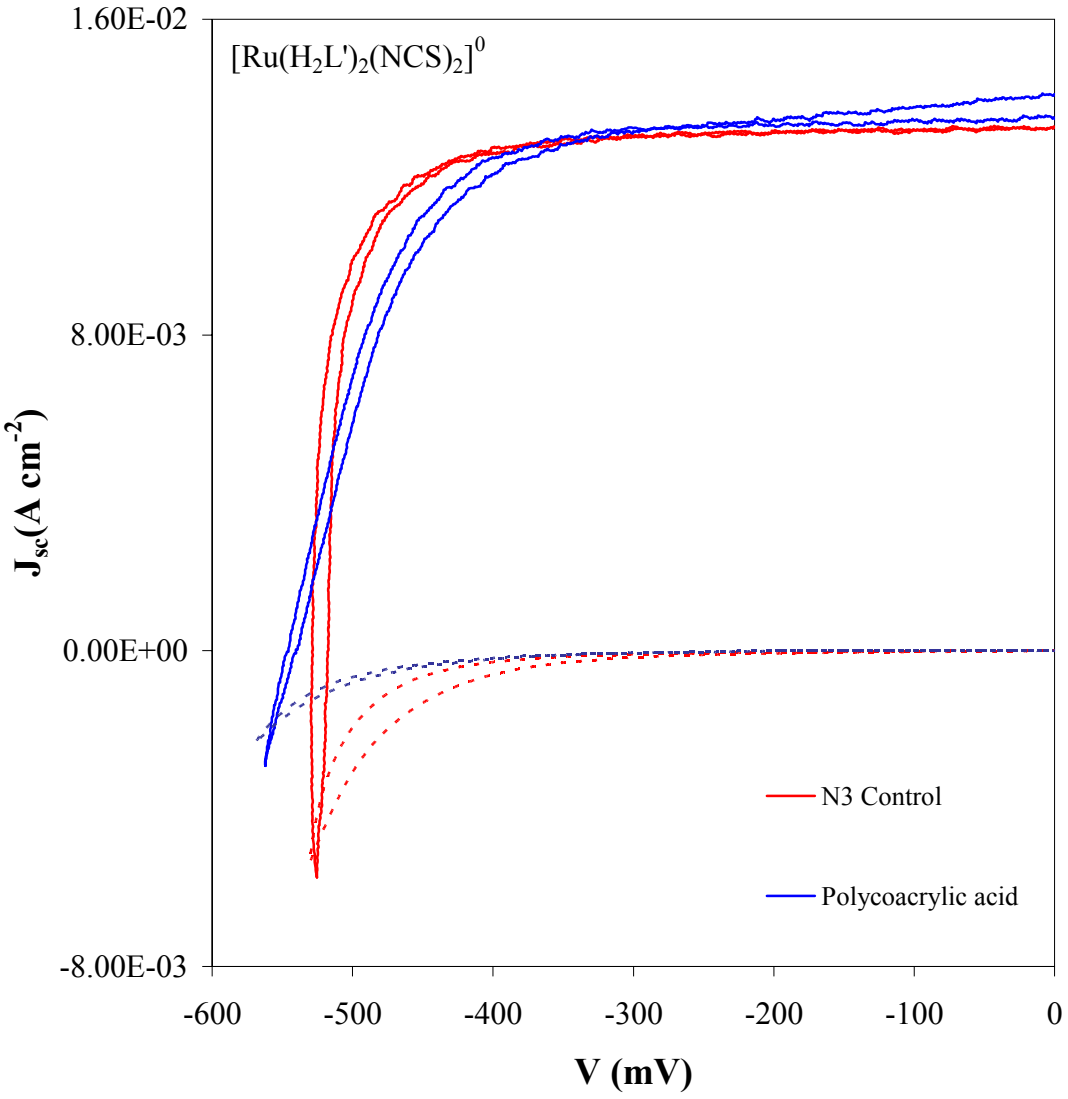

Figure 36. Current versus potential characteristics under AM 1.0 illumination of $[Ru(H_2L')_2(NCS)_2]^0$ sensitized TiO_2 electrodes treated with polyacrylic acid. Electrolyte concentrations: 0.50 M LiI, 0.040 M I_2, 0.020 M pyridine and 0.020 M pyridinium triflate in acetonitrile. After treatment for 1 h in an ethanolic solution of 0.1 M polyacrylic acid (blue) and without acid treatment (red). Behavior under simulated Air Mass 1.0 (100 mW cm^{-2}) conditions (solid lines) and in the dark (dashed).

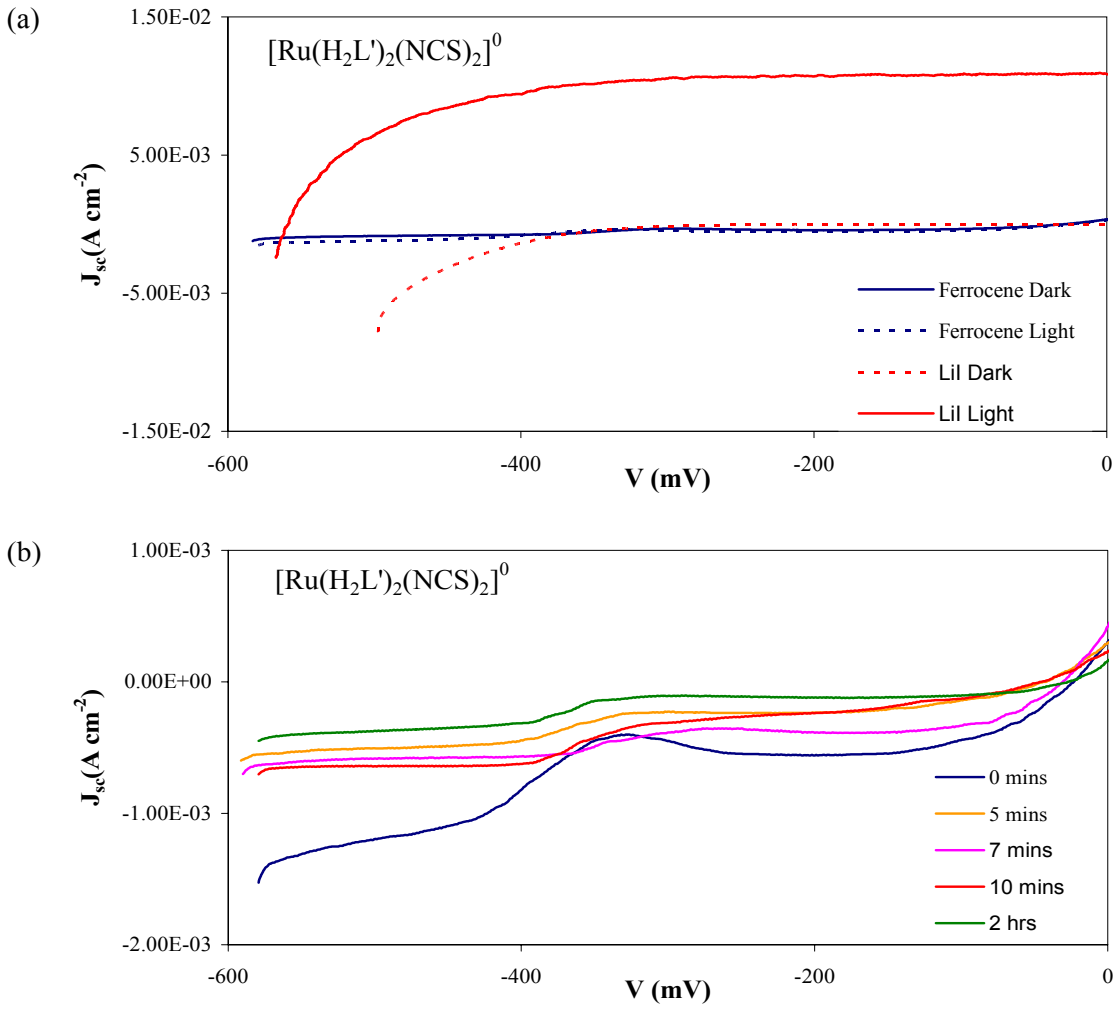

Figure 37. Current versus potential characteristics of $[Ru(H_2L')_2(NCS)_2]^0$ sensitized TiO_2 electrodes treated with silane polymerization. Electrolyte concentrations: 0.1 M ferrocene, 0.01 M ferrocenium, 1.0 M $LiClO_4$. (a) In the dark (blue, dashed) and under AM 1.0 illumination (blue, solid). Also included for comparison are the light (red, solid) and dark (red, dashed) curves for a similar system in contact with 0.5 M LiI and 0.04 M I_2 with 20 mM pyridine and 20 mM pyridinium triflate. (b) Effect of silane polymerization times on the current-potential behavior under AM 1.0 illumination. Electrolyte was composed of 0.1 M ferrocene, 0.01 M ferrocenium, 1.0 M $LiClO_4$.

After silane polymerization onto the dye-coated TiO_2 surface, XPS was used to confirm that polymer was formed on the surface. Figure **38** shows the XPS spectrum of an $[Ru(H_2L')_2(NCS)_2]^0$ dye-coated TiO_2 slide after polymerization. The carbon and silicon peaks clearly indicate the presence of the polymer on the surface. Perhaps more importantly, the Ti peak is present, indicating that the TiO_2 surface is not fully covered. XPS cannot determine the uniformity of the silane coverage or the degree of polymerization, only that polymerization occurred on the surface.

While a thick polymer layer is desired in order to insulate the exposed TiO_2 surfaces, an overly thick silane layer will cover the dyes completely, shutting down the regeneration mechanism of the oxidized dye by the redox couple. Figure **37**b shows the current-potential behavior in ferrocene/ferrocenium of a TiO_2 photoelectrode that was treated with the silane polymer. Clearly, polymerization had a minor effect at best on the current-voltage profile with no indication of rectification. Furthermore, increasing the polymerization time does not significantly affect the photoelectrochemical behavior. It should be noted that these are different samples in which polymerization was allowed to occur for different times, rather than the same sample tested at intervals during polymerization.

Discussion

Binding of the acids to the TiO_2 surface occurred very quickly upon immersion of the slide into the acidic solution. The minimal time required to achieve the maximum effect for most dyes was ~1 hour. Longer exposure times did not result in enhanced surface coverage or protection effects (Figure **35**a). Exposure of the carboxylic acids to

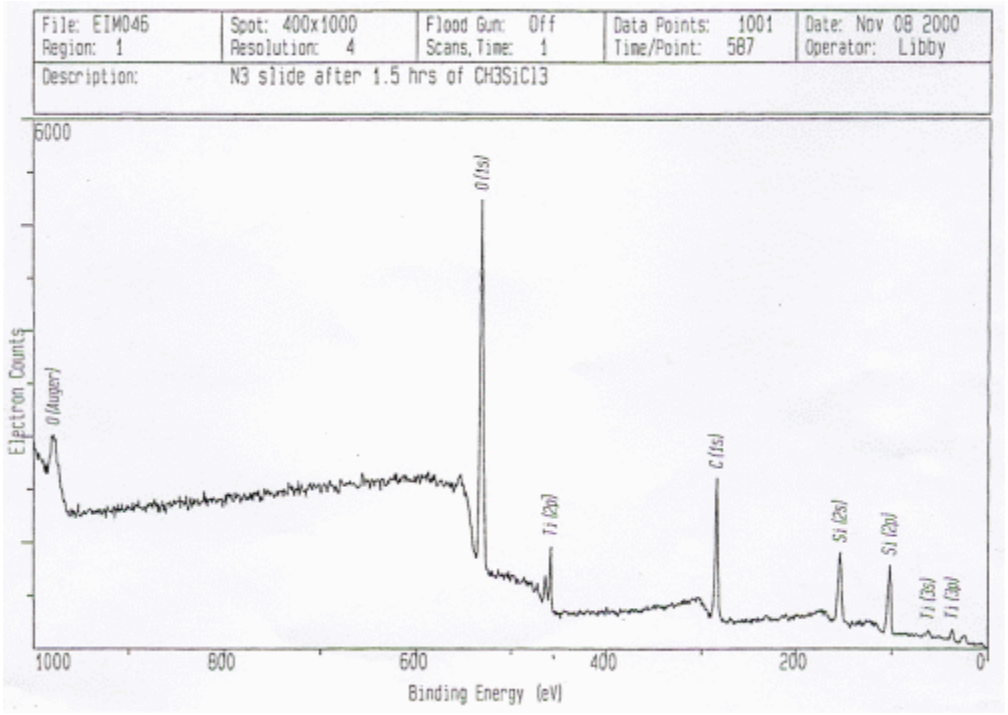

Figure 38. X-ray photoelectron spectrum after silane polymerization. $[Ru(H_2L')_2(NCS)_2]^0$ sensitized TiO_2 electrodes after silane polymerization for 1.5 h.

the surface prior to dye binding results in a significant decrease in the photocurrent (Figure **35**b). A similar effect was observed upon simultaneous exposure to the carboxylic acids and the dye. Both of these results are likely due to competitive binding between the carboxylic acids and the carboxyl-modified dyes for the TiO_2 sites. This indicates that the carboxylic acids rapidly bind to the available TiO_2 binding sites and can compete effectively with the dye for these sites. It is possible, however, that the increased acidity of the solution also allows for protons to compete for the available binding sites, resulting in protonation of the TiO_2 surface.

The shift in the dark current behavior of the blank and $[Ru(H_2L')_2(NCS)_2]^0$ coated TiO_2 slides indicates that electron transfer between the reduced TiO_2 and the electrolyte decreases as the length of the acid protecting group is increased. However, the effect was relatively minimal with the largest shift of 58 mV observed for the stearic acid treated surface. It is expected that this decreased electron transfer is a result of binding of the carboxylic acid to the surface in a similar fashion to the dye.

As mentioned previously, immersion in the acidic solutions likely also results in protonation of the TiO_2 surface. Addition of acetic acid to the electrolyte solution is known to shift the TiO_2 conduction band to more positive potentials.[68] In the dark, when the nanoparticles of TiO_2 come into contact with the redox electrolyte, they are likely to become depleted of electrons, resulting in a potential drop. However, this effect is negligible due to the small (nanometer) particles. Thus, the concentration of electrons in the nanoparticle in the dark is based on the difference between the conduction band edge, E_{cb} and the redox potential of the solution E_{A/A^-}. If the band edge is shifted in the dark by

the adsorption of charged species, the concentration of electrons in the semiconductor will vary as well. Since the recombination current depends directly on concentrations of electrons in the semiconductor in the dark, it is quite possible that the variance observed in the dark current is not simply a passivation effect, but a thermodynamic effect as a result of adsorption. This effect should be minimal for these experiments as the electrodes were rinsed with ethanol and dried under $N_2(g)$ after exposure to the carboxylic acid solutions.

The efficiency improvements under illumination did not seem to track with increasing carboxylic acid length. Rather, there was a small improvement for the majority of the acids, with a large increase for the longest acid. This indicates that the acids are binding to the surface, but that there is a minimum barrier distance required to achieve passivation. However, the extended polyacrylic acid showed only minimal effects, with an overall decrease in efficiency due to the decreased fill factor for this system. It is possible that the polyacrylic acid binding results in an overly thick blocking layer, while the acids shorter than stearic acid do not provide a sufficiently thick blocking layer.

Despite the promising previous report of rectification behavior in DSSCs with ferrocene/ferrocenium using silane polymer-modified TiO_2 electrodes, we were unable to achieve functional DSSCs with this one-electron redox couple. Silane polymerization on the TiO_2 surface was achieved, as evidenced by silicon peaks in the XPS. However, these samples showed no change in dark current behavior with the triiodide/iodide or ferrocene/ferrocenium redox couples, indicating that polymerization did not affect the

electron transfer kinetics between the TiO_2 surface and the redox couple in solution. Longer polymerization times had no significant effect on the current-potential behavior of these systems. The fact that the silane polymers do not act in a similar manner to the carboxylic and polyacrylic acid-modified surfaces could be a result of an insulating polymer layer that is too thin, non-uniform polymer coating, or a polymer that is too big to fit into the pores in order to cover the internal TiO_2 surfaces. All of these problems can in theory be solved through methodical probing of the polymerization process and tight control of the variables.

Conclusions

The desired effect of surface modification was minimization the rate of electron transfer between the TiO_2 surface and the triiodide in solution. A minimization of the dark current was achieved as a result of exposure of the TiO_2 surface to carboxylic acids of various lengths. This effect resulted in minor increases in the V_{oc} and slightly larger increases in J_{sc} upon illumination. The enhanced J_{sc} indicates that the increased efficiencies with the carboxylic acid modified surfaces are not simply a result of binding of the acids to the surface thereby minimizing the kinetics of the electron transfer process. It is possible that surface state charging or conduction band edge shifts may account for this observed phenomenon. The stearic acid modified TiO_2 photoelectrode showed the most promise with a greater than 20% increase in efficiency, significantly better than all of the other acid-modified surfaces. This could be an indication that the minimal effective blocking layer was achieved with the longest carboxylic acid.

CHAPTER 5:

EFFECTS OF BRIDGING LIGANDS ON PHOTOELECTROCHEMICAL BEHAVIOR

Chapter 5

EFFECTS OF BRIDGING LIGANDS ON PHOTOELECTROCHEMCIAL BEHAVIOR

Introduction.

For dyes that are derivatives of $[Ru(bpy)_3]^{2+}$ (bpy = 2,2'-bipyridine), the lowest excited state is formed by a metal-to-ligand charge-transfer (MLCT) transition.[69] The lifetime of this excited state usually exceeds 500 ns;[69] thus, CT reactions as slow as 1 – 10 ns can produce near unit quantum yields for the initial charge separation. In such dyes, electron injection occurs from the ligand attached to TiO_2, while recombination occurs between an electron in TiO_2 and the oxidized Ru center.[21] The latter reaction can lower the efficiencies of TiO_2 solar cells. Hence, an attractive way to minimize this deleterious process would be to increase the distance between TiO_2 and the dye metal center, thereby decreasing the rate of recombination. Although the injection dynamics would also be slower, a high quantum yield for charge separation should be maintained.

Accordingly, we have prepared a series of dyes in which the distance between the ruthenium center and the anchoring group has been varied systematically. We describe herein the changes in steady-state and kinetics properties of dye-sensitized TiO_2 photoelectrodes that result from this increase in linker length between Ru and the TiO_2 surface. The dyes are derivatives of $[Ru(bpy)_3]^{2+}$ and have a single anchoring carboxyl group attached via a rigid linker to one of the bipyridine ligands. The dyes (Figure **39**)

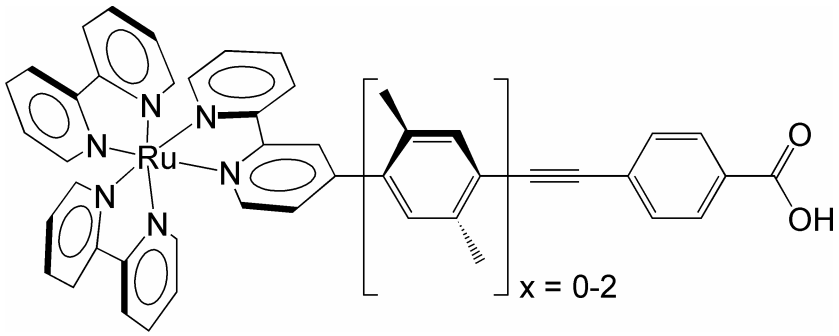

Figure 39. Structure of Rux dyes for bridge length studies. The dyes are abbreviated as Rux where x is the number of xylyl spacers.

are abbreviated Rux (x = 0, 1, 2), where x is the number of xylyl groups in the linker. Detailed descriptions of the syntheses of these dyes are provided elsewhere; NMR and mass spectrometry were used to validate the compositions and structures of the complexes.[70]

Results and Discussion.

The solution photophysical behavior of Ru0 was found to differ slightly from that of the other sensitizers (Figure **40**, Table **4**). Both the absorption and emission spectra were red-shifted for Ru0, with the emission 0-0 transition energy[71] ($\mathbf{E}_{00}$) being ~0.1 eV lower than Ru1 or Ru2 (Figure **40**). Although all of the radiative rate constants were similar, both the excited-state lifetime and the emission quantum yield[72] of Ru0 were greater than those of either Ru1 or Ru2. The excited-state lifetimes were all sufficiently long to ensure efficient charge separation, even for slow ($<10^7$ s^{-1}) electron-transfer processes. The Ru^{3+}/Ru^{2+} formal reduction potentials ($E^{o'}$) were nearly the same for all of the dyes, as the electronic core around the metal centers are virtually identical. However, owing to differences in the 0-0 energy, the Ru^{3+}/Ru^{2+*} potential ($E^{o'}$*) was found to be slightly more positive for Ru0. The excited-state energetics are comparable to those of other $[Ru(bpy)_3]^{2+}$-derivatives that exhibit efficient charge injection into the TiO_2 conduction band with similar driving forces for this charge separation process.[73,74] The ground-state energetics imply that the oxidized dyes also have comparable driving forces for oxidation of I_3^-/I^- in a photoelectrochemical cell.

To investigate the interfacial kinetics of the dye-sensitized TiO_2 photoelectrodes, we measured rate constants for electron injection (k_2), recombination of injected electrons

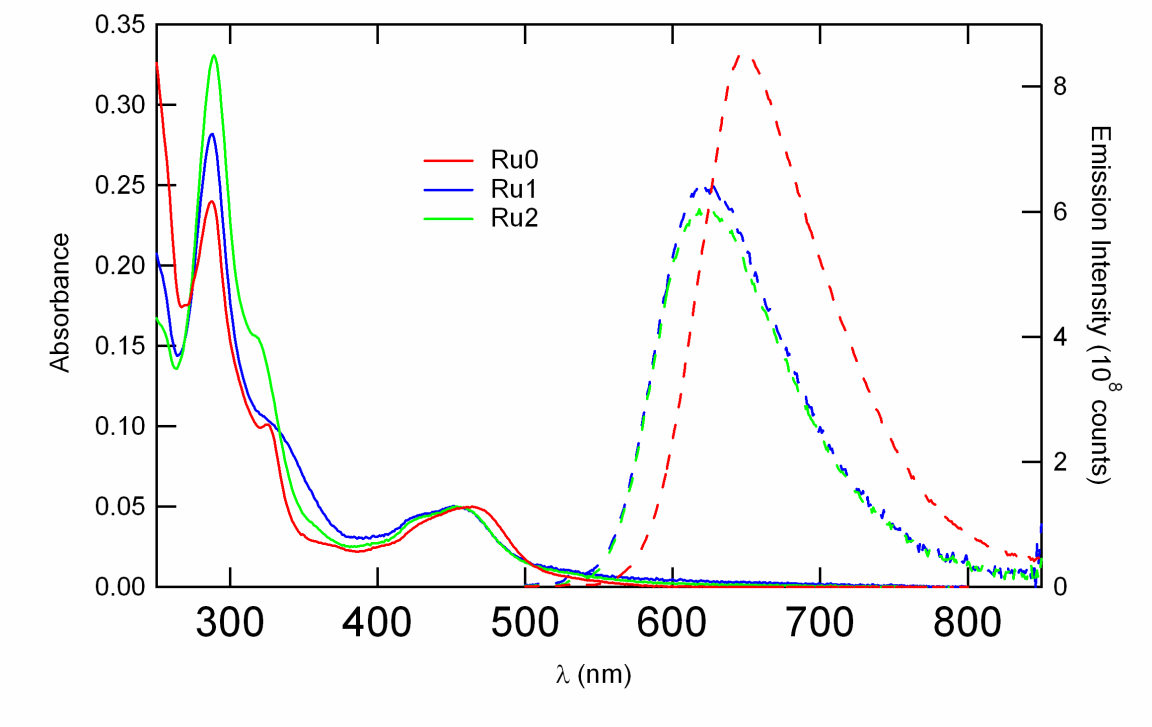

Figure 40. Spectroscopic characterization of Rux dyes. Emission (dashed) and absorbance (solid) spectra of Rux dyes in acetonitrile. Ru0 (red); Ru1 (blue); and Ru2 (green).

Table 4. Spectroscopic and electrochemical data for Rux dyes

		MLCT						vs. SCE	
	R	λ_{max}^{abs}	λ_{max}^{ems}	ϕ_{ems}	τ_{ems}	k_0	$\mathbf{E}_{00}$	$E^{o'}$	$E^{o'*}$
	(Å)[a]	(nm)[b]	(nm)[b]	(%)[b,c]	(μs)[b,d]	(s^{-1})[b,e]	(eV)[f]	(V)[g]	(V)[h]
Ru0	13.8	467	648	9.7	2.10	5×10^4	1.92	1.36	-0.56
Ru1	18.2	453	621	7.5	1.06	7×10^4	2.01	1.34	-0.67
Ru2	22.5	455	621	7.1	1.04	7×10^4	2.02	1.33	-0.69

a: Distance (± 0.2 Å) between the Ru metal center and carboxyl oxygens from MM2 calculations.

b: In degassed acetonitrile.

c: Emission quantum yields (± 0.5%) measured relative to $Ru(bpy)_3Cl_2$ (ϕ_{ems} = 4.2% in H_2O).[70]

d: Fitted to a single exponential decay (± 0.02 μs).

e: $k_0 = \phi_{ems}/\tau_{ems}$, where ϕ_{ems} is the quantum yield and τ_{ems} the lifetime of Rux.

f: 0-0 energy of the thermalized Ru^{2+} excited state obtained by fitting the emission spectra (±0.01 eV) to the theoretical expression reported by Caspar *et al.*[71]

g: Formal ground-state Ru^{3+}/Ru^{2+} reduction potential measured by cyclic voltammetry in acetonitrile with 0.1 M tetrabutylammonium hexafluorophosphate as supporting electrolyte, vs. ferrocene as internal standard (± 0.02 V).

h: Formal Ru^{3+}/Ru^{2+*} reduction potential of the thermalized excited state, calculated as $E^{o'*} = E^{o'} - \mathbf{E}_{00}/q$, where q is the elementary charge.

with the oxidized dye (k_3), and regeneration of the oxidized dye by iodide in the electrolyte (k_5) (Figure **5**) using nanosecond time-resolved absorption and emission spectroscopy. The conduction band edge energy of TiO_2 was fixed by controlling the H^+ and Li^+ activities.[49,74] The rate of reduction of I_3^-/I^- by electrons in the TiO_2 (k_4) was estimated from the potential required to produce a given amount of cathodic current density in the dark (*vide infra*).

To determine the rates of electron injection, we compared the Rux excited-state lifetimes in solution to those obtained when the dyes were bound to TiO_2. Clearly, adsorption to TiO_2 resulted in substantial quenching (Figure **41**). In degassed acetonitrile, Rux emission decays were single exponentials, but on TiO_2 the quenching dynamics exhibited multi-exponential behavior (Table **5**). This heterogeneity is probably due to different binding-site microenvironments. The data can be satisfactorily described by a sum of three exponentials. It is very likely that the fastest decay is itself a sum of decay processes, although this cannot be resolved as the shortest measurable lifetime was close to the width of the instrument response function (≈10 ns). Likewise, the amplitude of the fastest component is likely to be a lower limit. In order to achieve a single rate constant from these multi-exponential curves, we have used

$$\langle k \rangle = \frac{1}{\int_0^\infty I(t)dt} \qquad (20)$$

where I(t) is the normalized intensity. The difference between the integrated emission decay on TiO_2 and in solution yields an average quenching rate constant ($<k_2>$). These are plotted as a function of the Ru center – anchoring group distance (R) in Figure **42**a. It

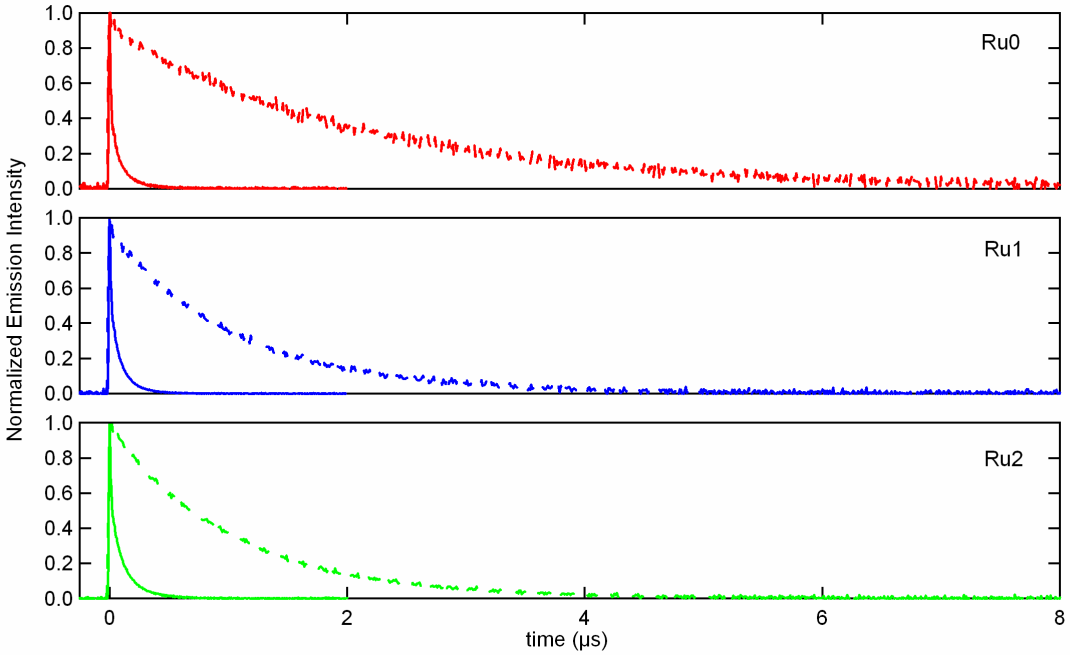

Figure 41. Emission quenching of Rux dyes bound to TiO_2. λ_{ex} = 480 nm, λ_{ems} = 630 nm. Emission decay (dashed lines) of Rux dyes in acetonitrile. Emission decay (solid lines) of Rux dyes adsorbed on TiO_2 in the presence of 0.50 M $LiClO_4$, 0.020 M pyridine and 0.020 M pyridinium triflate.

Table 5. Rate constants for emission and ground-state recovery of Rux dyes.[a]

Dye	k_{-1}^{MeCN} (s^{-1})[b]	$k_{-1}^{TiO_2}$ (s^{-1})[c,d]	k_2 (s^{-1})[e]	k'_3 (s^{-1})[c,f]	k_3 ($cm^3\ s^{-1}$)[g]	k'_5 (s^{-1})[d,h]
Ru0	4.8×10^5	1.1×10^8 (0.69) 1.4×10^7 (0.27) 4.5×10^6 (0.04)	1.1×10^8 1.4×10^7 4.0×10^6	4.8×10^6 (0.51) 3.3×10^4 (0.49)	1.1×10^{-13} 0.76×10^{-15}	2.4×10^6 (0.58) 1.1×10^5 (0.42)
Ru1	9.4×10^5	1.1×10^8 (0.61) 1.3×10^7 (0.35) 4.7×10^6 (0.04)	1.0×10^8 1.2×10^7 3.8×10^6	5.0×10^6 (0.44) 5.3×10^4 (0.56)	1.2×10^{-13} 1.2×10^{-15}	2.1×10^6 (0.78) 5.7×10^4 (0.22)
Ru2	9.6×10^5	1.0×10^8 (0.57) 1.1×10^7 (0.36) 4.2×10^6 (0.07)	0.98×10^8 0.95×10^7 3.2×10^6	8.8×10^6 (0.44) 7.7×10^4 (0.56)	2.0×10^{-13} 1.8×10^{-15}	3.9×10^6 (0.44) 4.9×10^5 (0.39) 1.9×10^4 (0.17)

a: Standard deviations over multiple trials are 0.05 in amplitude and 30% in rate constants.

b: In degassed acetonitrile.

c: On TiO_2 with acetonitrile containing 0.50 M $LiClO_4$, 0.020 M each of pyridine and pyridinium triflate. The amplitude of each term is given in parentheses.

d: Fitted to a sum of exponentials.

e: $k_2 = k_{-1}^{TiO_2} - k_{-1}^{CH_3CN}$

f: According to Eq. 20. Amplitudes are in parentheses.

g: $k_3 = \Delta\varepsilon d k'_3$ with $\Delta\varepsilon = 2.3 \times 10^{-15}$ cm^3 $mole^{-1}$ (ground-state molar absorptivity) and d (thickness of the TiO_2 film) = 1.0×10^{-3} cm.

h: On TiO_2 with acetonitrile containing 0.49 M $LiClO_4$, 0.010 M LiI, 0.020 M pyridine and 0.020 M pyridinium triflate. Amplitudes are given in parentheses.

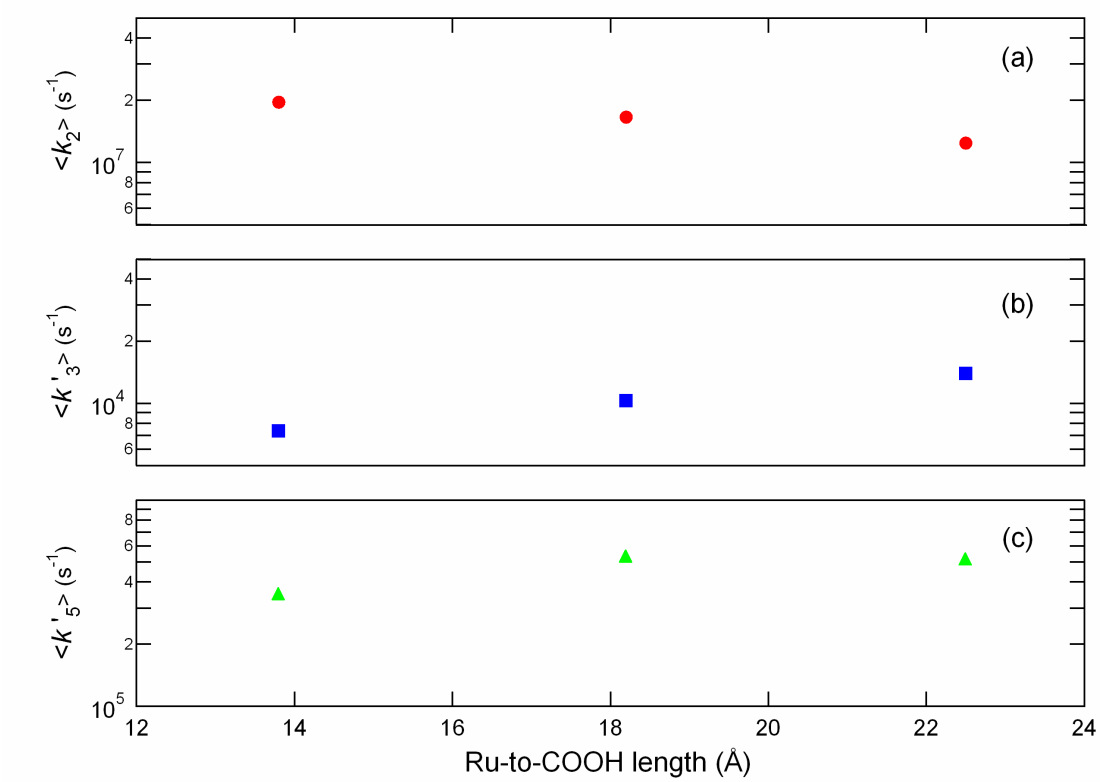

Figure 42. Average rates for injection (<k_2>), recombination (<k'_3>) and regeneration (<k'_5>) as a function of the Ru to TiO_2 distance. Note the different y-scales; in each case the ordinate on the graph spans a factor of two. (a) Injection rate constants (k_2) obtained from the difference between the excited-state lifetimes of the dye in acetonitrile solution (single-exponential) and when bound to TiO_2 (a sum of three exponentials) in the presence of 0.50 M $LiClO_4$, 0.020 M pyridine, and 0.020 M pyridinium triflate in acetonitrile (λ_{ex} = 480 nm, λ_{ems} = 630 nm). (b) Recombination constants (k'_3) of the oxidized dye with electrons in the TiO_2 from the time-resolved recovery of the ground state (λ_{ex} = 480 nm, λ_{ta} = 450 nm) for dyes bound to TiO_2 in the presence of 0.50 M $LiClO_4$, 0.020 M pyridine, and 0.020 M pyridinium triflate in acetonitrile. The recovery

was fitted to a sum of two second-order equal-concentration kinetics functions, and the value plotted is the average of the two recombination constants weighted by the relative amplitudes of the two processes. (c) Regeneration rate constants (k'_5) of the oxidized dye with iodide from the time-resolved recovery of the ground state (λ_{ex} = 480 nm, λ_{ta} = 450 nm) for dyes bound to TiO_2 in the presence of 0.49 M $LiClO_4$, 0.010 M LiI, 0.020 M pyridine, and 0.020 M pyridinium triflate in acetonitrile. The recovery was fitted to a sum of two or three exponentials assuming pseudo-first-order kinetics.

is clear from Table **5** and Figure **42**a that there is little to no dependence in quenching rates on linker length as the quenching rate constants decreased only slightly as the linker length increased.

Figure **43** shows the transient absorption data monitored at the MLCT absorption band for the Rux dyes adsorbed on TiO_2. At very high excitation laser power, saturation condition, a lower limit of the injection quantum yield can be roughly approximated as $QY_{inj} \approx -\Delta A_{sat}/A_{ground}$. This value only takes into account species that live long enough to be detected after 10 ns, i.e., fast geminate recombination resulting from injection on the femtosecond timescale would not be detected. For the Rux (x = 0,1,2) series, these lower bounds on the quantum yield for injection under saturation conditions are 0.09, 0.07 and 0.07, respectively. These values are comparable to that obtained under similar conditions for $[Ru(H_2L')_3]^{2+}$ (0.07),[73] which has high photoelectrochemical efficiencies and injects electrons into TiO_2 with a high quantum yield.[73,74] Furthermore, for low excitation power, linear regime, the $\Delta A/A_{ground}$ was within a factor of two for all of the dyes and was once again comparable to $[Ru(H_2L')_3]^{2+}$. The emission quenching of Figure **41** is thus a result of electron injection into the TiO_2 producing Ru^{3+} with high quantum yield, as opposed to self-quenching, triplet annihilation processes or the emission monitoring of only a minor fraction of the excited states. This indicates that the Rux systems should be capable of electron injection into TiO_2 with yields high enough to result in efficient photoelectrochemical cells for energy conversion applications.

The non-geminate back reaction between electrons in TiO_2 and the oxidized dye was investigated by monitoring the recovery of the ground-state MLCT absorption using

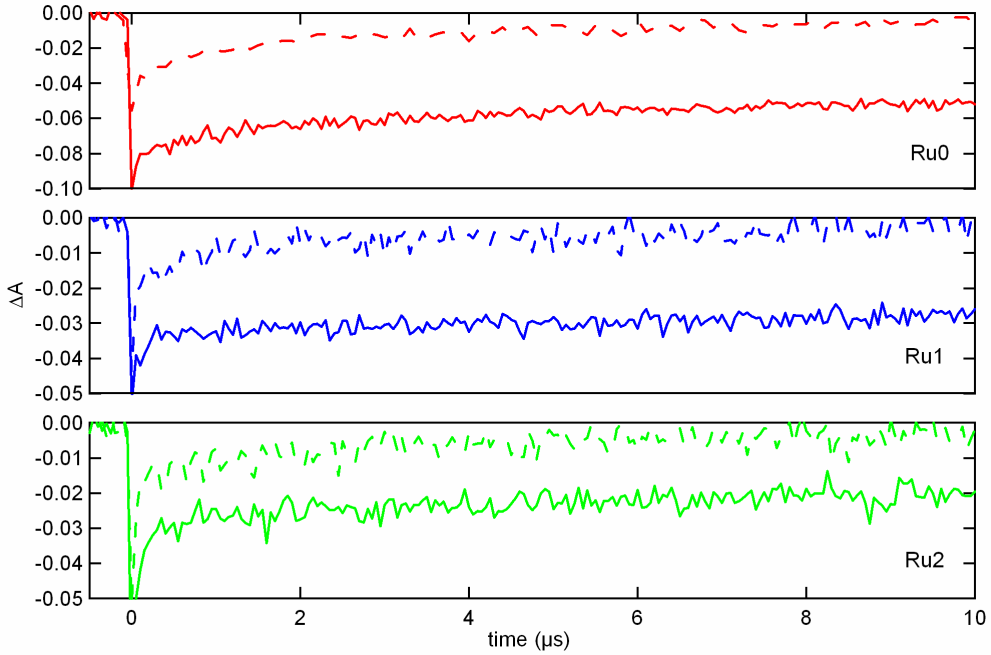

Figure 43. Transient kinetics data for Rux dyes bound to TiO_2. λ_{ex} = 480 nm, λ_{ta} = 450 nm. Transient absorption (solid lines) of Rux dyes on TiO_2 in the presence of 0.50 M $LiClO_4$, 0.020 M pyridine and 0.020 M pyridinium triflate in acetonitrile. Transient absorption (dashed lines) of Rux dyes on TiO_2 in presence of 0.49 M $LiClO_4$, 0.010 M LiI, 0.020 M pyridine and 0.020 M pyridinium triflate in acetonitrile.

transient spectroscopy (Figure **43**). As Ru^{2+*} on TiO_2 is very short-lived and the absorbance of the Ru^{3+} species is negligible at 450 nm, the bleach at this wavelength can be attributed solely to depletion of the Ru^{2+} ground state.[70] In accord with the behavior observed previously for $[Ru(H_2L')_2(NCS)_2]^0$ sensitized TiO_2 photoelectrodes, the recovery was fitted to a sum of two equal-concentration second-order kinetics functions:[49]

$$-\Delta A = \frac{a_i}{1 + a_i k'_{3i}\, t} + \frac{a_j}{1 + a_j k'_{3j}\, t} \qquad (21)$$

In Eq. 21, *a* relates absorbance and concentration, and the recombination constants (k'_3) have units of s^{-1}. For each sensitizer, the ratio of the fractions of the two populations ($a_i/(a_i+a_j)$ and $a_j/(a_i+a_j)$) was approximately 1:1. Since the samples were heterogeneous, there could be many more reaction rates, but their inclusion was not necessary to obtain satisfactory fits.

The k'_3 recombination rate constants were converted to true second-order rate constants using the thickness of the film and the ground-state molar absorptivity (Table **5**).[49] However, since these factors were essentially equal for all three sensitizers (x = 0, 1, 2), the relative distance dependence of k_3 was the same as that of k'_3. For both the slow and fast reaction processes, the corresponding rate constants increased slightly with increasing linker length. However, it should be noted that the differences may be within the experimental uncertainties. The integrated $<k'_3>$recombination constants, Eq. 1, for each dye are plotted as a function of R in Figure **42**b. Since back electron transfer occurs from TiO_2 to the Ru center, we would expect a significant decrease in rate as x increases,

rather than the little to no increase observed.[75] If the small observed trend is significant, it is opposite to that expected. The likely explanation for this finding is that the single anchoring group on Rux makes the connection to TiO_2 flexible, allowing the sensitizer to approach the surface and thereby decreasing the Ru-TiO_2 electron-tunneling distance. The flexibility in the linker could also contribute to the shallow distance dependence of the injection rates.

An analogous trend in rates was observed for the regeneration of the oxidized dye by iodide in the electrolyte. The recovery of the MLCT absorption following pulsed-laser excitation accelerated significantly when iodide was added to the electrolyte (Figure **43**). Fitting the data to a sum of two or three exponentials produced a minimum ensemble of $[I^-]$-dependent rate constants (k'_5) (Table **5**, Figure **42**c). For each complex, a 0.010 M I^- solution regenerated the reduced dye competitively with recombination from injected electrons (Figure **43**). Again, the fastest reaction was found for Ru2-sensitized TiO_2 photoelectrodes. This behavior could indicate that the assumed flexibility and resultant sensitizer interaction with the surface is affecting the iodide oxidation. Flash/quench experiments were also performed on the unbound dyes in acetonitrile, using methyl viologen as the electron acceptor to generate the Ru^{3+} form of the dyes. The pseudo-first-order rate constants for reduction of the oxidized dyes by iodide under these conditions were essentially identical for all three dyes, with $k'_5 = 2 \times 10^5\ s^{-1}$ for $[I^-] = 1.0 \times 10^{-5}$ M. Importantly, regeneration is significantly faster when the dyes are free in solution than when bound to TiO_2.

The emission decay of Rux on TiO_2 is much faster than in solution, implying that electron injection is still efficient, although a minor fraction of the excited-state population injects slowly. Given that injection of electrons into TiO_2 is much faster than excited-state decay, and that regeneration competes effectively with recombination, it is surprising that Rux-sensitized TiO_2 photoelectrodes are not more efficient (Figure **44**, Table **6**). The overlap of the Rux MLCT absorption with the solar spectrum is not very favorable; thus solar cells containing these dyes are expected to be less efficient than $[Ru(H_2L')_2(NCS)_2]^0$ sensitized solar cells. Based on the similarities with the absorption spectrum of $[Ru(H_2L')_3]^{2+}$, we would expect Rux solar cell efficiencies comparable to that of $[Ru(H_2L')_3]^{2+}$ sensitized TiO_2. However, the remarkably similar interfacial kinetics observed for the Rux dyes fail to explain the large differences in their photoelectrochemical behavior. The limiting photocurrent densities under simulated solar illumination depended strongly on the linker length in the Rux series (Figure **44**, Table **6**). The short-circuit current density (J_{sc}) decreased by approximately a factor of 2 for x = 1. At such low current densities, it is not unusual to observe some hysteresis at these scan rates (20 mV s^{-1}). The decrease in J_{sc} cannot be explained by a change in light absorption of the various complexes, as the spectra of the adsorbed dyes are very similar. The quantum yield for conversion of absorbed photons to current is less than 0.1 for all three dyes, with the quantum yield decreasing with increasing linker length (Table **6**). Also, the magnitude of the open-circuit voltage (V_{oc}) decreased with linker length (Table **6**). Part of the decrease in V_{oc} with increasing x is attributable to the lower photocurrent density produced by Ru1 and Ru2. Overall, the J_{sc}, V_{oc} and the shape of the current

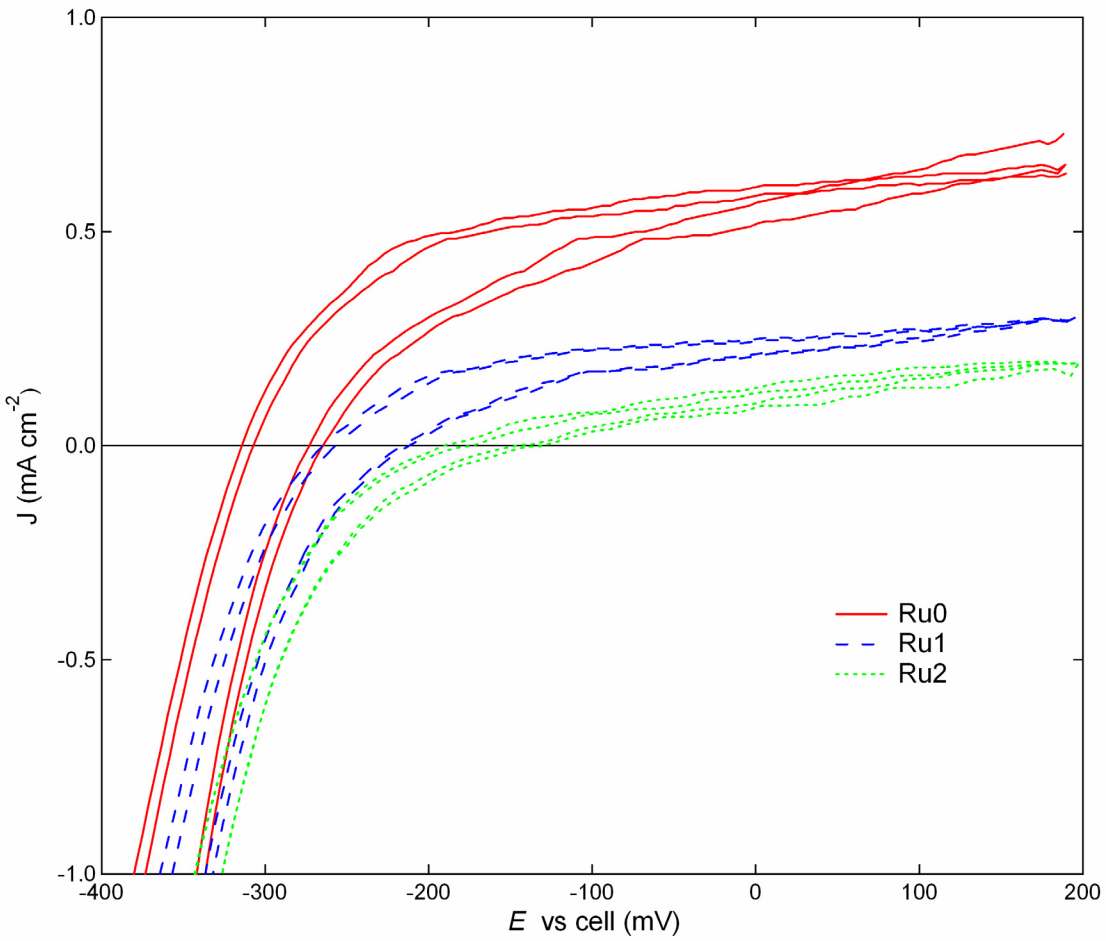

Figure 44. Current versus potential characteristics under AM 1.0 illumination for Rux-sensitized TiO_2 electrodes. Ru0 (red, ——), Ru1 (blue, – – –), and Ru2 (green, · · ·) (A_{MLCT} = 1.5 ± 0.3). The data (corrected for uncompensated cell resistance, 64 ohms) were measured under simulated Air Mass 1.0 100 mW cm^{-2} conditions in a potentiostatic three-electrode apparatus at 20 mV s^{-1} scan rate between 0.20 and –0.60 V vs. the Nernstian potential of the cell. The electrolyte was acetonitrile containing 0.50 M LiI, 0.040 M I_2, 0.020 M pyridine and 0.020 M pyridinium triflate.

Table 6. Photoelectrochemical data for Rux dyes.[a]

	Air Mass 1.0				Dark
	J_{sc} (mA cm^{-2})[b]	V_{oc} (V)[c]	Efficiency (%)[d]	Ext. QY[e]	V_{dark} (V)[f]
Ru0	0.59	-0.29	0.1	0.09	-0.23
Ru1	0.23	-0.24	0.03	0.03	-0.23
Ru2	0.11	-0.16	0.004	0.02	-0.16

a: The electrolyte was acetonitrile containing 0.50 M LiI, 0.040 M I_2, 0.020 M each of pyridine and pyridinium triflate.

b: Standard deviations over many trials are ±0.05 mA cm^{-2}.

c: Standard deviations over many trials are ±0.03 V.

d: Calculated as P_{max}/P_{light}, where P_{light} = 100 mW cm^{-2} and P_{max} is the largest value of –(J × V).

e: Calculated as the ratio of the observed J_{sc} to the value expected for a unity quantum yield when the measured absorbance of the dyes on TiO_2 electrodes are convoluted with the spectral irradiance of the solar simulator between 1100 nm and 360 nm.

f: Standard deviations over many trials are ±0.05 V.

density–potential curve (Figure **44**) for the Rux dyes gave low photoelectrode energy conversion efficiencies (Table **6**) under 100 mW cm^{-2} of simulated Air Mass 1.0 solar illumination conditions. The performance of these photoelectrodes can be compared to that of a $[Ru(bpy)_3]^{2+}$ derivative in which a single carboxyl groups is directly attached to one of the bipyridine ligands. The value of J_{sc} for this compound was 4 times higher than for Ru0, and the magnitude of V_{oc} was slightly higher as well.[73] Clearly, placing any one of the linkers (x = 0, 1, 2) between TiO_2 and the Ru center has a negative effect on photoelectrode performance.

The back reaction that determines the photovoltage in sensitized TiO_2 systems is electron transfer from nanocrystalline TiO_2 to oxidized species in the I_3^-/I^- electrolyte solution (represented by the rate process k_4 in Figure **5**).[67] Trends in the rate of this back reaction were evaluated from the forward-bias potential necessary to produce a fixed amount of cathodic dark current density (0.1 mA cm^{-2}) at the TiO_2–solution interface, where a less negative potential is indicative of more facile electron transfer between TiO_2 and the I_3^-/I^- electrolyte. Interestingly, the magnitudes of these potentials were similar for the three sensitizers (Figure **45**, Table **6**); thus, we would expect the rate of back transfer to be similar in each case. The potential required to drive 0.1 mA m^{-2} of cathodic dark current density for every Rux dye was less negative than for $[Ru(H_2L')_3]^{2+}$ sensitized TiO_2 (under low photocurrent density conditions),[74] which implies that the lower Rux efficiencies are in part due to enhanced electron transfer from TiO_2 to the solution redox couple. This conclusion is also supported by comparison with non-sensitized TiO_2 electrodes, which were observed to require –0.23 V to produce a cathodic current density

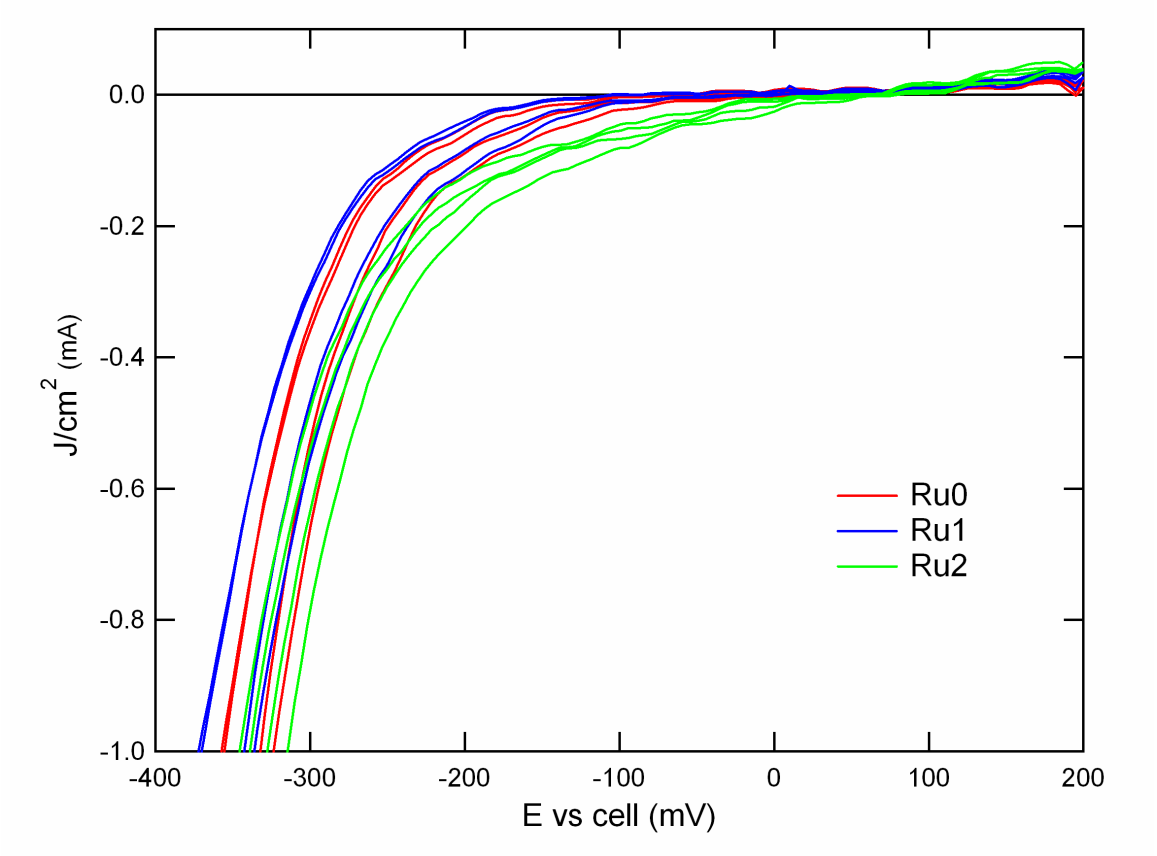

Figure 45. Dark Current versus potential characteristics for Rux-sensitized TiO_2 electrodes. Ru0 (red, ——), Ru1 (blue, – – –), and Ru2 (green, · · ·) (A_{MLCT} = 1.5 ± 0.3). The data (corrected for uncompensated cell resistance, 64 ohms) were measured in the absence of illumination in a potentiostatic three-electrode apparatus at 20 mV s^{-1} scan rate between 0.20 and –0.60 V vs. the Nernstian potential of the cell. The electrolyte was acetonitrile containing 0.50 M LiI, 0.040 M I_2, 0.020 M pyridine and 0.020 M pyridinium triflate.

of 0.1 mA cm^{-2} to the I_3^-/I^- electrolyte. These data indicate that the deleterious dark cathodic reduction of I_3^-/I^- by electrons in the TiO_2 as a result of adsorption of the monocarboxyl-xylyl linkers is similar, or even slightly accelerated, to that of unmodified TiO_2.

The present data indicate that even when injection and regeneration compete favorably with recombination in a dynamics experiment in the presence of I^-, high quantum yields for photocurrent flow are not necessarily obtained at steady state in a photoelectrochemical cell containing I_3^-/I^-. This behavior suggests that species resulting from the addition of I_3^- are present under steady-state conditions that deleteriously increase the ratio of recombination to regeneration for the long linkers. It is possible that the presence of triiodide in the current density-potential experiments plays a crucial role in the interfacial kinetics of these systems.

Conclusions

In summary, we have shown that ruthenium-based dyes with one carboxyl anchoring group and various xylyl-linker lengths sensitize nanocrystalline TiO_2. Despite the small overlap with the solar spectrum, the dyes function in photoelectrochemical cells under simulated solar illumination, albeit with low efficiencies and with photocurrent densities that decrease with linker length. Injection is slightly faster for Ru0, but both recombination and regeneration are faster for Ru2, although the variation in the dynamics among the dyes is less than a factor of two. The measured kinetics do not satisfactorily explain the low efficiencies, nor the trends among the steady-state photoelectrochemical behavior of the dyes, and suggest that there are other possible quenching mechanisms or

electron-transfer processes which are not included in the current kinetics model. We suggest that the Ru-TiO_2 electron tunneling distance is roughly the same for x = 0, 1, and 2, as the one-carboxyl attachment to the surface is flexible enough for the Ru center to approach the TiO_2 surface in all three cases. Furthermore, electron transfer from Rux-sensitized TiO_2 to I_3^-/I^- is more pronounced than for $[Ru(H_2L')_3]^{2+}$ sensitized as well as unsensitized photoelectrodes, in accord with the lower efficiencies of the Rux-based cells.

CHAPTER 6:

ANCHORING GROUP AND AUXILIARY LIGAND EFFECTS ON BINDING MODES

Chapter 6

ANCHORING GROUP AND AUXILIARY LIGAND EFFECTS ON BINDING MODES

Introduction

One of the key features responsible for the high efficiencies of the $TiO_2/[Ru(H_2L')_2(NCS)_2]^0$ photoelectrode system is the ultrafast electron injection from the excited state of the dye into the semiconductor particles.[19,76] The chemical factors that produce such rapid electron injection have not yet been fully elucidated. Differences in the modes of binding of the dye to the semiconductor are likely to influence the electronic coupling between the dye and the semiconductor, thereby affecting the dynamics of both injection and recombination of the charge-separated state of the dye/TiO_2 moieties.[77-79] Accordingly, we have investigated the binding of dyes to nanocrystalline TiO_2 as a function of the number of anchoring groups and the type of auxiliary ligands on the metal complex. Three of the dyes investigated are ruthenium trisbipyridine derivatives, $[Ru(H_2L')_3]^{2+}$, $[Ru(H_2L')L_2]^{2+}$, and $[Ru(HL'')L_2]^{2+}$ where L is 2,2′-bipyridine, H_2L' is 4,4′-dicarboxylic acid-2,2′-bipyridine, HL" is 4-carboxylic acid-4′-methyl-2,2′-bipyridine, and L′ and L″ are the corresponding deprotonated carboxylate bipyridine ligands (Figure **46**). These dyes will be referred to collectively as $[Ru(bpy)_3]^{2+}$-type dyes and differ structurally only in the number of carboxy groups. The complexes $[Ru(H_2L')_2(CN)_2]^0$ and $[Ru(H_2L')_2(NCS)_2]^0$, which contain four carboxy

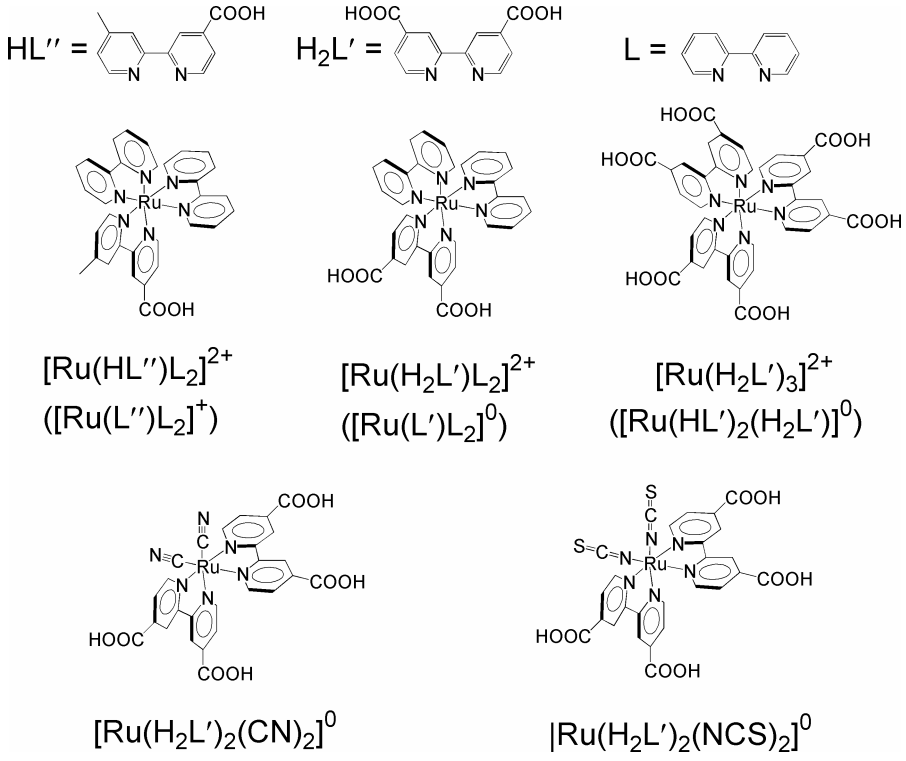

Figure 46. Structures of the fully protonated ligands, HL′′, H_2L', and L, and of the fully protonated complexes, $[Ru(HL'')L_2]^{2+}$, $[Ru(H_2L')L_2]^{2+}$, $[Ru(H_2L')_3]^{2+}$, $[Ru(H_2L')_2(CN)_2]^0$, and $[Ru(H_2L')_2(NCS)_2]^0$. The protonation states depicted are for the dyes in powder form; the actual dye protonation states are dependent on solvent conditions. In buffered ethanol, all of the dyes are full protonated. For the $[Ru(bpy)_3]^{2+}$-type dyes, the abbreviations used for deprotonated species in ethanol ($[Ru(L'')L_2]^+$, $[Ru(L')L_2]^0$, or $[Ru(HL')_2(H_2L')]^0$) are given in parentheses.

groups, were also studied, and differ from the $[Ru(bpy)_3]^{2+}$-type dyes in the replacement of one bipyridine ligand with more electron rich auxiliary ligands. The protonation state of all dyes will be described throughout using the appropriate number of protons on the ligands as well as the resulting overall charge of the dye based on the solvent conditions (neat ethanol or buffered ethanol containing 1 mM pyridine and 1 mM pyridinium triflate) or, in the case of sensitized TiO_2 slides, based on the solvent conditions in which binding was performed.[73] $[Ru(H_2L')_2(CN)_2]^0$ and $[Ru(H_2L')_2(NCS)_2]^0$ are fully protonated in both neat and buffered ethanol, while $[Ru(H_2L')L_2]^{2+}$ and $[Ru(HL'')L_2]^{2+}$ are protonated in buffered ethanol and fully deprotonated in neat ethanol. $[Ru(H_2L')_3]^{2+}$ is also fully protonated in buffered ethanol, but loses two protons to form $[Ru(HL')_2(H_2L')]^0$ in neat ethanol.

Several binding modes are possible for dyes that use carboxy groups to anchor to TiO_2. For example, either one (ester linkage) or both (carboxylato linkage) oxygen atoms in the carboxy group can bind to either one or two titanium atoms (Figure **47**). If only one carboxy group (1C) is attached, the binding is expected to be rather flexible. In contrast, dyes with two carboxy groups binding from the same (2S) or from neighboring (2N) bipyridine ligands are expected to produce a more robust linkage to the surface (Figure **47**). The $[Ru(H_2L')_2(CN)_2]^0$, $[Ru(H_2L')_2(NCS)_2]^0$, and $[Ru(H_2L')_3]^{2+}$ dyes can in principle access all of the suggested binding modes, whereas $[Ru(H_2L')L_2]^{2+}$ can potentially bind through either the 1C or 2S modes but $[Ru(HL'')L_2]^{2+}$ can only bind through the 1C mode (Figure **47**). The nature of the binding has been evaluated using infrared spectroscopy, and the thermodynamics and kinetics of binding have been

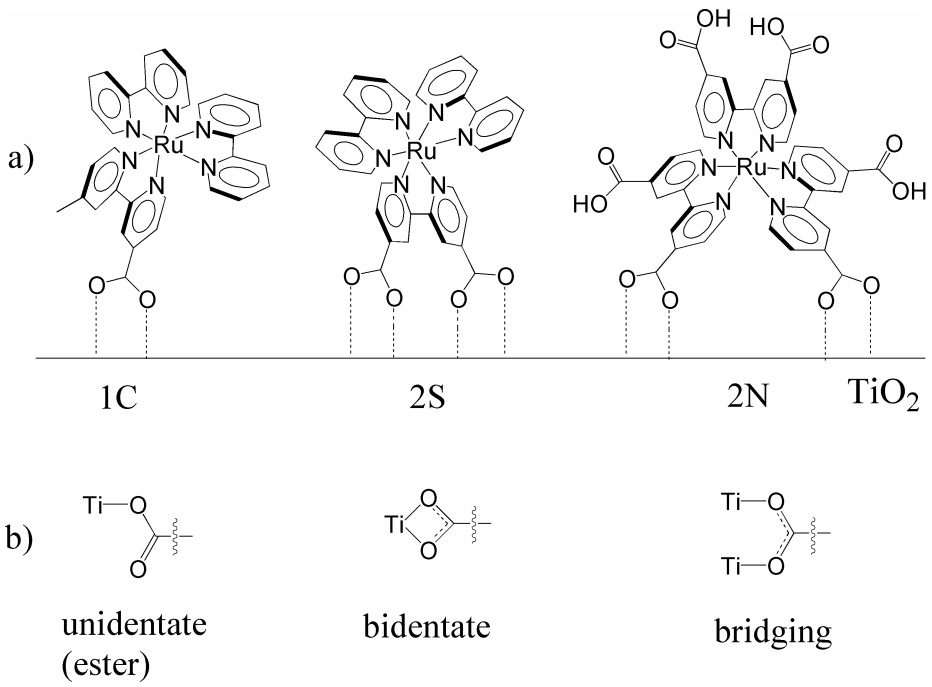

Figure 47. Possible binding modes. a) 1C indicates binding through a single carboxy group; 2S indicates binding through two carboxy groups located on the same bipyridine ligand; 2N indicates binding through two carboxy groups located on neighboring bipyridine ligands. b) In all cases, a single carboxy group can bind in a unidentate (ester), bidentate, or bridging mode.

measured on nanocrystalline TiO_2 for each member of the series. We have also investigated the influence of protonation of the carboxy moieties on the various binding properties of the metal complexes to TiO_2 and have elucidated the effect of variations in binding mode on the performance of DSSCs.

Experimental

Materials

Acetonitrile (Merck) was freshly distilled over calcium hydride prior to use, ethanol (EtOH) (Aapor), and anhydrous pyridine (Aldrich) were used as received, and 17.8 MΩ cm resistivity water was obtained from a Barnstead NANOpure filtration system. Lithium iodide (Aldrich) and anhydrous lithium perchlorate (J. T. Baker) were stored under N_2(g), iodine (Alfa-Aesar) was sublimed under vacuum and stored under N_2(g), and pyridinium triflate (Aldrich) was recrystallized from diethyl ether and stored in an inert atmosphere until use.

The $[Ru(H_2L')_2(CN)_2]^0$ and $[Ru(H_2L')_2(NCS)_2]^0$ complexes were used as received from Solaronix, and $[Ru(H_2L')L_2](PF_6)_2$ and $[Ru(H_2L')_3](PF_6)_2$ were synthesized as described previously.[32] The ligand H_2L'' was prepared by oxidation of 4,4′-dimethyl-2,2′-bipyridine.[31] The $[Ru(HL'')L_2](PF_6)_2$ complex was synthesized in the same manner as $[Ru(H_2L')L_2](PF_6)_2$ except that L″ was substituted for L′ in the synthesis.[32] The counter ion for all $[Ru(bpy)_3]^{2+}$-type dyes was PF_6^-.

Nanocrystalline titanium dioxide films (thickness 7±1 μm, crystallite size ~15 nm) deposited by screen printing on conductive (SnO_2:F) glass were obtained from the

Institut für Angewandte Photovoltaik, Germany. Before adsorption of sensitizers, the slides were cut into the desired size, typically 1 – 1.5 cm^2 in area. The conductive glass was then cleaned with acetone, and the TiO_2 electrodes were covered with several drops of freshly prepared acidic solution of 0.2 M Ti(IV)(aq) and left overnight in a sealed chamber to prevent evaporation of the solvent. After rinsing with water and ethanol, the slides were then annealed at 450ºC in air for 30 min, and slowly cooled to 120ºC. The hot electrodes were then submerged into ethanolic solutions of the various complexes to be adsorbed onto the semiconductor. Sensitized slides were then rinsed with ethanol and dried under a stream of N_2(g) prior to use.

Spectroscopy

The steady-state electronic absorption spectra of the dyes in solution were obtained using a 1 cm optical path length quartz cuvette in an Agilent 8453 UV-vis diode array spectrometer. Solvents were either neat ethanol or ethanol containing 1 mM pyridine and 1 mM pyridinium triflate, with the latter denoted as buffered ethanol.

Corrected steady-state emission spectra were recorded on a Jobin Yvon/SPEX Fluorolog3 flourimeter. The excitation wavelength was in the metal-to-ligand charge transfer (MLCT) band of the complexes. The quantum yields for emission of the dyes in solution were calculated by referencing each observed emission intensity to that of $Ru(bpy)_3Cl_2$ in degassed water, which has been reported to have an emission quantum yield of 0.042.[72] The emission lifetime of $[Ru(H_2L')_2(NCS)_2]^0$ was measured with single-photon-counting methods using a PicoQuant FluoTime200. All other time-resolved

emission decays were measured in the μs range using a Nd:YAG laser and an optical parametric oscillator.[49]

The UV-vis and diffuse reflectance FTIR spectra of the dye sensitizers adsorbed onto TiO_2 were measured on dry films. Slides coated with TiO_2 that did not contain any adsorbed sensitizer were used for baseline spectra. The FTIR spectra were obtained using a BioRad SPC 32000 spectrometer and were analyzed using the Kubelka-Munk procedure for diffuse reflectance.[80,81]

Electrochemistry

The formal reduction potentials of the dyes in either ethanol or buffered ethanol containing 1.0 M $LiClO_4$ were measured by cyclic voltammetry (CV) or differential pulse voltammetry (DPV) using a BAS model 100B potentiostat equipped with a glassy carbon working electrode, a methanolic saturated calomel reference electrode, and a Pt flag counter electrode. The CV scan rate was 50 mV s^{-1}, and the pulse amplitude in the DPV measurements was 50 mV. The potential of the methanolic saturated calomel electrode was determined both by measurement against a standard saturated calomel electrode and by calibration relative to the formal potential of ferrocene in ethanol obtained from a CV scan. The formal reduction potential data obtained from the DPV measurements are reported versus a standard calomel electrode (SCE).

Photoelectrochemical cell characteristics were recorded in acetonitrile containing 0.50 M LiI, 0.040 M I_2, 0.020 M pyridine, and 0.020 M pyridinium triflate as the electrolyte using a BAS 100 potentiostat connected to a custom-designed three-electrode cell.[49] The illuminated area of the TiO_2 was 0.25 cm^2 and the measured currents are

reported herein as the resultant current densities. The current density vs. potential characteristics were measured either at constant photocurrent density or at 100 mW cm^{-2} of a simulated Air Mass (AM) 1.0 spectrum produced by an Oriel Inc. solar simulator. All samples had approximately the same coverage as determined by the absorbance (0.7 ±0.1) at the MLCT maximum with correction for the differences in extinction coefficients. The measurements were performed versus a platinum wire in solution with a 20 mV s^{-1} scan rate. The cell resistance (65 ohms) was measured by replacing the TiO_2 electrode with a platinum foil working electrode and the J-*E* data were corrected for this ohmic resistance, but no corrections were made for any concentration overpotentials. The internal quantum yields, Φ, were calculated as the ratio of the observed J_{sc} to the value expected for a unity quantum yield when the measured absorbance of the dyes on TiO_2 electrodes was convoluted with the spectral irradiance of the solar simulator between 360 and 1100 nm.

Results

Characterization of the Dyes

Increasing the number of carboxy groups on the bipyridyl ligand shifted the $Ru^{3+/2+}$ reduction potentials ($E^{o\prime}$) of the dyes to more positive values (Figure **48** and **49**, Table **7**). In each case, the formal reduction potential for formation of Ru^{3+} from the

$$E^{o'*} = E^{o'} - \mathbf{E_{00}} / q \qquad (22)$$

excited state of the $Ru^{3+/2+*}$ dye, ($E^{o\prime *}$), was calculated from Eq. 22:

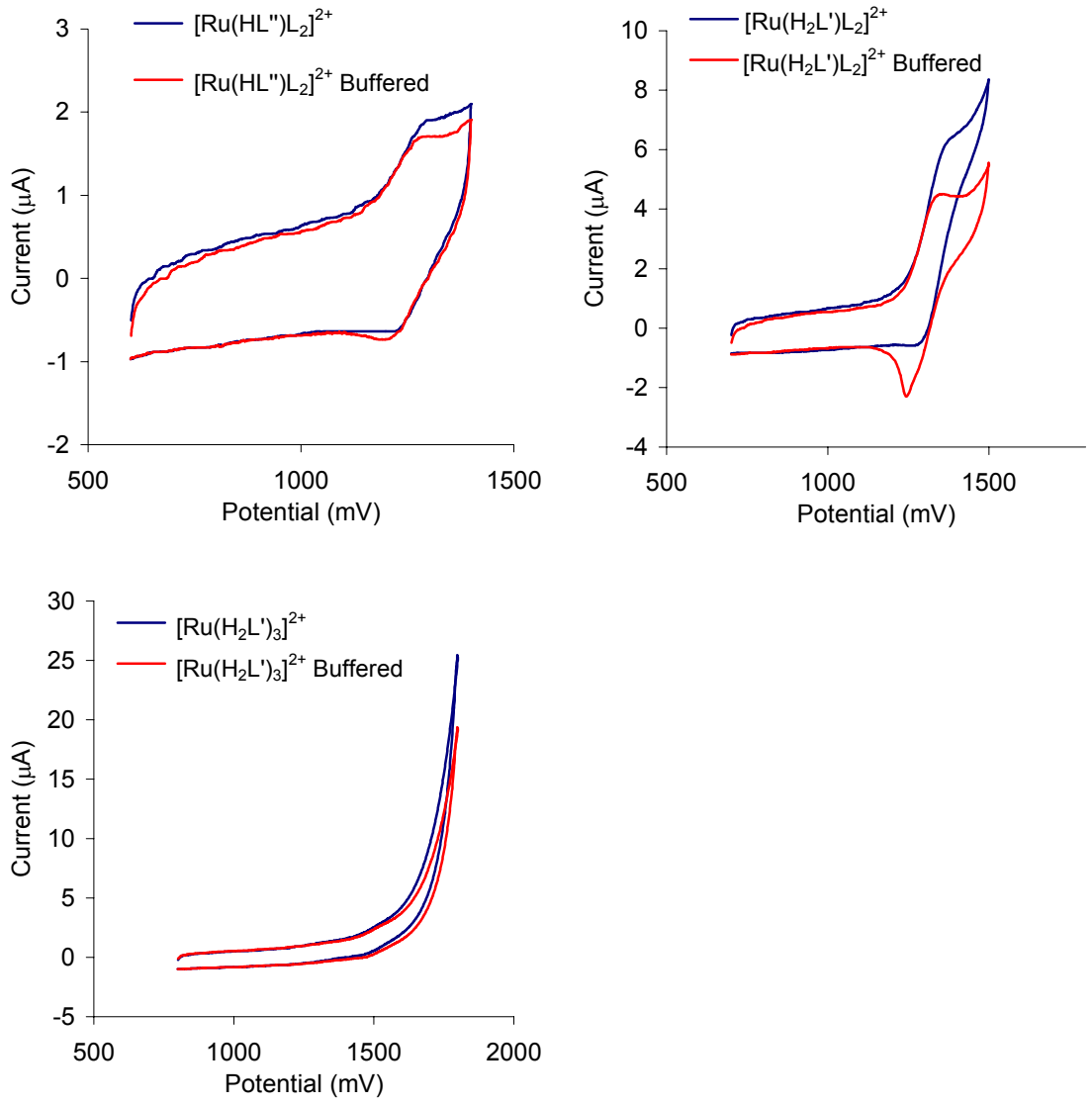

Figure 48. Cyclic voltammograms of the $[Ru(bpy)_3]^{2+}$-type dyes. Measured in absolute ethanol (blue) and in ethanol buffered with 20 mM pyridine, 20 mM pyridinium triflate (red). All solutions contained 1 M $LiClO_4$ as a supporting electrolyte.

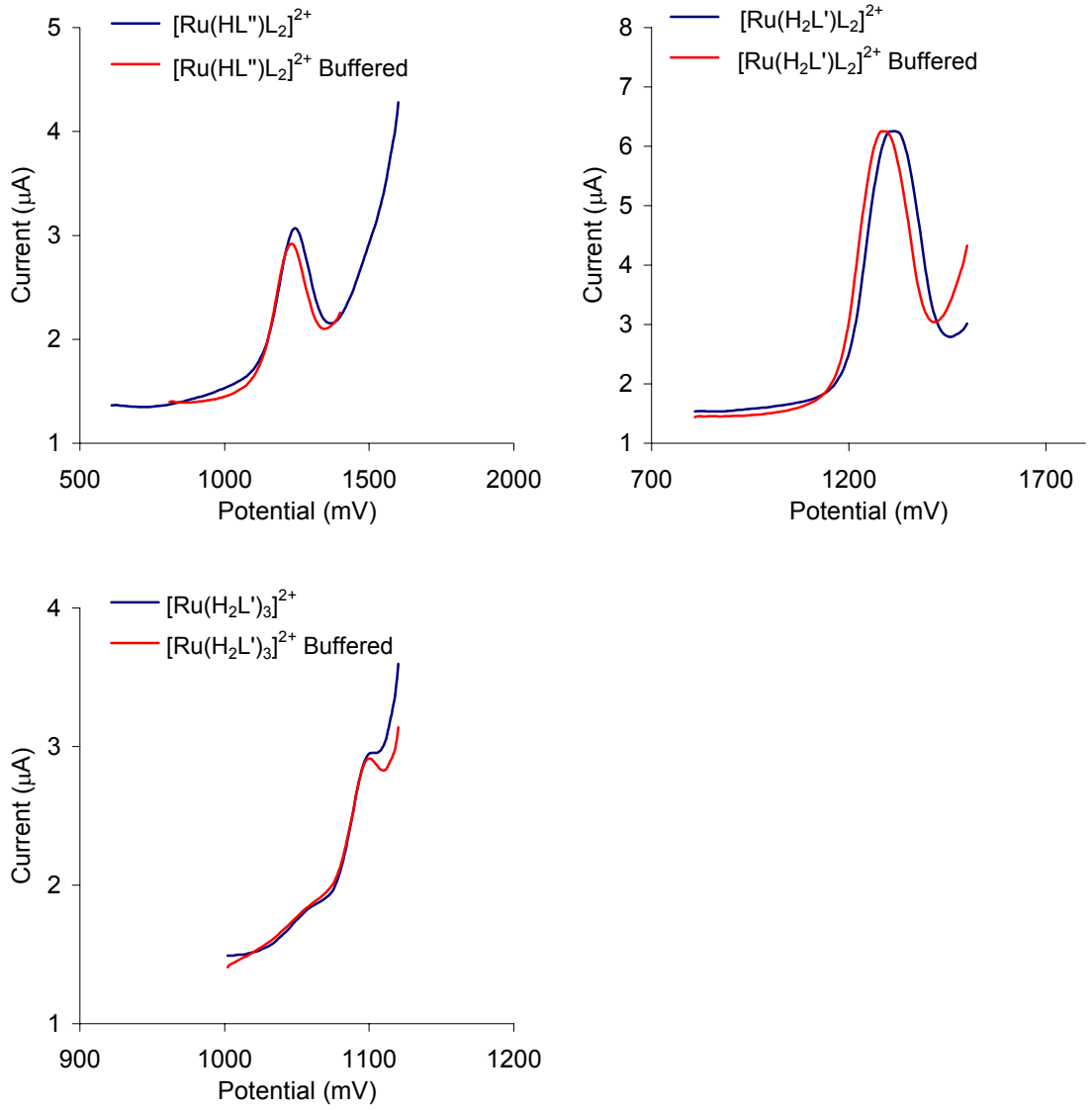

Figure 49. Differential pulse voltammograms of the $[Ru(bpy)_3]^{2+}$-type dyes. Measured in absolute ethanol (blue) and in ethanol buffered with 20 mM pyridine, 20 mM pyridinium triflate (red). All solutions contained 1 M $LiClO_4$ as a supporting electrolyte

Table 7. Spectroscopic and electrochemical data in neat and buffered ethanol.

Dye	Solvent	$\lambda_{max}^{absMLCT}$ (nm)	λ_{max}^{ems} (nm)	φ_{ems} (%)	τ_{ems} (μs)	$\mathbf{E}_{00}$[a] (eV)	$E^{o\prime}$[b] (V vs. SCE)	$E^{o\prime *}$[c] (V vs. SCE)
$[Ru(HL'')L_2]^{2+}$	Buffered EtOH	455	661	4	0.8	2.11	1.03	-1.08
$[Ru(L'')L_2]^{+}$	EtOH	454	621	5	1.0	2.24		
$[Ru(H_2L')L_2]^{2+}$	Buffered EtOH	469	676	5	0.8	2.00	1.09	-0.99
$[Ru(L')L_2]^{0}$	EtOH	455	636	7	1.1	2.24		
$[Ru(H_2L')_3]^{2+}$	Buffered EtOH	465	650	11	1.6	2.11	1.30[d]	-0.81
$[Ru(HL')_2(H_2L')]^{0}$	EtOH	465	656	7	1.3	2.08		
$[Ru(H_2L')_2(CN)_2]^{0}$	Buffered EtOH	498	706	1.5	0.3	1.95	0.91	-1.04
$[Ru(H_2L')_2(CN)_2]^{0}$	EtOH	495	713	1	0.2	1.94		
$[Ru(H_2L')_2(NCS)_2]^{0}$	Buffered EtOH	538	809	0.2	0.007	1.72	0.53	-1.19
$[Ru(H_2L')_2(NCS)_2]^{0}$	EtOH	535	808	0.2	0.006	1.72		

a: Obtained by fitting the emission spectra to the theoretical expression of Caspar *et al.*[71]

b: Determined from DPV measurements in buffered ethanol.

c: Calculated according to Eq. 22.

d: In ethanol with pyridinium triflate.

Figure **50** shows the ground-state absorption spectra of the three $[Ru(bpy)_3]^{2+}$-type dyes. The energy of the 0-0 transition, $\mathbf{E_{00}}$, was determined from a fit of the emission spectrum (Figure **50**), assuming that one bipyridyl vibrational mode of 1350 cm^{-1} was dominant (Table **7**).[71] The $[Ru(H_2L')_3]^{2+*}$ species had the least negative excited-state reduction potential for formation of $[Ru(H_2L')_3]^{3+}$ (E^{o}*, Table **7**), and therefore had the lowest driving force for injection of electrons from its thermalized excited state into TiO_2.

Binding Modes

To probe for possible differences in binding modes of the various complexes, IR spectra were collected for the dyes adsorbed onto TiO_2-coated glass slides. Diffuse reflectance IR spectra could not be collected while the coated slides were in contact with solution, so all IR data were obtained on films in the dry state.

Figure **51** shows the resulting diffuse reflectance IR spectra for films prepared by adsorption of the dyes from neat ethanol. All of the dyes adsorbed under these conditions showed vibrations in the 1300–1550 cm^{-1} region from the bipyridine rings.[82] To facilitate comparison of the various spectra, the 1545 cm^{-1} ring mode was used to normalize the relative peak intensities. As expected, the $[Ru(H_2L')_2(CN)_2]^0$ and $[Ru(H_2L')_2(NCS)_2]^0$ complexes showed an absorption band near 2100 cm^{-1} that resulted from the –CN stretch of the auxiliary ligand.[83] The spectra of $[Ru(L'')L_2]^+$ and $[Ru(L')L_2]^0$ on TiO_2 contained a broad artifact between 1700 and 1900 cm^{-1} due to optical interference arising from the specific thickness of TiO_2 films used for those samples. Peaks assigned to bound carboxylato (1380 and 1610 cm^{-1}) were found for all dyes, while carbonyl stretches

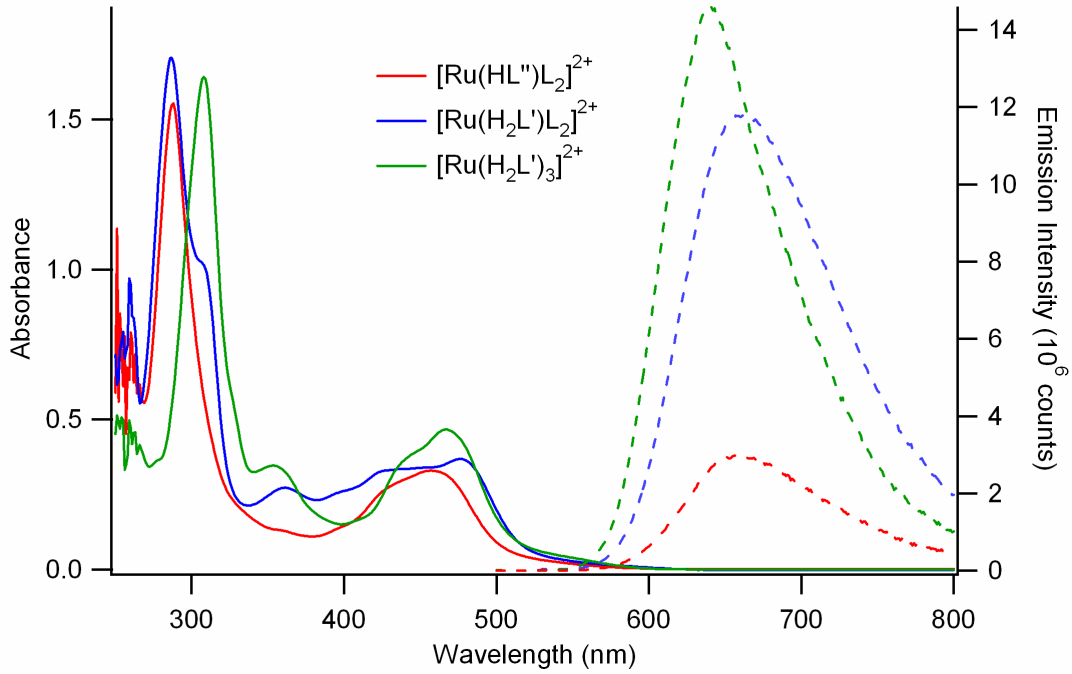

Figure 50. Spectroscopic characterization of the $[Ru(bpy)_3]^{2+}$-type dyes. Absorbance (solid) and emission (dashed)spectra of the various carboxylated dyes. In each case, the initial state was the fully protonated powder: $[Ru(H_2L')_3]^{2+}$ (blue); $[Ru(H_2L')L_2]^{2+}$ (pink); $[Ru(HL'')L_2]^{2+}$ (green).

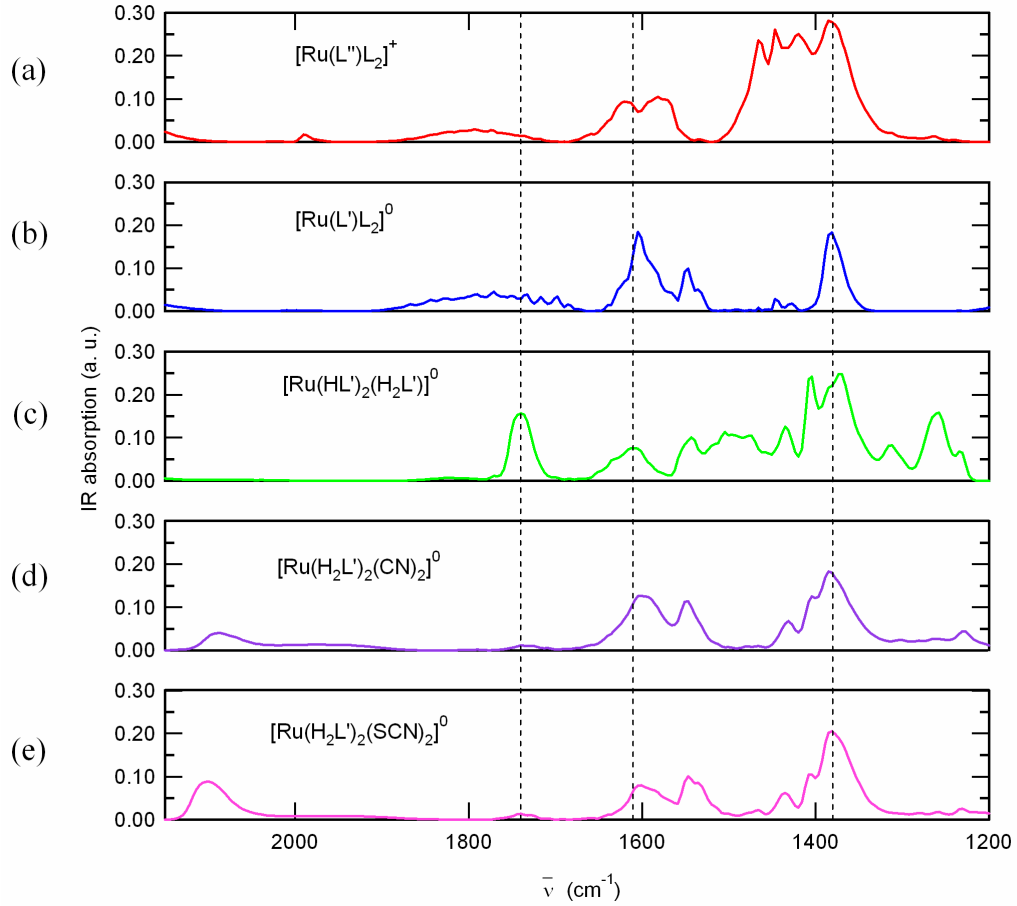

Figure 51. IR spectra on dry slides of dyes adsorbed from ethanol onto TiO_2. a) $[Ru(L'')L_2]^+$; b) $[Ru(L')L_2]^0$; c) $[Ru(HL')_2(H_2L')]^0$; d) $[Ru(H_2L')_2(CN)_2]^0$; and e) $[Ru(H_2L')_2(NCS)_2]^0$. Dye nomenclature refers to the protonation states in ethanol, the solvent from which binding occurred, and the protonation states after binding are not indicated. Dashed lines indicate the position of the key absorptions; from left to right: 1740 cm^{-1} (H-bonded carboxylic acid groups), 1610cm^{-1} (asymmetric bound carboxylato groups, and 1380 cm^{-1} (symmetric carboxylato groups).

arising from non-bound carboxylic acids were present only for $[Ru(H_2L')_2(CN)_2]^0$, $[Ru(H_2L')_2(NCS)_2]^0$, and $[Ru(HL')_2(H_2L')]^0$ (*vide infra*).

Photoelectrochemical Cell Properties

Significant differences were observed in photoelectrochemical performance for the different dye-sensitized photoelectrodes in contact with 0.50 M LiI, 0.040 M I_2, 0.020 M pyridine and 0.020 M pyridinium triflate (Figure **52**, Table **8**). Spectral response measurements indicated that the steady-state, short-circuit quantum yields for photocurrent flow from TiO_2 photoelectrodes coated with $[Ru(H_2L')_2(NCS)_2]^0$, $[Ru(H_2L')_2(CN)_2]^0$, or $[Ru(HL')_2(H_2L')]^0$ were all approximately 1.0 (Table **8**) for excitation in the MLCT bands of the adsorbed dyes. Hence the larger short-circuit photocurrent densities, J_{sc}, produced by adsorption of $[Ru(H_2L')_2(CN)_2]^0$ or $[Ru(H_2L')_2(NCS)_2]^0$ on TiO_2 (Figure **52**) arose primarily from the enhanced spectral overlap of these dyes with the AM 1.0 solar spectrum relative to that of $[Ru(HL')_2(H_2L')]^0$. For the $[Ru(bpy)_3]^{2+}$-type dyes, the photoelectrodes had approximately the same absorbance in the MLCT band (0.7±0.1) and had mutually similar overlap with the AM 1.0 spectrum, so any significant differences in J_{sc} or photoelectrode energy conversion efficiency between dyes in this series were not due to differences in light absorption. For the $[Ru(bpy)_3]^{2+}$-type dyes, the J_{sc} values and the efficiencies decreased in the order $[Ru(HL')_2(H_2L')]^0 > [Ru(L')L_2]^0 > [Ru(L'')L_2]^+$. The $[Ru(L'')L_2]^+$ system additionally exhibited significant variability in photoelectrode performance.

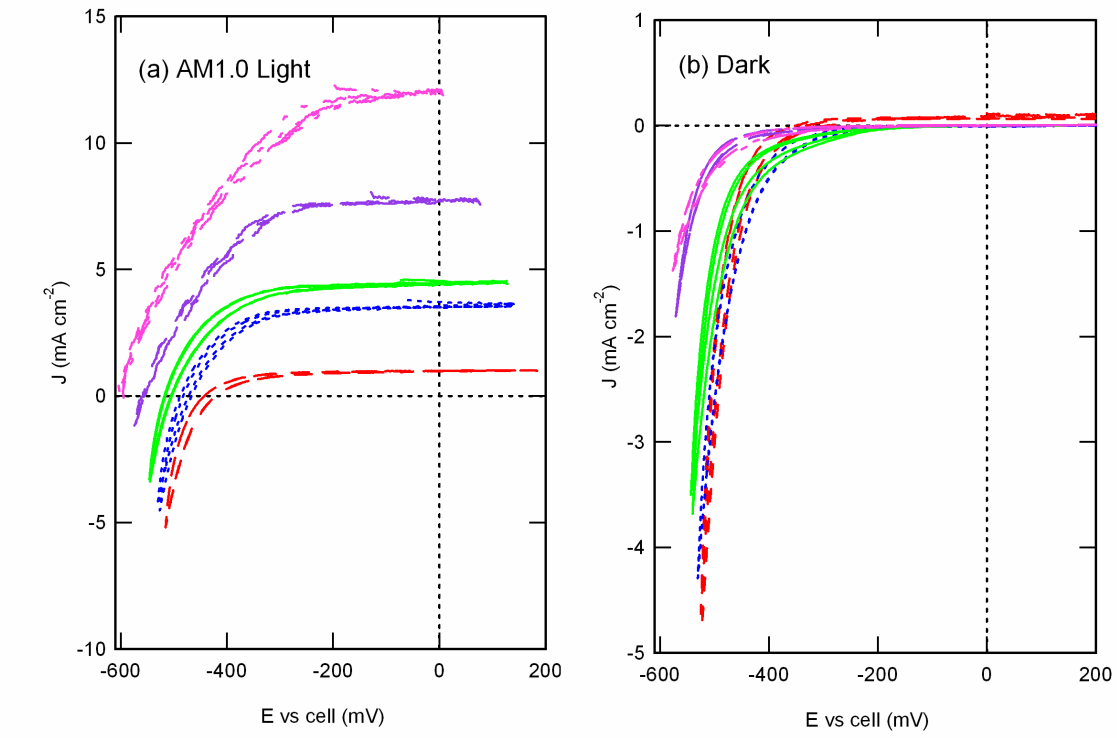

Figure 52. Current density versus potential behavior as a function of binding mode. TiO_2 photoelectrodes sensitized with adsorbed dyes in contact with 0.50 M LiI, 0.040 M I_2, 0.020 M pyridine and 0.020 M pyridinium triflate in acetonitrile. Sensitizers adsorbed from ethanol are: $[Ru(L'')L_2]^+$ (red, – – –); $[Ru(L')L_2]^0$ (blue, . . .); $[Ru(HL')_2\ (H_2L')]^0$ (green, ___); $[Ru(H_2L')_2(CN)_2]^0$ (purple, — — —); and $[Ru(H_2L')_2(NCS)_2]^0$ (pink, – . . – . . –). Dye nomenclature refers to the protonation states in neat ethanol, the solvent from which binding occurred. (a) J-E behavior under simulated Air Mass 1.0 (100 mW cm^{-2}) conditions. (b) J-E behavior in the dark.

Table 8. Photoelectrochemical data as a function of binding mode.

	J_{sc} [a] (mA cm^{-2})	V_{oc} [a] (V)	ff[b]	Efficiency. [c] (%)	Φ[d]	Dark Voltage [e] (V)
$[Ru(L'')L_2]^+$	1.5±1	-0.38±0.1	0.7	0.2	0.4	-0.33±0.1
$[Ru(L')L_2]^0$	3±0.5	-0.48±0.05	0.5	0.7	0.7	-0.42±0.05
$[Ru(HL')_2(H_2L')]^0$	4±0.5	-0.49±0.05	0.6	1.1	1.0	-0.44±0.05
$[Ru(H_2L')_2(CN)_2]^0$	6±2	-0.52±0.05	0.6	1.4	0.9	-0.51±0.05
$[Ru(H_2L')_2(NCS)_2]^0$	10±2	-0.56±0.05	0.5	2.1	1.0	-0.51±0.05

a: Acetonitrile with 0.50 M LiI, 0.040 M I_2, 20 mM pyridine 20 mM pyridinium triflate under AM 1.0 conditions. Values are averages of measurements using 5 different TiO_2 electrodes.

b: The fill factor (ff) is calculated as $P_{max}/(J_{sc} \times V_{oc})$, where P_{max} is the most negative value of $J \times V$.

c: Calculated as $(J_{sc} \times V_{oc} \times ff \times 100\%)/I_{light}$, where I_{light} = 100 mW cm^{-2}.

d: The integrated quantum yield (Φ) was determined by comparing the experimentally measured value of J_{sc} with the maximum calculated J_{sc} assuming a unity quantum yield when the measured absorbance of the dyes on TiO_2 electrodes are convoluted with the spectral irradiance of the solar simulator between 1100 and 360 nm.

e: Potential required to drive a cathodic current density of 0.1 mA cm^{-2} in the dark.

Electrochemical measurements of the dye-coated photoelectrodes in the absence of illumination were performed to investigate the rate of reaction of electrons in TiO_2 with the redox couple in solution (Figure **52**). The relative rates of this reaction for different dyes can be inferred from the dark current density as a function of electrode potential. Less negative potentials required to drive the same current density in the dark indicate more facile electron transfer processes between TiO_2 and oxidized species in the electrolyte. Because the dyes produced similar surface coverages, similar rates of back electron transfer from reduced TiO_2 to the redox couple in solution would be expected for all the systems. However, all of the $[Ru(bpy)_3]^{2+}$-type dyes showed an enhanced dark current density compared to $[Ru(H_2L')_2(CN)_2]^0$ and $[Ru(H_2L')_2(NCS)_2]^0$. A non-dye-coated TiO_2 slide showed the largest dark current density under these conditions. Furthermore, in the case of $[Ru(L'')L_2]^+$, the average dark current density was significantly greater than that observed for the other two $[Ru(bpy)_3]^{2+}$-type dyes. Consistently, the open-circuit voltages, V_{oc}, were quite similar for $[Ru(HL')_2(H_2L')]^0$ and $[Ru(L')L_2]^0$, and were lower (less negative) for $[Ru(L'')L_2]^+$ (Table **8**). No significant difference was observed in the photoelectrochemical response between dyes adsorbed onto the TiO_2 from buffered ethanol relative to dyes adsorbed from pure ethanol.

Discussion

Binding Modes

Unprotonated carboxylate or bound carboxylato groups exhibit symmetric and asymmetric stretches at ≈1380 and ≈1610 cm^{-1}, respectively, whereas the carbonyl

stretches associated with free carboxylic acids appear at ≈1740 cm^{-1} for H-bonded acid groups and at ≈1770 cm^{-1} for non-H-bonded acid groups.[82,84] The IR bands associated with bound carboxylato and non-bound carboxylate groups are expected to be very close to 1600 cm^{-1}, so the IR spectra do not allow facile differentiation between these two groups. All of the complexes bound to TiO_2 exhibited IR stretches at ≈1380 and ≈1610 cm^{-1} (Figure **51**).

The splitting observed between the symmetric and asymmetric carboxylato stretches (≈230 cm^{-1}) of all of the complexes bound to TiO_2 is close to the splitting reported for the ionic species $[Ru(L')_2(NCS)_2]^{4-}$ (≈250 cm^{-1}).[82] A much larger separation between the symmetric and asymmetric carboxylato stretching frequencies is expected in unidentate ester linkages, due to the different environments of the two oxygens in the ester group.[82,85] Such a large separation was not observed in any of the IR spectra recorded in this work. Thus the observed splitting indicates that in the dry state, the carboxylato groups used both oxygen atoms to attach to either one (i.e., the bidentate binding mode) or two (i.e., the bridging binding mode) titanium atoms. Furthermore, the lack of a significant shift between the stretching frequency observed for the bound carboxylato groups and that observed for ionic carboxylates in solution (1588 and 1387 cm^{-1}) suggests that the complexes predominantly used the bridging mode of binding.[84,86]

The bound $[Ru(H_2L')_2(CN)_2]^0$, $[Ru(H_2L')_2(NCS)_2]^0$, and $[Ru(HL')_2(H_2L')]^0$ complexes additionally exhibited a spectral feature at 1740 cm^{-1} attributable to carbonyl stretches arising from protonated carboxylic acids. The ratio of bound carboxylato to protonated (non-bound) carboxylic acid groups can be estimated from the ratio of the

intensities of the bands corresponding to carboxylato stretches (1610 cm^{-1}) relative to those corresponding to non-bound acids (1740 cm^{-1}).[82] For binding of either $[Ru(H_2L')_2(CN)_2]^0$ or $[Ru(H_2L')_2(NCS)_2]^0$ to TiO_2, a series of trials resulted in a mean ratio of the intensity at 1740 cm^{-1} to that at 1610 cm^{-1} of 1.0 ± 0.5. Assuming that all the carboxylato and carboxylic acid groups are bound and unbound, respectively, either a 2:2 or 3:1 ratio of bound to unbound carboxy groups is compatible with the IR intensity data. Individual molecules may bind through a mixture of binding modes with, for example, one molecule attached to the surface with three carboxylato groups.

For binding of $[Ru(HL')_2(H_2L')]^0$ to TiO_2, the ratio of the absorption intensities at 1740 and 1610 cm^{-1} was ≈2, consistent with this species having twice as many protonated as unprotonated groups (4 carboxylic acids : 2 carboxylato groups). This intensity ratio therefore suggests that on average only two of the six carboxy groups are used in binding this dye to TiO_2. For the two remaining dyes, $[Ru(HL'')L_2]^{2+}$ and $[Ru(H_2L')L_2]^{2+}$, the 1740 cm^{-1} band assigned to free, non-bound acid groups was less than 10% of the intensity of the 1610 cm^{-1} carboxylato stretch regardless of the initial protonation state of the dye in the binding solution, i.e., binding from buffered (protonated) or neat (deprotonated) ethanol. This suggests that all of the available carboxy groups (1 or 2, respectively) in these two dyes are used in binding to TiO_2.

Previous work has shown that even when a fully deprotonated dye in solution binds to TiO_2, the non-bound acid groups are protonated due to deprotonation of the TiO_2 surface.[82] Consistently, the IR spectra were observed to be essentially identical for dyes bound from either buffered or nonbuffered ethanolic solution, with both being indicative

of protonated, non-bound carboxylic acids for bound $[Ru(H_2L')_2(CN)_2]^0$, $[Ru(H_2L')_2(NCS)_2]^0$, and $[Ru(HL')_2(H_2L')]^0$ regardless of the initial protonation state of these dyes in solution.

Photoelectrochemical Cell Properties.

Photoelectrodes sensitized with the $[Ru(H_2L')_2(CN)_2]^0$ and $[Ru(H_2L')_2(NCS)_2]^0$ complexes exhibited the highest energy conversion efficiencies under simulated solar illumination, primarily because their absorption spectra most closely matched the spectral irradiance profile of the excitation source. The internal quantum yield, Φ, which is independent of differences in spectral overlap, allows for a more direct comparison between the photoelectrochemical properties of these five dyes. The $[Ru(H_2L')_2(NCS)_2]^0$, $[Ru(H_2L')_2(CN)_2]^0$, and $[Ru(HL')_2(H_2L')]^0$ complexes, which can access the 2N mode with better overall binding properties than binding through the 2S or 1C mode, exhibited the highest quantum yields on TiO_2, whereas $[Ru(L')L_2]^0$, which can bind in the 2S but not the 2N mode, showed a lower quantum yield, and $[Ru(L'')L_2]^+$, which can only bind through 1C, exhibited the lowest quantum yield (Table **8**). Thus, the short-circuit quantum yields for sensitizers in the $[Ru(bpy)_3]^{2+}$-type series declined in the order 2N>2S>1C, correlating with the trends in the desorption kinetics of this system.

The quantum yield is a function of the competition between a number of processes, implying that at least one of the processes correlates with the variation in binding strength and desorption dynamics in this series of adsorbed complexes. The decrease in quantum yield for adsorbed $[Ru(L'')L_2]^+$ relative to the other sensitizers is not ascribable to less favorable energetics for this complex, because this sensitizer had the

most negative excited-state potential and therefore had the largest driving force of all the complexes studied in this work for injection of charge carriers into TiO_2 (Table **8**). Additionally, all of the complexes have ground-state $Ru^{3+/2+}$ formal potentials that are sufficiently positive to oxidize the I_3^-/I^- redox system and therefore readily regenerate the reduced form of the dye (Table **7**). Time-resolved spectroscopic experiments are in progress to elucidate more fully which of the fundamental rate processes, such as the electronic coupling to the semiconductor or the quenching by solution-based redox species, is most directly affected by the variation in the binding of the different dyes to the TiO_2 surface.

The photoelectrochemical behavior of the various dyes adsorbed onto TiO_2 exhibited trends in two different quantities, J_{sc} and V_{oc}, both of which contributed to changes in photoelectrode energy conversion efficiency as the adsorbed dye was varied. The open-circuit voltage also exhibited a correlation with the binding modes of the sensitizer to the TiO_2 surface. The open-circuit voltage is a photostationary state property that is primarily a function of the short-circuit current density and secondarily a function of the rate of the direct reduction of redox species in the electrolyte by electrons in the TiO_2. The effect of changes in the short-circuit current density can be removed either by comparing photovoltages at illumination intensities that produce comparable short-circuit photocurrent densities, or by comparing the potentials needed to produce a constant cathodic current density in the dark. In either comparison, TiO_2 electrodes sensitized with $[Ru(H_2L')_2(NCS)_2]^0$, $[Ru(H_2L')_2(CN)_2]^0$, or $[Ru(HL')_2(H_2L')]^0$ exhibited significantly smaller direct reduction rates than did electrodes sensitized with

$[Ru(L')L_2]^0$, which in turn had smaller direct reduction losses than those sensitized with $[Ru(L'')L_2]^+$. This indicates that adsorption of $[Ru(H_2L')_2(NCS)_2]^0$, $[Ru(H_2L')_2(CN)_2]^0$, or $[Ru(HL')_2(H_2L')]^0$ inhibited direct reduction of the electrolyte by the TiO_2 surface. Reducing the binding strength, and therefore producing a more labile complex, produced a higher direct reduction rate and a lower open-circuit voltage for such systems.

The temporal stability of the photoelectrodes of course should correlate to the binding strength and desorption kinetics of the various dyes. The large variance in photoelectrochemical performance that was observed when $[Ru(L'')L_2]^+$ was used to sensitize TiO_2 indicates that two or more carboxylic acids produce superior photoelectrochemical cell stabilities in this series of complexes under operating cell conditions. Hence, the linkage to the TiO_2 surface can play an important role in achieving temporal stability as well as in tuning both the steady-state quantum yield and the magnitude of the predominant back-reaction rate in dye-sensitized TiO_2-based photoelectrochemical solar cells. For the carboxylated ruthenium dyes investigated herein, both the temporal stability and photoelectrochemical performance were correlated since binding modes that improved the temporal stability (reduced desorption rates and improved binding constant) also produced improved energy-conversion performance.

Conclusions

For the series of carboxylated ruthenium dyes, a correlation was observed between the chemical nature of dye binding and the photoelectrochemical behavior of the resulting dye-sensitized TiO_2 electrodes. The IR spectra indicated that the dyes bound in a bridging fashion, i.e., with both oxygen atoms from an anchoring carboxy group

interacting with adjacent titanium atoms on the TiO_2 surface, but not all carboxy groups participated in binding to the TiO_2. Complexes having either a single monocarboxy ligand or a single dicarboxy ligand used essentially all of their carboxy groups to bind to the surface, whereas complexes having 4 or 6 carboxy groups used on average 2 carboxy groups in binding to TiO_2. TiO_2 photoelectrodes sensitized with $[Ru(H_2L')_2(CN)_2]^0$, $[Ru(H_2L')_2(NCS)_2]^0$, and $[Ru(H_2L')_3]^{2+}$ displayed internal quantum yields that approached unity, indicating that differences in the short-circuit current density under solar illumination can be ascribed primarily to differences in overlap of these various dyes with the solar spectrum. However, the efficiencies within the series of dyes decreased in the order $[Ru(H_2L')_3]^{2+}>[Ru(H_2L')L_2]^{2+}>>[Ru(HL'')L_2]^{2+}$, indicating that the short-circuit current density and steady-state quantum yield correlated with the available binding type (2N>2S>>1C). In addition, the dark current was largest for the monocarboxy dye that used the weakest, most labile 1C mode of binding. The $[Ru(HL'')L_2]^{2+}$ complex was significantly less stably bound to TiO_2 over time than the other dyes, and consequently produced a wide range of photoelectrochemical responses. Hence, the linkage to the TiO_2 surface plays an important role in achieving temporal stability of the photoelectrochemical properties as well as in tuning both the steady-state quantum yield and the magnitude of the predominant back-reaction rate in dye-sensitized TiO_2-based photoelectrochemical solar cells.

CHAPTER 7:

EFFECT OF BINDING MODES ON INJECTION, RECOMBINATION AND REGENERATION DYNAMICS

Chapter 7

EFFECT OF BINDING MODE ON INJECTION, RECOMBINATION AND REGENERATION DYNAMICS

Introduction

A model for the internal kinetics of DSSCs is schematically shown in Figure **5**. Upon excitation (k_1), an electron is promoted through a metal to ligand charge transfer (MLCT) process from the t_{2g} orbital on the ruthenium metal center to a π^* orbital on a bound bipyridyl ligand. The excited state of the dye can either deactivate directly to the ground state (k_{-1}) or inject an electron into the conduction band of TiO_2 (k_2). In a working solar cell, the injection is efficient and the oxidized dye is regenerated by the iodide/triiodide electrolyte in solution (k_5). However, two non-geminate back reactions from the TiO_2 can occur; one is recombination of the injected electrons with the oxidized dye (k_3), the other is escape of the injected electrons to the solution redox couple (k_4).

Both electron injection and recombination of the injected electrons with the oxidized dye are dependent on the electronic coupling between the semiconductor and dye. For injection, the coupling is typically between the lowest excited state of the dye molecule and the TiO_2 conduction band. As such, the quantum yield for injection will be based not only on the relative energy levels, but on the lifetime of the excited state and the efficiency of intersystem crossing. In recombination, the coupling is between the oxidized dye and reduced TiO_2.

The photophysical properties of ruthenium bipyridyl based dyes are well suited for these applications because photon absorption results in formation of a singlet excited state that undergoes intersystem crossing to form a long lived triplet excited state.[69] Electron injection into TiO_2 occurs from this long lived ^{3}MLCT state.

We have recently investigated a series of dyes that varied in the number of carboxylic acid anchoring groups (Figure **46**), $[Ru(H_2L')_3]^{2+}$, $[Ru(H_2L')L_2]^{2+}$ and $[Ru(HL'')L_2]^{2+}$ where L is 2,2'-bipyridine, L' is 4,4'-dicarboxy-2,2'-bipyridine, and L" is 4-carboxy-4'-methyl-2,2'-bipyridine. Within this series, there were significant differences in the photoelectrochemical behavior as a function of the available binding modes. The solar cell efficiencies within the series of $[Ru(bpy)_3]^{2+}$-type complexes decreased in the order $[Ru(H_2L')_3]^{2+}>[Ru(H_2L')L_2]^{2+}>>[Ru(HL'')L_2]^{2+}$ (Table **8**), indicating that the short-circuit current density and steady-state quantum yield correlated with the available binding mode (2N>2S>>1C) (Figure **47**). In addition, the dark current was largest for the monocarboxy dye that used the weakest, most labile 1C mode of binding.

In an effort to elucidate the kinetics effects behind the decreased quantum yield of the monocarboxylated dye, we have investigated injection, recombination and regeneration rate processes as a function of the number of anchoring groups in this series of nearly identical ruthenium trisbipyridine derivatives.

Experimental

Materials

17.8 MΩ cm resistance water was obtained from a Barnstead NANOpure filtration system. Ethanol (Aapor) and anhydrous pyridine (Aldrich) was used as received. Acetonitrile (MeCN) (Merck) was freshly distilled over CaH_2 prior to use. Lithium iodide (Aldrich) and anhydrous lithium perchlorate (J. T. Baker) were stored under nitrogen until use; pyridinium triflate (Aldrich) was recrystallized from diethyl ether and stored in a drybox. $HClO_4$ and PbO_2 were purchased from Aldrich and were used as received. The syntheses of all dye complexes have been described previously.[32,73]

Nanocrystalline titanium dioxide films (thickness 6 μm, crystallite size ~15 nm) deposited by screen printing on conductive glass (SnO_2:F) were obtained from the Institut für Angewandte Photovoltaik, Germany. Before adsorption of sensitizers, the films were cut into the desired size and pretreated as follows: the conductive glass was cleaned with acetone, and the TiO_2 electrodes were covered with several drops of freshly prepared 0.2 M $TiCl_4$(aq) and left overnight in a sealed chamber to prevent evaporation. After rinsing with water and ethanol, the slides were annealed at 450°C in air for 30 min, then slowly cooled to 120°C. The hot electrodes were then submerged into ethanolic solutions of the various dye complexes. Sensitized TiO_2 slides were rinsed with ethanol and dried with nitrogen prior to use.

Spectroscopy

Steady-state absorption spectra were measured using a diode array Agilent 8453 UV-vis spectrometer. Absorbance of the sensitizer coated onto TiO_2 was measured on dry films. In all cases the scattering signal from TiO_2 slides without sensitizer was subtracted.

Nanosecond transient absorption and time-resolved emission were measured using a setup described previously.[49] Full transient spectra of the samples were found by recording the transient absorption trace for each desired wavelength in the region 390 – 800 nm. Parts of the spectra were recorded with λ_{ex} = 450 nm (470 –490 nm), while for the rest of the spectra λ_{ex} = 480 nm was used, with excitation intensity high enough to saturate the signal. The traces were described using a multi-exponential function, and the intensities at a fixed time were use to construct the spectrum.

For kinetics measurement for the dye complexes bound to TiO_2, the TiO_2 slides were positioned in a 5 mm path length quartz cuvette filled with acetonitrile containing 0.50 M $LiClO_4$, 0.020 M pyridine and 0.020 M pyridinium triflate. Dye coverage on the TiO_2 slides was controlled such that all samples had a similar MLCT absorbance max (A = 1±0.2). For kinetics measurements, the excitation energy (λ_{ex} = 480 nm) was 1 mJ for a ~1 cm^2 beam, unless otherwise stated. Transient absorption was measured at λ_{obs} = 450 nm and emission at λ_{em} = 630 nm. A broad beam was necessary to ensure uniform excitation of the samples and to prevent photobleaching. Time-resolved TiO_2 data are very sample specific; thus the reported data were obtained on the same day with slides

from the same preparation. Day-to-day variances are factors of 2 to 5 in actual rate constants, and 5 to 10% points in fractions.

Results

Dye Characterization

The three dyes used in this study have been previously characterized spectroscopically and electrochemically.[73] Selected ground and excited-state parameters are set out in Table **7**. However, it is of interest to have a full understanding of the spectral features of the various states of the metal complexes. Transient absorption spectroscopy was used to collect the difference spectra between the ground and excited state for the three $[Ru(bpy)_3]^{2+}$-type dyes. The ΔOD versus time profiles were measured every 5 nm from 350 nm to 800 nm. Fits of these spectra to a single (Eq. 3) or biexponential (Eq. 4) function were used to generate the difference spectra at various time points between 0 ns (laser excitation) and 1 μs (Figure **53**). Addition of the Ru^{2+} ground-state absorption spectra gave the excited-state spectrum of the dyes at the various time points (Figure **54**). The most characteristic features were the bleach of the MLCT band (centered around 460 nm) and the stimulated emission seen from 600 – 800 nm. The excited-state spectra of this series of dyes when bound to TiO_2 have been previously measured.[87] The transient absorption spectra after 0.5 μs for the dyes in solution and bound to TiO_2 are shown in Figure **55**. When bound to TiO_2, the MLCT bleach was still present, but the emission was quenched so that a small, but broad, positive signal around

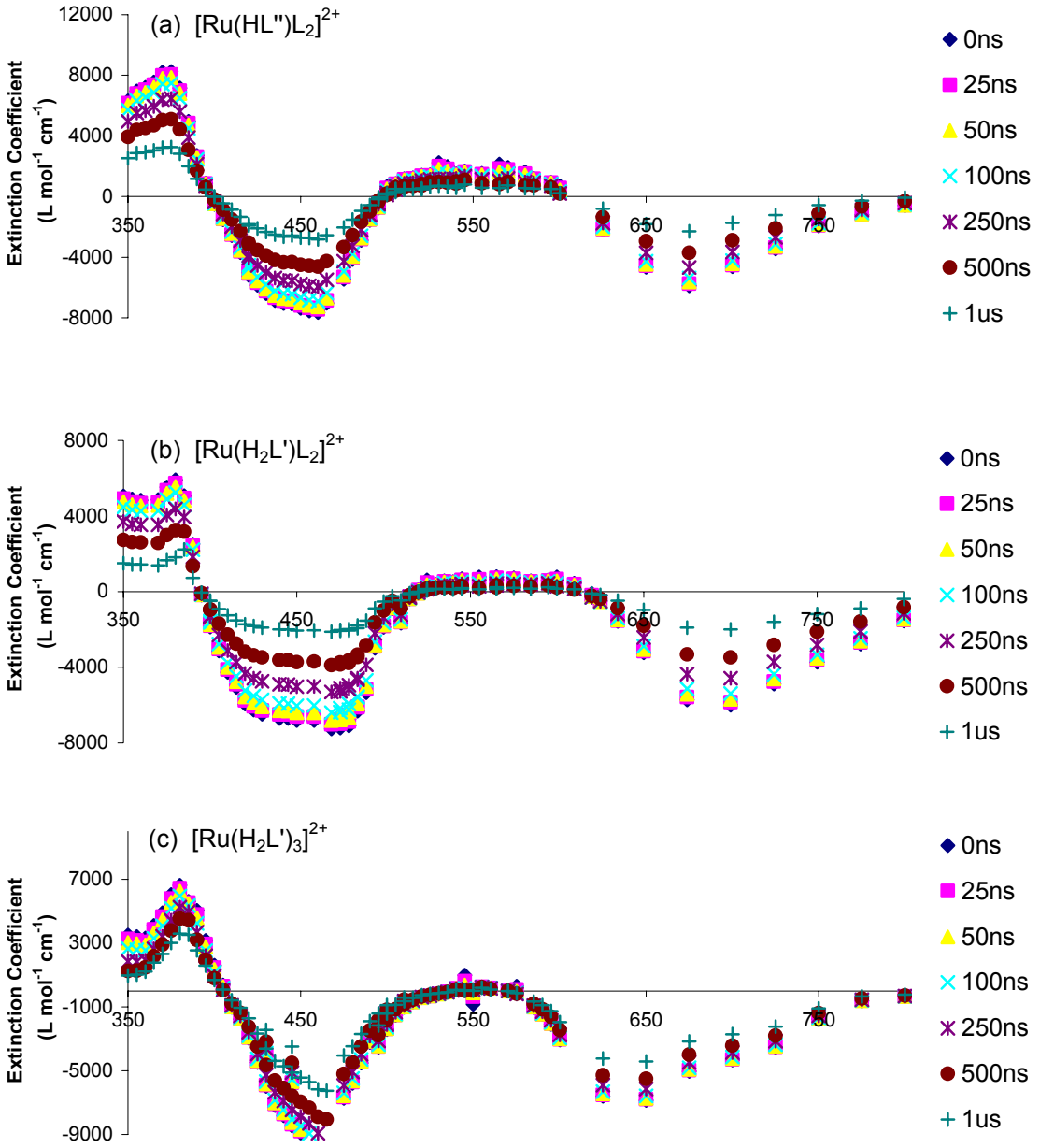

Figure 53. Difference spectra for $[Ru(bpy)_3]^{2+}$-type dyes. (a) $[Ru(HL'')L_2]^{2+}$; (b) $[Ru(H_2L')L_2]^{2+}$; (c) $[Ru(H_2L')_3]^{2+}$; 30 mM dye in acetonitrile with 0.5 M $LiClO_4$. Emission was monitored every 5 nm from 350 nm to 800 nm.

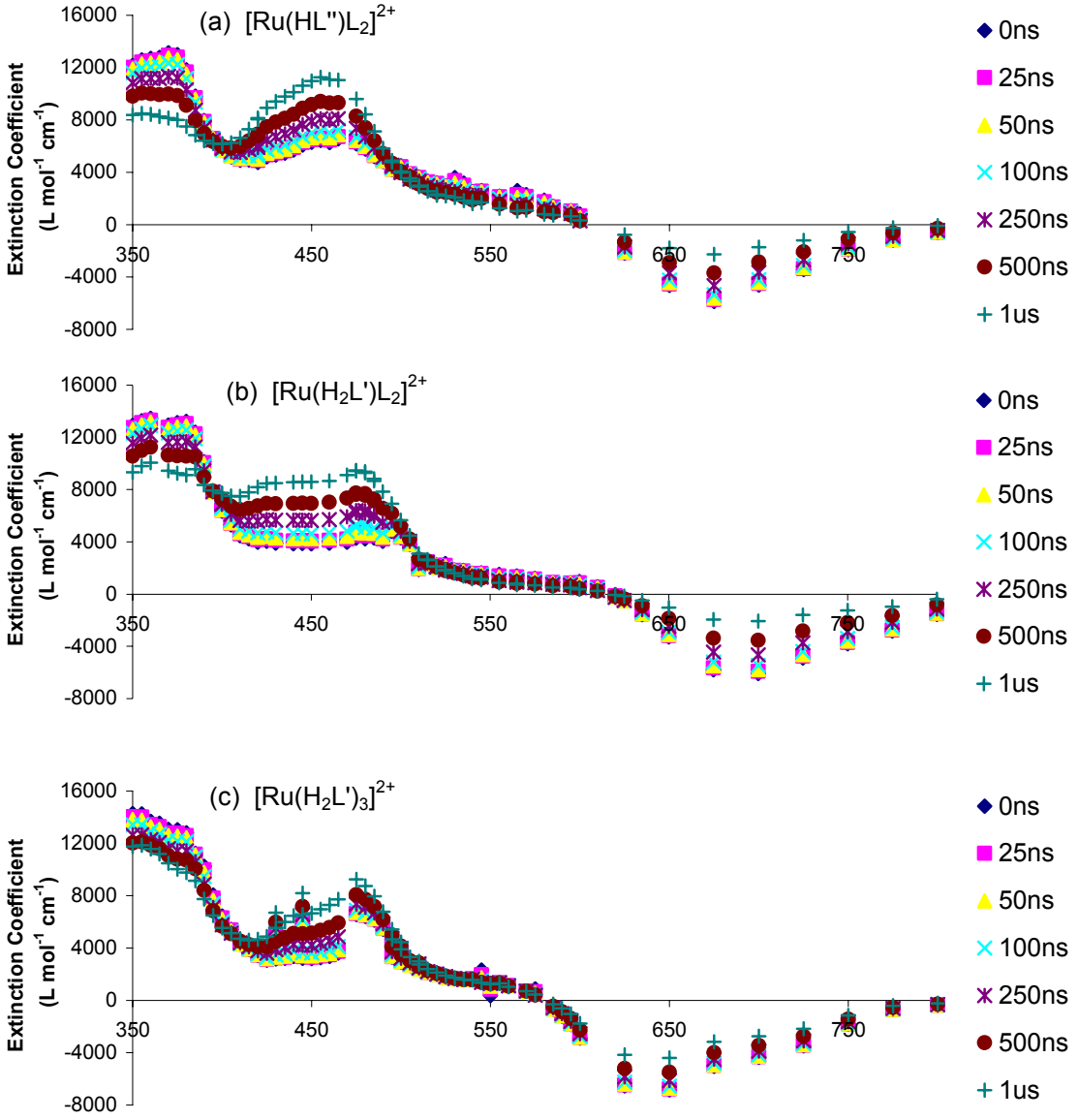

Figure 54. Solution excited-state spectra for $[Ru(bpy)_3]^{2+}$-type dyes. (a) $[Ru(HL'')L_2]^{2+}$; (b) $[Ru(H_2L')L_2]^{2+}$; (c) $[Ru(H_2L')_3]^{2+}$; 30 mM dye in acetonitrile with 0.5 M $LiClO_4$. Emission was monitored every 5 nm from 350 nm to 800 nm.

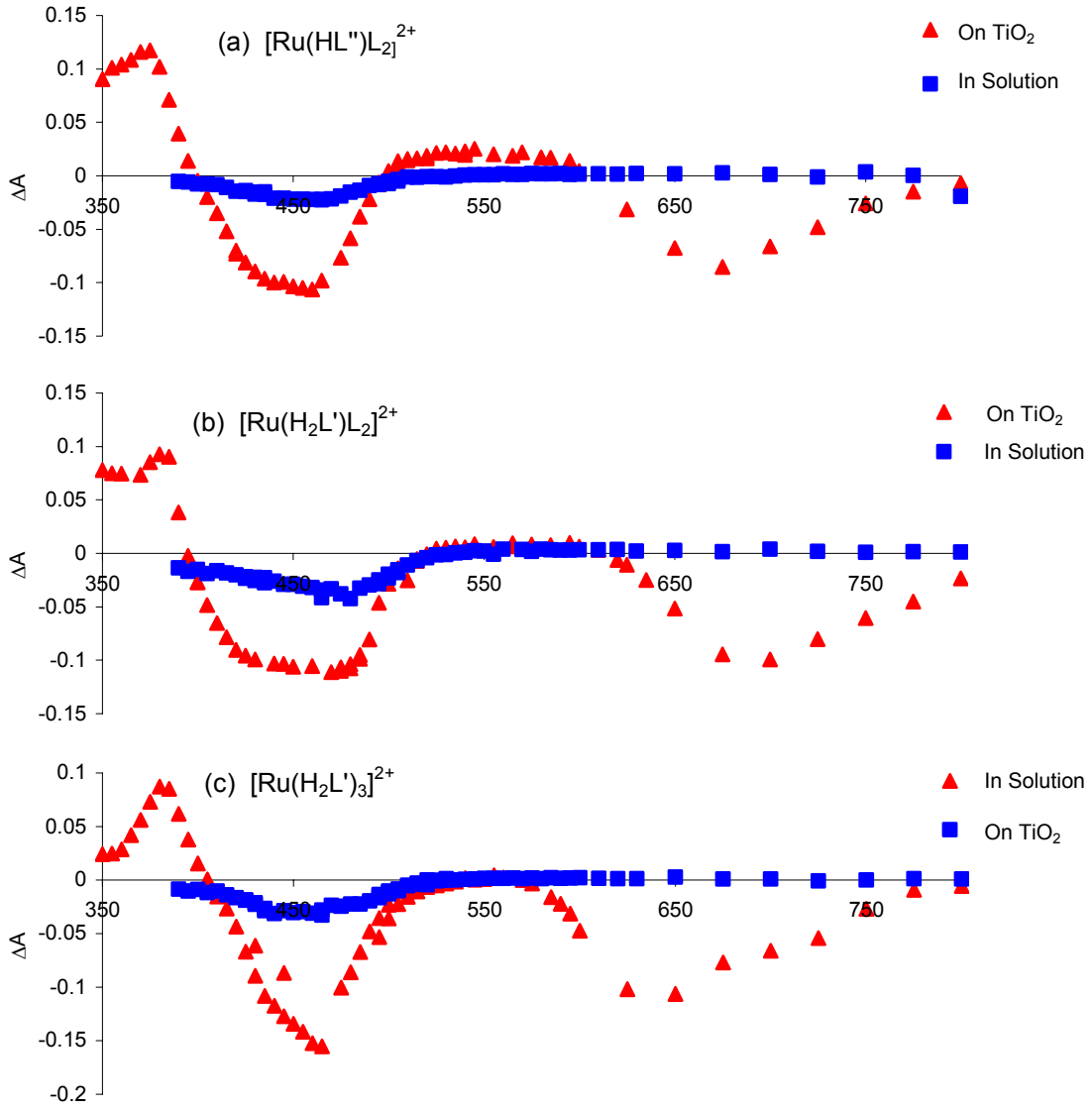

Figure 55. Difference spectra for the $[Ru(bpy)_3]^{2+}$-type dyes in solution versus adsorbed onto TiO_2. Comparison of the difference spectra in solution (red triangles) and adsorbed on a TiO_2 electrode (blue squares) for (a) $[Ru(HL'')L_2]^2$; (b) $[Ru(H_2L')L_2]^{2+}$; (c) $[Ru(H_2L')_3]^{2+}$; 30 mM dye in acetonitrile with 0.5 M $LiClO_4$.

700 nm due to oxidized dye was observed. However, for times shorter than 500 ns, this part of the spectrum was still dominated by the stimulated emission.

The Ru^{3+} spectra were obtained by oxidation with PbO_2 in acidic ($HClO_4$) ethanol (Figure **56**). For all of the dyes, oxidation shifted the MLCT to slightly higher energy and a weak absorption was present around 700 nm. The high energy π to π^* ligand based transitions were shifted to lower energy upon oxidation, with the monocarboxylated dye showing the largest shift.

When we are measuring the kinetics processes of injection and recombination for dyes adsorbed onto TiO_2, all three species are present in varying amounts depending on the relative rates of injection and recombination at any point in time. As such, it is necessary to have wavelength handles where a single transient species can be monitored. An overlay of the key spectra allowed determination of the isosbestic points and the key wavelengths at which Ru^{3+}, Ru^{2+} and Ru^{2+*} can be monitored (Figure **57**, Table **9**). At the first isosbestic point between the ground and excited state (≈400 nm), the extinction coefficients of the ground and excited species were the same. As such, this wavelength should allow direct monitoring of the kinetics related to the oxidized dye. A second isosbestic point between the ground and excited state was observed (≈500 nm) and could also be used to monitor the oxidized species. However, absorptions of the oxidized species both here and at 400 nm are very small. The oxidized species also absorbs at higher wavelengths (≈700 nm), where there is essentially no absorbance from the ground state (Figure **56**). However, once again the signal was quite small and measurement of the small changes in ΔOD were difficult. The kinetics traces at the wavelengths

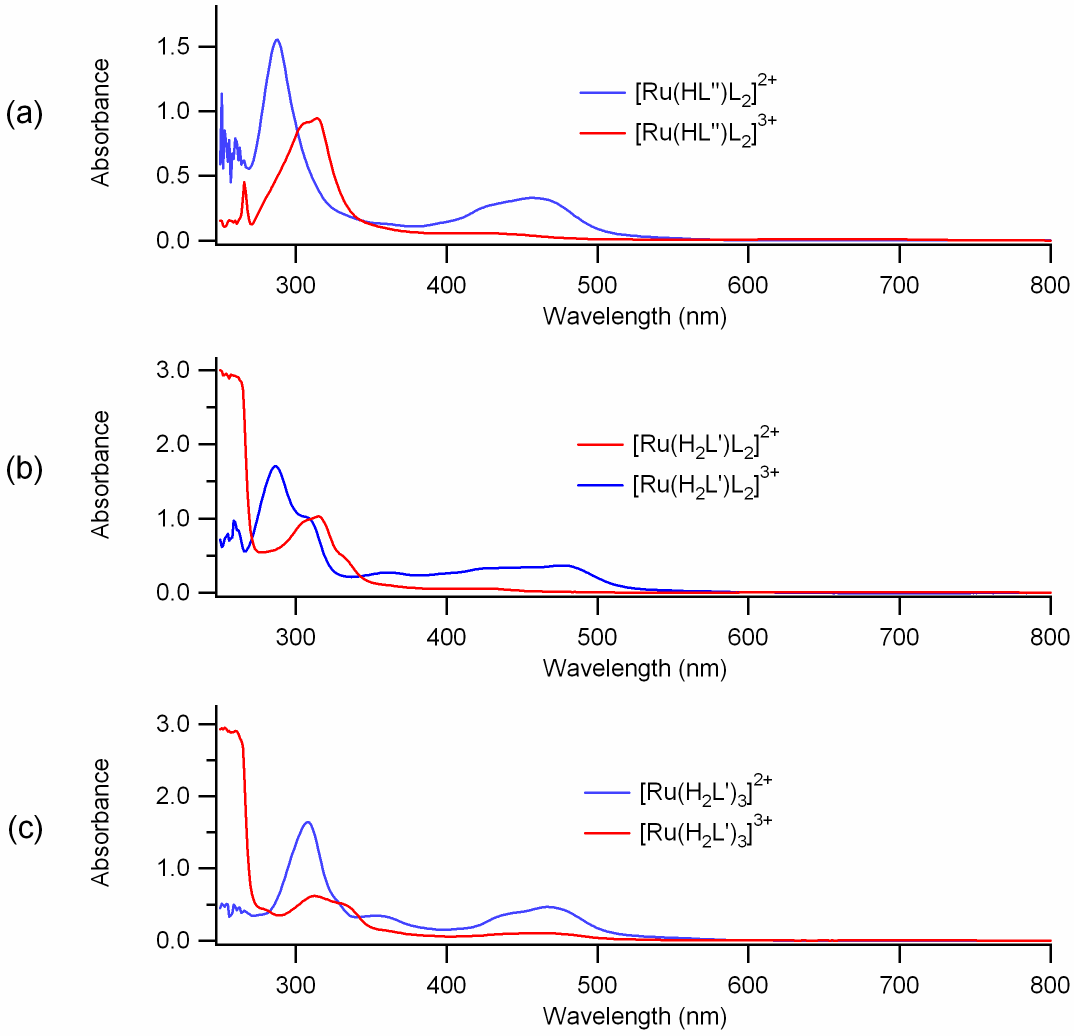

Figure 56. Absorption spectra of oxidized $[Ru(bpy)3]^{2+}$-type dyes. Ru^{3+} (red) and Ru^{2+} (blue) of the dyes in ethanol for (a) $[Ru(HL'')L_2]^x$, (b) $[Ru(H_2L')L_2]^x$ and (c) $[Ru(H_2L')L_2]^x$.

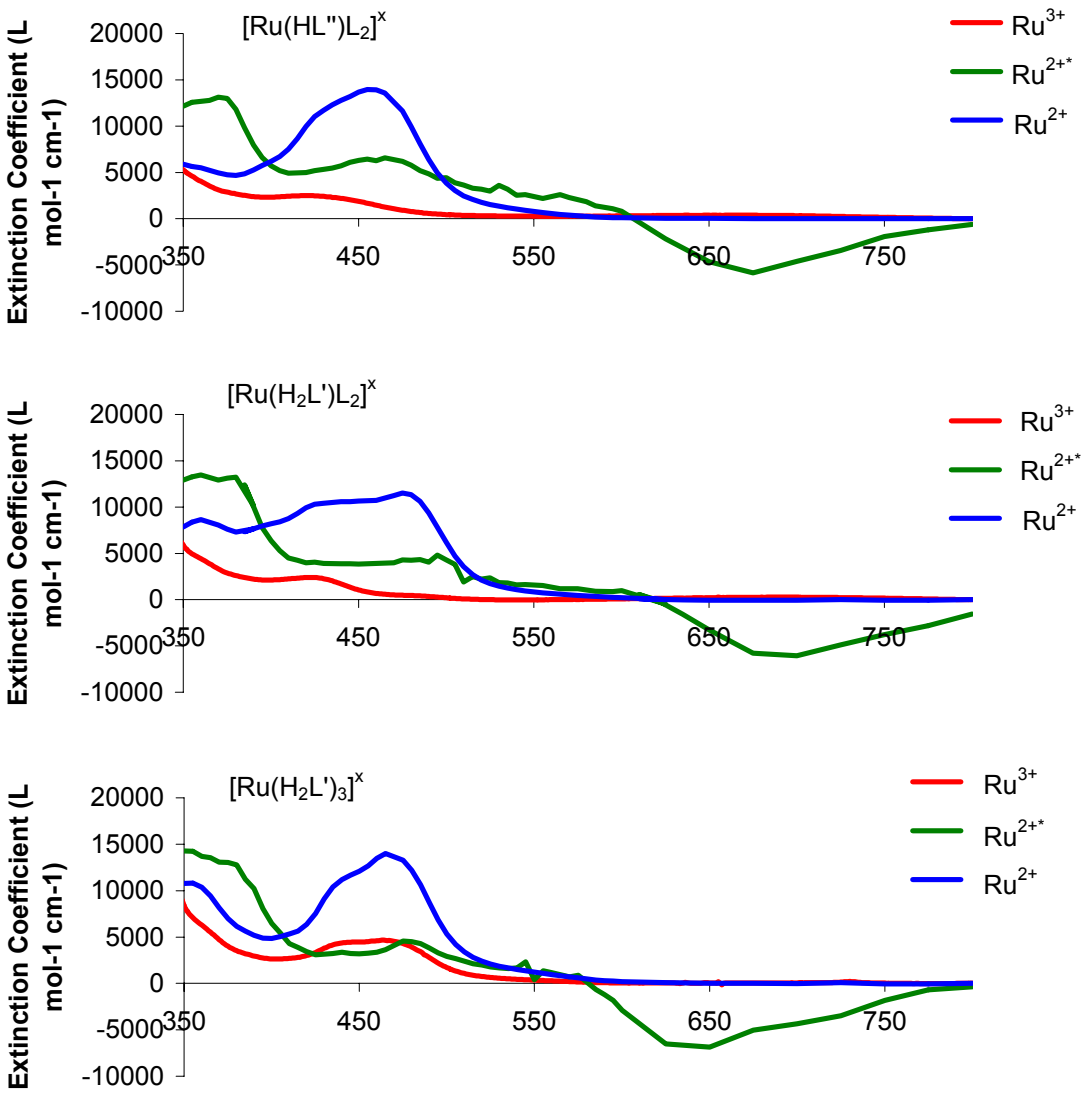

Figure 57. Overlay of spectra for $[Ru(bpy)_3]^{2+}$-type dyes. Ru^{2+} ground state (blue), the Ru^{2+*} excited-state spectrum (green) and the Ru^{3+} spectrum for (a) $[Ru(HL'')L_2]^x$ (b) $[Ru(H_2L')L_2]^x$ (c) $[Ru(H_2L')_3]^x$.

Table 9. Wavelengths for monitoring kinetics processes of $[Ru(bpy)_3]^{2+}$-type dyes.

	Ru^{2+} MLCT (nm)	Ru^{2+*} (nm)	Ru^{3+} (nm)	Isosbestic Points (nm)
$[Ru(HL'')L_2]^x$	480	577	680	398, 498
$[Ru(H_2L')L_2]^x$	495	600	695	394, 520
$[Ru(H_2L')_3]^x$	475	555	700	405, 538

corresponding to the two isosbestic points (≈400 nm, 500 nm) and at 700 nm were in excellent agreement on the microsecond timescale with the kinetics found when observing the recovery of the ground state at the MLCT. For these reasons, kinetics traces used in determining the actual rate constant for recombination were taken as the recovery of dye ground-state MLCT band and measured at 450 nm where the absorption of the oxidized dye is minimal. Time-resolved emissions for samples both in solution and coated on TiO_2 slides were monitored at ~630 nm.

Excited-state Quenching

When the dyes were bound to TiO_2, the excited-state lifetimes were strongly quenched (Figure **58**, Table **10**). The extent of this quenching is a measure of the injection rates. In solution, the emission showed single exponential decay kinetics. In contrast, the emission of a bound dye exhibited multiexponential behavior. To obtain satisfactory fits, the data were deconvoluted with a Gaussian response function (fwhm≈9 ns) and analyzed as a sum of three exponentials. The shortest lifetime was very close to that of the response function, and thus the pre-exponential factor and rate constant are lower limits. The quenching rate constants (k_2) determined on this nanosecond timescale (Table **10**) were taken as the difference between the rates of decay on TiO_2 and in acetonitrile:

$$k_2 = \tau_{TiO_2}^{-1} - \tau_{CH_3CN}^{-1} \qquad (23)$$

From integration of the time-resolved decay, the overall quenching was found to be greater than 97% for all three dyes.

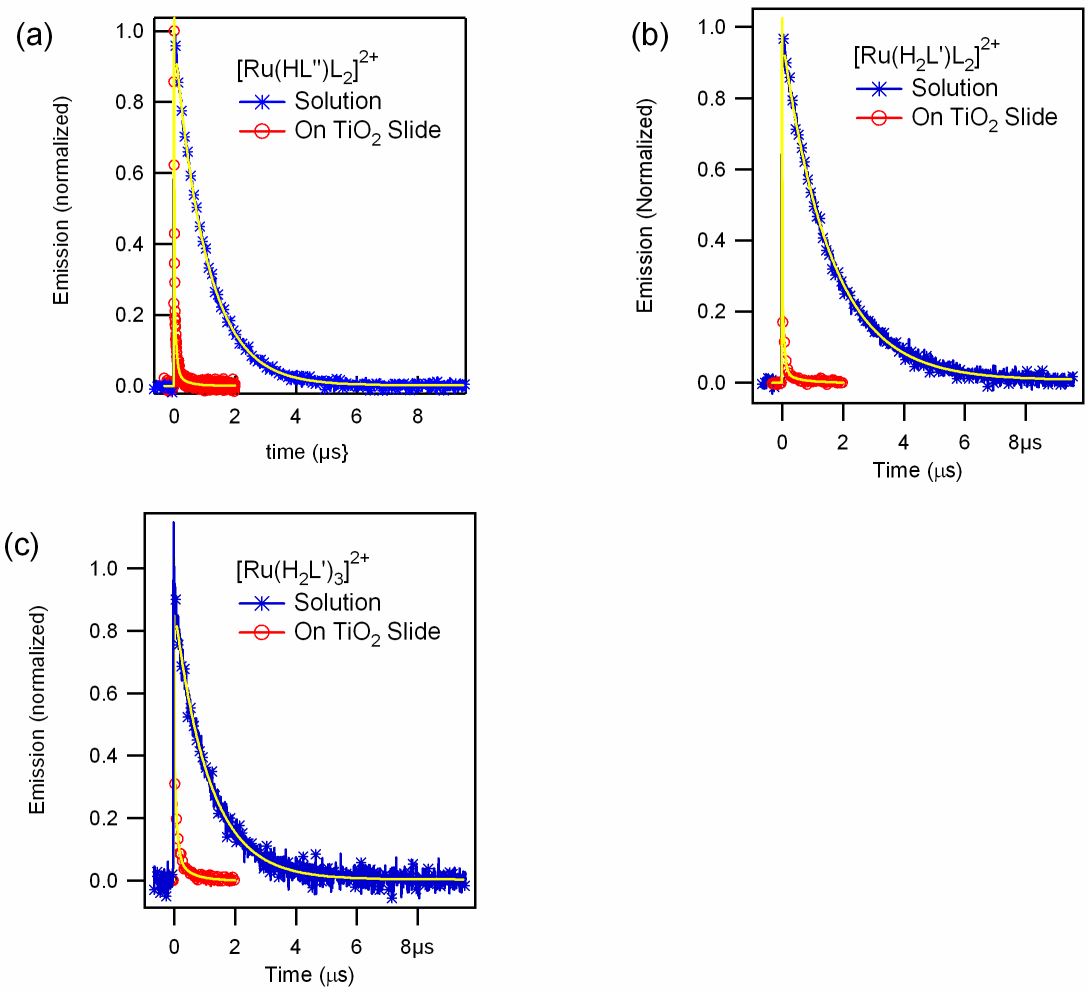

Figure 58. Emission quenching of $[Ru(bpy)3]^{2+}$-type dyes adsorbed onto TiO_2. Time-resolved emission (λ_{ex} = 480 nm, λ_{em} = 630 nm) of $[Ru(bpy)_3]^{2+}$-type dyes in degassed acetonitrile (blue, ∗), and bound to TiO_2 (red, o) with 0.50 M $LiClO_4$, 0.020 M pyridine, and 0.020 M pyridinium triflate in acetonitrile. Solid lines (yellow) are best exponential fits (see text for details) (a) $[Ru(HL'')L_2]^{2+}$; (b) $[Ru(H_2L')L_2]^{2+}$; (c) $[Ru(H_2L')_3]^{2+}$.

Table 10. Emission decays, quenching rate constants and recombination rate constants for $[Ru(bpy)_3]^{2+}$-type dyes measured on the nanosecond timescale.

Complex	$\tau^{-1}_{CH_3CN}$ (s^{-1})[a]	$\tau^{-1}_{TiO_2}$ (s^{-1})[b]	k_2 (s^{-1})[c]	k'_3 (s^{-1})[b,d]	k_3 (cm^3 s^{-1})[e]
	9.5×10^5	1.6×10^8 (0.84)	1.6×10^8	7×10^6 (0.60)	1×10^{-13}
$[RuL''L_2]^{2+}$		1.7×10^7 (0.14)	1.6×10^7	8×10^4 (0.40)	1×10^{-15}
		2.8×10^6 (0.02)	1.9×10^6		
	6.2×10^5	1.5×10^8 (0.85)	1.5×10^8	1×10^7 (0.35)	1×10^{-13}
$[RuL'L_2]^{2+}$		1.5×10^7 (0.13)	1.5×10^7	4×10^5 (0.65)	6×10^{-15}
		1.9×10^6 (0.01)	1.3×10^6		
	5.1×10^5	1.2×10^8 (0.73)	1.2×10^8	9×10^7 (0.60)	1×10^{-13}
$[RuL'_3]^{2+}$		1.2×10^7 (0.22)	1.2×10^7	1×10^6 (0.40)	1×10^{-15}
		2.1×10^6 (0.05)	1.6×10^6		

a: In degassed acetonitrile.

b: On TiO_2 with acetonitrile containing 0.5 M $LiClO_4$, 20 mM pyridine and 20 mM pyridinium triflate as electrolyte. Fractions of each component are given in parentheses (±0.01).

c: According to Eq. 23.

d: According to Eq. 24.

e: According to Eq. 25 with $\Delta\varepsilon = 2.3 \times 10^{-15}$ cm^3 m^{-1} and d = 6 μm.

Recombination

The recombination rate of TiO_2 electrons with the oxidized dye can be found by monitoring the time-resolved disappearance of the MLCT transient absorption bleach. Previous work has shown that when bound to TiO_2, the ground-state recovery of the dye depends on the excitation intensity and that the reaction between oxidized dye and reduced TiO_2 is bimolecular.[49] For a second-order reaction with an equal number of electrons and oxidized dyes, the change in absorbance (ΔA) follows Eq. 24 where k_3' is the recombination rate constant, t is the time, and a is a dimensionless constant that relates the absorbance to the concentration.

$$\Delta A = \frac{a}{1 + ak_3't} \qquad (24)$$

In this form, k_3' has units of s^{-1}. As seen in Figure **59**, the recombination rates for dyes used in this study were also dependent on the intensity of the pump beam. The transient absorption signal was proportional to the pump intensity for intensities of 1 mJ or lower. Recombination was measured for several different intensities and timescales and all data were analyzed globally. To fit the data satisfactorily, a sum of two second-order functions of the type found in Eq. 24 was necessary. The fraction of each component was found by comparing the *a*-constants, which were equal for all data sets used in the global analysis (Table **10**). To convert the observed rate constants to true second-order rate constants, it is necessary to take into account the molar absorptivity of the species detected at the wavelength where the recovery is observed. When bound to TiO_2, the dye excited state is very short-lived, and the Ru^{3+} absorbance is negligible at 450 nm (Figure

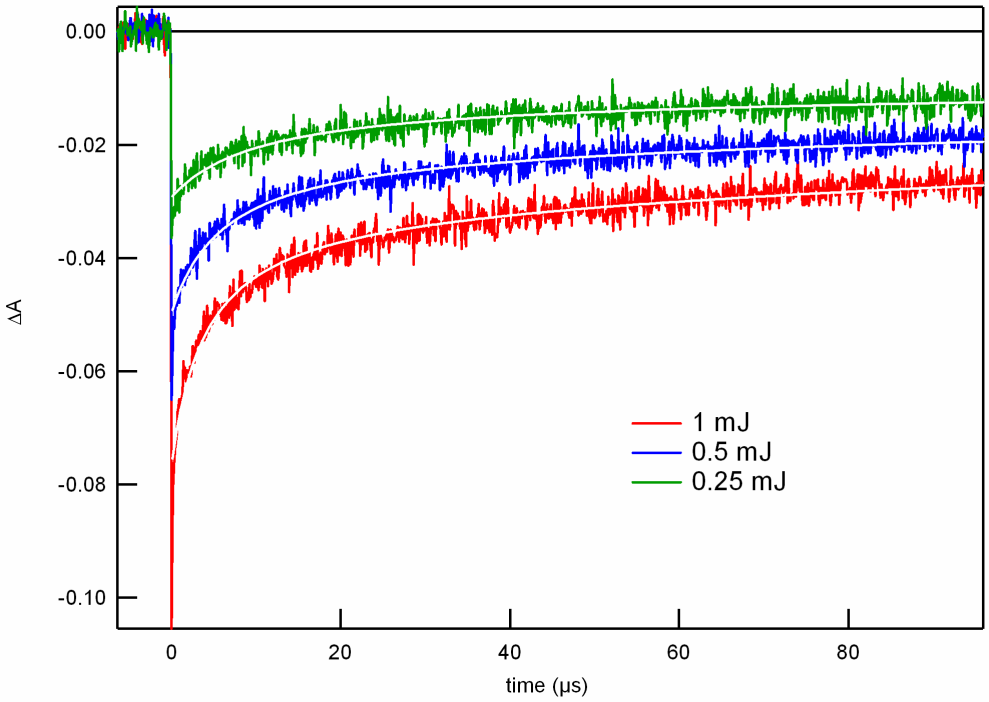

Figure 59. Power dependence of the transient absorption of a RuL''L_2^{2+} sensitized TiO_2 electrode. MLCT recovery for increasing excitation intensities; 1 mJ (red); 0.5 mJ (blue) and 0.25 mJ (green). Electrolyte concentrations were 0.50 M $LiClO_4$, 0.020 M pyridine and 0.020 M pyridinium triflate in acetonitrile. Solid lines are global fits to two second-order functions (Eq. 24) (λ_{ex} = 480 nm, λ_{obs} = 450 nm).

57).[88] Therefore, with signal only due to the Ru^{2+} bleach, we can convert the recombination rates using:

$$k_3 = \Delta\varepsilon d k'_3 \qquad (25)$$

where $\Delta\varepsilon$ is equal to the ground-state molar absorptivity, and d is the thickness of the TiO_2 film.[49]

By increasing the excitation power until the MLCT bleach signal is saturated, it is possible to compare the magnitude of the t_0 transient with the 450 nm ground-state absorption of the same slide. In all cases, the magnitude of the bleach was much smaller than the maximum possible. For the monocarboxylated dye, 20–25% of the available injecting molecules were sufficiently long-lived to be detected on the nanosecond timescale. For both of the other dyes, slightly fewer that inject were detected, 10–15%, presumably either because of lower injection quantum yields or higher geminate recombination yields. A similar comparison of the MLCT bleach magnitude for all the samples at the same (low) laser intensity showed a bleach 10 –20% of the maximum attainable for all dyes.

Regeneration

The regeneration of oxidized dye with iodide (0.295 V vs. SCE) can be measured in a manner similar to that for recombination, with the exception that the surrounding solution is changed to contain a known concentration of iodide. Figure **60** shows a comparison of the ground-state recovery of the $[Ru(bpy)_3]^{2+}$-type dyes adsorbed onto TiO_2 in the absence and the presence of iodide. It is clear that recovery of the ground state is much faster with iodide. The recovery is not a simple first-order process.

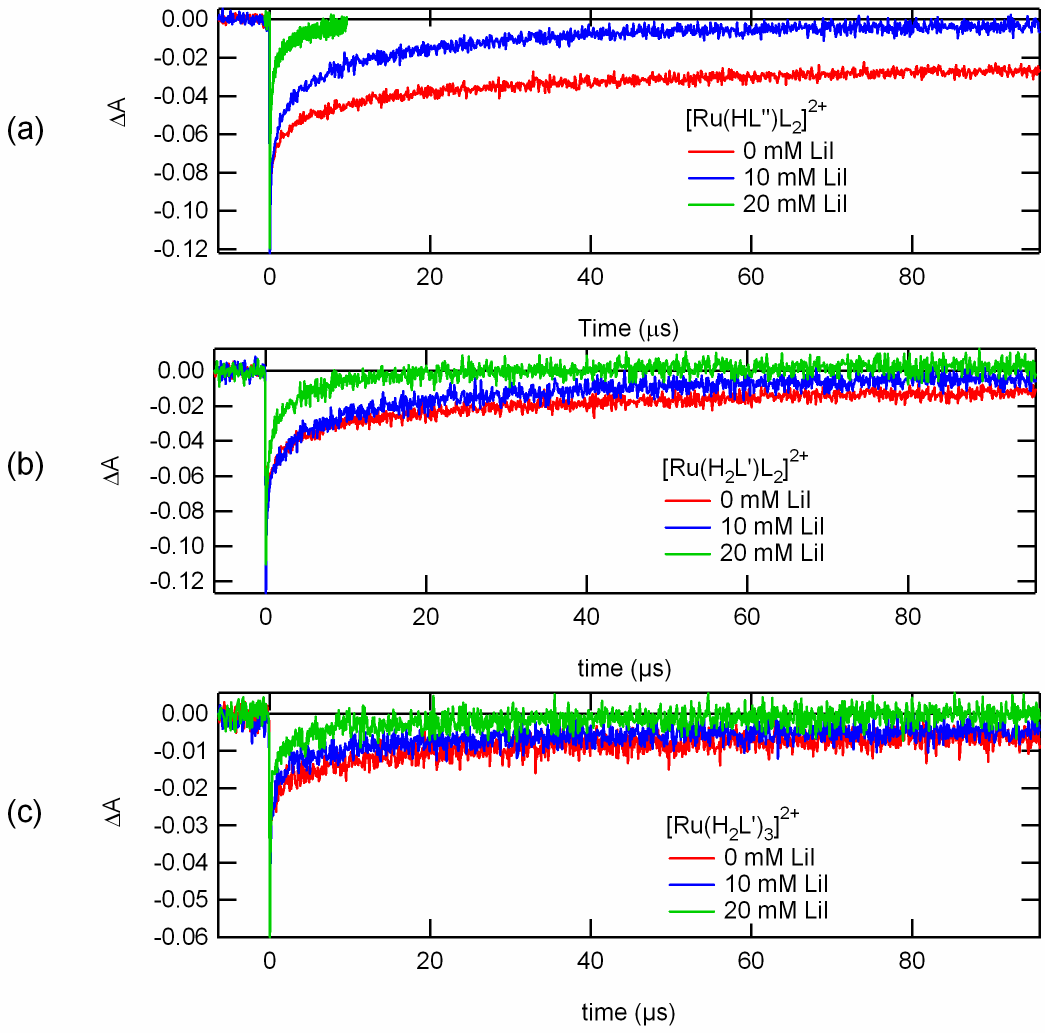

Figure 60. Transient absorption spectra of TiO_2 electrodes sensitized with $[Ru(bpy)_3]^{2+}$-type dyes. Electrolyte concentrations: 0.50 M $LiClO_4$, 0.020 M pyridine, and 0.020 M pyridinium triflate in acetonitrile (red); 0.49 M $LiClO_4$, 0.010 M LiI, 0.020 M pyridine, and 0.020 M pyridinium triflate in acetonitrile (blue); 0.48 M $LiClO_4$, 0.020 M LiI, 0.020 M pyridine, and 0.020 M pyridinium triflate in acetonitrile (green). λ_{ex} = 480 nm, λ_{ta} = 450 nm. (a) $[Ru(HL'')L_2]^{2+}$; (b) $[Ru(H_2L')L_2]^{2+}$; and (c) $[Ru(H_2L')_3]^{2+}$.

we can empirically characterize the recovery by fitting the data to a sum of three exponentials with deconvolution of the Gaussian response function. The fit parameters obtained when the solution contained 20 mM LiI are set out in Table **11**.

More precisely, the overall rate expression for recovery is a combination of recombination and regeneration rates. For the least ideal case, namely $[Ru(H_2L')_3]^{2+}$, where recombination is fastest and regeneration slowest, it is likely that the recovery is a combination of both processes, and as such, the regeneration rate constants are uncertain. For $[Ru(HL'')L_2]^{2+}$, where regeneration is the fastest and recombination is the slowest, it is more reasonable to disregard the recombination, meaning only regeneration is observed in the recovery. However, as the recovery signal for all three bound dyes goes back to zero much faster with iodide present, we believe that the major part of the recovery is due to regeneration.

Discussion

In solution, the excited-state lifetimes of the dyes were slightly different, where increasing the number of carboxyl groups on the bipyridine ligands resulted in increased lifetimes. The overall emission quenching yield of the TiO_2-bound dyes was greater than 97% and the quenching rate constants measured on the slow timescale were virtually identical within the series. Since dye emission on TiO_2 exhibits multi-exponential behavior, it is quite likely that more than one quenching mode is involved. This could be the result of heterogeneity in the samples, giving rise to several binding modes that can each injected electrons into TiO_2 on different timescales. Also, neither self-quenching

Table 11. Regeneration rate constants of $[Ru(bpy)_3]^{2+}$-type dyes adsorbed onto TiO_2.

Complex	Fit Parameters (s^{-1})[a]
$[Ru(HL'')L_2]^{2+}$	3×10^7 (0.55)
	2×10^6 (0.30)
	2×10^5 (0.15)
$[Ru(H_2L')L_2]^{2+}$	1×10^7 (0.60)
	1×10^6 (0.20)
	1×10^5 (0.20)
$[Ru(H_2L')_3]^{2+}$	0.9×10^7 (0.80)
	0.4×10^6 (0.15)
	0.3×10^5 (0.05)

a: On TiO_2 in acetonitrile containing 0.020 M LiI with 0.48 M $LiClO_4$, 20 mM pyridine and 20 mM pyridinium triflate. Fractions are given in parentheses (±0.05).

nor triplet annihilation can be ruled out as a possible mechanism, since the dyes are closely packed on the TiO_2.

It has been shown for other dyes that at least some fraction of the injection from both singlet and triplet excited states occurs on the femtosecond timescale,[18,19] and such ultrafast injection should also occur for these dyes. Although very rapid injection is of importance for overall solar cell efficiency, it may have a drawback in that there could be enhanced probability of fast geminate recombination from TiO_2 'hot-states'. Injection is believed to occur with almost unit quantum yield for the commonly used dye, $[Ru(H_2L')_2(SCN)_2]^0$.[89] Since the excited-state lifetimes are much longer for these three dyes than for $[Ru(H_2L')_2(SCN)_2]^0$, even the slower processes occur with a high quantum yield. However, the observed emission quenching may not be due solely to injection, as only ≈20% of oxidized dye is present after the 10 ns laser pulse in our transient absorption experiments. It is interesting that the quenching rates are so similar as the measured photocurrents, and consequently the cell efficiencies, varied significantly amongst the series. It is possible that the ultrafast injection is affected by differences in the binding mode, but that such a variance is not observable on this timescale. Direct measurement of the femtosecond transient absorption spectra of these dyes when adsorbed onto TiO_2 is currently underway via collaboration with the McCusker group at Michigan State University.

As all of the dyes appear to efficiently inject electrons in to TiO_2, it is possible that the decreased solar cell efficiencies are due to enhanced deleterious recombination processes. Recombination rates of electrons in TiO_2 with oxidized dye were determined

by analyzing the recovery of the Ru^{2+} ground state as a sum of two second-order rate expressions. There is approximately an order of magnitude difference in the largest rate constant and a factor of 5 variation in the smallest rate constant among the dyes, with the order being $[Ru(HL'')L_2]^{2+}<[Ru(H_2L')L_2]^{2+}<[Ru(H_2L')_3]^{2+}$ (Table **10**). This could indicate that the electronic coupling between the oxidized dye and TiO_2 is smallest for the weakest binding dye, $[Ru(HL'')L_2]^{2+}$. However, it might simply be an effect of the smaller driving force for recombination for this dye. The latter explanation correlates with the quenching results, as the detectable quenching is slightly faster for $[Ru(HL'')L_2]^{2+}$, and this dye has the largest driving force for injection (Table **7**, Table **10**).

All of the carboxyl modified $[Ru(bpy)_3]^{2+}$-type dyes were shown to be efficiently regenerated by iodide when adsorbed onto TiO_2. The observed lifetime for regeneration of these dyes were all on the order of $1/10^7$ s, which is comparable to the known lifetime for regeneration of $[Ru(H_2L')_2(NCS)_2]^0$ sensitized TiO_2 systems. The regeneration of the bound dyes was slightly slower as the number of carboxylic acid groups increased, with the slowest rate found for the hexacarboxylated dye. It is possible that the effect of increasing the number of these electron withdrawing groups not only affects the metal center, but also modulates the interaction of the negatively charged species that must collide with the oxidized dye for regeneration.

As was the case for the injection and recombination experiments, the regeneration data suggested heterogeneity. It is reasonable to assume that there is a wide distribution of environments and binding sites which result in the observed heterogeneities. Based on

the idea of a surface-mediated regeneration mechanism, it is not surprising that the surface heterogeneity affects regeneration.

Overall, the dye regeneration rates were similar, with a variance of only a factor of 2 or 3 from dye to dye. However, the relative order is opposite to that for recombination, with the fastest regeneration rate observed for $[Ru(HL'')L_2]^{2+}$. It is clear that a diminished regeneration rate cannot be used to explain the decreased solar cell efficiency for the monocarboxylated dye that was discussed in the previous chapter. Furthermore, for all three dyes, regeneration is quite rapid and competes effectively for recombination of the injected electrons.

Conclusions

The extent of quenching, and consequently injection, appears to be independent of the mode of binding as the excited states of all three dyes are more than 97% quenched on the ns timescale upon binding to TiO_2. The recombination rate of injected electrons with the oxidized dye was slightly decreased for the monocarboxylated dye, $[Ru(HL'')L_2]^{2+}$. This is likely a result of the decreased coupling resulting from the more labile binding mode (1C) for this dye. The dyes are rapidly reduced and regeneration competes effectively with recombination. Furthermore, the regeneration rates are quite similar for all of the dyes, with $[Ru(HL'')L_2]^{2+}$ having the fastest regeneration rates. As such, the measured kinetics do not satisfactorily explain the low efficiency observed for the mono- and dicarboxylated dyes ($[Ru(HL'')L_2]^{2+}$ and $[Ru(H_2L')L_2]^{2+}$, respectively) when compared to the hexacarboxylated dye ($[Ru(H_2L')_3]^{2+}$) (Table **8**). In fact, the dye that showed the best overall kinetics with the fastest quenching, the slowest deleterious

recombination reaction, and the fastest regeneration was $[Ru(HL'')L_2]^{2+}$, which also had the lowest solar energy conversion efficiency. It is possible that the decreased efficiency is the result of variance in the ultrafast injection that could not be measured on this timescale. Through a collaboration with Dr. McCusker at Michigan State University, we are measuring the ultrafast transient kinetics of injection for these dyes. If the ultrafast injection rates are similar for these three dyes, it will be clear that the current kinetics model cannot accurately describe the dynamics of DSSCs, suggesting that there are other possible quenching mechanisms or electron-transfer processes which are crucial to the solar cell performance.

CHAPTER 8:

REGENERATION RATES IN SOLUTION

Chapter 8

REGENERATION RATES IN SOLUTION

Introduction

A persistent theme throughout this thesis is the goal of developing an understanding of the mechanism of the I_3^-/I^- redox couple in functional DSSCs. The mechanism by which this redox couple reduces the oxidized dye is currently still under debate. This two-electron couple is composed of an array of possible one-electron reactions that can in principle take place. Chapter 3 includes an in-depth discussion of the possible pathways through which the oxidized dye is reduced by this complex couple. While a step-by-step mechanism is not fully developed, it is clear that the various one-electron reactions that take place are key to controlling the regeneration rates, and it is quite likely that one or more surface adsorbed species participate in the regeneration process.

In this chapter, the regeneration rates of a series of ruthenium bipyridine based dyes were investigated in solution. These five dyes can be collectively referred to as $[Ru(bpy)_3]^{2+}$-type dyes. Three of the dyes that varied in the number of carboxylic acid groups have been previously studied when bound to TiO_2, $[Ru(HL'')L_2]^{2+}$, $[Ru(H_2L')L_2]^{2+}$ and $[Ru(H_2L')L_3]^{2+}$. Two other dyes, $[RuL_3]^{2+}$, with unmodified bipyridyl ligands and $[RuM_3]^{2+}$, with methyl groups instead of carboxy groups in the 4,4' positions on the bipyridine ligand were included in the solution regeneration study (Figure **61**). A more detailed understanding of the regeneration mechanism of these dyes

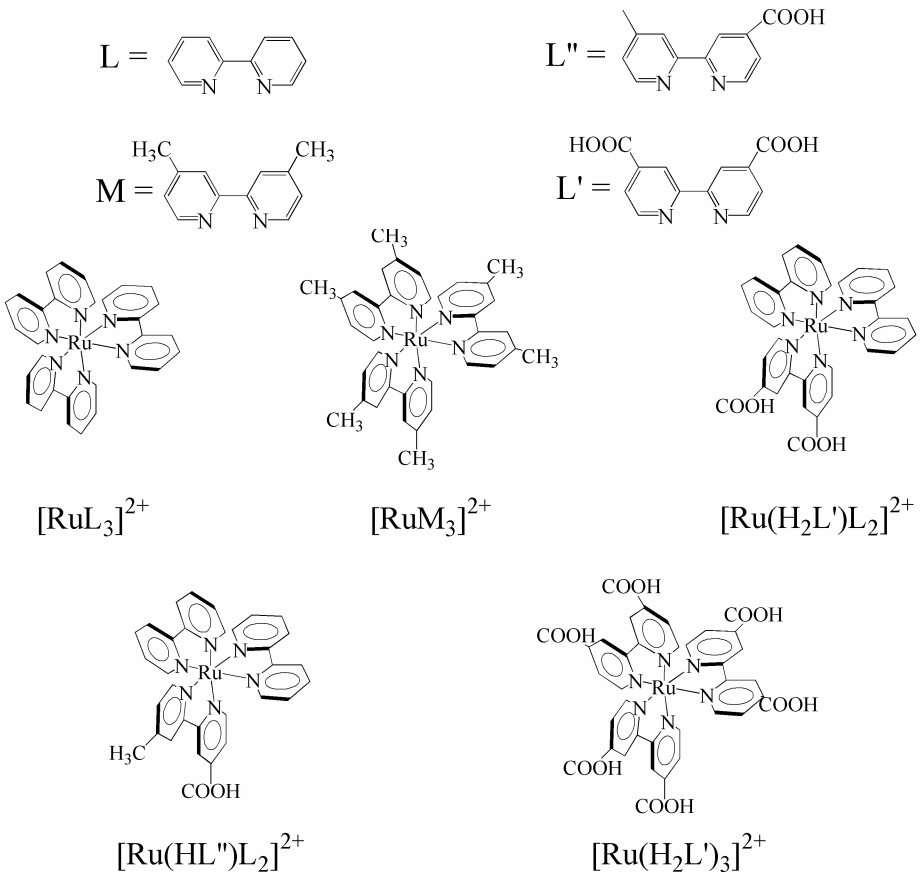

Figure 61. Structures of the fully protonated ligands, HL′′, H_2L', and the ligands L and M, and of the fully protonated complexes, $[Ru(HL'')L_2]^{2+}$, $[Ru(H_2L')L_2]^{2+}$, $[Ru(H_2L')_3]^{2+}$, $[RuL_3]^{2+}$, and $[RuM_3]^{2+}$. The protonation states depicted are for the dyes in powder form; the actual dye protonation states are dependent on solvent conditions.

by iodide in the absence of any surface effects and as a function of the electronic nature of the pendant ligands may ultimately lead to a better understanding of the role of iodide in functional DSSCs.

Experimental

Materials

17.8 MΩ cm resistance water was obtained from a Barnstead NANOpure filtration system. Ethanol (Aapor) was used as received. Acetonitrile (MeCN) (Merck) was freshly distilled over CaH_2 prior to use. Lithium iodide (Aldrich) and anhydrous lithium perchlorate (J. T. Baker) were stored under nitrogen. The syntheses of all complexes have been described previously.[30,74] Methyl viologen (MV^{2+}) dichloride (Aldrich) was converted to the PF_6^- salt by mixing $MVCl_2$(aq) and NH_4PF_6(aq). The precipitate ($MV(PF_6)_2$) was washed with ether and dried under vacuum before use. KPF_6 (Aldrich) was dissolved in MeCN, filtered and the solvent evaporated to give dry KPF_6 prior to use. $HClO_4$ and PbO_2 were purchased from Aldrich and used as received.

Spectroscopy

Steady-state absorption spectra were measured using a diode array Agilent 8453 UV-vis spectrometer. Nanosecond transient absorption and emission were measured using a setup described previously.[49] All samples were degassed through 3 freeze-pump-thaw cycles, and back filled with N_2(g). Measurements were done in atmosphere controlled 1 cm path length quartz cuvettes using dry acetonitrile as the solvent. The excitation energy (λ_{ex} = 480 nm) was 1 mJ for a ~1 cm^2 beam, unless otherwise stated. A

broad beam was necessary to ensure uniform excitation of the samples. Transient absorption was measured at λ_{obs} = 450 nm and emission at λ_{em} = 630 nm.

Results and Discussion

The synthesis and characterization of the modified $[Ru(bpy)_3]^{2+}$-type dyes has been previously reported.[73] Table **12** is a compilation of the spectroscopic and electrochemical properties of the dyes. The reduction potential of the dyes becomes more positive as the number of carboxyl groups is increased. This is consistent with the electron donating character of the carboxyls. All of the dyes have similar absorptions in the visible, with the MLCT of the dyes varying less than 20 nm. The emission shifts to lower energy as the number of pendant carboxyl groups is increased. The emission lifetimes are similar for all dyes, with the exception of $[Ru(H_2L')_3]^{2+}$, which has a lifetime twice as long as the other dyes.

In the absence of injection into TiO_2, MLCT excitation results in an excited state that decays back to the ground state. The oxidized form of the dyes (Ru^{3+}) can be generated by the flash-quench method (Figure **11**a). Excitation of the MLCT results in the formation of an excited state that is subsequently oxidatively quenched by MV^{2+} (Figure **62**). The bimolecular quenching rate constant (k_q) of the excited state by MV^{2+} can be found by comparing either emission intensity (I) or emission lifetime (τ) of the dye in absence (subscript 0) and presence (no subscript) of MV^{2+} using the Stern-Volmer equation where [Q] is the quencher concentration:

$$\frac{I_0}{I} = \frac{\tau_0}{\tau} = 1 + k_q \tau_0 [Q] \qquad (26)$$

Table 12. Spectroscopic and electrochemical parameters for $[Ru(bpy)_3]^{2+}$-type dyes.

	$(\lambda_{max}^{abs})^a$ (nm)	$(\lambda_{max}^{ems})^a$ (nm)	τ^{ems} (μs)	$\mathbf{E}_{00}$ (eV)	$E^{o'}$ (V vs. SCE)	$E^{o'*}$ (V vs. SCE)
$[RuL_3]^{2+}$	455	622	0.93	2.19	1.24	-0.95[b]
$[RuM_3]^{2+}$	460	635	0.88	2.16	1.14	-1.02[b]
$[Ru(HL'')L_2]^{2+}$	455	674	0.97	2.11	1.19	-0.92[c]
$[Ru(H_2L')L_2]^{2+}$	480	693	0.74	1.98	1.26	-0.72[c]
$[Ru(H_2L')_3]^{2+}$	470	643	2.0	2.11	1.44	-0.67[c]

a: In degassed acetonitrile with ~100 mM KPF_6 and 1 mM pyridine and 1 mM pyridinium triflate.

b: In acetonitrile from Elliott *et al*.[90]

c: In ethanol from Kilså *et al*.[47]

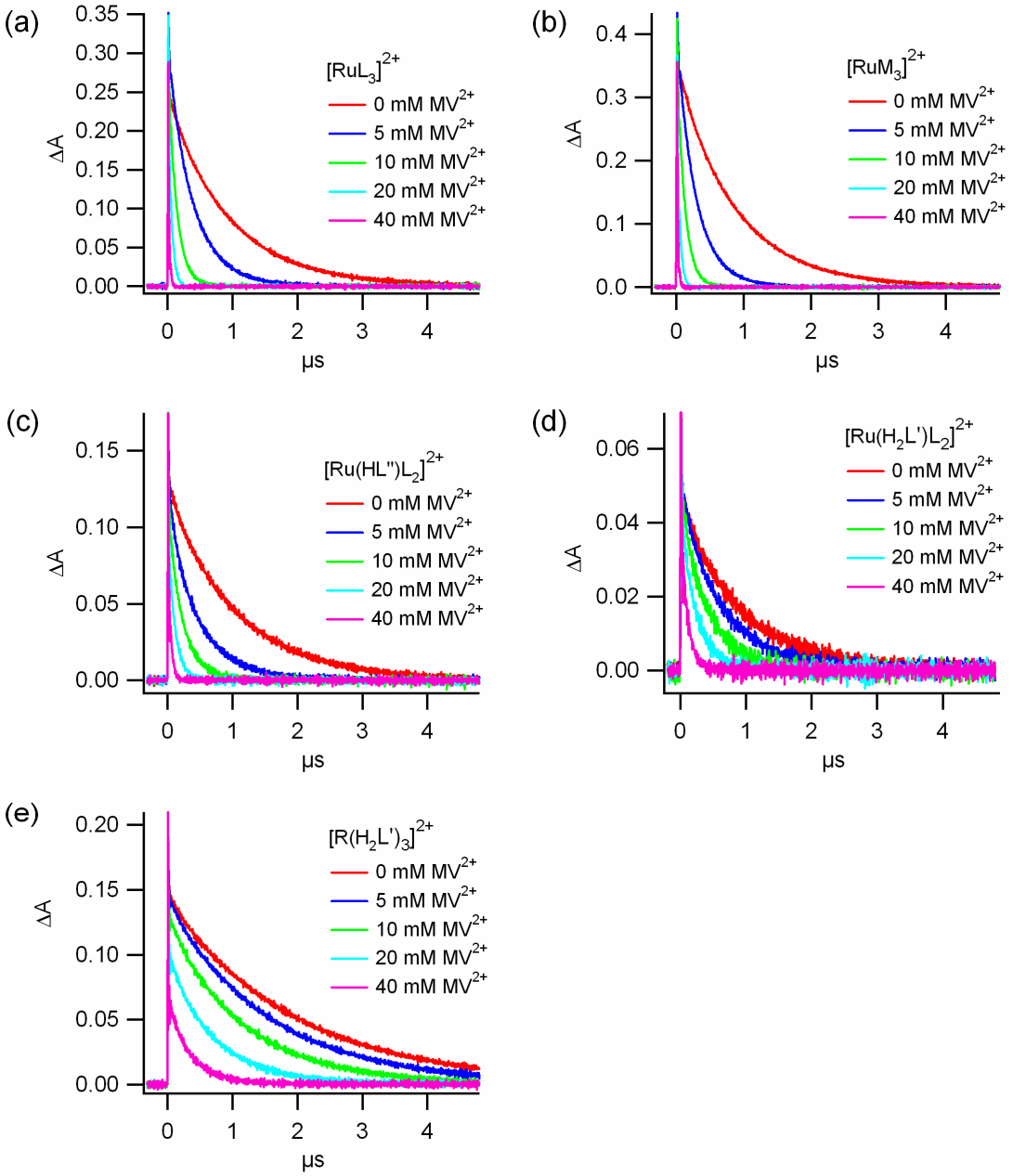

Figure 62. Emission quenching of $[Ru(bpy)_3]^{2+}$-type dyes in solution by MV^{2+}. Time-resolved emission (λ_{ex} = 480 nm, λ_{em} = 630 nm) of $[Ru(bpy)_3]^{2+}$-type dyes in degassed acetonitrile with increasing concentration of MV^{2+} (a) $[RuL_3]^{2+}$; (b) $[RuM_3]^{2+}$; (c) $[Ru(HL'')L_2]^{2+}$; (d) $[Ru(H_2L')L_2]^{2+}$; (e) $[Ru(H_2L')_3]^{2+}$.

For all dyes I_0/I or τ_0/τ generated a straight line as a function of MV^{2+} concentration (Figure **63**). The quenching rates were essentially the same for both static and dynamic measurements, indicating a purely dynamic quenching process (Table **13**). The slope, and thereby, the quenching rate constant were highly dependent on the dye structure (Table **13**), with the quenching rate constant decreasing with increasing number of pendant carboxylic acids.

Upon excitation, there is a bleach in the MLCT corresponding to excited-state formation, which naturally decays to the Ru^{2+} ground state (Figure **64**). Upon addition of MV^{2+}, the excited state is oxidatively quenched to Ru^{3+}, which is very long lived (Figure **64**). The kinetics of this long-lived excited state were difficult to fit and attempts to measure the recovery rate in the presence of the reduced MV^{+} were inconclusive. An alternative approach was used to measure the relative stabilities of the oxidized dyes. As discussed in Chapter 7, the M^{3+} form of the $[Ru(bpy)_3]^{2+}$-type dyes can be generated by oxidation with PbO_2 in acidic solution. The spectra of oxidized $[Ru(HL'')L_2]^{2+}$, $[Ru(H_2L')L_2]^{2+}$ and $[Ru(H_2L')_3]^{2+}$ (Chapter 7, Figure **56**) can be compared with those of the non-carboxylated dyes (Figure **65**). By measuring the absorption spectra of these dyes immediately after oxidation by PbO_2 and as a function of time, the relative kinetics for reduction of Ru^{3+} in the absence of any electron donors (such as the reduced form of MV^{2+}, MV^{+} radical) can be determined. The natural reduction kinetics for these five dyes are shown in Figure **66**. The dyes were monitored for the appearance of the Ru^{2+} π-π^* (Figure **66**, red) at 308 nm for $[Ru(H_2L')_3]^{2+}$ and 288 nm for the other dyes. The

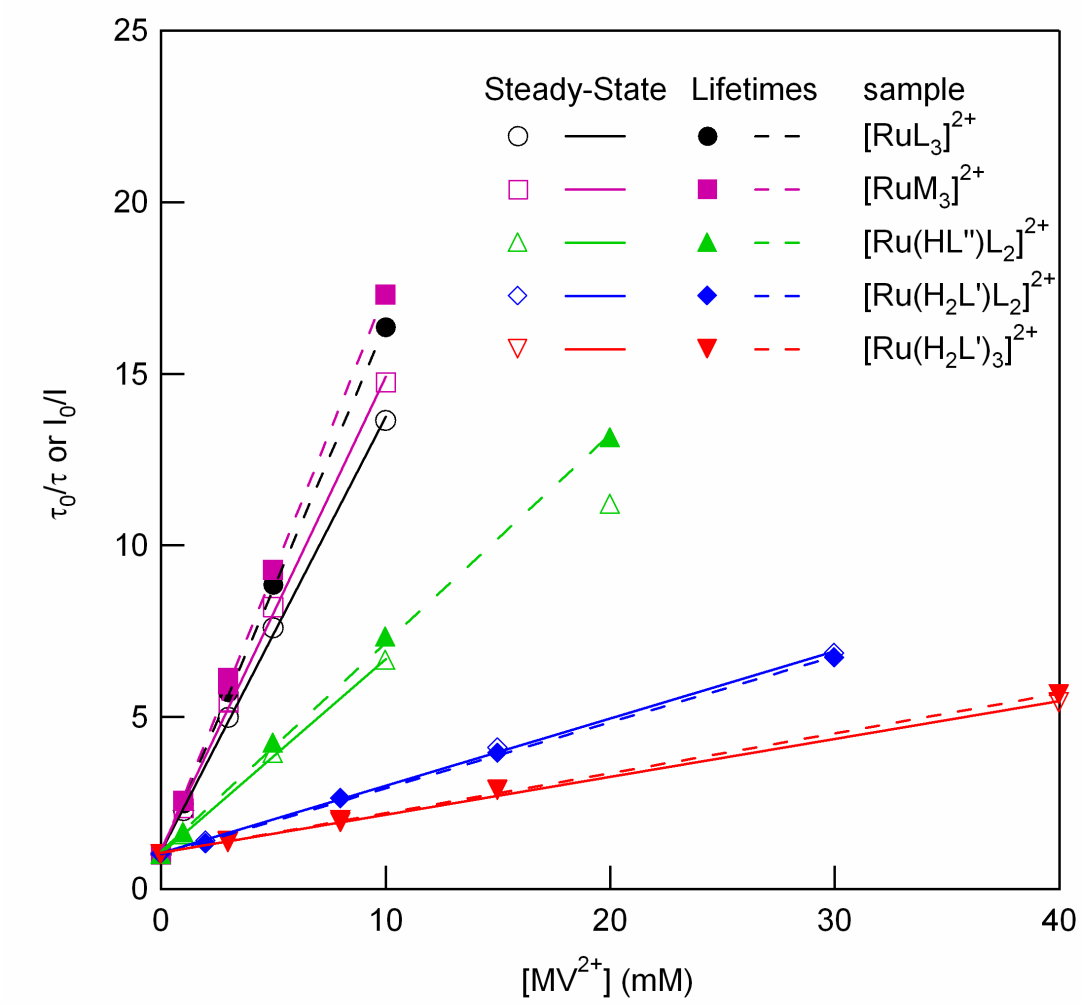

Figure 63. Stern-Volmer plots of emission quenching of the $[Ru(bpy)_3]^{2+}$dyes by MV^{2+} in solution. Determined from fluorescence measurements (solid lines) and lifetime measurements (dashed). $[RuL_3]^{2+}$ black; $[RuM_3]^{2+}$ purple; $[Ru(HL'')L_2]^{2+}$ green; $[Ru(H_2L')L_2]^{2+}$ blue; $[Ru(H_2L')_3]^{2+}$ red.

Table 13. Quenching rate constants for the $[Ru(bpy)_3]^{2+}$-type dyes in solution with MV^{2+}.

	Static k_q (M^{-1} s^{-1})[a]	Dynamic k_q (M^{-1} s^{-1})[b]
$[RuL_3]^{2+}$	1.4×10^9	1.7×10^9
$[RuM_3]^{2+}$	1.6×10^9	1.9×10^9
$[Ru(HL'')L_2]^{2+}$	5.9×10^8	6.3×10^8
$[Ru(H_2L')L_2]^{2+}$	2.6×10^8	2.6×10^8
$[Ru(H_2L')_3]^{2+}$	5.6×10^7	5.8×10^7

a: Rate constant for quenching of Ru^{2+*} with MV^{2+} determined from static measurements of the fluorescence intensity.

b: Rate constant for quenching of Ru^{2+*} with MV^{2+} determined from dynamic measurements of the lifetimes.

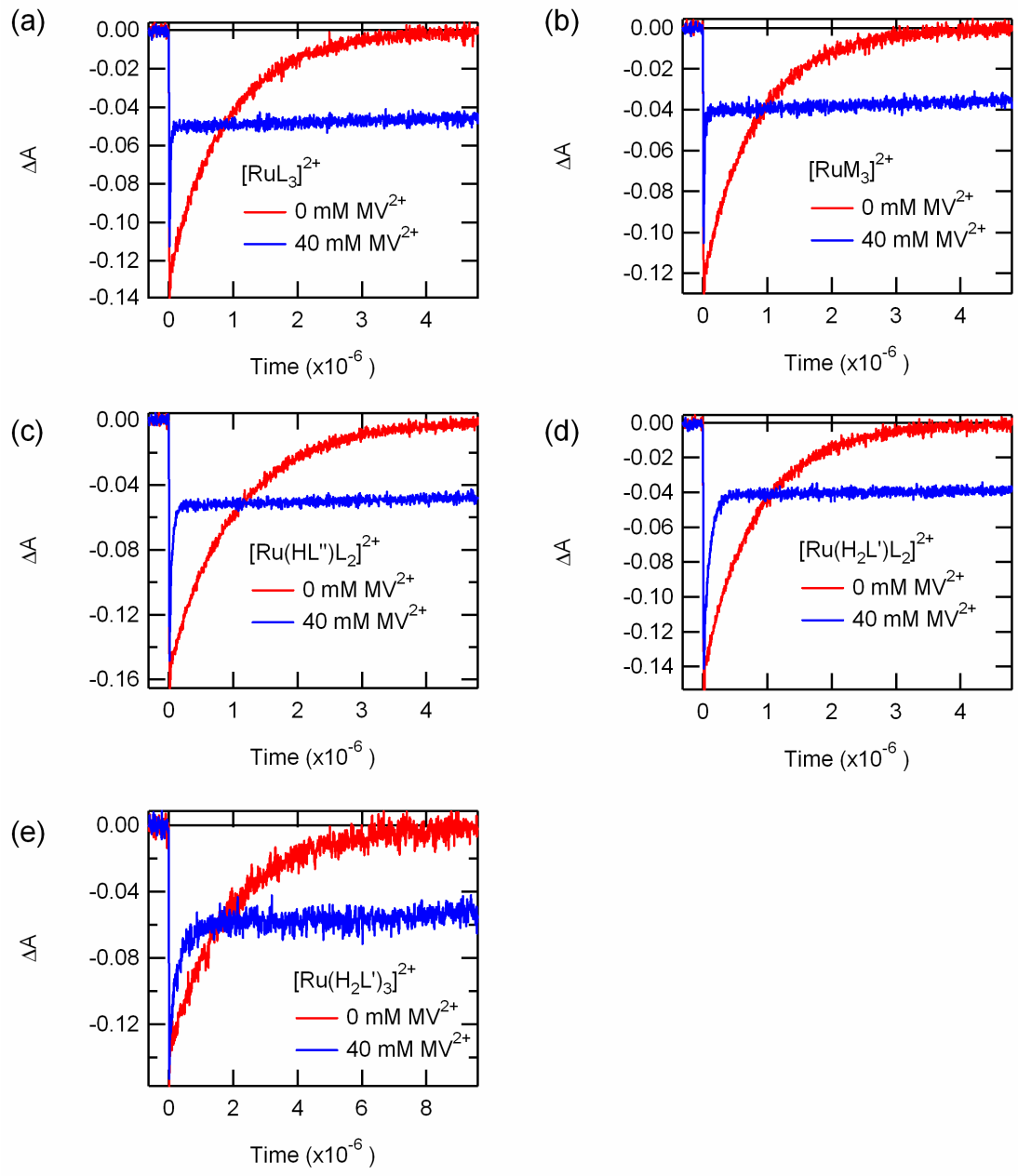

Figure 64. Transient absorption spectra for $[Ru(bpy)_3]^{2+}$-type dyes with MV^{2+}. MLCT recovery of the ground state (λ_{ex}=480) in the absence (red) and presence (blue) of 40 mM MV^{2+}.

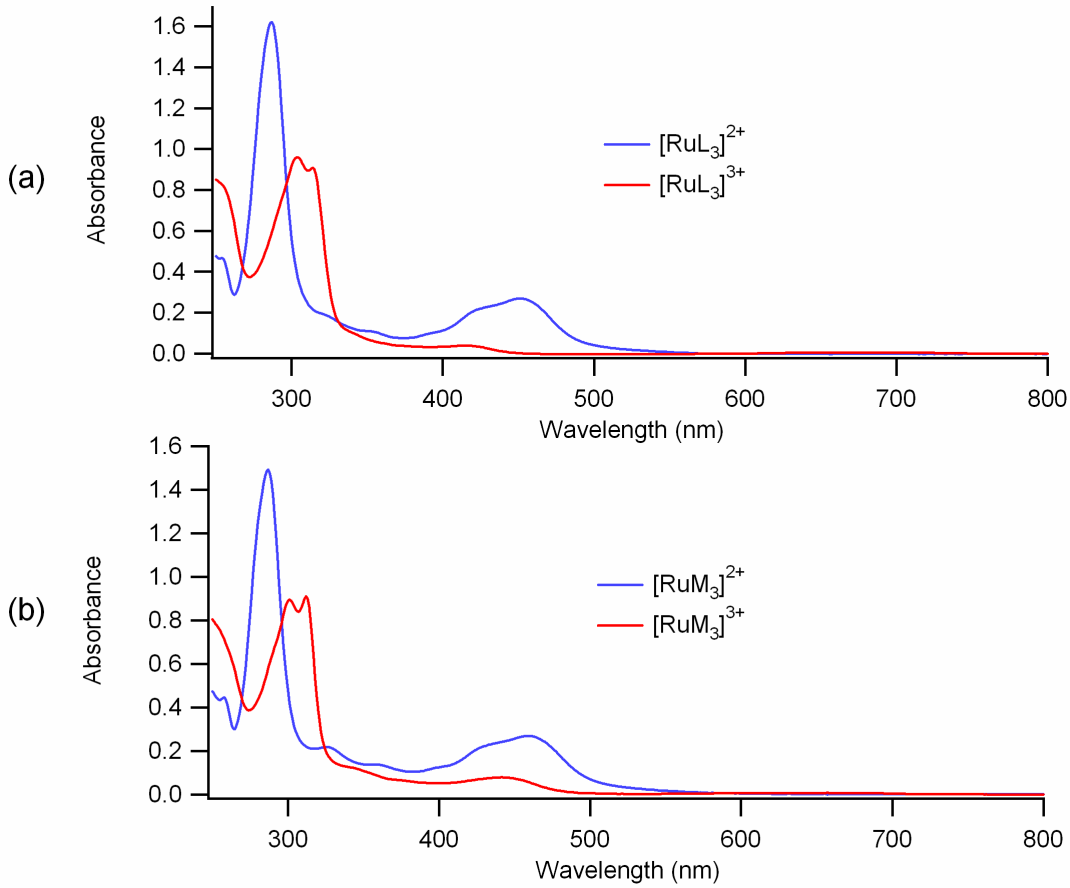

Figure 65. Absorption spectra of oxidized non-carboxylated $[Ru(bpy)_3]^{2+}$-type dyes. Oxidized (red) and ground state (blue) of the dyes in ethanol for (a) $[RuL_3]^x$, (b) $[RuM_3]^x$.

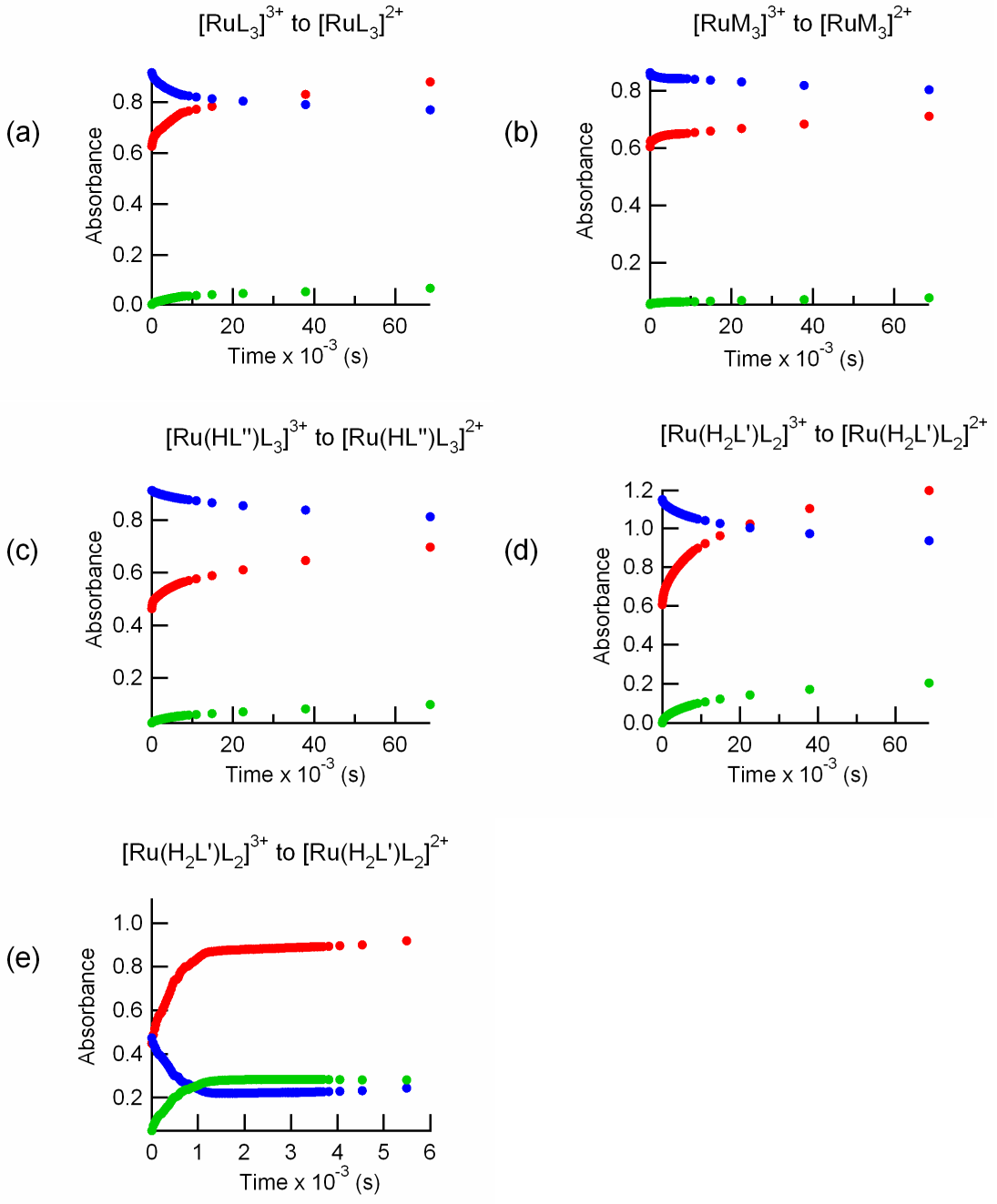

Figure 66. Kinetics of reduction of Ru^{3+} to Ru^{2+} for the $[Ru(bpy)_3]^{2+}$-type dyes. The absorbance of the π- π^* band for the oxidized and reduced forms (~300 nm, blue and red)

and ground-state MLCT band (~450 nm). See text for the specific wavelength values for each dye.

bleach of Ru^{3+} π- π^* (Figure **66**, blue) was monitored at 334 nm for $[Ru(H_2L')_3]^{2+}$ and 314 nm for the remaining dyes. All dyes were monitored for the recovery of the ground state (Ru^{2+}) at the MLCT maximum (Table **12**) of the corresponding sensitizer (Figure **66**, green). Clearly, the addition of electron withdrawing groups significantly decreases the stability of the oxidized form of the dye.

To ensure the maximum concentration of Ru^{3+}, 40 mM MV^{2+} quencher was used for all dyes. Addition of LiI to the oxidized dyes significantly accelerates the recovery. The conversion of Ru^{3+} to Ru^{2+} can be measured as a function of halide concentration, and assuming pseudo-first-order conditions, a bimolecular rate constant can be determined. Figures **67–71** show the transient kinetics and pseudo-first-order rate constant plots for the series of dyes. The regeneration rate constant is slightly dependent on the number and electron withdrawing nature of the pendant groups on the bipyridine ligands, with the regeneration rate being the fastest, $1.33x10^{10}$ $M^{-1}s^{-1}$, for the unsubstituted $[RuL_3]^{2+}$ and the slowest, $9.28x10^{9}$ $M^{-1}s^{-1}$, for the hexacarboxylated $[Ru(H_2L')_3]^{2+}$ though regeneration is very rapid for all dyes and approaches the diffusion controlled limit. For the same concentration of LiI, there was no difference in the regeneration rate as function of the relative concentration of oxidized dye as controlled by the relative concentration of MV^{2+} (Figure **72**). This indicates that the quenching kinetics are first order in Ru^{3+}.

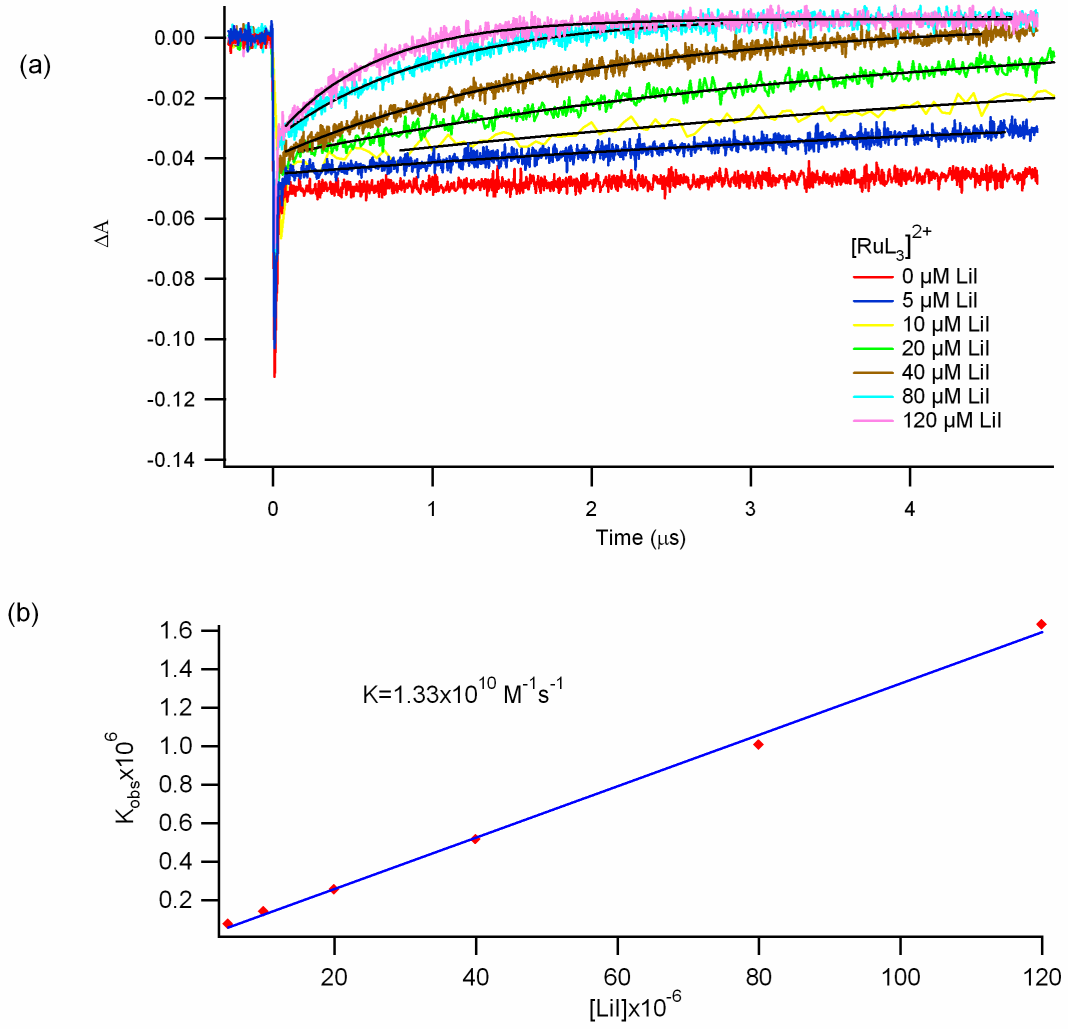

Figure 67. Pseudo-first-order regeneration kinetics for $[RuL_3]^{2+}$ in solution. (a) Kinetics of regeneration of $[RuL_3]^{2+}$ in solution with 40 mM MV^{2+} (b) Pseudo-first-order rate plot.

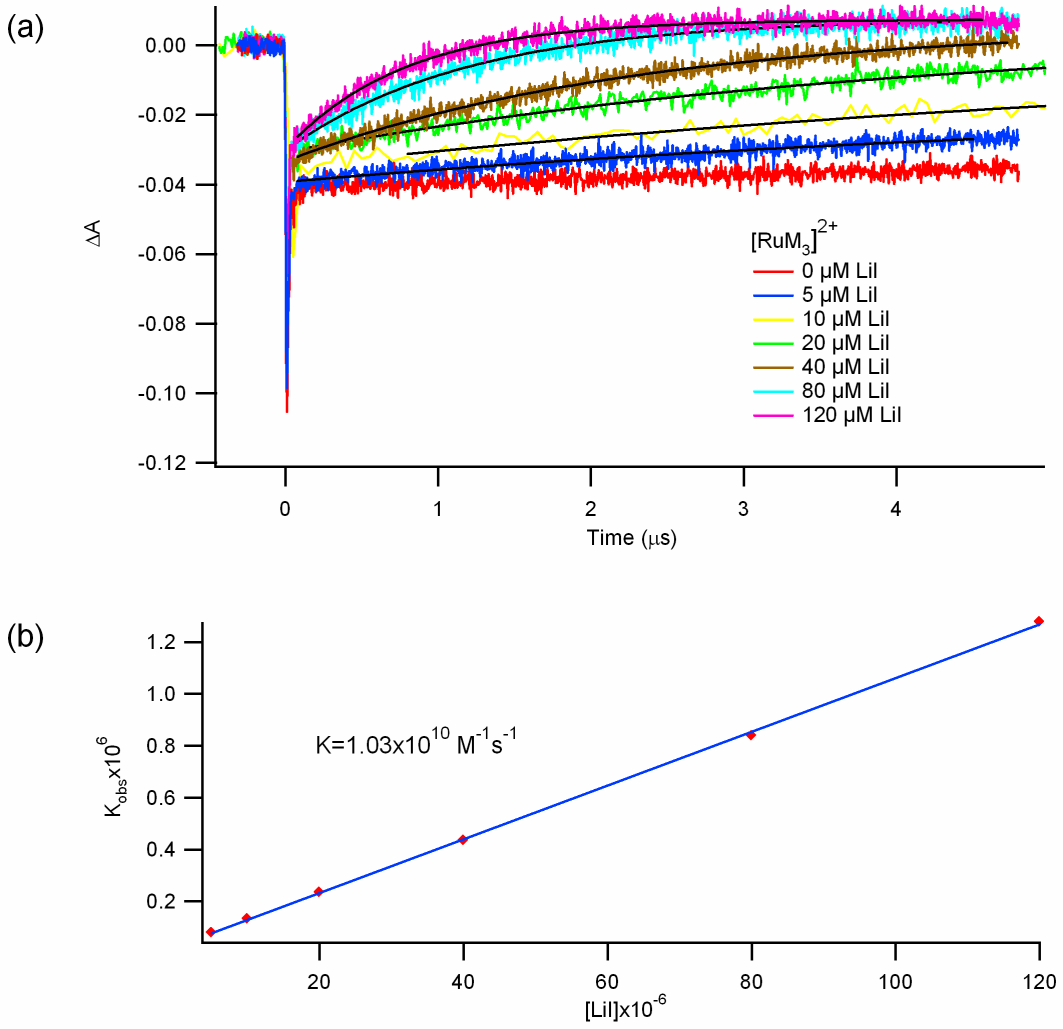

Figure 68. Pseudo-first-order regeneration kinetics for $[RuM_3]^{2+}$ in solution. (a) Kinetics of regeneration of $[RuM_3]^{2+}$ in solution with 40 mM MV^{2+} (b) Pseudo-first-order rate plot.

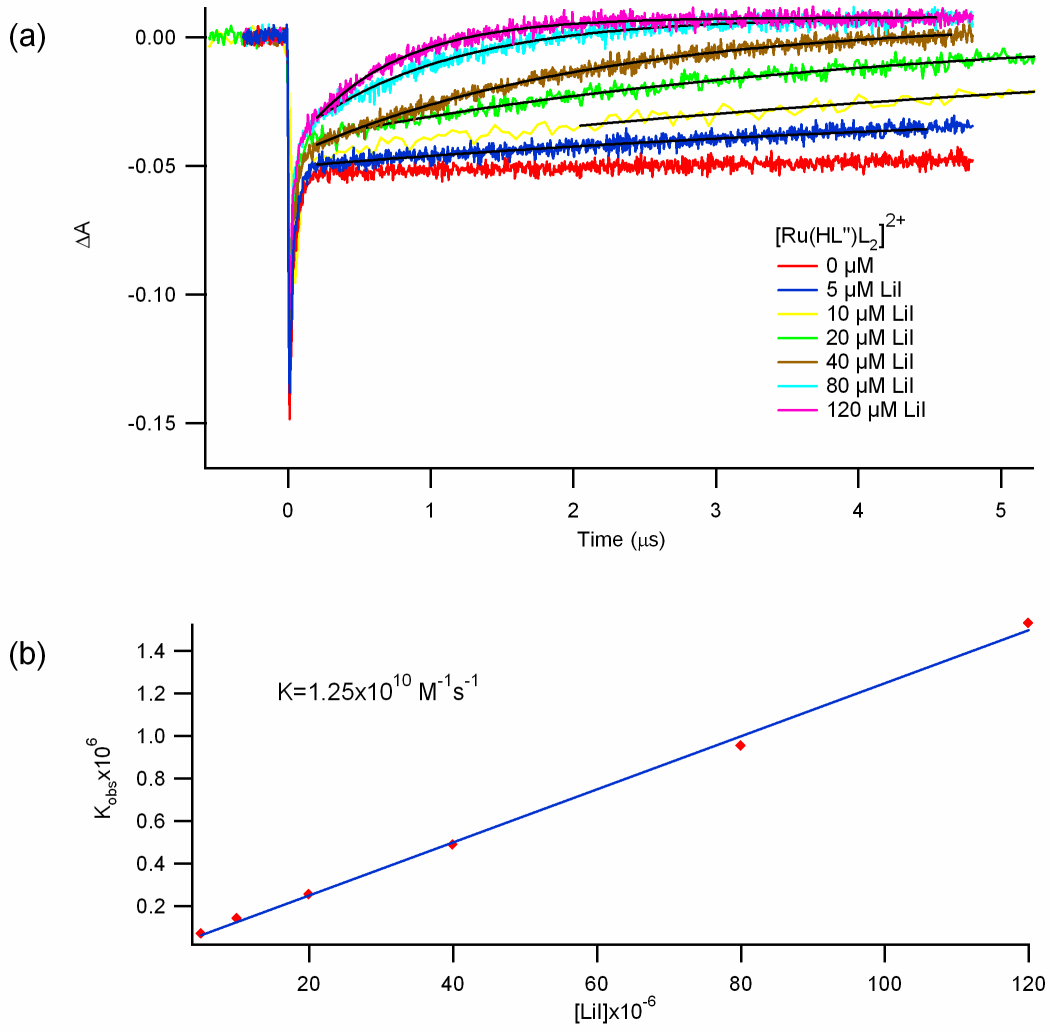

Figure 69. Pseudo-first-order regeneration kinetics for $[Ru(HL'')L_2]^{2+}$ in solution. (a) Kinetics of regeneration of $[Ru(HL'')L_2]^{2+}$ in solution with 40 mM MV^{2+} (b) Pseudo-first-order rate plot.

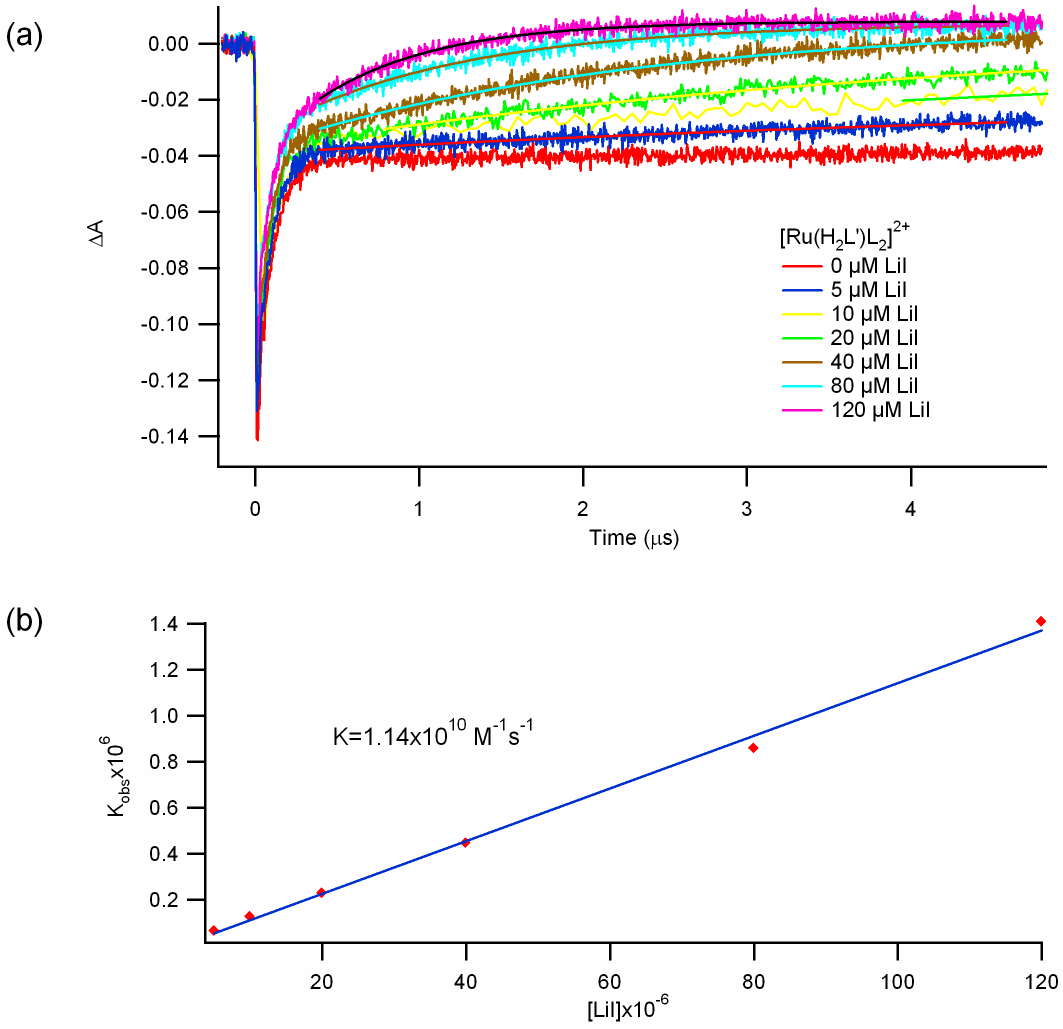

Figure 70. Pseudo-first-order regeneration kinetics for $[Ru(H_2L')L_2]^{2+}$ in solution. (a) Kinetics of regeneration of $[Ru(H_2L')L_2]^{2+}$ in solution with 40 mM MV^{2+} (b) Pseudo-first-order rate plot.

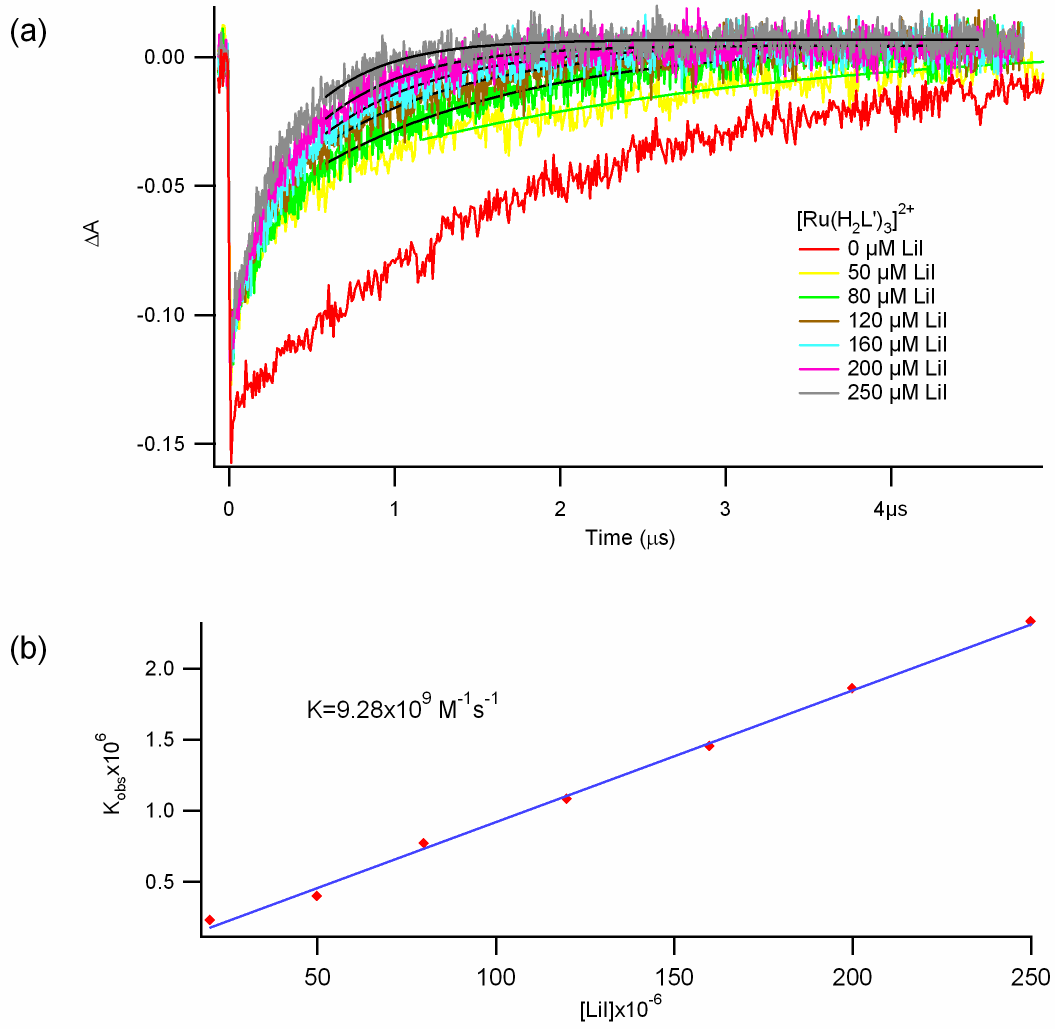

Figure 71. Pseudo-first-order regeneration kinetics for $[Ru(H_2L')_3]^{2+}$ in solution. (a) Kinetics of regeneration of $[Ru(H_2L')_3]^{2+}$ in solution with 40 mM MV^{2+} (b) Pseudo-first-order rate plot.

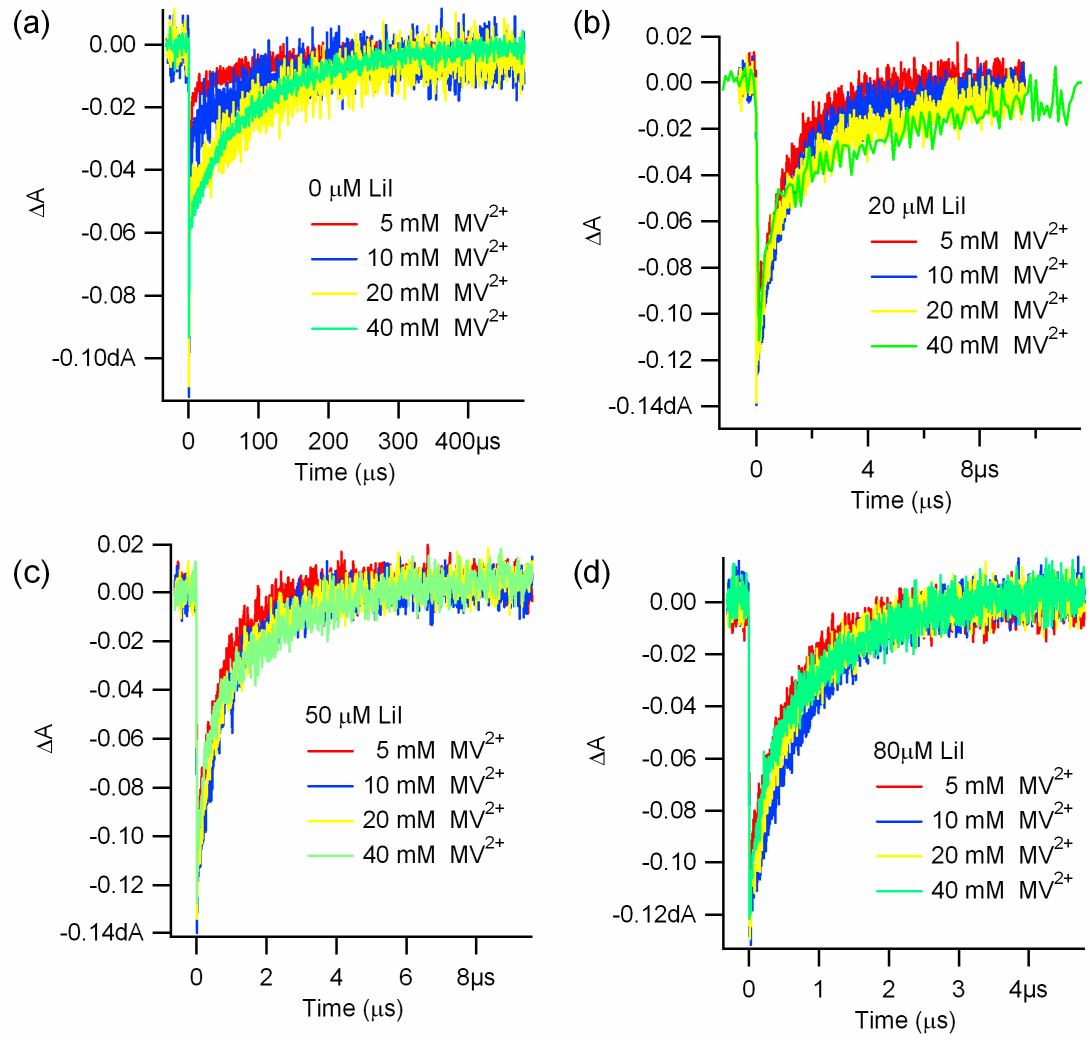

Figure 72. Transient absorption spectra of the $[Ru(bpy)_3]^{2+}$-type dyes in solution with LiI: first order in Ru^{3+}. MLCT recovery at varying concentrations of Ru^{3+} with (a) 0 μM LiI (b) 20 μM LiI (c) 50 μM LiI (d) 80 μM LiI.

Conclusions

In solution, the regeneration rates for the oxidized $[Ru(bpy)_3]^{2+}$-type dyes were diffusion controlled, on the order of 10^{10} M^{-1} s^{-1} for $[RuL_3]^{2+}$. The regeneration rate was slightly dependent on the number and electron-withdrawing nature of the pendant groups, with the rate decreasing with increasing number of electron-withdrawing substituents. Furthermore, these studies showed that regeneration was first order in oxidized dye concentration. The addition of electron-withdrawing groups on the bipyridine ligands affected not only the regeneration rates, but the quenching rates of the excited state by MV^{2+} and the relative stability of the oxidized dye.

CHAPTER 9:

PHOSPHONIC ACIDS AS ANCHORING GROUPS

Chapter 9

PHOSPHONIC ACIDS AS ANCHORING GROUPS

Introduction

We have extensively studied the effect of the number of available carboxylic acid anchoring groups (Chapters 6, 7 and 8), and the subsequent binding modes, on the kinetics and photoelectrode performance of DSSCs. These studies showed that the anchoring group is an important parameter to consider in the design of efficient sensitizers as it affects both the stability of the linkage and the life span and efficiency of the cell. Furthermore, the anchoring group dominates the electronic coupling between the dye and the semiconductor.[91,92] It is also likely that the electronic properties of the anchoring group will affect the absorption properties of the resultant dye.

An alternative anchoring group is the phosphonic acid functionality, which forms very stable bonds with hard Lewis acid metals such as Ti(IV).[93,94] The utilization of phosphonic acid anchoring groups in DSSCs has been reported previously.[95-98] In binding to the surface, the method of anchoring is expected to involve both the coordination of the phosphoryl oxygen to Lewis acid sites and the condensation of P-OH groups with surface hydroxyl groups, Ti-OH.[99]

Of particular interest is the fact that these anchoring groups will introduce a new binding mode, tridentate, not available in the carboxylic acid modified $[Ru(bpy)_3]^{2+}$-type dyes. In theory, all three oxygens of the phosphonic acid group can coordinate to the

titanium surface and up to three titanium atoms may be involved in the anchoring of the phosphonic acids to the surface.

This chapter reports the synthesis of two $[Ru(bpy)_3]^{2+}$-type dyes that vary only in the number of phosphonic acid anchoring groups. In particular, a mono and a diphosphonated $[Ru(bpy)_3]^{2+}$-type dye have been synthesized and characterized (Figure **73**).

Materials

Water (17.7 MΩ cm resistivity) was obtained from a Barnstead NANOpure Inc. filtration system. Carbon tetrachloride (anhydrous, 99.5%) was purchased from Aldrich and used as received. All solvents were reagent grade and were purchased from EM Science. Sodium bicarbonate ($NaHCO_3$, Mallinckrodt), 4-4'-dimethyl-2,2'-bipyridine (Alfa Aesar) and cis-ruthenium bis-bipyridine dichloride hydrate (cis-$[Ru(bpy)_2Cl_2]\cdot 2H_2O$, Strem) were used as received. Ferrous ammonium sulfate ($Fe(NH_4)_2(SO_4)_2\cdot 6H_2O$) and hexafluorophosphoric acid (60 wt %) were purchased from Aldrich and used as received. N-bromosuccinimide (NBS) (99%) and Azobis-butyronitrile (AIBN) was purchased from Aldrich and were purified as follows. NBS was recrystallized from H_2O and stored under argon in the dark at -10ºC. AIBN was precipitated from a saturated chloroform solution by addition of petroleum ether and stored under vacuum in the dark at -10ºC. Triethylphosphite (Aldrich) was distilled prior to use and stored under nitrogen.

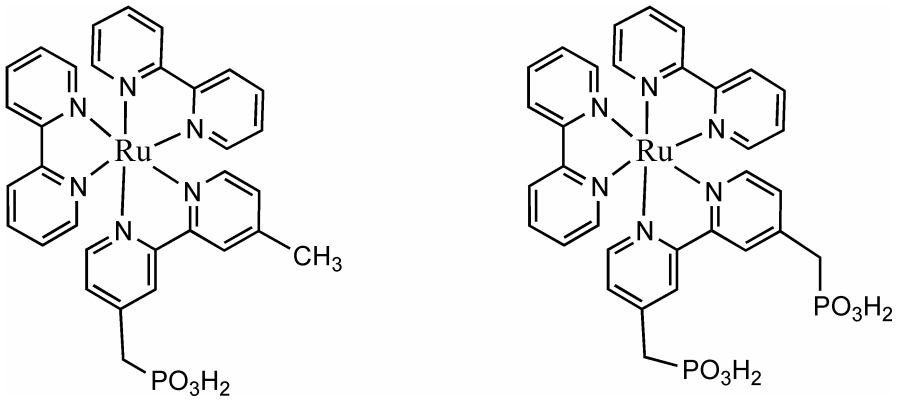

Figure 73. Structures of the phosphonated dyes. (a) Ru(bipyridine)$_2$[4,4′-($CH_2PO(OCH_2CH_3)_2$)$_2$-2,2′-bipyridine]Cl_2 and (b) Ru(bipyridine)$_2$[4-methyl, 4′-($CH_2PO(OCH_2CH_3)_2$)-2,2′-bipyridine]Cl_2 in ethanol.

Dyes Synthesis

4-4′-bis(bromomethyl)-2,2′-bipyridine

NBS (16.0 g, 89.9 mmol) was added to a solution of 4,4′-dimethyl-2,2′-bipyridine (8.0 g, 43.5 mmol) in carbon tetrachloride (300 mL). The solution was brought to reflux under argon and 500 mg of azobis(butyronitrile) was added. The resultant mixture was heated at reflux for 4 h under argon. The reaction was then cooled over an ice bath causing succinimide to precipitate. The cooled mixture was filtered to remove succinimide and evaporated to a brown oil using a rotary evaporator. The crude product was dissolved in a minimal amount of dichloromethane and purified by column chromatography on silica gel (98:2 dichloromethane:acetone). Thin layer chromatography, TLC, was used to identify the products and the bipyridine fractions were visualized by exposure of the TLC plates to $Fe(NH_4)_2(SO_4)_2$. The final product had an R_f value of 0.34 (3:7 ethyl acetate:hexanes). The pure fractions were combined and evaporated to dryness to give the crude product as a white powder. The crude product was washed with hexane and dried to give white crystals (0.80g, 2.34 mmol, 5% yield). ^{1}H NMR (300 MHz, $CDCl_3$) δ 4.47 (s, 4H) 7.35 (dd, 2H) 8.42 (d, 2H), 8.72 (d, 2H)

4-bromomethyl-4′-methyl-2,2′-bipyridine

This product can be obtained as a byproduct in the synthesis of 4-4′-bis(bromomethyl)-2,2′-bipyridine (0.9 g, 3.4 mmol, 7.8% yield). However, a higher yield of this product can be achieved by a modification of the original procedure.

To a solution of 4,4′-dimethyl-2,2′-bipyridine (4.7 g, 25.6 mmol) in carbon tetrachloride (150 mL) was added NBS (9.0 g, 24.47 mmol). The solution was slowly brought to reflux under argon before addition of AIBN (260 mg). The resultant mixture was allowed to gently reflux under argon for 4 h. The reaction mixture was cooled over an ice bath and filtered by vacuum filtration to remove precipitated succinimide. The filtrate was concentrated by rotary evaporation and purified on a silica column (7.5:2.5 dichloromethane:acetone). Product fractions were identified by TLC (30:70 ethyl acetate:hexanes, R_f = 0.35) and were the last to come off the column. These were combined and evaporated to dryness. The product was washed with hexane to yield white crystals (1.37 g, 4.0 mmol, 15% yield). ^{1}H NMR (300 MHz, $CDCl_3$) δ 2.45 (s, 3H) 4.45 (s, 2H) 7.08 (dd, 1H) 7.28 (dd, 1H) 8.23 (d, 1H) 8.42 (d, 1H) 8.56 (d, 1H) 8.65 (d, 1H)

4,4′-($CH_2PO(OCH_2CH_3)_2)_2$-2,2′-bipyridine

4-4′-Bis(bromomethyl)-2,2′-bipyridine (0.99 g, 2.9 mmol) was refluxed in triethylphosphite (35 mL) for 6 h under argon. The reaction was cooled with an ice bath and stored at -10ºC for 12 h to precipitate yellow crystals. These were collected by vacuum filtration, rinsed with diethyl ether (200 mL) and dried under vacuum to yield the crude product (0.86 g, 2.1 mmol, 72% yield). The crude product was purified on a silica column using 80:20 ethyl acetate:methanol as the eluent. The fractions were monitored with TLC (80:20 ethyl acetate:methanol) using $Fe(NH_4)_2(SO_4)_2$ to identify the bipyridine fractions. The fractions containing pure product (R_f = 0.50) were combined and evaporated to dryness to give the product as a white powder (0.77 g , 1.4 mmol, 64%

yield). ^{1}H NMR (300 MHz, $CDCl_3$) δ 1.22 (t, 12H) 3.25 (s, 2H) 3.38 (s, 2H) 4.02 (quintet, 8H) 7.38 (d, 2H) 8.38 (s, 2H) 8.60 (d, 2H).

4-methyl,4′-($CH_2PO(OCH_2CH_3)_2$)-2,2′-bipyridine

4-bromomethyl-4′-methyl-2,2′-bipyridine (430 mg, 1.0 mmol) was gently refluxed in triethylphosphite (20 mL) under argon for 4 h and then allowed to cool to 0ºC using an ice bath. The triethylphosphite was removed by vacuum distillation with gentle warming (~40ºC). The dried product was collected from the flask and washed with ether to give white crystals of the pure product (200 mg, 0.6 mmol, 60% yield). ^{1}H NMR (300 MHz, $CDCl_3$) δ 1.25 (t, 6H) 2.48 (s, 3H) 3.25 (d, 2H) 4.05 (quintet, 4H) 7.30 (d, 2H) 8.38 (d, 1H) 8.60 (dd, 2H)

Ru(bipyridine)$_2$[4,4′-($CH_2PO(OCH_2CH_3)_2$)$_2$-2,2′-bipyridine]Cl_2

Cis-$[Ru(bpy)_2Cl_2]\cdot 2H_2O$ (0.1 g, 0.18 mmol) and 4,4′-$(CH_2PO(OCH_2CH_3)_2)_2$-2,2′-bipyridine (0.13 g, 0.29 mmol) were added to DMF (40 mL) and refluxed under argon for 5 hours. The reaction was cooled in an ice bath and then evaporated to dryness on a rotary evaporator to give the crude product.

Ru(bipyridine)$_2$[4-methyl, 4′-($CH_2PO(OCH_2CH_3)_2$)-2,2′-bipyridine]Cl_2

Cis-$[Ru(bpy)_2Cl_2]\cdot 2H_2O$ (0.832 g, 0.16 mmol), 4,4′-$(CH_2PO(OCH_2CH_3)_2)_2$-2,2′-bipyridine (0.050 g, 0.173 mmol) and $NaHCO_3$ (0.04 g) were added to a mixture of methanol (2 mL) and water (3 mL). The mixture was brought to reflux under nitrogen for 2.5 hours. The reaction was cooled in an ice bath and the product was precipitated by the dropwise addition of 1M HPF_6. The precipitate was collected by vacuum filtration

and washed with 0.1M HPF_6 (~10 mL) followed by ethyl ether (~20 mL) to yield the crude product.

Results and Discussion

Isolation of the mono and dibrominated bipyridine intermediate was difficult. These compounds were quite reactive and decomposed rapidly. The methyl spacer between the phosphonic acid anchoring group and the bipyridyl ligand is not desired as it can affect the electronic coupling of the dye with the TiO_2 surface. This will make it difficult to make a direct comparison of injection and recombination rates of these dyes with the carboxylated analogues reported here. Initial attempts to obtain the directly brominated bipyridine products failed. This was due to the inability to isolate the desired bromination product from the wide distribution of brominated bipyridine byproducts. However, we can make an initial determination of the spectral differences between the phosphonated series and the carboxylated dyes. Figure **74** shows the absorption spectra of these dyes in ethanol. The spectral overlap of the phosphonated dyes was not

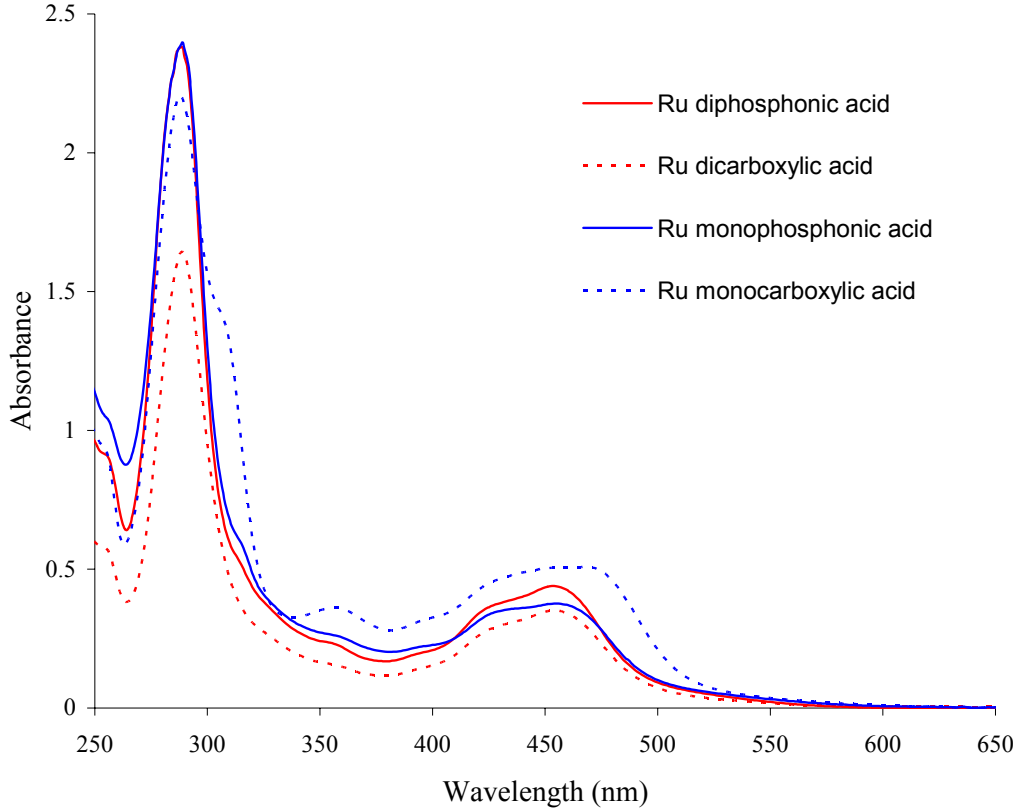

Figure 74. Absorption spectra of the phosphonated dyes. Ru(bipyridine)$_2$[4,4′-($CH_2PO(OCH_2CH_3)_2$)$_2$-2,2′-bipyridine]Cl_2 (red) and Ru(bipyridine)$_2$[4-methyl, 4′-($CH_2PO(OCH_2CH_3)_2$)-2,2′-bipyridine]Cl_2 (blue) in ethanol. For comparison, the absorption spectra of the carboxylic acid analogues are included, Ru(bipyridine)$_2$[4,4′-(COOH)-2,2′-bipyridine]Cl_2 (dashed red) and Ru(bipyridine)$_2$[4-methyl, 4′-(CH_2COOH)-2,2′-bipyridine]Cl_2 (dashed blue) in ethanol.

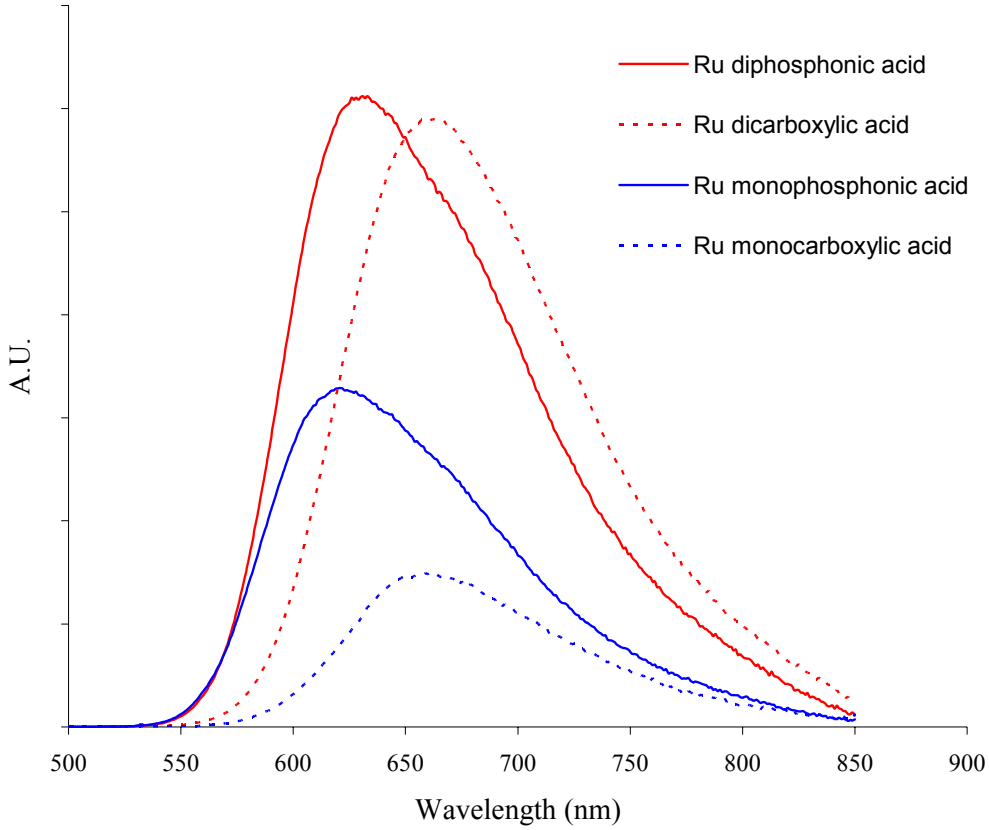

Figure 75. Emission spectra of the phosphonated dyes. Ru(bipyridine)$_2$[4,4′-($CH_2PO(OCH_2CH_3)_2$)$_2$-2,2′-bipyridine]Cl_2 (red) and Ru(bipyridine)$_2$[4-methyl, 4′-($CH_2PO(OCH_2CH_3)_2$)-2,2′-bipyridine]Cl_2 (blue) in ethanol. For comparison, the emission spectra of the carboxylic acid analogues are included, Ru(bipyridine)$_2$[4,4′-(COOH)-2,2′-bipyridine]Cl_2 (dashed red) and Ru(bipyridine)$_2$[4-methyl, 4′-(CH_2COOH)-2,2′-bipyridine]Cl_2 (dashed blue) in ethanol.

significantly shifted from that of the carboxylated analogues. Furthermore, the emission spectra (Figure **75**) of the phosphonated dyes were similar to those of the carboxylated analogues, although the emissions of the phosphonated dyes were shifted to slightly higher energy. As such, these dyes are expected to have similar spectral responses and similar current-potential characteristics to those observed for the carboxylated dyes. Of particular interest is the enhanced binding strength that these dyes will afford. Phosphoesters are less susceptible to hydrolysis than carboxyl based esters. This may allow for the use of water based electrolytes in DSSCs. A new graduate student in our labs has tested the diphosphonate $[Ru(bpy)_3]^{2+}$-type dye, Ru(bipyridine)$_2$[4,4′-($CH_2PO(OCH_2CH_3)_2$)$_2$-2,2′-bipyridine]Cl_2, in a functional DSSC with 0.5M LiI, 0.018M I_2, 20 mM pyridine and 20 mM pyridinium triflate in water rather than acetonitrile (Figure **76**).[58] While the photocurrent was minimal relative to the same electrolyte concentrations in acetonitrile (Figure **76** inset), this system clearly showed rectification behavior, indicating the potential of combining phosphonic acid anchoring groups with water based electrolytes.

Conclusions

The ability of these phosphonic acid modified dyes to sensitize TiO_2 and operate in a functional DSSC with an aqueous electrolyte is quite promising. The methyl phosphonates reported here will serve as an excellent starting point for the development of water based systems. In addition, synthesis of the directly phosphonated bipyridines is currently underway in our labs. It will be interesting

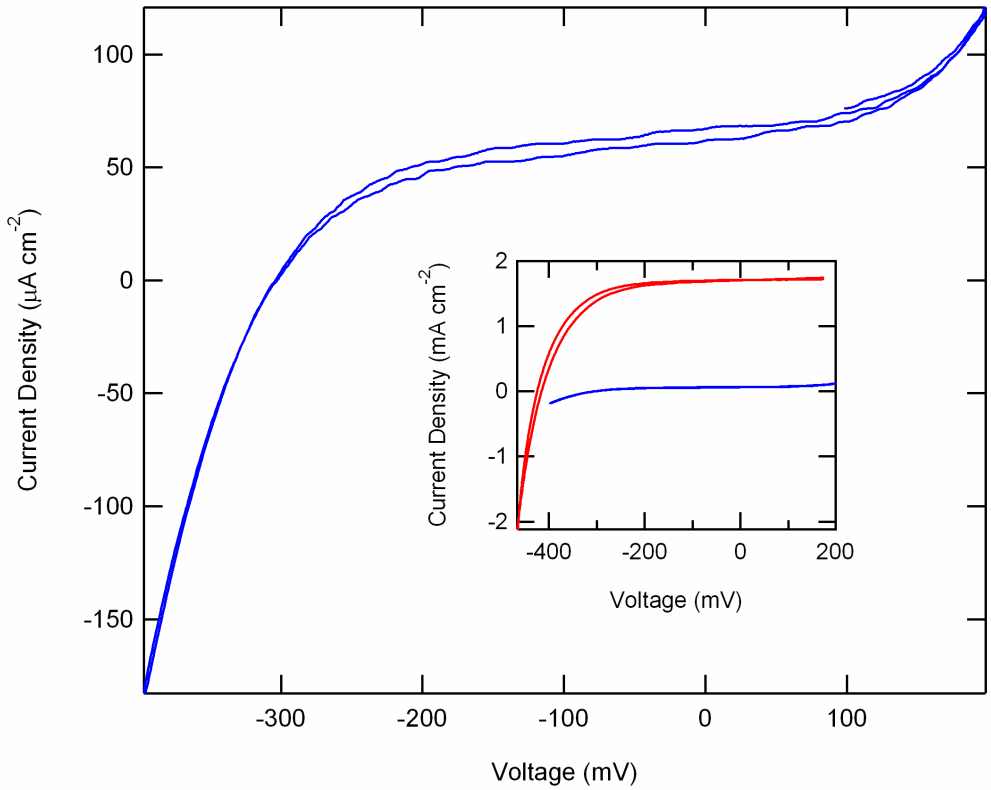

Figure 76. Current versus potential behavior under AM 1.0 illumination in aqueous electrolyte. Nanocrystalline TiO_2 photoelectrodes sensitized with the diphosphonated ruthenium dye, Ru(bipyridine)$_2$[4,4′-($CH_2PO(OCH_2CH_3)_2$)$_2$-2,2′-bipyridine]Cl_2, in contact with 0.50 M LiI, 0.018 M I_2, 0.020 M pyridine, and 0.020 M pyridinium triflate in water (blue). The behavior of the same dye-coated TiO_2 photoelectrode with an acetonitrile based electrolyte at the same concentration is included for comparison (inset, red).

to compare the injection and recombination properties of these systems with directly phosphonated bipyridines to determine the effect of the single methylene spacer on the electronic coupling associated with the forward and reverse electron transfer reactions.

CHAPTER 10:

CYCLOMETALATED IRIDIUM BASED SENSITIZERS

Chapter 10

CYCLOMETALATED IRIDIUM BASED SENSITIZERS

Introduction

Dye-sensitized nanocrystalline TiO_2 photoelectrodes have attracted much recent attention because they offer the possibility of using inexpensive absorber materials for the conversion of sunlight into electricity.[12,100] Efficiencies in excess of 10% have been observed in "champion" samples of such devices.[14] Although the quantum yield for photocurrent production is close to unity for light absorbed above the absorption threshold (typically 1.7-2.0 eV) the dye, the photovoltage is only 0.7-0.8 V under 1 Sun Air Mass 1.0 illumination.[13,14] Hence a large portion of the remaining energy loss in such devices, and much of the potential for improvement in the operating performance of such systems, lies in improving the photovoltage of such cells.

Efficient sensitization has been achieved with a variety of species, including organic chromophores,[101] porphyrins,[102] $Fe(bipyridyl)_3$ complexes,[103] and Re complexes,[104] but the most efficient reported devices use Ru(bipyridyl) derivatives.[14] Excitation of each of these complexes involves a metal-to-ligand charge transfer (MLCT) transition,[13,69] and electron injection into the TiO_2 occurs approximately equally in quantum yield from the Franck-Condon state produced promptly after optical excitation and from a thermally relaxed ("triplet") excited state.[69] The former process occurs on the fs timescale while the latter process occurs on the ps timescale.[19]

Energy dissipated upon conversion from the Franck-Condon state to the thermally relaxed excited state is lost as potential device output, so either accelerating the injection from the Franck-Condon state and/or reducing the energy gap between the Franck-Condon state and the lowest accessible thermal excited state of such sensitizers are worthy goals. Os(polypyridyl) complexes have been investigated in this context; notably, relaxation of spin restrictions in the optical absorption process introduces more absorption intensity to the red of the ^{1}MLCT band.[32] This strategy has been shown to be successful, but a significant energy loss still exists between the ^{1}MLCT and ^{3}MLCT states in such systems. Additionally, the intensity of the red-shifted optical transition could also be improved to obtain full extinction of light in a monolayer coverage of the 5-10 micron thick nanoporous TiO_2 films that are used in such systems.

To this end, we have investigated the use of Ir complexes as sensitizers in TiO_2-based photoelectrochemical cells. Cyclometalated iridium compounds have recently found a wide variety of uses, ranging from photoreductants,[105] sensors,[106] biological labeling reagents,[107] and organic light emitting diodes.[108] The combination of cyclometalating ligands with a third row metal ion results in enhanced mixing of the singlet and triplet excited states via spin-orbit coupling, and provides a reduced Stokes shift between absorption and emission maxima in complexes in which the lowest excited state is MLCT in character.[108] Additionally, through variation in the nature of the ligand, members of this family of iridium dyes have been shown to absorb over a wide range of the visible spectrum.[106,108]

Results and Discussion

Two representative iridium-based dyes, $[Ir(ppz)_2dcbpy]^+$ and $[Ir(ppz)_2dcbq]^+$ (where ppz=diphenylpyrazolyl, dcbpy=4,4'-dicarboxybipyridine and dab=4,4'-dicarboxy-2,2'-biquinoline; with PF_6^- counter ions) (Figure **77**) were investigated. These dyes have spectroscopic and electrochemical behavior (Table **14**) that is quite similar to that of a ruthenium bipyridyl based analogue, $[Ru(bpy)_2(dcbpy)]^{2+}$ (where bpy=bipyridine; with PF_6 counter ion) (Figure **77**), which has previously been shown to efficiently sensitize TiO_2 (Table **14**).[32] Both iridium dyes exhibit a ligand based π to π^* transition at high energy and a weak absorption band in the visible.

Density functional theory (DFT) calculations indicate that this absorption is attributable to a ligand-to-ligand charge transfer (LLCT) from the cyclometalating ligand to the bipyridine or the biquinoline ligand, rather than MLCT as in the case of ruthenium dyes. This assignment is consistent with the diminished extinction coefficient for these particular dyes. While the low extinction coefficient can be disadvantageous for a DSSC photosensitizer, the LLCT excited state provides a large spatial separation between the hole and electron which may facilitate charge injection into TiO_2.

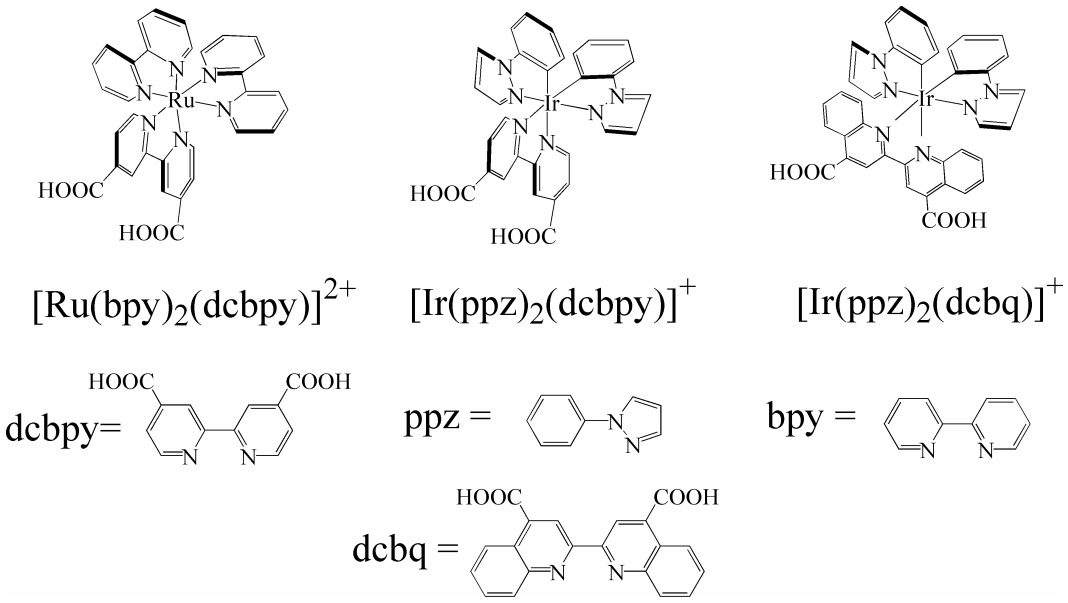

Figure 77. Structures of the iridium based sensitizers. Investigated dyes and the corresponding bipyridyl and cyclometalating ligands.

Table 14. Spectroscopic and electrochemical data for iridium based sensitizers.

Dye	λ_{abs} (nm)	$(\varepsilon/10^3)$ (M^{-1} cm^{-1})	λ_{em} (nm)	φ_{ems} (%)	τ_{ems} (μs)	$\mathbf{E}_{00}$[a] (eV)	$E^{o\prime}$[b] (V)	$E^{o\prime *}$[f] (V)
$[Ir(ppz)_2dcbq]^+$	495	(1.3)	644	10	0.7	2.17	1.42[c]	-0.8
$[Ir(ppz)_2dcbpy]^+$	455	(0.7)	604	12	0.3	2.46	1.35[d]	-1.0
$[Ru(bpy)_2dcbpy]^{2+}$	469	(14)	676	5	0.8	2.00	1.09[e]	-0.9

a: Estimated from the intersection of the absorption and emission spectra.

b: Reported versus SCE.

c: Estimated from the CV measurement of the non-carboxylated dye, $[Ir(ppz)_2bq]^+$ in acetonitrile with tetra-butylammonium hexafluorophosphate, where bq=biquinoline.

d: Determined from CV measurements in acetonitrile with tetra-butylammonium hexafluorophosphate.

e: Determined from DPV measurements in buffered ethanol containing pyridine and pyridinium triflate (1 mM each).

f: Calculated according to $E^{o\prime *} = E^{o\prime} - \mathbf{E}_{00}/q$.

These iridium complexes have excited-state lifetimes and excited-state energies comparable to those of the ruthenium complex. Thus, the Ir complexes should readily inject electrons into TiO_2. As the emission decays are multiexponentials, the difference between the integrated emission decay on TiO_2 and in solution was used to determine the extent of quenching (Figure **78**); the average quenching rate constants were 1.0×10^8 s^{-1} or 3.8×10^7 s^{-1} for $[Ir(ppz)_2dcbpy]^+$ and $[Ir(ppz)_2dcbq]^+$, respectively. In each case the shortest lifetime is very close to that of the response function, and thus the pre-exponential factor and rate constant are lower limits.

The diminished extinction coefficient for these Ir dyes in the visible region indicates that their optical absorption overlap with the solar spectrum is not very favorable. Thus, nanocrystalline TiO_2-based photoelectrochemical cells containing these dyes would be expected to display lower energy conversion efficiencies under solar-simulated illumination than the analogous $[Ru(bpy)_2(dcbpy)]^{2+}$ sensitized photoelectrochemical cells. Figure **79** shows the current-potential curves measured under 100 mW cm^{-2} of simulated Air Mass 1.0 solar illumination conditions. All photoelectrodes were fabricated to have the same absorbance, 0.7±0.1 at the MLCT or LLCT maximum, to take into account the differences in extinction coefficients among the various dyes.

The quantum yield for conversion of absorbed photons to current was nearly unity for $[Ir(ppz)_2dcbpy]^+$ and was 0.6 for $[Ir(ppz)_2dcbq]^+$. Overall, the short-circuit current density, J_{sc}, the open-circuit voltage, V_{oc}, and the shapes of

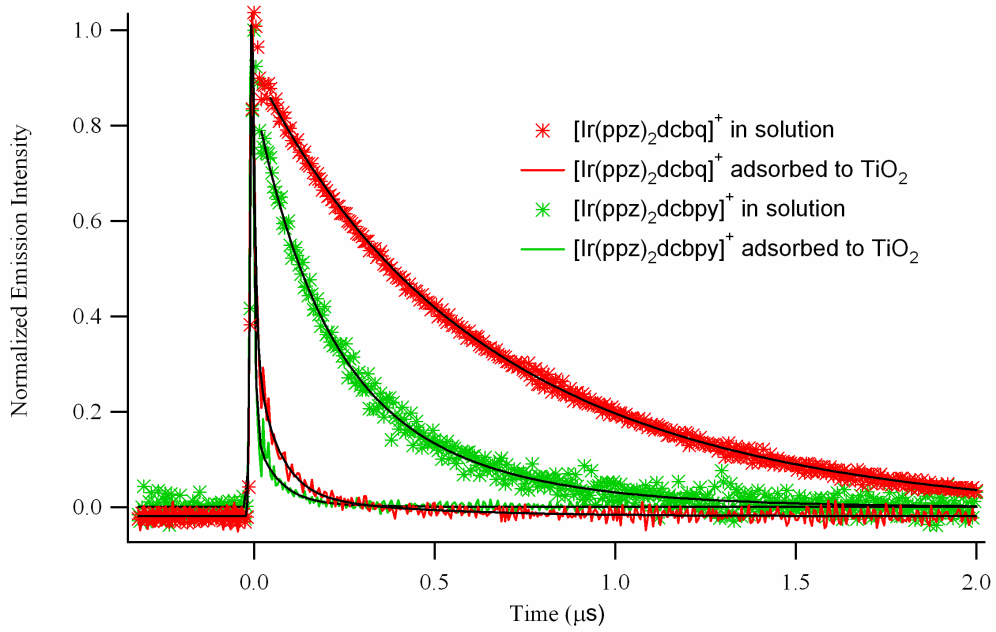

Figure 78. Emission quenching of iridium sensitizers adsorbed onto TiO_2. Time-resolved emission (λ_{ex} = 480 nm, λ_{em} = 630 nm) of $[Ir(ppz)_2dcbpy]^+$ (red stars); and $[Ir(ppz)_2dcbq]^+$ (green stars) dyes in degassed acetonitrile. Also shown are the time-resolved emission of $[Ir(ppz)_2dcbpy]^+$ (red lines); and $[Ir(ppz)_2dcbq]^+$ (green lines) when bound to TiO_2 with the electrolyte being 0.50 M $LiClO_4$, 0.020 M pyridine, and 0.020 M pyridinium triflate in acetonitrile. Solid lines are best exponential fits (see text for details).

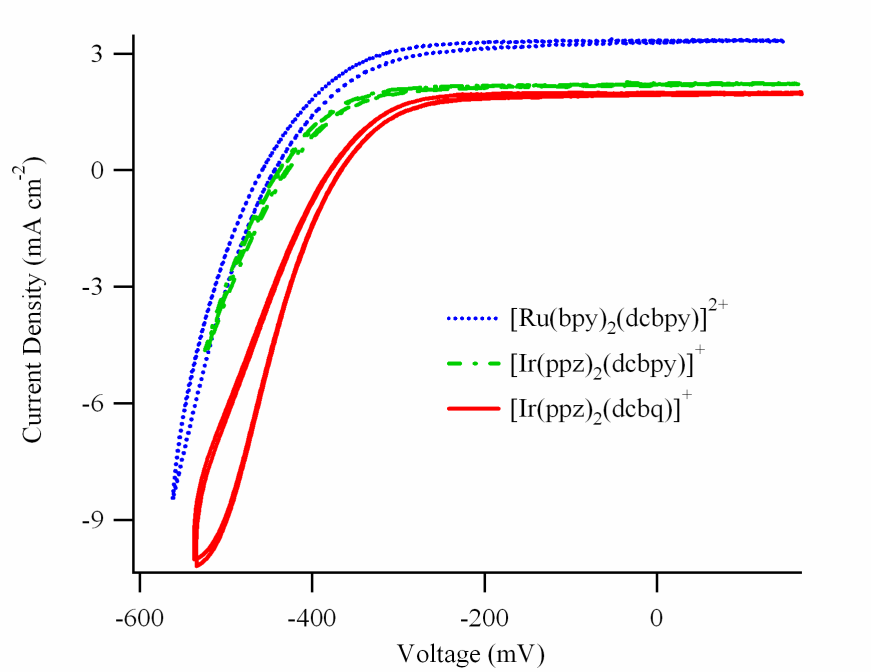

Figure 79. Current versus potential characteristics under AM 1.0 illumination for TiO_2 electrodes sensitized with iridium based dyes. Electrolyte concentrations: 0.50 M LiI, 0.040 M I_2, 0.020 M pyridine and 0.020 M pyridinium triflate in acetonitrile. Sensitizers are $[Ru(dcbpy)(bpy)_2]^{2+}$ (blue); $[Ir(ppz)_2dcbpy]^{+}$ (green); and $[Ir(ppz)_2dcbq]^{+}$ (red).

the current density-potential curves (Figure **79**) for the two Ir dyes were comparable to the corresponding properties of the ruthenium-based analogue under these test conditions (Table **15**).

The back reaction that determines V_{oc} in sensitized TiO_2 systems is electron transfer from reduced nanocrystalline TiO_2 to the oxidized species in the I_3^-/I^- electrolyte solution.[13] Trends in the rate of this back reaction were evaluated from the forward bias potential necessary to produce a fixed amount of cathodic dark current density (0.1 mA cm^{-2}) at the TiO_2-solution interface, where a less negative potential is indicative of more facile electron transfer between TiO_2 and the I_3^-/I^- electrolyte (Figure **80**). Interestingly, the magnitudes of these potentials were similar for $[Ir(ppz)_2dcbpy]^+$ and $[Ru(bpy)_2(dcbpy)]^{2+}$, with almost a 100 mV difference towards a more facile back reaction for $[Ir(ppz)_2dcbq]^+$. All three of these dyes should bind in a similar fashion to the TiO_2 surface, and thus the enhanced electron transfer between TiO_2 and the redox couple for the $[Ir(ppz)_2dcbq]^+$ sensitizer is surprising.

Conclusions

In summary, iridium dyes have been used for the first time to sensitize TiO_2 in a functional DSSC. The iridium dyes were employed in photoelectrochemical cells that gave quantum yields approaching unity for conversion of absorbed photons to current under AM 1.0 sunlight. The iridium dye based solar cells provide specific benefits over typical ruthenium based systems. In particular, the ability to easily tune the spectral overlap between

Table 15. Photoelectrochemical data for iridium sensitized TiO_2 photoelectrodes.

Dye	J_{sc} [a] (mA cm^{-2})	V_{oc} [f] (V)	ff [b]	Eff [c] (%)	Φ [d] (%)	V_{dark} [e] (V)
$[Ir(ppz)_2dcbq]^+$	1.99	-380	0.66	0.50	60	-386
$[Ir(ppz)_2dcbpy]^+$	2.24	-438	0.67	0.7	100	-436
$[Ru(bpy)_2dcbpy]^{2+}$	3.35	-458	0.65	1.0	100	-476

a: Acetonitrile with 0.50 M LiI, 0.040 M I_2, 20 mM pyridine, 20 mM pyridinium triflate under AM 1.0 conditions.

b: The fill factor (ff) is calculated as $P_{max}/(J_{sc} \times V_{oc})$, where Pmax is the most negative value of $J \times V$.

c: Calculated as $(J_{sc} \times V_{oc} \times ff \times 100\%)/I_{light}$, where $I_{light} = 100$ mW cm^{-2}.

d: The integrated quantum yield (Φ) was determined by comparing the experimentally measured value of J_{sc} with the maximum calculated J_{sc}, assuming a unity quantum yield when the measured absorbance of the dyes on TiO_2 electrodes are convoluted with the spectral irradiance of the solar simulator between 1100 and 360 nm.

e: Potential required to drive a cathodic current density of 0.1 mA cm^{-2} in the dark.

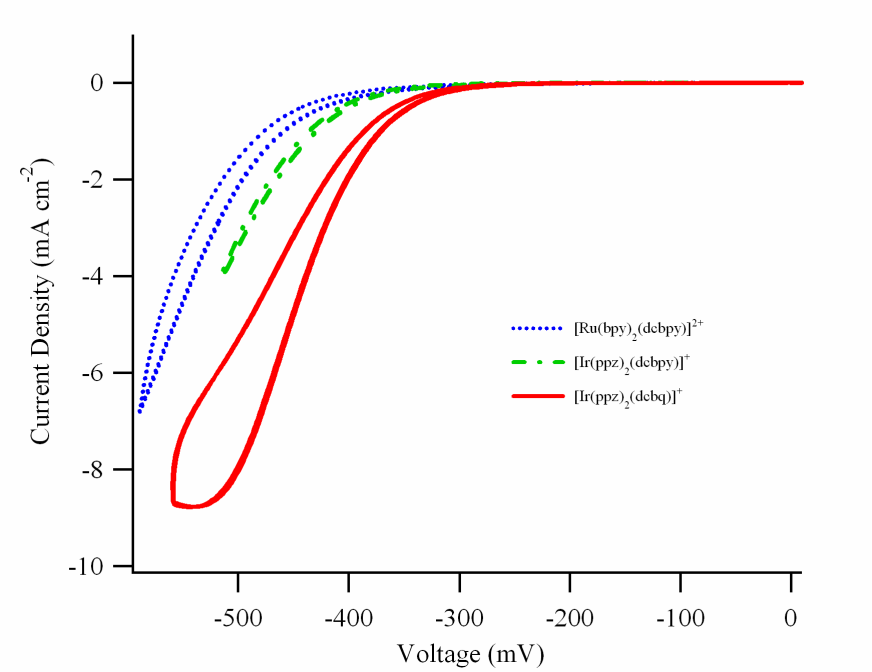

Figure 80. Dark current versus potential characteristics for TiO_2 electrodes sensitized with iridium based dyes. Electrolyte concentrations: 0.50 M LiI, 0.040 M I_2, 0.020 M pyridine and 0.020 M pyridinium triflate in acetonitrile. Sensitizers are: $[Ru(dcbpy)(bpy)_2]^{2+}$ (blue); $[Ir(ppz)_2dcbpy]^{+}$ (green); and $[Ir(ppz)_2dcbq]^{+}$ (red).

the Ir dye and the solar spectrum could lead to improved power efficiency. Furthermore, modification of the cyclometalating ligands in the Ir system offers new avenues to elucidate the mechanism of the I_3^-/I^- regeneration process. Efforts in these directions are currently underway in our laboratories.

CHAPTER 11:

GENERAL CONCLUSIONS

Chapter 11

GENERAL CONCLUSIONS

The body of work reported in this dissertation represents a step-by-step approach aimed at not only increasing the efficiencies of DSSCs, but at developing a more detailed description of the mechanisms of charge-transfer in these devices. We report results from a comprehensive series of kinetics and thermodynamics experiments in conjunction with steady-state current density versus potential measurements.

Efforts to replace the I_3^-/I^- redox couple with alternative two-electron redox couples with more positive ground-state potentials were successful, with efficiency increases of a factor of two observed for the Br_3^-/Br^- redox couple. The Br_3^-/Br^- redox couple appeared to behave in a similar fashion to the I_3^-/I^- couple in that it maintains slow electron transfer rates with TiO_2. By using the more positive Br_3^-/Br^- couple, significant enhancements in the open circuit potential were achieved under AM 1.0 illumination. This increase in V_{oc} (>300 mV) correlated with nearly a twofold increase in the solar cell efficiency over DSSCs using the I_3^-/I^- couple in conjunction with dyes with ground-state reduction potentials more positive than 1.08 V vs. SCE. Our work indicates that the potential of the $[Ru(H_2L')_2(CN)_2]^{2+}$ dye is a lower limit for use in DSSCs with the Br_3^-/Br^- couple. This may ultimately limit the usefulness of this couple in DSSCs as dyes with such positive potentials usually have limited spectral overlap.

Interhalide species formed upon addition of Cl^- and Br^- to the I_3^-/I^- couple exhibited similar dark currents and shifted the solution redox potentials to more positive values. This resulted in significant enhancements in the efficiency due to increases in both V_{oc} and J_{sc} (>40% efficiency increase). It is surprising that these mixed halide systems exhibited enhanced photocurrents, as they should not affect absorption or injection properties. More likely is that these species show enhanced rates of regeneration or a decreased rate of quenching of the dye excited state. This indicates that the ability of the I_3^-/I^- and Br_3^-/Br^- couples to form polyhalide species is likely key to their slow electron transfer properties with TiO_2.

The pseudohalogens, $(SCN)_2/SCN^-$ and $(SeCN)_2/SeCN^-$, while having more positive redox potentials, exhibited facile electron transfer with the TiO_2 surface, rendering them useless in functional DSSCs. Attempts to control this rate of electron transfer between the TiO_2 surface and triiodide in solution were undertaken by modifying the surface with carboxylic acids. Minimization of the dark current was achieved as a result of exposure of the TiO_2 surface to carboxylic acids of various lengths, with the stearic acid-treated surface showing the lowest dark current. This effect resulted in minor increases in the V_{oc} and slightly larger increases in J_{sc} upon illumination. The enhanced J_{sc} indicates that the increased efficiencies observed with the carboxylic acid-modified surfaces were not simply a result of binding of the acids to the surface, thereby minimizing the kinetics of the electron transfer process. It is possible that surface-state charging or conduction band edge shifts account for this phenomenon. The stearic acid-modified TiO_2 photoelectrode showed the most promise with a greater than 20% increase

in efficiency, significantly better than any of the other acid-modified surfaces. This could be an indication that the minimal effective blocking layer was achieved with the longest carboxylic acid.

Attempts to minimize the recombination of injected electrons with the oxidized dye by lengthening the dye linker were generally part unsuccessful. While the ruthenium-based dyes with one carboxyl anchoring group and various xylyl-linker lengths sensitized nanocrystalline TiO_2, DSSCs using these sensitizers resulted in low efficiencies and photocurrent densities that decreased with linker length. The measured kinetics did not satisfactorily explain the low efficiencies, nor the trends among the steady-state photoelectrochemical behavior of the dyes. This suggests that there are other possible quenching mechanisms or electron-transfer processes which are not included in the current kinetics model. The lack of a distance dependence was suggested to be due to the fact that the Ru-TiO_2 electron tunneling distance may be roughly the same for x = 0, 1, and 2, for the Rux dyes where x is the number of xylyl spacers, as the one-carboxyl attachment to the surface is flexible enough for the Ru center to approach the TiO_2 surface in all three cases. Furthermore, electron transfer from TiO_2 sensitized with these modified dyes to I_3^-/I^- is more pronounced than for $[Ru(H_2L')_3]^{2+}$ sensitized as well as unsensitized photoelectrodes, in accord with the lower efficiencies of the Rux-based cells.

For the series of carboxylated ruthenium dyes, a correlation was observed between the chemical nature of dye binding and the photoelectrochemical behavior of the resulting dye-sensitized TiO_2 electrodes. The IR spectra indicated that the dyes bound in

a bridging fashion, i.e., with both oxygen atoms from an anchoring carboxyl group interacting with adjacent titanium atoms on the TiO_2 surface, but not all carboxy groups participated in binding to the TiO_2. Complexes having either a single monocarboxy ligand or a single dicarboxy ligand used essentially all of their carboxyl groups to bind to the surface, whereas complexes having four or six carboxy groups used on average two carboxy groups in binding to TiO_2. TiO_2 photoelectrodes sensitized with $[Ru(H_2L')_2(CN)_2]^0$, $[Ru(H_2L')_2(NCS)_2]^0$, and $[Ru(H_2L')_3]^{2+}$ displayed internal quantum yields that approached unity, indicating that differences in the short-circuit current density under solar illumination can be ascribed primarily to differences in overlap of these various dyes with the solar spectrum. However, the efficiencies within the series of the carboxylated $[Ru(bpy)_3]^{2+}$-type dyes decreased in the order $[Ru(H_2L')_3]^{2+}>[Ru(H_2L')L_2]^{2+}>>[Ru(HL'')L_2]^{2+}$, indicating that the short-circuit current density and steady-state quantum yield correlated with the available binding type (2N>2S>>1C). In addition, the dark current was largest for the monocarboxy dye that used the weakest, most labile 1C mode of binding. The $[Ru(HL'')L_2]^{2+}$ complex was significantly less stably bound to TiO_2 over time than the other dyes, and consequently produced a wide range of photoelectrochemical responses. Hence, the linkage to the TiO_2 surface plays an important role in achieving temporal stability of the photoelectrochemical properties as well as in tuning both the steady-state quantum yield and the magnitude of the predominant back-reaction rate in dye-sensitized TiO_2-based photoelectrochemical solar cells.

The extent of quenching, and consequently injection, appears to be independent of the mode of binding as the excited states of all three dyes are more than 97% quenched on the ns timescale upon binding to TiO_2. The recombination rate of injected electrons with oxidized dye was slightly decreased for the monocarboxylated dye. This is likely a result of the decreased coupling resulting from the more labile binding mode (1C) for this dye. All of the carboxyl modified $[Ru(bpy)_3]^{2+}$-type dyes were shown to be efficiently regenerated by iodide when adsorbed onto TiO_2. The observed lifetime for regeneration of these dyes were all on the order of $1/10^7$ s, which is comparable to the known lifetime for regeneration of $[Ru(H_2L')_2(NCS)_2]^0$ sensitized TiO_2 systems. The regeneration of the bound dyes was slightly slower as the number of carboxylic acid groups increased, with the slowest rate found for the hexacarboxylated dye. It is possible that the effect of increasing the number of these electron withdrawing groups not only affects the metal center, but also modulates the interaction of the negatively charged species that must collide with the oxidized dye for regeneration.

Neither the injection dynamics measured on this timescale nor the recombination or regeneration kinetics explain the observed decrease in efficiency for the monocarboxylated dye. Through a collaboration with Dr. McCusker at Michigan State University, we are in the progress of measuring the ultrafast transient kinetics of injection for these dyes. If the ultrafast injection rates are similar for these three dyes, it will be clear that the current kinetics model cannot accurately describe the dynamics of DSSCs, once again suggesting that there are other possible quenching mechanisms or electron-transfer processes which are crucial to solar cell performance.

In solution, the regeneration rates for the oxidized $[Ru(bpy)_3]^{2+}$-type dyes were diffusion controlled, on the order of 10^{10} M^{-1} s^{-1} for $[RuL_3]^{2+}$. The regeneration rate was slightly dependent on the number and electron-withdrawing nature of the pendant groups, with the rate decreasing with increasing number of electron-withdrawing substituents. Furthermore, these studies showed that regeneration was first order in oxidized dye concentration. The addition of electron-withdrawing groups on the bipyridine ligands affected not only the regeneration rates, but the quenching rates of the excited state by MV^{2+} and the relative stability of the oxidized dye.

Two phosphonic acid-modified $[Ru(bpy)_3]^{2+}$-type dyes were synthesized and characterized. The phosphonic acid modified dyes do sensitize TiO_2 and operate in a functional DSSC with an aqueous electrolyte showing rectification behavior. The methyl phosphonated dyes reported here will serve as an excellent starting point for the development of water-based DSSCs. Synthesis of the directly phosphonated bipyridines is currently underway in our labs. It will be interesting to compare the injection and recombination properties of the directly phosphonated bipyridines with the methyl phosphonic acid-modified dyes in order to determine the effect of the single methylene spacer on the electronic coupling associated with the forward and reverse electron transfer reactions.

Cyclometalated iridium dyes were used for the first time to sensitize TiO_2 in a functional DSSC. The iridium dyes were employed in photoelectrochemical cells that gave quantum yields approaching unity for conversion of absorbed photons to current under AM 1.0 sunlight. These iridium-based solar cells provide some specific benefits

over typical ruthenium-based systems. In particular, the ability to tune the overlap of the Ir dye absorption and the solar spectrum could lead to improved power efficiency. Furthermore, modification of the cyclometalating ligands in the Ir system offers new avenues to elucidate the mechanism of the I_3^-/I^- regeneration process. Efforts in these directions are currently underway in our laboratories.

REFERENCES

C h a p t e r 1 1

REFERENCES

(1) Licht, S. *Sol. Eng. Mater. Sol. Cells* **1995**, *38*, 305-319.

(2) United Nations Development Programme; UN Department of Economic and Social Affairs; Council, W. E. "World Energy Assessment," United Nations Publications, 2000.

(3) Tan, M. X.; Laibinis, P. E.; Nguyen, S. T.; Kesselman, J. M.; Stanton, C. E.; Lewis, N. S. *Prog. Inorg. Chem.* **1994**, *41*, 21-144.

(4) Greunbaum, P.; Gan, J.; Swanson, R. *Appl. Phys. Lett.* **1991**, *58*, 945-947.

(5) Cuevas, A.; Sinton, R.; Midkiff, N.; Swanson, R. *IEEE Electron Device Lett.* **1990**, *11*, 6-8.

(6) Singh, S.; Singh, P. *IETE J. Res.* **1997**, *43*, 97-124.

(7) Smestad, G. *Sol. Eng. Mater. Sol. Cells* **1998**, *55*, 157-178.

(8) Grätzel, M. *Nature* **2001**, *414*, 338-344.

(9) Grätzel, M. *Cat. Tech.* **1999**, *3*, 4.

(10) Vlachopoulos, N.; Liska, P.; Augustynski, J.; Grätzel, M. *J. Am. Chem. Soc.* **1988**, *110*, 1216.

(11) Grätzel, M.; Moser, J. Solar Energy Conversion. In *Electron Transfer in Chemistry*; Gould, S., Ed.; Wiley: New York, 2001; Vol. 5.

(12) O'Regan, B.; Grätzel, M. *Nature* **1991**, *353*, 737-740.

(13) Hagfeldt, A.; Grätzel, M. *Accounts Chem. Res.* **2000**, *33*, 269-277.

(14) Nazeeruddin, M. K.; Pechy, P.; Renouard, T.; Zakeeruddin, S. M.; Humphry-Baker, R.; Comte, P.; Liska, P.; Cevey, L.; Costa, E.; Shklover, V.; Spiccia, L.; Deacon, G. B.; Bignozzi, C. A.; Grätzel, M. *J. Am. Chem. Soc.* **2001**, *123*, 1613-1624.

(15) Amirnasr, M.; Nazeeruddin, M. K.; Grätzel, M. *Thermochim. Acta* **2000**, *348*, 105-114.

(16) Smestad, G.; Bignozzi, C.; Argazzi, R. *Sol. Eng. Mater. Sol. Cells* **1994**, *32*, 259-272.

(17) Kallioinen, J.; Benkö, G.; Sundström, V.; Korppi-Tommola, J. E. I.; Yartsev, A. P. *J. Phys. Chem. B* **2002**, *106*, 4396-4404.

(18) Benkö, G.; Kallioinen, J.; Korppi-Tommola, J. E. I.; Yartsev, A. P.; Sundström, V. *J. Am. Chem. Soc.* **2002**, *124*, 489-493.

(19) Kuciauskas, D.; Monat, J. E.; Villahermosa, R.; Gray, H. B.; Lewis, N. S.; McCusker, J. K. *J. Phys. Chem. B* **2002**, *106*, 9347-9358.

(20) Nazeeruddin, M. K.; Zakeeruddin, S. M.; Humphry-Baker, R.; Jirousek, M.; Liska, P.; Vlachopoulos, N.; Shklover, V.; Fischer, C. H.; Grätzel, M. *Inorg. Chem.* **1999**, *38*, 6298-6305.

(21) Hagfeldt, A.; Grätzel, M. *Chem. Rev.* **1995**, *95*, 49-68.

(22) Stipkala, J. M.; Castellano, F. N.; Heimer, T. A.; Kelly, C. A.; Livi, K. J. T.; Meyer, G. J. *Chem. Mat.* **1997**, *9*, 2341-2353.

(23) Pichot, F.; Gregg, B. A. *J. Phys. Chem. B* **2000**, *104*, 6-10.

(24) Nazeeruddin, M. K.; Kay, A.; Rodicio, I.; Humphry-Baker, R.; Müller, E.; Liska, P.; Vlachopoulos, N.; Grätzel, M. *J. Am. Chem. Soc.* **1993**, *115*, 6382-6390.

(25) Cahen, D.; Hodes, G.; Grätzel, M.; Guillemoles, J. F.; Riess, I. *J. Phys. Chem. B* **2000**, *104*, 2053-2059.

(26) Asbury, J. B.; Ellingson, R. J.; Ghosh, H. N.; Ferrere, S.; Nozik, A. J.; Lian, T. Q. *J. Phys. Chem. B* **1999**, *103*, 3110-3119.

(27) Sapp, S. A.; Elliott, C. M.; Contado, C.; Bignozzi, C. A. *J. Am. Chem. Soc.* **2002**, 11215-11222.

(28) Nusbaumer, H.; Moser, J. E.; Zakeeruddin, S. M.; Nazeeruddin, M. K.; Grätzel, M. *J. Phys. Chem. B* **2001**, *105*, 10461-10464.

(29) Oskam, G.; Bergeron, B. V.; Meyer, G. J.; Searson, P. C. *J. Phys. Chem. B* **2001**, *105*, 6867-6873.

(30) Sauvé, G. Dye-sensitization of nanocrystalline TiO_2 with osmium and ruthenium polypyridine complexes. Ph. D., California Institute of Technology, 1999.

(31) Strouse, G. F.; Schoonover, J. R.; Duesing, R.; Boyde, S.; Jones, W. E., Jr.; Meyer, T. J. *Inorg. Chem.* **1995**, *34*, 473-487.

(32) Sauvé, G.; Cass, M. E.; Coia, G.; Doig, S. J.; Lauermann, I.; Pomykal, K. E.; Lewis, N. S. *J. Phys. Chem. B* **2000**, *104*, 6821-6836.

(33) Miller, J. E. Radical Formation and Electron Transfer in Biological Molecules, California Institute of Technology, 2003.

(34) Chang, I. J.; Gray, H. B.; Winkler, J. R. *J. Am. Chem. Soc.* **1991**, *113*, 7056-7057.

(35) Lewis, F. D. Electron Transfer in Chemistry; Balzani, V., Ed.; Wiley-VCH: Weinheim, 2001; Vol. 3; pp 105-175.

(36) Nogueira, A. F.; De Paoli, M. A.; Montanari, I.; Monkhouse, R.; Nelson, J.; Durrant, J. R. *J. Phys. Chem. B* **2001**, *105*, 7517-7524.

(37) Kebede, Z.; Lindquist, S. E. *Sol. Eng. Mater. Sol. Cells* **1998**, *51*, 291-303.

(38) Stanley, A.; Matthews, D. *Aust. J. Chem.* **1995**, *48*, 1293-1300.

(39) Gregg, B. A.; Pichot, F.; Ferrere, S.; Fields, C. L. *J. Phys. Chem. B* **2001**, *105*, 1422-1429.

(40) Bonhote, P.; Moser, J.; Humphry-Baker, R.; Vlachopoulos, N.; Zakeeruddin, S. M.; Walder, L.; Grätzel, M. *J. Am. Chem. Soc.* **1999**, *121*, 1324-1336.

(41) Nord, G.; Pedersen, B.; Farver, O. *Inorg. Chem.* **1978**, *17*, 2233-2238.

(42) Nord, G.; Pedersen, B.; Floryan-Lovborg, E.; Pagsberg, P. *Inorg. Chem.* **1982**, *21*, 2327-2330.

(43) Moser, J.; Grätzel, M. *Helv. Chim. Acta.* **1982**, *65*, 1436.

(44) Kelly, C. A.; Farzad, F.; Thompson, D. W.; Meyer, G. J. *Langmuir* **1999**, *15*, 731-737.

(45) Tachibana, Y.; Haque, S. A.; Mercer, I. P.; Durrant, J. R.; Klug, D. R. *J. Phys. Chem. B* **2000**, *104*, 1198-1205.

(46) Pelet, S.; Moser, J.; Grätzel, M. *J. Phys. Chem. B* **2000**, *104*, 1791-1795.

(47) Kilså, K.; Mayo, E. I.; Kuciauskas, D.; Villahermosa, R.; Lewis, N. S.; Winkler, J. R.; Gray, H. B. *J. Phys. Chem. A* **2003**, *107*, 3379-3383.

(48) Fisher, A.; Peter, L.; Ponomarev, E.; Walker, A.; Wijayantha, K. *J. Phys. Chem. B* **2000**, *104*, 949-958.

(49) Kuciauskas, D.; Freund, M. S.; Gray, H. B.; Winkler, J. R.; Lewis, N. S. *J. Phys. Chem. B* **2001**, *105*, 392-403.

(50) Okada, T.; Hata, J. *Mol. Phys.* **1981**, *43*, 1151-1161.

(51) Mizuno, M.; Tanaka, J.; Harada, I. *J. Phys. Chem.* **1981**, *85*, 1789-1794.

(52) Tasker, P. *Mol. Phys.* **1977**, *33*, 511-518.

(53) Gabes, W.; Nijmanme, M. *Inorg. Chem.* **1973**, *12*, 589-592.

(54) Awtrey, A.; Connick, R. *J. Am. Chem. Soc.* **1951**, *73*, 1842-1843.

(55) Choi, H.; Bise, R. T.; Hoops, A. A.; Neumark, D. M. *J. Chem. Phys.* **2000**, *113*, 2255-2262.

(56) Bard, A. J. *Encyclopedia of electrochemistry of the elements*; M. Dekker: New York, 1973.

(57) Nasr, C.; Hotchandani, S.; Kamat, P. V. *J. Phys. Chem. B* **1998**, *102*, 4944-4951.

(58) Fitch, T., Unpublished Results.

(59) Weng, Y. X.; Wang, Y. Q.; Asbury, J. B.; Ghosh, H. N.; Lian, T. Q. *J. Phys. Chem. B* **2000**, *104*, 93-104.

(60) Nelson, J. *Phys. Rev. B* **1999**, *59*, 15374-15380.

(61) Ferber, J.; Sangl, R.; Luther, J. *Sol. Eng. Mater. Sol. Cells* **1998**, *53*, 29.

(62) Lindford, M. R.; Fenter; Eisenberger, P. M.; Chidsey, C. E. D. *J. Am. Chem. Soc.* **1995**, *117*, 3145.

(63) Lindford, M. R.; Chidsey, C. E. D. *J. Am. Chem. Soc.* **1993**, *115*, 12631.

(64) Bansal, A.; Li, X.; Lauermann, I.; Lewis, N. S. *J. Am. Chem. Soc.* **1996**, *118*, 7225.

(65) Grätzel, M.; Kalyansundaram, K. *Curr. Sci.* **1994**, *66*, 706.

(66) Parkinson, B. A.; Furtak, T. E.; Canfield, D.; Kam, K.; Kline, G. *Discuss. Faraday Soc.* **1980**, *70*.

(67) Huang, S. Y.; Schlichthörl, G.; Nozik, A. J.; Grätzel, M.; Frank, A. J. *J. Phys. Chem. B* **1997**, *101*, 2576-2582.

(68) Kang, T.; Chun, K.; Hong, J. S.; Moon, S.; Kim, K. *J. Electrochem. Soc.* **2000**, *147*, 3049-3053.

(69) Roundhill, D. M. Photochemistry, photophysics, and photoredox reactions of $Ru(bpy)_3^{2+}$ and related compounds. In *Photochemistry and Photophysics of Metal Complexes*; Plenum Press: New York, 1994; pp Chapter 5.

(70) Villahermosa, R. Electron tunneling through phenylene bridges. Ph. D., California Institute of Technology, 2002.

(71) Caspar, J. V.; Westmoreland, T. D.; Allen, G. H.; Bradley, P. G.; Meyer, T. J.; Woodruff, W. H. *J. Am. Chem. Soc.* **1984**, *106*, 3492-3500.

(72) van Houten, J.; Watts, R. J. *J. Am. Chem. Soc.* **1976**, *98*, 4853-4858.

(73) Kilså, K.; Mayo, E. I.; Lewis, N. S.; Winkler, J. R.; Gray, H. B. *J. Phys. Chem.* **In Press**.

(74) Sauvé, G.; Cass, M. E.; Doig, S. J.; Lauermann, I.; Pomykal, K.; Lewis, N. S. *J. Phys. Chem. B* **2000**, *104*, 3488-3491.

(75) Ponce, A.; Gray, H. B.; Winkler, J. R. *J. Am. Chem. Soc.* **2000**, *122*, 8187-8191.

(76) Benkö, G.; Myllyperkiö, P.; Pan, J.; Yartsev, A. P.; Sundström, V. *J. Am. Chem. Soc.* **2003**, *125*.

(77) Murakoshi, K.; Kano, G.; Wada, Y.; Yanagida, S.; Miyazaki, H.; Matsumoto, M.; Murasawa, S. *J. Electroanal. Chem.* **1995**, *396*, 27-34.

(78) Hara, K.; Sugihara, H.; Singh, L. P.; Islam, A.; Katoh, R.; Yanagida, M.; Sayama, K.; Murata, S.; Arakawa, H. *J. Photochem. Photobiol. A-Chem.* **2001**, *145*, 117-122.

(79) Fillinger, A.; Parkinson, B. A. *J. Electrochem. Soc.* **1999**, *146*, 4559-4564.

(80) Wesley, W.; Wendlandt, M.; Hecht, H. G. In *Reflectance Spectroscopy*; Interscience Publishers: New York, 1966; pp 55-65.

(81) Kubelka, P. *J. Opt. Soc. Am.* **1948**, *38*, 448-457.

(82) Finnie, K. S.; Bartlett, J. R.; Woolfrey, J. L. *Langmuir* **1998**, *14*, 2744-2749.

(83) Argazzi, R.; Bignozzi, C. A.; Heimer, T. A.; Castellano, F. N.; Meyer, G. J. *Inorg. Chem.* **1994**, *33*, 5741-5749.

(84) Duffy, N. W.; Dobson, K. D.; Gordon, K. C.; Robinson, B. H.; McQuillan, A. J. *Chem. Phys. Letters* **1997**, *266*, 451-455.

(85) Deacon, G. B.; Phillips, R. J. *Coord. Chem. Rev.* **1980**, *33*, 227-250.

(86) Mehrotra, R. C.; Bohra, R. *Metal Carboxylates*; Academic Press: New York, 1983.

(87) Kilså, K., Unpublished results.

(88) Liu, D. K.; Brunschwig, B. S.; Creutz, C.; Sutin, N. *J. Am. Chem. Soc.* **1986**, *108*, 1749-1755.

(89) Moser, J. E.; Noukakis, D.; Bach, U.; Tachibana, Y.; Klug, D. R.; Durrant, J. R.; Humphry-Baker, R.; Grätzel, M. *J. Phys. Chem. B* **1998**, *102*, 3649-3650.

(90) Elliott, C.; Freitag, R.; Blaney, D. *J. Am. Chem. Soc.* **1985**, *107*, 4647-4655.

(91) Sayama, K.; Sugihara, H.; Arakawa, H. *Chem. Mat.* **1998**, *10*, 3825-3832.

(92) Asbury, J. B.; Hao, E.; Wang, Y.; Lian, T. Q. *J. Phys. Chem. B* **2000**, *104*, 11957-11964.

(93) Olivera-Pastor, P.; Maireles-Torres, P.; Rodriguez-Castellon, E.; Jimenez-Lopez, A. *Chem. Mater.* **1996**, *8*, 1758-1769.

(94) Guerrero, G.; Mutin, P. H.; Vioux, A. *Chem. Mater.* **2001**, *13*, 4367-4373.

(95) Pechy, P.; Rotzinger, F. P.; Nazeeruddin, M. K.; Kohle, O.; Zakeeruddin, S. M.; Humphry-Baker, R.; Grätzel, M. *Chem. Commun.* **1995**, *1*, 65-66.

(96) Yan, S. G.; Hupp, J. T. *J. Phys. Chem.* **1996**, *100*, 6867-6870.

(97) Gillaizeau-Gauthier, I.; Odobel, F.; Alebbi, M.; Argazzi, R.; Costa, E.; Bignozzi, C.; Meyer, G. J. *Inorg. Chem.* **2001**, *40*, 6073-6079.

(98) Zabri, H.; Gillaizeau, I.; Bignozzi, C.; Caramori, S.; Charlot, M.; Cano-Boquera, J.; Odobel, F. *Inorg. Chem.* **2003**, *42*, 6655-6666.

(99) Guerrero, G.; Mutin, P.; Vioux, A. *Chem. Mater.* **2001**, *13*, 4367-4373.

(100) Grätzel, M. *J. Photochem. Photobiol., C* **2003**, *4*, 145-153.

(101) Hara, K.; Sato, T.; Katoh, R.; Furube, A.; Ohga, Y.; Shinpo, A.; Suga, S.; Sayama, K.; Sugihara, H.; Arakawa, H. *J. Phys. Chem. B* **2003**, *107*, 597-606.

(102) Odobel, F.; Blart, E.; Lagree, M.; Villieras, M.; Boujtita, H.; El Murr, N.; Caramori, S.; Bignozzi, C. *J. Mater. Chem.* **2003**, *13*, 502-510.

(103) Ferrere, S. *Chem. Mat.* **2000**, *12*, 1083-1089.

(104) Hasselmann, G. M.; Meyer, G. J. *Z. Phys. Chemie-Int. J. Res. Phys. Chem. Chem. Phys.* **1999**, *212*, 39-44.

(105) King, K. A.; Spellane, P. J.; Watts, R. J. *J. Am. Chem. Soc.* **1985**, *107*, 1431-1432.

(106) Gao, R.; Ho, D. G.; Hernandez, B.; Selke, M.; Murphy, D.; Djurovich, P. I.; Thompson, M. E. *J. Am. Chem. Soc.* **2002**, *124*, 14828-14829.

(107) Lo, K. K.-W.; Chung, C.-K.; Lee, T. K.-M.; Lui, L.-H.; Tsang, K. H.-K.; Zhu, N. *Inorg. Chem.* **2003**, *42*, 6886-6897.

(108) Lamansky, S.; Djurovich, P. I.; Murphy, D.; Abdel-Razzaq, F.; Lee, H.-E.; Adachi, C.; Burrows, P. E.; Forrest, S. R.; Thompson, M. E. *J. Am. Chem. Soc.* **2001**, *123*, 4304-4312.